

**A Thesis Submitted for the Degree of PhD at the University of Warwick**

**Permanent WRAP URL:**

<http://wrap.warwick.ac.uk/83225>

**Copyright and reuse:**

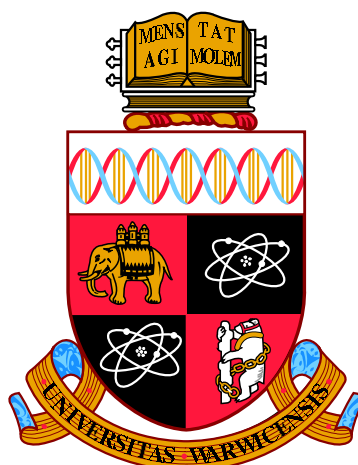
This thesis is made available online and is protected by original copyright.

Please scroll down to view the document itself.

Please refer to the repository record for this item for information to help you to cite it.

Our policy information is available from the repository home page.

For more information, please contact the WRAP Team at: [wrap@warwick.ac.uk](mailto:wrap@warwick.ac.uk)



# Development of Boron Doped Diamond Electrodes for Heavy Metal Detection

by

**Tania Louise Read**

**Thesis**

Submitted to the University of Warwick

for the degree of

**Doctor of Philosophy**

**Department of Chemistry**

June 2016

THE UNIVERSITY OF  
**WARWICK**

*To My Parents,  
My Grandparents,  
My Siblings,  
And the rest of my wonderful family,  
None of this would have been possible without your love and support.*



*"It Doesn't Stop Being Magic Just Because You Know How It Works."*

*~ Sir Terry Pratchett ~*

# Table of Contents

Table of Contents.....	i
Table of Figures.....	vi
Table of Tables.....	xiii
Abbreviations.....	xiv
Acknowledgements.....	xvi
Declarations.....	xvii
Abstract.....	xviii
1 Introduction.....	1
1.1 Overview.....	1
1.2 Heavy Metal Detection.....	1
1.2.1 Heavy Metal Speciation.....	3
1.2.2 Effect of pH on Heavy Metal Detection.....	3
1.2.3 Conventional Heavy Metal Detection Techniques.....	5
1.3 Electrochemistry.....	10
1.3.1 Electrodes.....	11
1.3.2 Cyclic Voltammetry.....	13
1.3.3 Stripping Voltammetry.....	16
1.3.4 Increasing Mass Transport.....	18
1.3.5 Current Issues with electrochemical detection of heavy metals.....	20
1.4 Boron Doped Diamond.....	21
1.4.1 Growth.....	22
1.4.2 Structure, doping and resulting properties.....	24
1.4.3 Electrode Properties.....	26
1.4.4 Electrode Fabrication.....	30
1.4.5 XRF.....	32
1.5 Confocal Laser Scanning Microscopy.....	36
1.6 Aims and Objectives.....	37
1.7 References.....	38
2 Experimental.....	45
2.1 Chemicals.....	45
2.2 Boron Doped Diamond.....	46



2.2.1	Laser Micromachining Electrodes.....	46
2.2.2	Back contacting and Electrode Fabrication .....	49
2.3	Characterisation of BDD Electrodes .....	50
2.3.1	Raman Analysis of BDD .....	50
2.3.2	Electrochemical Characterisation of BDD .....	51
2.3.2.1	Capacitance.....	51
2.3.2.2	Solvent Window .....	52
2.3.2.3	Redox Electrochemistry .....	52
2.4	Field-Emission Scanning Electron Microscopy (FE-SEM) .....	53
2.5	References.....	53
3	<i>In situ</i> Control of Local pH using a Boron Doped Diamond Ring Disc Electrode: Optimising Heavy Metal (Mercury) Detection .....	54
3.1.	Overview .....	54
3.2.	Introduction .....	55
3.3.	Experimental.....	57
3.3.1.	Solutions.....	57
3.3.2.	BDD probe fabrication .....	58
3.3.3.	pH generation .....	60
3.3.4.	Mercury Detection .....	60
3.3.5.	COMSOL Simulation .....	61
3.4.	Results and Discussion .....	64
3.4.1.	Effect of pH on Hg stripping .....	64
3.4.2.	Electrochemical Characterisation of Electrodes .....	66
3.4.3.	<i>In situ</i> $\Delta$ pH generation .....	67
3.4.4.	Simulation of pH profile at varied time and applied currents .....	70
3.4.5.	Simultaneous $\Delta$ pH generation and Hg detection.....	73
3.5.	Conclusion.....	74
3.6.	References .....	75
4	Manipulation and measurement of pH sensitive metal–ligand binding using electrochemical proton generation and metal detection .....	80
4.1	Overview .....	80
4.2	Introduction .....	80
4.3	Experimental .....	83
4.3.1	Solutions .....	83

4.3.2	Electrode Fabrication .....	83
4.3.3	UV-Vis Spectroscopy .....	85
4.3.4	Mineql+ speciation simulation.....	85
4.3.5	Electrochemistry .....	86
4.4	Results and Discussion .....	87
4.4.1	Preliminary Studies.....	87
4.4.1.1	TETA interference.....	87
4.4.1.2	Investigating Deposition Potential .....	90
4.4.1.3	Investigation of Proton Wave as a method to measure pH .....	92
4.4.2	UV-Vis Titration of Cu TETA vs. simulated speciation curves .....	96
4.4.3	UV-Vis titration of different ratios of Cu:TETA .....	98
4.4.4	UV-Vis of Cu TETA in the visible range .....	100
4.4.5	Bulk pH electrochemistry vs. simulated speciation curves .....	101
4.4.6	pH generation results .....	103
4.5	Conclusion.....	105
4.6	References.....	106
5	Development of Coplanar, Diamond Insulated, Boron Doped Diamond Ring Disc Electrodes. ....	108
5.1.	Overview .....	108
5.2.	Introduction .....	109
5.3.	Experimental.....	113
5.3.1.	Solutions.....	113
5.3.2.	COMSOL Simulation .....	114
5.3.3.	Dual Ring Discs .....	114
5.4.	Results and Discussion .....	114
5.4.1.	Electrode Fabrication .....	114
5.4.1.1.	Laser micromachining and back contacting.....	115
5.4.2.	Initial All-Diamond Ring Discs .....	118
5.4.2.1.	Initial Results .....	118
5.4.2.2.	Characterisation.....	123
5.4.3.	Effect of Geometries on pH Generation (simulation).....	129
5.4.3.1.	Disc Radius .....	130
5.4.3.2.	Ring Width.....	131
5.4.3.3.	Electrode Separation.....	133

5.4.4.	Electrochemical Characterisation of dual-ring discs .....	135
5.5.	Conclusions .....	138
5.6.	References .....	139
6	Investigating pH generation in buffered systems .....	141
6.1.	Outline.....	141
6.2.	Introduction .....	141
6.3.	Experimental .....	147
6.3.1.	Solutions.....	147
6.3.2.	Confocal Laser Scanning Microscopy .....	147
6.3.3.	FEM Simulation of Borate Buffer .....	150
6.4.	Results and Discussion .....	153
6.4.1.	Confocal fluorescence microscopy for investigation of pH generation in borate buffer. 153	
6.4.2.	Simulation of pH generation in borate buffer .....	158
6.5.	Conclusion .....	161
6.6.	References .....	162
7	Towards EC-XRF Analysis of Hg and Cd.....	165
7.1.	Outline.....	165
7.2.	Introduction .....	166
7.3.	Experimental .....	169
7.3.1.	Solutions.....	169
7.3.2.	Electrochemistry .....	169
7.3.3.	XRF .....	171
7.4.	Results and Discussion .....	171
7.4.1.	Cd Detection .....	175
7.4.1.1.	<i>Choice of Supporting Electrolyte</i> .....	175
7.4.1.2.	<i>Optimising Deposition Parameters</i> .....	176
7.4.1.3.	<i>Deposition Time</i> .....	176
7.4.1.4.	<i>Calibration</i> .....	179
7.4.2.	Hg Detection .....	180
7.4.2.1.	<i>Calibration</i> .....	180
7.4.2.2.	<i>Effect of Electrode Washing and Rotation</i> .....	181
7.4.3.	Selective Deposition From a Mixed Metal Solution.....	184
7.5.	Conclusion.....	187

7.6.	References .....	188
8	Conclusions and Future Directions .....	191
8.1.	Conclusions .....	191
8.2.	Future Directions .....	196
8.2.1.	Towards Ideal All Diamond Ring Disc Devices for pH Generation and control....	196
8.2.2.	Towards Ideal All Diamond Ring Disc Devices for <i>in situ</i> pH Generation and measurement with simultaneous analyte detection.....	198
8.3.	References .....	199

# Table of Figures

<b>Figure 1.1:</b> Schematic showing the ICP torch and sample introduction process of an ICP-MS. ....	6
<b>Figure 1.2:</b> Schematic showing the sampling arrangement in an ICP-MS. ....	7
<b>Figure 1.3:</b> Block diagram schematic of an AAS experiment. ....	9
<b>Figure 1.4:</b> Diagram of a three electrode cell. <sup>70</sup> .....	12
<b>Figure 1.5:</b> (a) Typical waveform of a cyclic voltammetry experiment. (b) Resulting cyclic voltammogram for a reversible system. ....	14
<b>Figure 1.6:</b> (A) Electrodeposition of metal ions, whereby at a suitable cathodic potential $X^{n+} + ne^-$ is electrodeposited as $X(s)$ on the electrode surface. (B) Stripping voltammetry, whereby solid metal is stripped from the surface by applying a suitable oxidative potential, resulting in a characteristic stripping peak. ....	16
<b>Figure 1.7:</b> Illustration depicting mass transport to a RDE. ....	19
<b>Figure 1.8:</b> Example of CVs in a reversible redox mediator under stationary (black) and rotating (blue) conditions. ....	19
<b>Figure 1.9:</b> Stripping response on BDD electrode for 0.5 $\mu M$ , 10 $\mu M$ and 30 $\mu M$ $Pb^{2+}$ in 0.1 M $KNO_3$ supporting electrolyte. Demonstrating the variation in peak shape and position in a single metal solution. Adapted from Hutton et al (2011). <sup>84</sup> .....	20
<b>Figure 1.10</b> - Diagram of the $sp^3$ carbon lattice structure of diamond. Black atoms represent carbon and blue is used to represent boron doping. ....	25
<b>Figure 1.11:</b> Comparison of solvent windows in 0.1 M $KNO_3$ solution for Freestanding BDD (black), Glassy Carbon (blue), and Platinum (green) electrodes. <sup>134</sup> .....	26
<b>Figure 1.12:</b> Illustration comparing inner sphere and outer electron transfer at an electrode surface. <sup>140</sup> .....	28
<b>Figure 1.13:</b> (a) Schematic showing the approximate position for $Ru(NH_3)_6^{3+}$ with respect to the potential of the valence band ( $E_{vb}$ ) and the conduction band ( $E_{cb}$ ) for $O^-$ terminated semiconducting BDD. $E_{1/2}$ values for several outer sphere redox mediators and $Fe(CN)_6^{4-/3-}$ are presented in the table. (b) Example CVs in 1mM $Ru(NH_3)_6^{3+/2+}$ taken on 1 mm BDD disc electrodes of varying dopant density. Both figures adapted from Macpherson (2015). <sup>73</sup> ....	29
<b>Figure 1.14:</b> Schematic of an energy dispersive XRF with secondary targets. Adapted from "Theory of XRF". <sup>158</sup> .....	32
<b>Figure 1.15:</b> (a) Schematic of the XRF process in which secondary X-ray fluorescence is produced via the irradiation of elements in a sample. (b) Example XRF spectrum for an environmental sample, each peak is representative of a single elemental fluorescence. ....	33
<b>Figure 1.16:</b> Schematic of a confocal laser scanning microscope. ....	36
<b>Figure 2.1:</b> Schematic illustrating a line of laser pulses at different focus on the diamond surface. There is a 100 $\mu m$ separation between the centre of each pulse in the x direction, and each adjacent pulse differs by 30 $\mu m$ in the z direction. The smallest dot indicates the best focus. ....	48
<b>Figure 3.1:</b> Schematic showing the process for assembling an epoxy sealed BDD ring disc electrode. ....	59

<b>Figure 3.2:</b> Schematic diagram of the simulation domain; an axisymmetric section of a water cylinder on top of a ring disc electrode arrangement defined by points $w_{1-3}$ and lengths $h$ and $w_r$ .	62
<b>Figure 3.3:</b> Stripping peaks recorded at a 0.922 mm diameter pBDD disc electrode at $0.1 \text{ V s}^{-1}$ in 1 mM $\text{Hg}^{2+}$ solutions (0.1 M $\text{KNO}_3$ ) at pH 2.0, pH 5.0, and pH 6.4. Starting potential was +1.5 V scanning negative to -1.2 V and then back to +1.5 V. Inset shows the full Hg deposition and stripping CV for a pH 2.0 solution.	65
<b>Figure 3.4:</b> Simulated speciation of 1 mM Hg in solution from Mineql+ speciation software, showing the % total Hg concentration in each form across the pH range 1-7.	66
<b>Figure 3.5:</b> CVs in 1 mM $\text{Ru}(\text{NH}_3)_6^{3+}$ for the BDD disc (left) and ring (right) electrodes at scan rates in the range $10 - 500 \text{ mV s}^{-1}$ .	67
<b>Figure 3.6:</b> (a) Schematic of the co-planar ring disc electrode geometry (not to scale) under constant current conditions where $\text{H}^+$ is generated at the ring and Hg is detected at the disc. (b) A typical OCP vs. pH calibration curve for the iridium oxide coated pBDD disc electrode. Inset shows the behaviour of the iridium oxide film in 1 M $\text{H}_2\text{SO}_4$ , as the electrode is cycled between 0 V and +1 V. (c) axisymmetrical $r$ - $z$ $\text{H}^+$ concentration profile for $\text{H}^+$ generation at the pBDD ring electrode at $t = 60 \text{ s}$ , for $i_{\text{ring}} = +50 \mu\text{A}$ . (d) pH response vs $t$ of the iridium oxide pBDD electrode (in the ring disc geometry) over a timescale of 600 s for $i_{\text{ring}}$ (at the ring electrode) = 0, +10, +20, +30, +40 and +50 $\mu\text{A}$ (solid = experimental data, dashed = simulated data).	68
<b>Figure 3.7:</b> Simulated pH profiles for $i_{\text{ring}} = +50 \mu\text{A}$ at $t =$ (a) 1 s, (b) 5 s, (c) 10 s, (d) 30 s, (e) 60 s, and (f) 600 s, showing the evolution of the pH profile with time. The pH colour scale is identical for all six profiles and the ring and disc placements are illustrated above the $r$ axis.	71
<b>Figure 3.8:</b> Simulated pH profiles after 60 s generation for $i_{\text{ring}} =$ (a)+ 10 $\mu\text{A}$ , (b)+ 20 $\mu\text{A}$ , (c)+ 30 $\mu\text{A}$ , and (d)+ 40 $\mu\text{A}$ . The pH colour scale is identical for all four profiles and the ring and disc placements are illustrated above the $r$ axis.	72
<b>Figure 3.9:</b> Hg stripping peaks recorded on the disc of the ring disc electrode at $0.1 \text{ V s}^{-1}$ in 1 mM $\text{Hg}^{2+}$ solutions at pH 6.4 (red), pH 2.0 solution (blue), and pH 6.4 solution (purple) but with $i_{\text{ring}} = +50 \mu\text{A}$ to generate a local pH of 2.0 over the disc electrode.	74
<b>Figure 4.1:</b> Schematic of BDD ring disc assembly in the teflon mould. Conductive silver epoxy is used to attach copper wires to the Ti/Au contacts on the rear of the electrodes, before sealing the arrangement with non-conductive epoxy.	85
<b>Figure 4.2:</b> CVs in 100 $\mu\text{M}$ TETA solution with 0.1 M $\text{KNO}_3$ supporting electrolyte at different bulk pH values, pH adjusted using 0.1 M HCl and 0.1 M KOH. Inset shows zoomed region where $\text{Cu}^{2+}$ stripping signal would appear in Cu containing solutions.	88
<b>Figure 4.3:</b> UV-Vis absorbance between 200 – 400 nm for (a) 100 $\mu\text{M}$ $\text{Cu}^{2+}$ and (b) 100 $\mu\text{M}$ TETA solutions at a range of pH values between pH 1.5 – 6.0 (adjusted using HCl).	90
<b>Figure 4.4:</b> CV for 100 $\mu\text{M}$ Cu in 0.1 M $\text{KNO}_3$ supporting electrolyte at pH 2, showing calculation of $E_{1/2}$ .	91
<b>Figure 4.5:</b> CVs in 1 mM Cu and 1 mM TETA mixture in 0.1 M $\text{KNO}_3$ supporting electrolyte at pH 2 (adjusted using 0.1 M $\text{HNO}_3$ ), scanned out to varying cathodic potentials (-0.3 V, -0.4 V, -0.5 V, -0.6 V, -0.8 V, -0.9 V, -1 V). Inset shows a zoomed area of the $\text{Cu}^{2+}$ stripping peak.	91

<b>Figure 4.6:</b> CVs in 1 mM Cu and 1 mM TETA mixtures with 0.1 M KNO <sub>3</sub> supporting electrolyte at pH 2.00 (Grey) 2.30 (Pink) and 6.03 (Turquoise), adjusted using 0.1 M HNO <sub>3</sub> and 0.1 M KOH at 0.1 mVs <sup>-1</sup> . Inset shows copper stripping peaks. ....	93
<b>Figure 4.7:</b> CV at 0.1 Vs <sup>-1</sup> in 1 mM Cu <sup>2+</sup> and 1 mM TETA solution with 0.1 M KNO <sub>3</sub> supporting electrolyte adjusted to bulk pH 6.03 using KOH. A range of generator currents (10, 15, 50 and 70 µA) were applied to the ring electrode for 3 mins prior to, and during, CV recordings. Dashed lines denote the pH value calculated using peak current. ....	94
<b>Figure 4.8:</b> CVs at 0.1 Vs <sup>-1</sup> in 100 µM Cu <sup>2+</sup> and 100 µM TETA solution with 0.1 M KNO <sub>3</sub> for bulk pH 6.35 (turquoise) and 2.3 (pink) solutions (adjusted using 0.1 M HNO <sub>3</sub> and KOH), dashed lines show theoretical proton wave currents. A CV in pH 6.35 solution with 15 µA applied to the generator electrode for 3 mins prior to, and during, the CV is shown in black, the average pH across the disc is calculated to be pH 3.00. ....	95
<b>Figure 4.9:</b> Simulation of the average pH vs. time across the disc (detector) electrode for an applied generator current of 15 µA. At 300s a CV is run on the disc electrode at 0.1 V s <sup>-1</sup> , the resulting pH change is highlighted in grey. ....	96
<b>Figure 4.10:</b> (a) Simulated speciation curves for 100 µM Cu <sup>2+</sup> (Cu(NO <sub>3</sub> ) <sub>2</sub> ) and 100 µM TETA (ionic strength = 300 µM) across the pH range 1 - 10, expressed as % of total copper for free Cu <sup>2+</sup> (black), Cu[HTETA] <sup>3+</sup> (blue), Cu[TETA] <sup>2+</sup> (red) and total Cu[HTETA] <sup>3+</sup> + Cu[TETA] <sup>2+</sup> (purple). (b) UV-Vis data, corresponding to Cu[HTETA] <sup>3+</sup> + Cu[TETA] <sup>2+</sup> for a pH titration of 100 µM Cu <sup>2+</sup> and 100 µM TETA mixture via 25 dropwise additions of HCl (starting pH = 5.23, end pH = 1.69). Peak maxima / peak maximum (for maximum absorbance) × 100 % (■) is plotted on (a). ....	98
<b>Figure 4.11:</b> Calibration data for absorbance peak maxima when Cu <sup>2+</sup> is 100% bound by TETA (pH 5.0) at concentrations between 10 and 200 µM (1:1 ratio) Slope = 0.00392 ± 0.0000314, R <sup>2</sup> = 0.9997. ....	99
<b>Figure 4.12:</b> Absorbance peak maximum data for mixtures of Cu <sup>2+</sup> and TETA at different ratios 1:1 (■), 1:2 (■), and 2:1 (■), Cu:TETA, where 1 part is equivalent to 100 µM. ....	100
<b>Figure 4.13:</b> UV-Vis data, corresponding to Cu <sup>2+</sup> , and Cu[HTETA] <sup>3+</sup> + Cu[TETA] <sup>2+</sup> for a pH titration of 10 mM Cu <sup>2+</sup> and 10 mM TETA mixture via dropwise additions of HCl (starting pH = 1.69, end pH = 5.23). Inset shows an enlarged version of the free Cu <sup>2+</sup> peak at acidic pH for clarity. ....	101
<b>Figure 4.14:</b> (a) ASV curves for Cu <sup>2+</sup> stripping for solution pH values in the range 2.50, 2.99, 3.52, 4.05, 5.01, in a 100 µM Cu <sup>2+</sup> and 100 µM TETA solution with 0.1 M KNO <sub>3</sub> added as supporting electrolyte, scan rate = 0.1 V s <sup>-1</sup> . (b) ASV (i <sub>p</sub> / i <sub>p,max</sub> × 100 %) data (◆) plotted as a function of pH. Also shown are the simulated speciation curves for the equivalent solution experimental conditions for free Cu <sup>2+</sup> (black), Cu[HTETA] <sup>3+</sup> (blue), Cu[TETA] <sup>2+</sup> (red), ionic strength = 0.1003 M. ....	103
<b>Figure 4.15:</b> LSV data corresponding to Table 1 in the main text, showing normalised stripping peaks (i <sub>p</sub> /i <sub>p,max</sub> × 100%) of 100 µM Cu <sup>2+</sup> in the presence of 100 µM TETA at the detector electrode, for a range of constant currents applied to the generator (0.1 – 1.98 mA cm <sup>-2</sup> ). ....	104
<b>Figure 5.1:</b> Schematic showing the process used to create BDD UME arrays encased in insulating diamond. Figure taken from Macpherson et al. <sup>17</sup> ....	111

<b>Figure 5.2:</b> Nanocrystalline BDD UME array developed by Nebel et al. <sup>20</sup> (a) and (b) show SEM images of the array and a single UME respectively. (c) Illustrates the layered structure. Figure taken from Nebel et al. <sup>20</sup> .....	112
<b>Figure 5.3:</b> Figure demonstrating (a) the process developed to produce co-planar all diamond electrodes, (b) some example electrode geometries possible using this method, and (c) SEM and optical images of actual all diamond devices created using this method. Figure taken from Joseph et al. <sup>23</sup> .....	113
<b>Figure 5.4:</b> Schematic illustrating the process for creating BDD ring disc electrodes sealed in an insulating diamond substrate. Insulating diamond is laser micromachined into trenches of the desired geometry, overgrown with BDD, then polished back to reveal the electrode faces. ....	115
<b>Figure 5.5:</b> Illustration of the process of laser back contacting the disc of an all diamond ring disc electrode. A circular laser program is applied for 1 pass, before the depth is measured using interferometry, this is repeated and the depths used to calculate the number of laser passes needed to reach the rear of the BDD electrode (shown in the final step). ....	116
<b>Figure 5.6:</b> Schematic illustrating the Ti/Au sputter contacting of a back contacted all-diamond ring disc device. Firstly, a Lasered kapton mask is placed over the rear of the electrode, leaving only the lasered back contact holes clear. A 10 nm layer of Ti is sputtered over the entire surface, followed by a 300 nm layer of Au. The mask is peeled back revealing the Ti/Au sputtered contacts; the electrode is now ready to be annealed. ....	117
<b>Figure 5.7:</b> Scaled up diagram of the first substrate of all-diamond ring disc electrodes. Disc radii range from 125 $\mu\text{m}$ to 500 $\mu\text{m}$ , ring widths used were either 50 $\mu\text{m}$ or 100 $\mu\text{m}$ , and electrode separation was either 25 $\mu\text{m}$ or 50 $\mu\text{m}$ (sizes as programmed for lasering). Electrodes are numbered 1 to 25, "Failed" denotes electrodes with large defects present after growth. The black circles represent the locations of the outer circumference of the ring and disc electrodes for each device. ....	119
<b>Figure 5.8:</b> SEM images showing representative examples of (a) a "Good", successful all-diamond ring disc electrode, yellow dashes highlight the "halo" where sidewall and bottom growth meet, (b) an "OK" all-diamond ring disc electrode, which is successful but has some small defects (highlighted in red), and (c) a "Bad" all-diamond ring disc electrode, with dark cracks visible around the centre of the ring. Note, the darker areas in each image with clear grain structure are BDD and the paler areas are insulating diamond. ....	120
<b>Figure 5.9:</b> Schematics illustrating BDD overgrowth in (a) a shallow trench where lateral and vertical growth are similar, (b) a deep trench where lateral growth dominates and vertical growth is limited, and (c) a deep trench where lateral growth completely shadows the bottom of the trench, preventing vertical growth and leaving a void. ....	122
<b>Figure 5.10:</b> Representative example of raman data on an insulating diamond area of a generation 1 all-diamond ring disc electrode using a 514.5 nm laser and 50 $\times$ magnification. ....	124
<b>Figure 5.11:</b> Representative examples of Raman data for a BDD ring and disc in a generation 1 all-diamond ring disc for (a) Ring, light grain. (b) Ring, dark grain. (c) Disc, light grain. (d) Disc, dark grain. This data was collected from RD1 using a 514.5 nm laser and 50 $\times$ magnification. ....	125
<b>Figure 5.12:</b> Example solvent window, recorded in 0.1 M $\text{KNO}_3$ at 100 mVs <sup>-1</sup> for the disc of RD20, diameter 500 $\mu\text{m}$ . ....	126



<b>Figure 5.13:</b> (a) Simulated average pH vs. time profiles at the disc electrode for a range of ring discs with different disc radii, 1500 $\mu\text{m}$ , 500 $\mu\text{m}$ , 250 $\mu\text{m}$ , 125 $\mu\text{m}$ . Ring width was maintained at 100 $\mu\text{m}$ , and electrode separation at 50 $\mu\text{m}$ for all simulations. The current density applied to the ring (generator) was 6.63 $\text{mA cm}^{-2}$ . Inset shows plot of disc radius vs. plateau pH, $R^2 = 0.9996$ . Schematics illustrating electrodes with disc radius (b) 1500 $\mu\text{m}$ , (c) 500 $\mu\text{m}$ , (d) 250 $\mu\text{m}$ , and (e) 125 $\mu\text{m}$ , not to scale.....	131
<b>Figure 5.14:</b> (a) Simulated average pH vs. time profiles across the disc electrode for a range of ring disc electrodes with different ring width, 50 $\mu\text{m}$ , 100 $\mu\text{m}$ , 200 $\mu\text{m}$ , 260 $\mu\text{m}$ . Disc radius was maintained at 500 $\mu\text{m}$ , and electrode separation at 50 $\mu\text{m}$ for all simulations. The current density applied to the ring (generator) was 6.63 $\text{mA cm}^{-2}$ . Schematics illustrating electrodes with ring width (b) 1500 $\mu\text{m}$ , (c) 500 $\mu\text{m}$ , (d) 250 $\mu\text{m}$ , and (e) 125 $\mu\text{m}$ , not to scale. ....	132
<b>Figure 5.15:</b> Simulated average pH vs. time profiles across the disc electrode for a range of ring disc electrodes with different electrode separations, 25 $\mu\text{m}$ , 50 $\mu\text{m}$ , 100 $\mu\text{m}$ , 200 $\mu\text{m}$ . Disc radius was maintained at 500 $\mu\text{m}$ , and ring width at 100 $\mu\text{m}$ for all simulations. The current density applied to the ring (generator) was 6.63 $\text{mA cm}^{-2}$ . Inset shows a plot of electrode separation vs. plateau pH. ....	133
<b>Figure 5.16:</b> Example data for an all-diamond dual-ring disc electrode, showing capacitance (double layer) for the outer ring; this electrode had two connections, capacitance data for each is shown (grey & black) to be almost identical. ....	138
<b>Figure 6.1:</b> Schematics illustrating literature examples of pH control. (a) Via electrochemical decomposition of water in hydroponic nutrient tanks, <sup>17</sup> (b) thin layer cell with proton pump and proton selective detector membrane, <sup>18</sup> and (c) experimental setup of the combined SECM-SMFS system, where the SECM tip is used to induce a pH change. <sup>19</sup> .....	146
<b>Figure 6.2:</b> Illustration of an all diamond dual-ring disc electrode (disc radius 250 $\mu\text{m}$ , separations = 100 $\mu\text{m}$ and ring widths = 100 $\mu\text{m}$ ), where black represents BDD and blue represents insulating diamond. Only the Inner ring was used for the experiments described in this chapter. ....	148
<b>Figure 6.3:</b> Illustration of the experimental electrode arrangement used for the imaging of proton generation via CLSM. ....	150
<b>Figure 6.4:</b> Confocal data for pH generation with 16.66 $\mu\text{A}$ (+6.63 $\text{mA cm}^{-2}$ ) applied to the ring of an all diamond dual-ring disc electrode. Measured $\sim 20 \mu\text{m}$ below the electrode surface in solutions containing 0.1 M $\text{KNO}_3$ and 8 $\mu\text{M}$ Fluorescein, initial pH 8.34. (a) xt data, and xyt data for (b) 0.2 s, (c) 0.4 s, (d) 1.6 s, and (e) 6 s after beginning generation. False coloured for clarity. ....	154
<b>Figure 6.5:</b> Schematic showing the location of the line scan 'x' in xt experiments.....	155
<b>Figure 6.6:</b> Confocal xt data for pH generation with 16.66 $\mu\text{A}$ (+6.63 $\text{mA cm}^{-2}$ ) applied to the ring of an all diamond dual-ring disc electrode. Measured $\sim 20 \mu\text{m}$ below the electrode surface in solutions containing 0.1 M $\text{KNO}_3$ , 8 $\mu\text{M}$ Fluorescein, and (a) 0.1 mM borate buffer (pH 8.67), (b) 1 mM borate buffer (pH 8.88), and (c) 10 mM borate buffer (pH 8.88), time (s) increases from top to bottom through individual images, and left to right through the 6 images. ....	157
<b>Figure 6.7:</b> Schematic demonstrating the analysis of confocal xt data in relation to the electrode surface (a) Vertical cross section, and (b) Horizontal view of the electrode surface with example xt data for comparison. ....	159

<b>Figure 6.8:</b> (a) Experimental and (b) simulated progression of the proton front at pH 6.1 (50% fluorescence intensity) across the disc electrode with time from confocal xt data for: 0 mM (black), 0.1 mM (grey), and 1 mM (pink), and 10 mM (purple) borate buffer solutions, in 0.1 M KNO <sub>3</sub> and 8 μM fluorescein. 10 mM data smoothed via adjacent averaging to remove noise. ....	160
<b>Figure 7.1:</b> In house built rotating disc assembly. ....	169
<b>Figure 7.2:</b> (a) Optical images of BDD electrode before and after electrochemical deposition of 10 ppm Pb. Gold on the 'before' image indicates the location of the Ti/Au contacts on the backside of the BDD disc. (b) Schematic showing the deconstructed rotating disc arrangement. (c) Schematic of the experimental set-up for electrochemical deposition using the BDD rotating disc electrode. ....	170
<b>Figure 7.3:</b> CVs in 1 mM Ru(NH <sub>3</sub> ) <sub>6</sub> <sup>3+/2+</sup> solution containing 0.1 M KNO <sub>3</sub> supporting electrolyte, using new rotator electrode for (a) Stationary conditions (b) Comparison of limiting currents for rotation rates of 10, 15, 20, 25 and 30 Hz (▪) with theoretical values predicted using the Levich equation (black line). Adapted from Hutton et al (2014). <sup>9</sup> .....	173
<b>Figure 7.4:</b> XRF data showing EC-XRF data for 0.25 ppm Hg (pink) vs. UltraCarry (purple) data for 0.25 ppm (solid), 0.5 ppm (dot), 1 ppm (dash), and 10 ppm (dot-dash). Experiments were conducted from solutions containing 0.1 M KNO <sub>3</sub> supporting electrolyte, deposition time for EC-XRF and drying time for UltraCarry were kept constant at 4000 s. Electrodeposition for EC-XRF was conducted at -1.75 V. ....	174
<b>Figure 7.5:</b> XRF data for Cd solutions in 0.1 M NaNO <sub>3</sub> , showing EC-XRF data (Pink) vs. UltraCarry XRF (Purple) data at 1 ppm (solid), and additionally for UltraCarry XRF 100 ppm (dash-dot), 50 ppm (dashed), 10 ppm (dot), and 0.5 ppm (half-dot) concentrations of Cd. ....	175
<b>Figure 7.6:</b> EC-XRF data demonstrating the effect of deposition time for 1 ppm Cd solutions deposited at -1.75 V for 4000 s (pink) and 2000 s (purple). ....	177
<b>Figure 7.7:</b> Solvent window for BDD EC-XRF electrode in 0.1 M KNO <sub>3</sub> . ....	178
<b>Figure 7.8:</b> (a) EC-XRF data demonstrating the effect of deposition potential for 1 ppm Cd solutions deposited for 4000 s at -1 V, -1.5 V, and -1.75V. (b) deposition potential vs. EC-XRF signal intensity. ....	179
<b>Figure 7.9:</b> (a) EC-XRF data and (b) Calibration data showing mean EC-XRF Cd <sub>IX</sub> peak intensity vs. Cd deposition solution concentration for 3 experimental repeats; slope = 6.21 ± 0.15 cpa mA <sup>-1</sup> ppm <sup>-1</sup> , R <sup>2</sup> = 0.997. Electrodeposition was conducted prior to experiments for 4000 s at -1.75 V for solutions of Cd concentrations between 0.05 ppm and 1 ppm. ....	180
<b>Figure 7.10:</b> (a) EC-XRF data and (b) XRF signal intensity vs. deposition solution concentration, for different concentrations of Hg (0.05 ppm to 1 ppm) deposited for 4000 s at -1.75 V. ....	181
<b>Figure 7.11:</b> EC-XRF data for 1 ppm Hg solutions deposited at -1.75 V for 4000 s with (purple) and without (pink) washing after deposition, demonstrating that some XRF signal intensity is lost after the washing process. ....	182
<b>Figure 7.12:</b> SEM images for 1 ppm Hg deposited under rotating conditions for 4000s at -1.75 V. All images are from different areas of the same electrode and the same instance of deposition. (a) Droplets (indicated by green lines); some appear to be coalescing into larger droplets (highlighted in green circles). (b) Droplets (e.g. highlighted in green) with clear channels (example bordered in yellow dashes). (c) Branched channels with square pools at	

<i>the terminus (e.g. Green highlighted area). (d) Square/rectangular terminus of branched structures (e.g. highlighted by green arrow). .....</i>	<i>183</i>
<b>Figure 7.13:</b> LSVs showing the onset of electrodeposition for (a) Cadmium and (b) Mercury at 0.5 ppm. ....	185
<b>Figure 7.14:</b> EX-XRF data for (a) Cd and (b) Hg, in mixed metal solutions of 1 ppm Hg and 1 ppm Cd deposited at -0.5 V and 1.75 V for 4000 s. ....	187
<b>Figure 8.1:</b> Schematic of the proposed method for all diamond ring-UME growth, step 1 forming the BDD UME disc in insulating diamond. ....	197
<b>Figure 8.2:</b> Schematic of the proposed method for all diamond ring-UME growth. Step 2, producing the ring. ....	197

# Table of Tables

<b>Table 1.1:</b> Acceptable limits for common heavy metals in drinking water <sup>12</sup> and the environment. <sup>13</sup> *Calculated guideline value is below achievable quantification level. † Dependent on water hardness. ....	2
<b>Table 2.1:</b> List of chemicals used in this thesis and the suppliers. ....	45
<b>Table 3.1:</b> Summary of boundary conditions used for the simulation of the pH during the ring generation experiment. ....	63
<b>Table 4.1:</b> Comparison of experimentally recorded ASV ( $i_p / i_{p,max} \times 100\%$ ) data as a function of the applied generator current in 100 $\mu\text{M}$ $\text{Cu}^{2+}$ and 100 $\mu\text{M}$ TETA solution with 0.1 M $\text{KNO}_3$ . ....	104
<b>Table 5.1:</b> Table of all-diamond ring disc devices in generation 1, measurements taken from FE-SEM images and analysis of successful electrode growth. Halo defines the region where diamond growing from the side wall meets diamond growing from the trench base. ....	121
<b>Table 5.2:</b> Summary of electrochemical characterisation data for all-diamond devices RD1 and RD20. ....	128
<b>Table 5.3:</b> Summary of electrochemical characteristics of dual-ring disc electrode 1. ....	137
<b>Table 6.1:</b> Initial conditions of the system defined as parameters according to experimental inputs. ....	151
<b>Table 6.2:</b> Parameters added to the pH generation simulation to describe borate buffer and dissolved carbon dioxide equilibria. * <sup>26</sup> ....	151
<b>Table 6.3:</b> Reaction equations for chemical species present in solution. FR denotes the rate constant, here assumed to be $1 \times 10^6$ , and $K_w$ is equal to $10^{-13.995}$ at 25°C. <sup>31</sup> ....	153

# Abbreviations

BDD	Boron Doped Diamond
CVD	Chemical Vapour Deposition
HPHT	High-Pressure-High-Temperature
MWCVD	Microwave Chemical Vapour Deposition
HFCVD	Hot-Filament Chemical Vapour Deposition
NDC	Non-diamond Carbon
CV	Cyclic Voltammogram/Voltammetry
ASV	Anodic Stripping Voltammetry
DPV	Differential Pulse Voltammetry
LSV	Linear Stripping Voltammetry
XRF	X-Ray Fluorescence
ICP	Inductively Coupled Plasma
ICP-MS	Inductively Coupled Plasma Mass Spectrometry
AAS	Atomic Absorption Spectroscopy
AFS	Atomic Fluorescence Spectroscopy
LOD	Limit of Detection
LOQ	Limit of Quantitation
EC-XRF	Electrochemical X-Ray Fluorescence
TR-XRF	Total Reflection X-Ray Fluorescence
WE	Working Electrode
RE	Reference Electrode
CE	Counter Electrode
SCE	Saturated Calomel Electrode
HDME	Hanging Drop Mercury Electrode
TFME	Thin Film Mercury Electrode

RDE	Rotating Disc Electrode
WJE	Wall Jet Electrode
SIMS	Secondary Ion Mass Spectrometry
TETA	Triethylenetetraamine
CNC	Computer Numerical Control
CLSM	Confocal Laser Scanning Microscopy
FE-SEM	Field-Emission Scanning Electron Microscopy
RF	Radio-Frequency
AFM	Atomic Force Microscopy
DE	Dual Electrode
OCP	Open Circuit Potential
PDA	Peripheral Differential Amplifier
FEM	Finite Element Methods
TETA	Triethylenetetraamine
UME	Ultra-Micro Electrode

# Acknowledgements

Firstly, I would like to thank my supervisor Prof. Julie Macpherson for her support and guidance (and, when necessary, patience) during my PhD - your encouragement and advice have been truly invaluable. Thank you also to Professors Mark Newton and Pat Unwin, for always being happy to share their time, knowledge and experience. Working with all three of you has been both inspiring and enjoyable. I would like to acknowledge Element Six, and WCPRS for providing the funding for this opportunity.

To everyone in the Warwick Electrochemistry and Interfaces Group who have helped me during my PhD, whether it be with something complicated or on occasion simply reminding me to actually attach the crocodile clips to my electrodes, my sincere thanks. Special thanks to Dr. Eleni Bitziou for being both mentor and friend, and to Dr. Max Joseph for never getting fed up with me breaking Comsol. To the wonderful friends I've made, it's been a great few years working alongside you and I must thank you for all the help, hilarity, and at times complete insanity that has got me through both the highs and the lows. Also to Liz and Zoë, for the motivational cat pictures. Thanks to Paul for being there throughout my PhD, for understanding (challenging sometimes I know!), and for always knowing how to make me laugh (often unintentionally).

To my parents, thank you for your support, for encouraging me to believe in myself, and for inspiring me to always do the best I can. To my siblings and cousins thank you for being both my family and my friends, never forget you can do anything if you put your mind to it! Finally, thanks to my grandparents and the rest of my family for always being there. Without you I could never have done this.

# Declarations

The work presented in this thesis is entirely original and my own work, except where acknowledged in the text. I confirm that this thesis has not been submitted for a degree at another university. Fluorescence Microscopy experiments in Chapter 6 were carried out with the help of Dr. Rehab Al Botros, Ashley Page, and David Perry.

Chapter 3 was published as:

*In-situ Control of Local pH using a Boron Doped Diamond Ring Disk Electrode: Optimizing Heavy Metal (Mercury) Detection.* T. L. Read, E. Bitziou, M. B. Joseph and J. V. Macpherson, *Anal. Chem.*, **2014**, 86 (1), 367–371.

Chapter 4 was published as:

*Manipulation and Measurement of pH sensitive Ligand-Metal Binding Using Electrochemical Proton Generation and Metal Detection.* T. L. Read, M. B. Joseph and J. V. Macpherson, *Chem. Comm.*, **2016**, 52, 1863-1866.

Work from Chapter 5 was published in:

*A Fabrication Route for the Production of Co-Planar, Diamond Insulated, Boron Doped Diamond Macro and Microelectrodes of any Geometry.* M. B. Joseph, E. Bitziou, T. L. Read, L. Meng, N. L. Palmer, T. P. Mollart, M. E. Newton and J. V. Macpherson, *Anal. Chem.*, **2014**, 86 (11), 5238–5244.



# Abstract

Due to their high toxicity and prevalence in natural waters, trace heavy metals are of great concern to environmental analysts. The development of techniques with the ability to detect and quantify ppb levels of heavy metal species in the environment, without the need for sample removal and pretreatment, is therefore a key interest. Popular methods for heavy metal detection such as X-ray Fluorescence (XRF) provide easy elemental identification but lack the low detection limits desirable, whereas electrochemical methods can provide low detection limits but signal assignment in complex samples is often difficult. In addition to this, one of the biggest issues with current methods is the non-ideal nature of the environmental matrices for analysis, for example where the pH of natural waters is usually in the range 6-9; Heavy metal analysis is generally improved under acidic conditions. In this thesis a number of methods are developed with the aim of addressing these issues and moving towards *in situ* heavy metal detection. Electrochemistry offers an ideal platform for *in situ* use due to its ease of portability and low power requirements, furthermore the use of conductive boron doped diamond (BDD) electrodes provide a robust sensor resistant to both corrosion and fouling and therefore ideal for long term environmental deployment. Herein BDD dual electrode systems are developed and employed for electrochemical heavy metal detection with simultaneous control of local pH. Fabrication and electrochemical characterisation of these devices is described and compared to finite element simulation. It is shown that using such devices it is possible to control the local pH of a solution even in solutions containing up to 10 mM buffer, allowing manipulation of heavy metal (Hg and Cu) speciation and therefore improved electrochemical detection. The development of all-diamond ring disc electrodes is described; by growing BDD electrodes in insulating diamond, robust well-sealed devices where the sensor and its housing both exhibit the desirable mechanical properties of diamond can be produced. Finally, the newly developed Electrochemical XRF (EC-XRF) technique is optimised and applied to the detection of Cd and Hg.

# 1 Introduction

## 1.1 Overview

In this thesis novel approaches to improving electrochemical heavy metal detection using Boron Doped Diamond (BDD) electrodes are developed and investigated. Several systems are explored and validated using a range of exemplar heavy metal systems (Hg, Cu, Cd). Electrode geometries are considered and fabrication methods developed with a view towards *in situ* heavy metal monitoring capabilities. This chapter introduces the reader to the principal techniques and tools used, and the theory behind them; particularly BDD, heavy metal measurement and electrochemical methods.

## 1.2 Heavy Metal Detection

Although there is arguably no standardized definition,<sup>1</sup> heavy metal is the term used to describe metals (and some metalloids) of relatively high atomic mass associated with negative health or environmental impact;<sup>2</sup> typical examples include mercury (Hg), cadmium (Cd), lead (Pb), copper (Cu) and arsenic (As).<sup>3</sup> Heavy metals are a key concern in the environment, due to their toxicity. They are present from both natural and anthropogenic sources and monitoring heavy metal levels in our surroundings is of vital importance.<sup>4,5</sup> When introduced into a biological system in excess heavy metals exhibit a variety of malign effects, including damage to the central nervous system, vital organs, blood and muscles. There is also evidence that some heavy metals e.g. Cd, As, Cr and their compounds are carcinogenic.<sup>6, 7</sup> Additionally, heavy

metals bioaccumulate in the food chain, increasing the risk they pose to apex predators such as humans.<sup>8</sup>

Industrialisation of the modern world has seen a dramatic increase in the heavy metal levels artificially released into the environment,<sup>9</sup> the significance of which has become apparent in more recent years, with heavy metals connected to multiple historical cases of widespread poisoning.<sup>10, 11</sup> In response to this, the World Health Organisation have dedicated much time and effort to studying the heavy metals of key importance, and their impact on health and the environment. As a result, a number of metals have been identified as a key concern to environmental scientists including Hg, Cu, and Cd, acceptable levels in drinking and environmental water have been defined in legislation and are presented in **Table 1.1**.

**Table 1.1:** Acceptable limits for common heavy metals in drinking water<sup>12</sup> and the environment.<sup>13</sup> \*Calculated guideline value is below achievable quantification level. † Dependent on water hardness.

Heavy Metal	Limit in Drinking Water (mg/L)	Environmental Freshwater Limits† (mg/L)
Hg (Inorganic)	0.006	0.00001
Cd	0.003	0.0001
Pb	0.01*	0.001 - 0.007
Cu	2	0.001
As	0.01*	0.05
Cr	0.05	0.0034 (IV) 0.0047 (III)

### **1.2.1 Heavy Metal Speciation**

Heavy metal analysis is not limited solely to the pure ionic form of the metal, but of the different species, and physicochemical forms related to other elements and compounds present.<sup>14</sup> The behaviour of a heavy metal in the environment and the body varies for different chemical forms, with some exhibiting more toxicity than others;<sup>15</sup> toxicity is inherently linked to the bioavailability of the metal species. Bioavailable metals, generally those not strongly complexed to organic ligands, are easily absorbed and can therefore accumulate in the body in toxic quantities.<sup>16</sup> As such, it is of importance to the analyst to understand the speciation of the analyte, that is, the nature of the forms present and the effect of external factors on these forms.<sup>17</sup> Measurement of solely the total metal content does not provide enough information on toxicity levels.<sup>18</sup> Speciation is affected not only by the presence of other species, but also by environmental conditions such as pH, water hardness, and temperature.<sup>19</sup> As a technique, speciation measurements are defined as the identification and quantitative determination of the chemical species that make up the total concentration of a particular element in a system.<sup>18</sup>

### **1.2.2 Effect of pH on Heavy Metal Detection**

Solution pH, and the ability to control it, is key to many processes,<sup>20,21, 22</sup> its importance in heavy metal detection is of interest for the purpose of sensitive analysis. As mentioned previously, solution pH can control metal complexation and therefore (bio)availability.<sup>23, 24</sup> Generally the analysis of

metals in natural waters requires the solution pH to stay close to that of the source, as any variation will affect speciation and potentially give an unrealistic measure of the (bio)available metal concentration.<sup>19</sup> However, it is often necessary to remove the sample from the source for analysis by most techniques, this is either due to their lack of portability (e.g. see section 1.2.3) or in order to avoid matrix effects and interferences via pretreatment.<sup>25</sup> Removal from the source and sample preparation methods often affect pH and therefore speciation, for example degassing via bubbling with nitrogen to remove O<sub>2</sub> interferences will also strip dissolved CO<sub>2</sub> and consequently raise the pH.<sup>26</sup> These pH changes affect analysis as at high pH metal activity is decreased, whereas low pH values favour the liberation of complexed metals so it is necessary to buffer the solution so the desired pH is maintained.<sup>27</sup> This is especially true for electrochemical studies, where commonly acetate buffer is used to this end (buffers to pH ~ 5 – 7);<sup>28</sup> acetate binds weakly to metal species in solution ( $K_f \sim 10^{-3}$ )<sup>29</sup> such that they are still labile and electrochemically accessible, as with hydrated ions.<sup>19</sup>

Different analytical techniques, discussed in section 1.2.3, provide different information about the system. For two of the most popular methodologies, Inductively Coupled Plasma (ICP) based techniques provide total metal content *i.e.* concentration of both ligand bound and free metal ions, whilst electrochemical analysis provides information on the free metal ions only.<sup>30</sup> By lowering the pH suitably in the sample, the number of bioavailable or labile metal ions will increase, due to liberation of metals as a result of protonation

of the binding ligands.<sup>31, 32</sup> If the pH is lowered sufficiently, ultimately all metal ions will be released from their ligands. Conversely if the pH is increased then the free metal activity will decrease due to precipitation,<sup>33</sup> colloidal adsorption<sup>34</sup> or stronger metal-ligand complexation.<sup>27, 35</sup> From an electrochemical perspective it can be seen that the pH of the solution thus strongly affects the free metal concentration measured.

### **1.2.3 Conventional Heavy Metal Detection Techniques**

Common techniques currently used for trace heavy metal detection include ICP Mass Spectrometry (ICP-MS),<sup>36</sup> Atomic Absorption Spectroscopy (AAS),<sup>37</sup> and Atomic Fluorescence Spectroscopy (AFS) which can also be coupled with separation techniques (Chromatography) to improve detection.<sup>38</sup> However, these techniques are costly and time consuming and require the samples to be removed from the source for pre-treatment. In addition they are not easily portable and samples must be removed to a laboratory for analysis, leading to potential for contamination or changes in sample environment *en route*.<sup>39</sup> Furthermore, due to the sample introduction methods used in such devices, information on speciation is lost and only total metal content can be determined.

#### **1.2.3.1 Inductively Coupled Plasma-Mass Spectrometry**

ICP-MS is a widely used method of elemental analysis, first introduced commercially in the 1980s. It holds several advantages over other techniques in this field including: superior detection limits for most elements, high sample throughput, low matrix interferences, and the ability to distinguish

isotopes.<sup>40, 41</sup> ICP-MS comprises a high temperature ICP source for sample ionisation, **Figure 1.1**, and a mass spectrometer for detection. An argon flow is directed through concentric channels of an ICP torch, where it is inductively heated with a radio-frequency (RF) coil. A spark is applied to the argon, ionising the gas; argon ions are trapped in the oscillating magnetic fields of the RF coil and collide with more argon atoms, producing an inductively coupled plasma.<sup>42</sup> Samples are introduced to the argon plasma generally in aerosol form produced in a nebuliser. The ICP desolvates and subsequently ionises elements in the sample aerosol, breaking the sample down completely.<sup>43</sup>

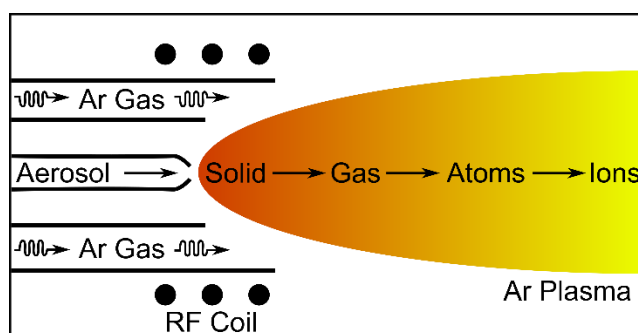


**Figure 1.1:** Schematic showing the ICP torch and sample introduction process of an ICP-MS.

The ionised sample is introduced to the mass spectrometer through a region of sampling and skimmer cones (cone shaped disks with small  $\sim 1$  mm sampling holes in the centre) illustrated in **Figure 1.2**, which sample the centre portion of the ion beam. Additionally, this region allows the transmission of ions in the ICP torch, at atmospheric pressure, to the mass spectrometer at high vacuum. Once in the mass spectrometer the ions are separated according to mass to charge ratio allowing detection of the elemental composition of the sample.<sup>44</sup>

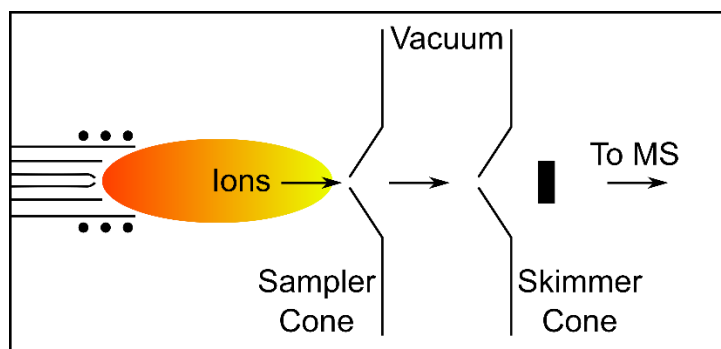


**Figure 1.2:** Schematic showing the sampling arrangement in an ICP-MS.

Although ICP-MS offers the benefit of superior detection limits, and fast sample throughput thanks in part to the automation of sampling, there are some downsides inherent to the method. Primarily it is a relatively expensive method which is not portable and requires specially trained technicians to use, but there are also technical issues when it comes to application to environmental samples. Firstly the presence of dissolved solids, which form a large part of environmental waters, can block the sampling holes of the cones causing decreased sensitivity and instrument downtime.<sup>45</sup> It is necessary therefore to filter samples prior to analysis via ICP-MS, potentially losing vital information about the sample composition. Secondly, the complete ionisation and breakdown of samples in the ICP torch means that this technique can only provide information on total ionic metal concentration, with no measure of the speciation or available metal content unless used in tandem with separation techniques, further complicating analysis.<sup>46</sup>

### **1.2.3.2 Atomic Absorption Spectroscopy**

With ppb detection limits, AAS is another popular analytical technique for measuring the concentration of elements in environmental samples. It is



based on the characteristic absorption of light by individual elements. Within an element there are a series of specific energy levels, when excited by incident light electrons in these energy levels can be promoted from one energy level to another. The energy required to promote an electron is equivalent to the difference in energy between levels and corresponds to a particular wavelength, this energy difference varies for each element and can therefore be used to identify them. As there is more than one energy level in an element there will be a series of absorption wavelengths associated with each particular element, and a characteristic “fingerprint” is observed.<sup>47</sup>

The AAS experiment is illustrated in **Figure 1.3**, during AAS analysis the sample is atomised, generally via aspiration, into the flame of an acetylene torch. The torch is mounted in a slot burner, providing a long optical path length and a stable flame; due to the relationship with absorbance described by the Beer’s Law (**Equation [1.1]**),<sup>48</sup> a longer path length increases detection sensitivity.

$$A_m = \epsilon Cl \quad [1.1]$$

Where,  $A_m$  is absorbance of the material of interest,  $\epsilon$  is the molar absorptivity ( $\text{L mol}^{-1} \text{cm}^{-1}$ ),  $C$  is the concentration ( $\text{mol L}^{-1}$ ), and  $l$  is the path length (cm). Analysis of the atomised sample is achieved via irradiation with light from either an element-specific radiation source, chosen for the element of interest, or a continuum radiation source. A monochromator is used to ensure only radiation of a particular wavelength is allowed to hit the sample. The

difference in incident radiation intensity, and transmitted radiation intensity is measured to provide a quantitative measure of the absorbance of the sample; this can be related to elemental concentration.<sup>49</sup> Once more, despite the low detection limits achievable with this technique it is not amenable to *in situ* use due to lack of portability; it also provides only information on total elemental composition of a sample rather than speciation due to the atomisation method of sampling used.

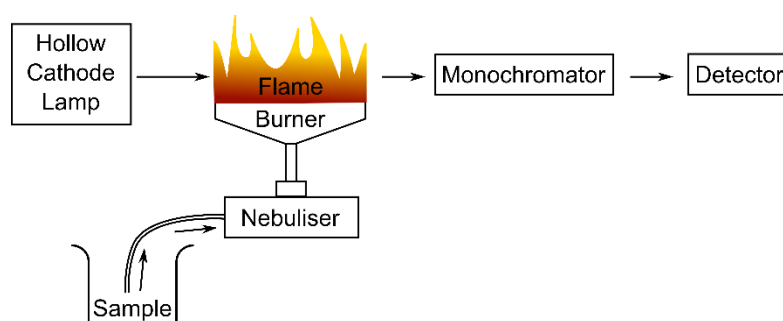


**Figure 1.3:** Block diagram schematic of an AAS experiment.

### 1.2.3.3 Pre-Treatment

Prior to analysis by any of these methods, it is often necessary to apply some form of pre-treatment to a sample as the matrix in a natural environment is often unsuitable for direct analysis.<sup>50</sup> This pre-treatment can take the form of anything from filtering the sample to remove dissolved solids,<sup>51</sup> to altering the pH (often via a strong acidic treatment) to improve analysis,<sup>52</sup> separation of components in the sample,<sup>53</sup> and pre-concentrating the sample to increase the analytical signal.<sup>54</sup> The necessity for pre-treatment of samples means that many analytical methods are not viable for use *in situ*.

It is of interest to the scientific community to develop heavy metal sensors which (1) are easy to operate; (2) can be used for *in situ* measurements; (3) can

account for variations in local pH of the environment and (4) are able to determine both free and total heavy metal content. In recent years the focus on development of *in situ* techniques for aqueous metal detection has increased.<sup>55-57</sup> Some analytical techniques, such as X-ray Fluorescence (XRF), are already in widespread use as handheld *in situ* devices.<sup>58</sup> However, in the case of XRF, detection sensitivities do not currently reach those necessary to cover environmental guidelines.

Another area of research showing great promise for *in situ* metal detection is electrochemical analysis.<sup>59, 60</sup> However, as mentioned in **section 1.2.2**, for the vast majority of heavy metal applications the sample still requires removal from the source and acidification for effective analysis.<sup>28, 61</sup> Furthermore, there are no current commercial heavy metal sensors on the market which are capable of *in situ* measurements.

### 1.3 Electrochemistry

In general, electrochemical sensors are well suited to heavy metal measurement; Anodic Stripping Voltammetry (ASV)<sup>62</sup>, the principles of which are outlined in **Figure 1.6**, and Differential Pulse Voltammetry (DPV)<sup>63,23</sup> are commonly used techniques for the electrochemical detection of trace metals in aqueous environments. Electrochemical methods exhibit low (ng/L) detection limits,<sup>64</sup> and in comparison with the aforementioned spectroscopic techniques are relatively cheap. The low operating power of such techniques and ability to simultaneously analyse multiple elements makes them ideal for use in portable, *in situ* devices.

The low cost and ease of use electrochemical techniques in general offer, means that electrochemistry can be widely exploited. This is discussed widely in the literature and covers applications from the immobilisation of molecules such as DNA onto electrodes to create optical biosensors,<sup>65</sup> to environmentally friendly disposable microfluidic sensors.<sup>66</sup> These examples demonstrate just how flexible electrochemical techniques can be; easy modification of the electrode surface to produce tailored devices is possible,<sup>67</sup> with the additional benefit of potential for small sample volume requirements.<sup>30</sup> Electrochemical methods are typically either potentiometric (measure an equilibrium voltage) or voltammetric (apply a potential, measure a current) in nature, with the latter including cyclic and ASV/DPV.<sup>68, 69</sup> Electrochemical techniques are thus typically defined by one or more of four parameters: Potential ( $E$ , volts), Current ( $I$ , amps), Charge, ( $Q$ , coulombs), and Time ( $t$ , seconds).<sup>70</sup> For the work described in this thesis the emphasis will be placed on voltammetric measurements.

### **1.3.1 Electrodes**

In electroanalytical experiments, the concentration of the species of interest is probed electrochemically (via an electron transfer reaction coupled to mass transfer) using a working electrode (WE), commonly made of a material that is a good conductor but chemically inert e.g. Au, Pt and C. To complete the electrochemical cell, the potential of the WE must be measured vs. a non-polarisable reference electrode (RE), which holds a stable, known potential. In order to maintain a stable potential the RE contains a stable redox couple

where the solution soluble concentrations of each component are saturated and therefore do not change. Common examples of reference electrodes include the saturated calomel electrode (SCE) and the Ag|AgCl electrode.<sup>70</sup>

The majority of analytical electrochemistry is conducted in a three electrode cell, with the addition of a counter, or auxiliary, electrode (CE). This means that when current flows in the electrochemical cell it can flow between the WE and the CE without compromising the RE, thus providing a system where both current and potential can be measured or applied independently. The area of the CE is generally much larger than that of the WE, to avoid limiting the reaction occurring at the WE.<sup>70</sup> The electrodes are connected in a circuit with a potentiostat. A voltmeter with high input impedance ensures no current flows at the RE, and an ammeter with low internal impedance allows the current to flow at the CE such that it is possible to solely measure the effect at the WE, **Figure 1.4**.

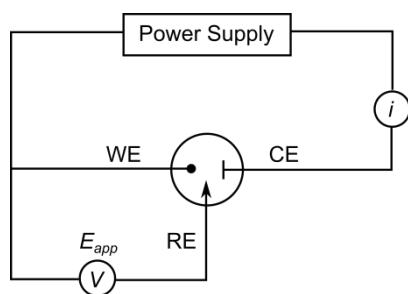


**Figure 1.4:** Diagram of a three electrode cell.<sup>70</sup>

In order to avoid ohmic drop (solution resistance) between the electrodes, a supporting electrolyte containing inert, non-electroactive species such as  $\text{KNO}_3$  or  $\text{KCl}$  is used. Supporting electrolyte is added in sufficiently high concentrations such that the ionic strength and conductivity is much larger

than that of the species of interest. When this is the case, migration of ions in the electric field is prevented.<sup>71</sup>

### 1.3.2 Cyclic Voltammetry

Although not commonly used as an analytical tool, due to its low concentration sensitivity in comparison to other methods, use of cyclic voltammetry (CV) is nevertheless very common. One of the key uses of CV experiments is in the characterisation of electrode properties,<sup>72, 73</sup> and electrochemical systems.<sup>74</sup> CV experiments are typically conducted via a triangular potential ramp applied using a potentiostat; the potential of the working electrode is swept in one direction before reversing and returning to the original potential, producing the waveform presented in **Figure 1.5(a)**. The current resulting from this potential sweep is measured by the potentiostat; a CV of current vs. potential is plotted. The shape of the resulting CV e.g. as shown in **Figure 1.5(b)** can provide information on the electron transfer kinetics of the redox couple under study (if the process is kinetically limited), and the concentration of redox species in the solution. The latter is typically made under mass transfer limited conditions.

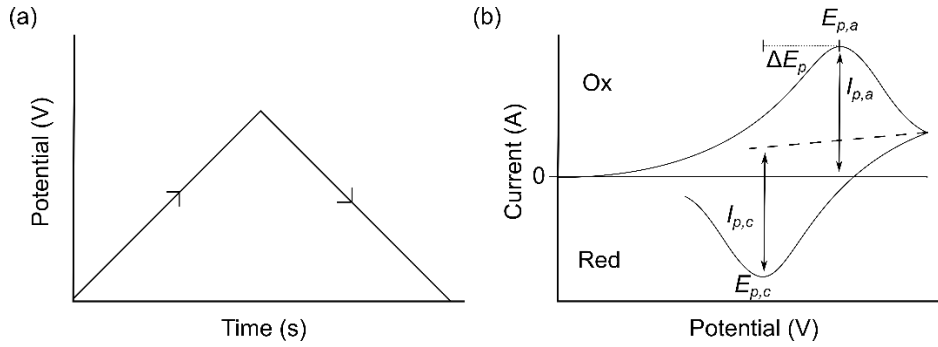


**Figure 1.5:** (a) Typical waveform of a cyclic voltammetry experiment. (b) Resulting cyclic voltammogram for a reversible system.

In **Figure 1.5(b)**, the peak current ( $i_p$ ) is indicative of the maximum current flowing in the system. Large electrodes e.g. > 1 mm tend to show peak-shaped CVs due to the reduced mass transport flux compared to a much smaller electrode. Under diffusion-limited conditions (i.e. reversible), where sufficient background electrolyte has been added to ignore migration effects, the CV has a distinctive shape. (1)  $i_{p,a} \approx i_{p,c}$ ; (2) under diffusion-controlled conditions, the Nernst equation, **Equation [1.2]**, can be used to predict the peak to peak separation,  $\Delta E_p$ .

$$E = E^0 - \frac{2.303RT}{nF} \log \frac{a_R}{a_O} \quad [1.2]$$

where,  $E$  is the electrode potential (V);  $E^0$  is the potential under standard conditions (V);  $R$  is the molar gas constant,  $8.314 \text{ J mol}^{-1} \text{ K}^{-1}$ ;  $T$  is temperature (K);  $n$  is the number of electrons transferred in the reaction;  $F$  is Faraday's constant,  $96485 \text{ C/mol}$ ; and  $a_R$  and  $a_O$  are the activities of the reduced and oxidised species respectively.  $\Delta E_p = 2.303 \text{ RT/nF}$  should be 59 mV for a one electron transfer at  $T = 298\text{K}$ .

Additionally, for a planar diffusion reversible electron transfer system, the relationship between  $i_p$  (A), electrode area ( $A$ , cm<sup>2</sup>), diffusion coefficient ( $D$ , cm<sup>2</sup> s<sup>-1</sup>), scan rate ( $v$ , Vs<sup>-1</sup>),  $C$  (mol cm<sup>-3</sup>) and  $n$  is given by the Randles-Sevcik equation, **Equation [1.3]**, written assuming  $T = 298\text{K}$ .<sup>75</sup>

$$i_p = 2.69 \times 10^5 n^{\frac{3}{2}} A D^{\frac{1}{2}} C v^{\frac{1}{2}} \quad [1.3]$$

Using this, experimental parameters, such as concentration can be varied to allow measurement of the diffusion coefficient of an electroactive species of interest, or concentration determined provided,  $D$  is known.<sup>70</sup> Alternatively, using a well-defined redox system the material properties of the electrode can be probed and compared to theory.<sup>73</sup>

CV measurements in solution containing only inert supporting electrolyte provide a further measure of electrode characteristics. Both the extent of the solvent window, that is the potential window in which the solvent is neither oxidised nor reduced at the WE,<sup>76</sup> and the double layer capacitance of the electrode material can be probed.<sup>77</sup> This provides an indication of the potential range in which the WE is useful with no interference from background processes.<sup>78</sup> Low capacitance materials are ideal for low concentration detection; a large solvent window might be thought preferable for detecting the largest range of species in solution, but as discussed in **Section 1.4.3**, and demonstrated in the voltammetric determination of dopamine on C electrodes by Patel *et al.*<sup>79</sup> it is important to understand the origin of this observation in order to qualify the statement.



### 1.3.3 Stripping Voltammetry

The electrochemical deposition and subsequent stripping of a metal from the surface of an electrode produces an analytical signal that can be used to quantify metal concentrations in solution. This process is illustrated in **Figure 1.6**. When the electrode is held at a sufficiently reducing potential, metal ions in solution are electroplated onto the surface, **Figure 1.6(A)**; the potential required varies according to the metal, and thus it is possible in some cases to selectively deposit a specific metal from a mixed metal solution. After the deposition step the potential is scanned in a positive direction, causing the metal deposit to be oxidised and thus removed (stripped) from the electrode surface, **Figure 1.6(B)**, resulting in a peak in the measured current of which the position and magnitude or area (charge transferred) can be used to identify and quantify the metal.

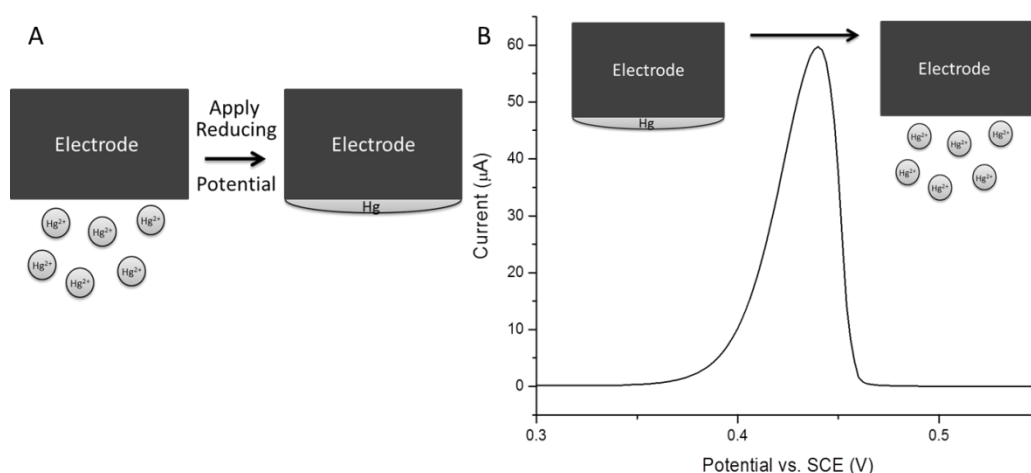


**Figure 1.6:** (A) Electrodeposition of metal ions, whereby at a suitable cathodic potential  $X^{n+} + ne^-$  is electrodeposited as  $X(s)$  on the electrode surface. (B) Stripping voltammetry, whereby solid metal is stripped from the surface by applying a suitable oxidative potential, resulting in a characteristic stripping peak.

The ideal WE for stripping voltammetry exhibits a reproducible surface and therefore defined surface area, and low background currents. Historically, Hg electrodes, such as the hanging mercury drop electrode (HDME) and thin film mercury electrode (TFME),<sup>80</sup> were used as their liquid nature makes them an ideal electrode surface.<sup>81,82</sup> Key to stripping voltammetry on Hg electrodes is the fact that metal ions in solution dissolve into the liquid Hg forming an amalgam.<sup>83</sup> When the potential is swept in the positive direction and the metal is stripped from this amalgam well defined symmetrical stripping peaks are formed with defined width at half maximum, which are easy to model and therefore analyse.<sup>84</sup> In addition, their high overpotential for hydrogen evolution and easily refreshable liquid metal surface made Hg electrodes the popular choice for such experiments.<sup>85</sup> However, due to the toxic nature of Hg and a move towards green chemistry, storage of the metal is now prohibited.<sup>86</sup> As such, it has become imperative to find new non-toxic solid electrode materials for use in ASV experiments. The most desirable property for a replacement electrode is a wide solvent window in the cathodic range, in addition to low background currents, resistance to both fouling and corrosion, and a well-defined surface area.<sup>87</sup> Potential electrode materials investigated in literature include conductive polymers,<sup>88, 89</sup> ceramics,<sup>90</sup> glassy carbon,<sup>91</sup> graphene,<sup>92</sup> carbon paste<sup>93</sup> and graphite.<sup>94</sup> Boron Doped Diamond (BDD) has also been widely studied in recent literature for a wide range of applications, including as a potential replacement for mercury electrodes in heavy metal analysis.<sup>95, 96,97, 98</sup>

### 1.3.4 Increasing Mass Transport

In a quiescent supporting electrolyte containing solution the mass transfer of species to an electrode occurs by diffusion only. For large electrodes, diffusion is fairly inefficient, being predominantly linear in nature. For ASV, pre-concentration of the metal is key and occurs via mass transport. To increase the time efficiency of this process, mass transfer must be increased which can be achieved in two ways (1) through the use of smaller electrodes,<sup>99</sup> although the current signal decreases; (2) through the use of forced convection<sup>100</sup> or by a combination of (1) and (2).<sup>101</sup>

Common examples of hydrodynamic electrodes include: Rotating Disc Electrodes (RDE),<sup>102</sup> Wall Jet Electrodes (WJE),<sup>103</sup> and Channel Electrodes (CE).<sup>104</sup> The common aim in all these examples is to introduce laminar flow into the system, to make the signal quantitative.<sup>105</sup> The choice of method used is dependent on the system of interest and the applicability of each technique; here we focus on the RDE system as it was the most appropriate for adaptation to the system of interest in this thesis.

The RDE consists of a disc shaped electrode, usually embedded coplanar to the surface of a plane, which is centred on the axis of rotation. In order to avoid interference from edge effects the sheath around the electrode is commonly much larger than the electrode, approximating an infinite surface.<sup>106</sup> Rotating the RDE results in a controlled laminar flow of solution towards the surface of the electrode, and then outwards radially as depicted in

**Figure 1.7.**<sup>75</sup>

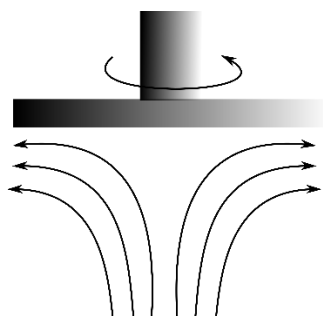


**Figure 1.7:** Illustration depicting mass transport to a RDE.

In an electrochemical system this increased mass transport enables the current response to attain a steady-state,<sup>70</sup> at sufficiently high driving potentials, as shown in **Figure 1.8**. The limiting current that is obtained is described by the Levich equation, **Equation [1.4]**.

$$i_L = 0.62nFAD^{\frac{2}{3}}\omega^{\frac{1}{2}}\nu^{-\frac{1}{6}}C \quad [1.4]$$

Where  $i_L$  is the limiting current (A),  $\omega$  is rotation speed ( $\text{rad s}^{-1}$ ),  $\nu$  is the kinematic viscosity ( $\text{cm}^2 \text{sec}^{-1}$ ), and  $C$  is in ( $\text{mol cm}^{-3}$ ).

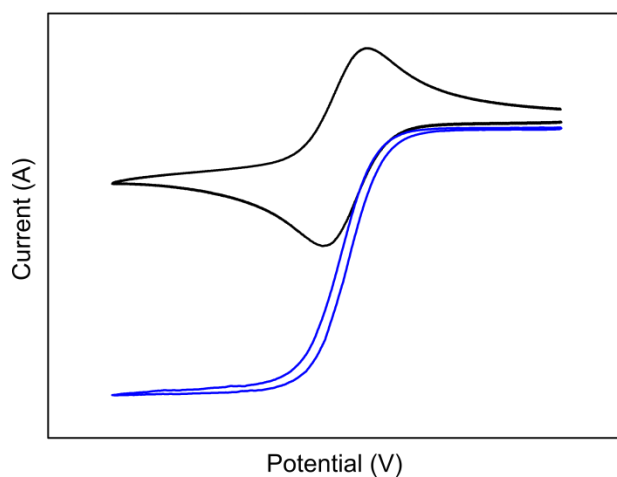


**Figure 1.8:** Example of CVs in a reversible redox mediator under stationary (black) and rotating (blue) conditions.

### 1.3.5 Current Issues with electrochemical detection of heavy metals

As mentioned previously, much work in literature is focused on finding appropriate solid electrode replacements for the Hg electrode. Although many promising alternatives have been investigated, there are issues associated with solid electrode materials. In contrast to Hg electrodes where the metal of interest is homogeneously dissolved into the electrode material, electrodeposited material on solid electrodes is often heterogeneous in morphology and spatial distribution due to the heterogeneous nature of the electrode surface;<sup>107</sup> the deposition morphology varies, and material deposits on both the electrode surface and onto previously formed metal deposits. This complicates analysis, as the stripping response varies depending on morphology of the species, becoming asymmetric and either broadening the signal<sup>107</sup> or producing multiple peaks as can be seen in **Figure 1.9** for detection of the single species, dissolved  $\text{Pb}^{2+}$ .<sup>84</sup>

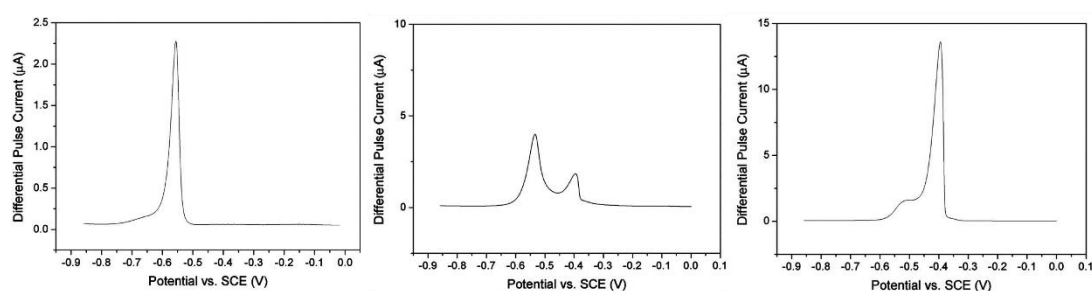


**Figure 1.9:** Stripping response on BDD electrode for 0.5  $\mu\text{M}$ , 10  $\mu\text{M}$  and 30  $\mu\text{M}$   $\text{Pb}^{2+}$  in 0.1 M  $\text{KNO}_3$  supporting electrolyte. Demonstrating the variation in peak shape and position in a single metal solution. Adapted from Hutton et al (2011).<sup>84</sup>

Additionally, in complicated systems, such as those with more than one electrochemically active species, it can be challenging to correctly identify the

species responsible for each electrochemical signal. Often signals overlap or one species may produce more than one signal due to co-deposits and alloying.<sup>108</sup> Other effects observed using solid electrodes in multi-metal systems include suppression (*e.g.* Cu presence reduces As signals)<sup>109</sup> or even enhancement (*e.g.* Bi codeposition enhances Cd and Pb)<sup>110</sup> of the analytical signal, caused by intermetallic interactions during deposition.<sup>111</sup> The mechanisms behind co-deposition are reliant on a number of factors including the affinities of the metals, their relative electroactivities, and the type of interaction.<sup>111</sup> Furthermore, during metal electrodeposition hydrogen can cause problems due to codeposition, adsorption,<sup>112</sup> and inhibition of metal deposition due to hydrogen bubble formation.<sup>113</sup>

These factors affect not only the size of the analytical signal, but also the ability to chemically identify the resulting peaks. Unlike in spectroscopic measurements, where the signal location provides unequivocal identification,<sup>114</sup> electrochemical results are not always easy to interpret. In general the thermodynamic  $E_0$  value can be used as a guide to the stripping peak location for a particular metal.<sup>71</sup> However, as this refers to the metal<sub>(solid)</sub>/metal<sub>(ion)</sub> system it is only qualitative,<sup>115</sup> as under low concentration conditions, the heavy metal strips from a surface which is not the pure form of its metal.

#### **1.4 Boron Doped Diamond**

Diamond is renowned for its remarkable properties both physical and mechanical.<sup>116</sup> In particular it is widely known as being both a highly desirable

gemstone, and as being the hardest natural material known to man.<sup>117</sup> It exhibits high mechanical stability and due to this is resistant to wear, making it ideal for use in many applications including industrial drilling and cutting tools. Other, perhaps less well known properties include chemical resistance, high thermal conductivity under standard conditions ( $\sim 4 \times$  that of copper), and transparency from deep ultraviolet wavelengths through to far infrared.<sup>118</sup> In recent years synthetic diamond growth technologies, such as chemical vapour deposition (CVD),<sup>119</sup> have improved such that diamond is now commercially available in a variety of forms and can be tailored to a wide range of applications. Moreover, modern growth techniques allow diamond to be doped with other elements (*e.g.* boron), which affects the electrical conductivity.<sup>120</sup>

#### **1.4.1 Growth**

Natural diamonds are formed in the Earth's mantle under specific temperature and pressure ranges, growing over billions of years before being brought close to the surface by deep volcanic activity, where they are traditionally obtained through mining. Due to diamond's useful properties and the high demand for diamond in both gem and industrial forms it has long been the aim of scientists to create diamond synthetically. Initial experiments focused on conversion of graphite to diamond, with minimal success.<sup>121</sup> Several successful methods have been developed and diamonds are now grown synthetically on an industrial scale by two main methods, High-Pressure-High-Temperature (HPHT)<sup>122</sup> and CVD (*vide infra*),<sup>123</sup> although other methods such as detonation

synthesis are used on smaller scales.<sup>124</sup> Continuing work towards improving diamond growth techniques has led to increasingly more reproducible, controllable, and reasonably inexpensive synthetic diamond, opening up new applications.

HPHT is a term used to describe several methods in which diamond is grown under high pressures and temperatures, imitating the natural process in the earth.<sup>122</sup> As the first commercialised growth method, HPHT diamonds have been in use since the late 1950s. All HPHT methods rely on the same process, using different press designs, wherein a solvent metal is heated in excess of 1800 K and compressed ( $\sim 5$  GPa). Under these conditions graphite is dissolved in the solvent metal, and subsequently, as the temperature is reduced, precipitates as diamond.<sup>125</sup> Three main commercial press designs are used for this process: the belt press; the cubic press; and BARS (split sphere).<sup>126</sup> The HPHT method generally produces small ( $\mu\text{m}$ -mm sized) diamond grit, useful for abrasive drilling and polishing tools, but under highly controlled conditions can produce reasonably high purity single crystals exceeding 1 carat.

In order to grow larger wafers or films of diamond, such as the freestanding polycrystalline BDD used in this thesis, CVD techniques are used. CVD growth of diamond, first demonstrated in the 1950s by Eversole at Union Carbide, occurs at much lower pressures than those used in HPHT and is most commonly achieved via one of two processes: Hot-filament CVD (HFCVD), and Microwave CVD (MWCVD). The general method common to all CVD



processes consists of three main steps, converting gas mixtures into growing diamond crystals: Firstly, the reaction gases are activated; next, reactions occur in the gas phase, leading to the final stage; gas species diffuse to a substrate surface causing diamond growth atom by atom.<sup>125</sup>

The diamond used herein was grown using MWCVD, via the following general process. The growth substrate (*e.g.* tungsten embedded with nanocrystalline diamond seeds) is placed in the reaction chamber, where the process gases are then introduced.<sup>127</sup> The gas composition used varies depending on manufacturer and desired diamond properties but will include a carbon source (*e.g.* methane), hydrogen, and if necessary a dopant (*e.g.* boron) source. A ball-shaped microwave plasma (typical excitation frequency 2.5 GHz) is ignited above the surface of the growth substrate, ionising the reaction mixture. The ionised carbon subsequently diffuses to the surface of the substrate and is deposited, building an  $sp^3$  diamond lattice layer by layer. The presence of atomic hydrogen is key, etching non-diamond carbon (NDC) with the diamond deposition and therefore increasing growth rates and purity. Note, some etching of the  $sp^3$  diamond carbon will occur however, this process is much slower than  $sp^2$  etching.<sup>119, 125</sup>

#### **1.4.2 Structure, doping and resulting properties**

As discussed earlier in **section 1.4**, diamond has many desirable properties, stemming from its ordered  $sp^3$  face central cubic carbon crystal lattice structure (*Figure 1.10*).<sup>123</sup>

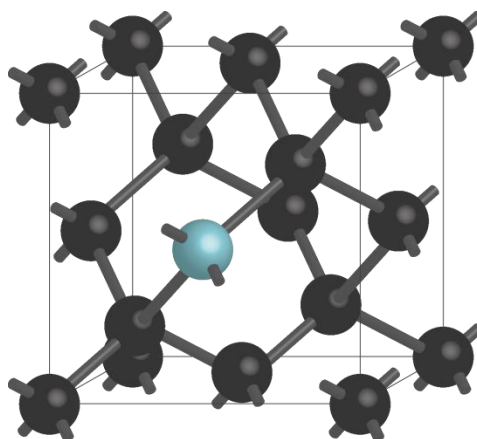


**Figure 1.10** - Diagram of the  $sp^3$  carbon lattice structure of diamond. Black atoms represent carbon and blue is used to represent boron doping.

During the growth process it is possible to incorporate other elements, such as nitrogen (n-type) and boron (p-type), into the diamond lattice in a process known as ‘doping’, allowing the physical and electrical properties of the diamond to be tailored to the desired application. Diamond is well known for its intrinsically low electrical conductivity, with a band gap of 5.5 eV at 300 K, making it an extremely poor electrode material. However, when doped sufficiently with substitutional boron during growth ( $10^{16}$ - mid  $10^{19}$  atom  $\text{cm}^{-3}$ )<sup>128</sup> an acceptor level is formed at 0.37 eV above the valence band. Diamond becomes a p-type semi-conductor.<sup>129</sup> By changing the concentration of boron the electrode performance of diamond can range from insulating, to semi-conducting and at very high concentrations of boron ( $> 10^{20}$  atom  $\text{cm}^{-3}$ ) even to metal-like behaviour.<sup>130</sup> The latter is ideal for electrode use.

For low boron concentrations (semi-conducting diamond) the boron atoms accept electrons from the valence band, creating ‘holes’, when the dopant concentration is increased (metal-like) these holes overlap to form a band.

Visually the dopant concentration increase can be observed in a transition from colourless insulating diamond, to blue semi-conducting diamond, and finally black diamond with metal-like conductivity.<sup>131</sup> In polycrystalline material, such as that used in this thesis, different crystal faces uptake boron at different rates during growth,<sup>132</sup> this can be observed in both colour differences by eye, and spectroscopically/spectrometrically *e.g.* Secondary Ion Mass Spectrometry (SIMS) and Raman spectroscopy, at different grains.

### 1.4.3 Electrode Properties

BDD is superior to other commonly used electrode materials, such as platinum,<sup>133</sup> for several reasons. Specifically; (1) BDD has a wide potential range over which negligible water electrolysis occurs ( $>3$  V in 0.1 M  $\text{KNO}_3$  between the bounds of  $\pm 0.4 \text{ mA cm}^{-2}$ ), known as the solvent window. **Figure 1.11** compares the solvent window for a freestanding BDD electrode with those of some other common electrode materials.

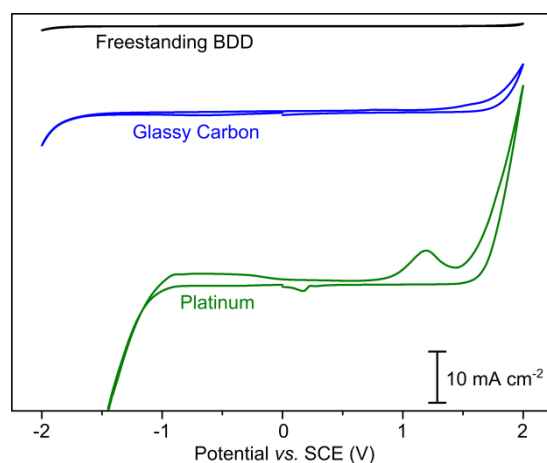


**Figure 1.11:** Comparison of solvent windows in 0.1 M  $\text{KNO}_3$  solution for Freestanding BDD (black), Glassy Carbon (blue), and Platinum (green) electrodes.<sup>134</sup>

This is due to its electrocatalytically inactive surface properties. Water is an inner sphere redox species.<sup>135</sup> This means that the redox reaction proceeds via a strong interaction with the electrode surface often by adsorption, as opposed to outer sphere where the interaction occurs through space and the electrode surface does not interact with the species, illustrated in **Figure 1.12**, where IHP and OHP denote the location of the Inner Helmholtz Plane and Outer Helmholtz Plane respectively.<sup>136</sup> As a result, inner sphere species such as water are sensitive to the electrode surface chemistry, and require the presence of catalytic sites for electrolysis to occur. The  $sp^3$  diamond surface is catalytically inert and lacks binding sites for inner sphere electron transfer, this makes it a poor surface for investigation of inner sphere species but also is responsible for its desirable wide solvent window.<sup>135</sup> (2) BDD shows no signature for oxygen reduction as this is also an inner sphere, electrocatalytic electron transfer process; oxygen cannot be reduced on the diamond surface due to the lack of binding sites.<sup>73</sup> (3) BDD also benefits from low background (capacitive) currents, due to the chemical stability of the BDD, the lack of surface processes,<sup>73</sup> and its lower density of states in comparison to classical electrode materials such as Pt,<sup>134</sup> allowing for a better signal to noise ratio.<sup>137,130</sup> (4) High stability, corrosion resistant under extreme pH,<sup>138</sup> temperature and pressure conditions.<sup>139</sup>

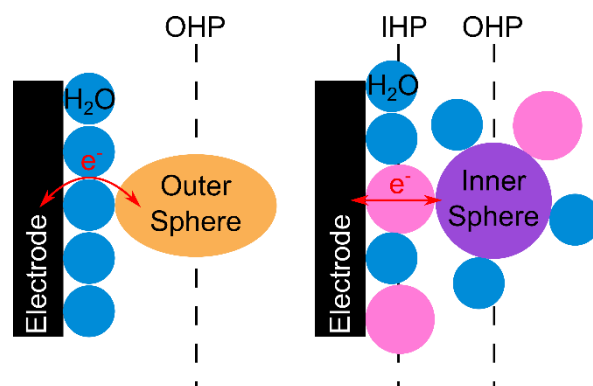


**Figure 1.12:** Illustration comparing inner sphere and outer electron transfer at an electrode surface.<sup>140</sup>

Incorporation of NDC ( $sp^2$ ) at grain boundaries into the BDD surface, typically during growth decreases the diamond quality. It is very challenging to grow  $sp^2$  free BDD at high boron concentrations, although it is possible, especially for thicker grown material.<sup>73</sup> Thin film BDD, in general tends to have a significantly higher concentration of  $sp^2$  present as is the case for nanocrystalline and ultra-nanocrystalline BDD. Grain size increases with film thickness.

$Sp^2$  presence has a knock on effect on the electrochemical properties of BDD. For example, oxygen reduction is catalysed on  $sp^2$  carbon and can be observed in the reductive window (negative potentials) in supporting electrolyte. In the oxidative window (positive potentials) oxidation of surface bound redox processes associated with  $sp^2$  carbon are also observed, both effects result in a narrowing of the solvent window and an increase in background (capacitive) currents.<sup>141, 142</sup>  $sp^2$  presence can also have an effect on the electrochemical response of redox species at the electrode, especially for inner sphere couples.<sup>141</sup> It is reportedly possible to remove some  $sp^2$  from BDD electrodes

using an acid cleaning process or alternatively by cycling the potential in acidic solutions.<sup>143, 144</sup>

BDD electrode doping levels can also be judged electrochemically using CV of well-defined redox couples. For a fast outer sphere redox couple, such as  $\text{Ru}(\text{NH}_3)_6^{3+/2+}$ ,<sup>73, 134, 145</sup> the peak current ( $i_p$ ) response is expected to be close to reversible and can be predicted using the Randles-Sevcik equation (Equation [2]). This is true for  $\text{Ru}(\text{NH}_3)_6^{3+/2+}$  on classical electrode materials but the formal potential ( $E_o'$ ) lies within the bandgap of BDD, this means that the resulting CV is directly affected by the boron doping levels; only for high enough doping levels, where the material approaches metal-like properties, will a reversible CV for  $\text{Ru}(\text{NH}_3)_6^{3+/2+}$  be achieved on BDD, as illustrated in

**Figure 1.13.**

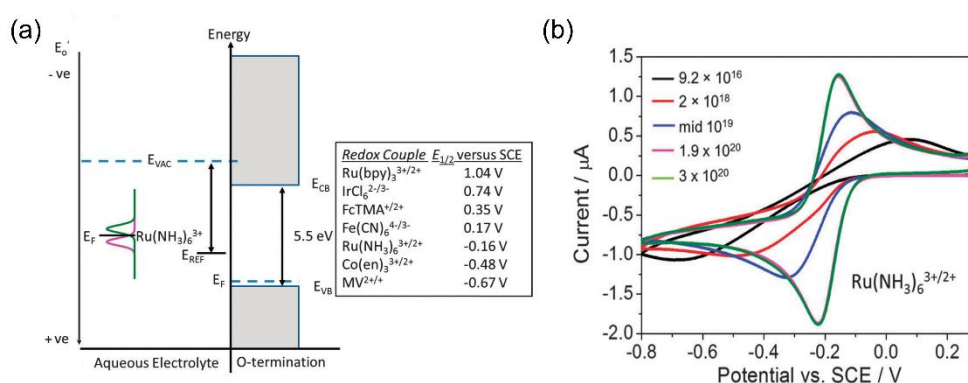


**Figure 1.13:** (a) Schematic showing the approximate position for  $\text{Ru}(\text{NH}_3)_6^{3+}$  with respect to the potential of the valence band ( $E_{vb}$ ) and the conduction band ( $E_{cb}$ ) for O<sup>-</sup> terminated semiconducting BDD.  $E_{1/2}$  values for several outer sphere redox mediators and  $\text{Fe}(\text{CN})_6^{4-/3-}$  are presented in the table. (b) Example CVs in 1mM  $\text{Ru}(\text{NH}_3)_6^{3+/2+}$  taken on 1 mm BDD disc electrodes of varying dopant density. Both figures adapted from Macpherson (2015).<sup>73</sup>

It is important to note that for highly doped BDD poor reversibility could indicate poor electrical contacts. Another indication of electrode quality

obtained through CV experiments is  $\Delta E_p$ , which is predicted by the Nernst equation (Equation [1.2]) to be 59 mV under standard conditions.

#### **1.4.4 Electrode Fabrication**

The majority of academic groups use thin film BDD (still attached to a non diamond growth wafer) as the electrode material, with an electrochemical cell clamped over the surface. With the advent of improved growth technology, freestanding diamond, grown thick enough so it can be safely removed from the growth substrate has become available. Freestanding BDD is advantageous in that it can be processed e.g. machined into a variety of geometries, and mounted in an insulating sheath using procedures similar to those used to mount metal microelectrodes.<sup>146</sup> BDD electrodes are typically cut from the wafer using laser micromachining.<sup>146</sup>

The term laser micromachining describes the act of drilling or cutting a material using a laser beam;<sup>147</sup> usually the laser beam used is pulsed with an energy chosen such that the ablation threshold of the material, in this case BDD, is exceeded.<sup>147</sup> The interaction between the laser and the material is generally material characteristic, and can be tuned selectively via parameters such as laser wavelength and pulse width for optimum ablation. The ablation of the material substrate takes place according to a series of processes.<sup>148</sup> Firstly, the laser radiation is absorbed by the material, resulting in the ejection of excited electrons; the energy from these electrons is transferred to the crystal lattice, melting the surrounding bulk material. The melted material

subsequently evaporates and is ejected into the ablation plume, this is heated by the laser radiation forming a plasma and further etching the substrate.<sup>149, 150</sup>

In metals, some of this material can become re-deposited on the surface due to cooling, in a mechanism known as recasting. For diamond recasting is less of an issue as the removed material is ejected in the form of CO<sub>2</sub> gas; although there is some residual sp<sup>2</sup> material left on the surface. The majority of laser ablated sp<sup>2</sup> can be removed from the surface using acid cleaning processes; in some cases it can actually be advantageous to have it present.

Laser machining is advantageous over mechanical methods of processing materials, in that the lack of applied mechanical cutting force results in the absence of mechanically induced damage to the material or tool. It is also able to machine materials on very small scales in relatively short times.<sup>151</sup> Laser micromachining has been used in applications ranging from creation of microfluidic structures<sup>152</sup> to medical implants.<sup>153</sup> It has also been applied to BDD in methods such as device manufacture and surface modification.<sup>154</sup>

Another key part of the fabrication process is the formation of ohmic contacts to the BDD electrode; it is important that good contacts are formed, as poor contact can lead to resistance. Where the BDD is in thin film form a contact can be created either directly to the conducting substrate, or via connections to the surface of the diamond. However, unlike most electrode materials an ohmic contact cannot be formed directly between the BDD (thin film or freestanding) and a metal, usually done via solder or conductive paste.<sup>155</sup> In order to successfully form an ohmic contact to BDD materials a carbide must



be formed, commonly via the sputtering of Ti onto the BDD; once annealed a Ti carbide contact is formed to the BDD.<sup>156</sup> In order to avoid oxidation of the Ti layer in air it is common practice to sputter a thin layer of an inert metal such as Au on top of the Ti prior to annealing.<sup>73</sup>

#### 1.4.5 XRF

As discussed in **Section 1.2**, common methods for heavy metal detection include ICP-MS and AAS, another alternative is X-Ray Fluorescence (XRF).<sup>37,13</sup> XRF has the advantage of being portable, allowing for easy application to *in situ* analysis. XRF also benefits from simple sample preparation procedures; unlike ICP-MS and AAS, solid, liquid, and powder samples can be analysed directly without the need for digestion. The internal calibration available with some XRF instruments<sup>157</sup> also removes the necessity of preparing accurate calibration solutions. A schematic showing an energy dispersive XRF system, such as that used in this thesis is presented in **Figure 1.14**.

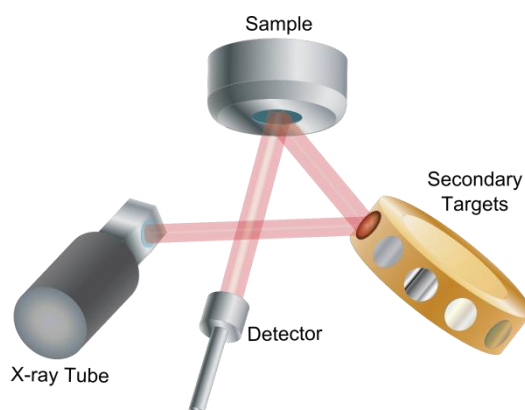


**Figure 1.14:** Schematic of an energy dispersive XRF with secondary targets. Adapted from “Theory of XRF”.<sup>158</sup>

When a sample is irradiated, X-ray photons with sufficient energy (higher than the binding energy of the electron) can expel an electron from atoms

within the sample. The removal of an electron leaves a 'hole' in the shell, otherwise known as an initial vacancy, leaving the atom in an excited state from which it is energetically favourable to return to its original configuration. In order for this to happen a higher energy electron from an outer shell is transferred into the initial vacancy, releasing its excess energy as an X-Ray photon (fluorescence), this process is illustrated in **Figure 1.15(a)**. The fluorescence is detected by the instrument and is observed as a line in the spectrum; the energy of the emitted X-ray photon relates to the difference in energy levels and, as this is different for every element, is characteristic. An example spectrum is presented in **Figure 1.15(b)**. As there are multiple possible shells within an atom in which the initial vacancy can occur, and similarly multiple possible shells for an electron to be transferred from it is possible to build up a characteristic XRF 'fingerprint' of an element.

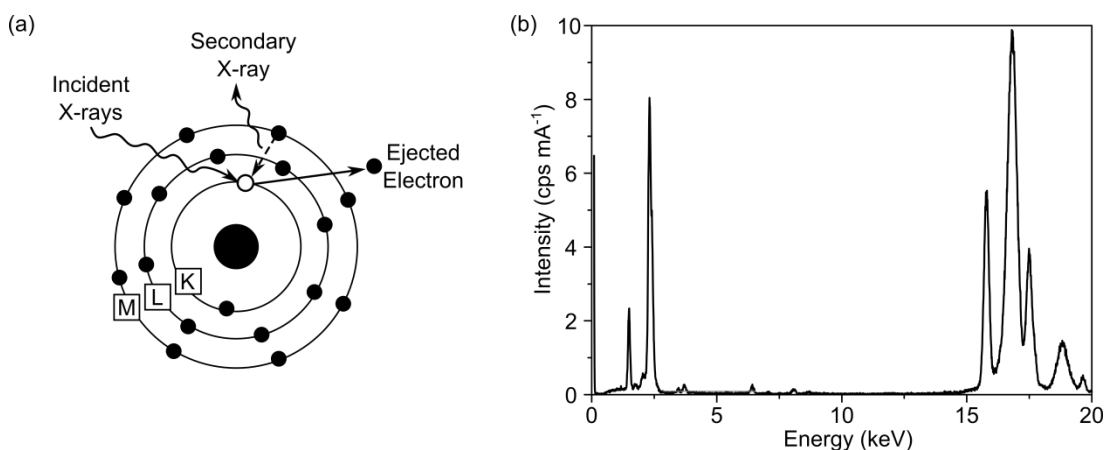


**Figure 1.15:** (a) Schematic of the XRF process in which secondary X-ray fluorescence is produced via the irradiation of elements in a sample. (b) Example XRF spectrum for an environmental sample, each peak is representative of a single elemental fluorescence.

Commercial XRF instruments can be capable of measuring any element between Na and U in the periodic table, and vary in size from heavy duty

freestanding devices to portable hand-held devices. They have been used in literature to study a wide range of elemental species in a variety of environments, such as: *in vivo* medical diagnosis,<sup>159</sup> pigments in artwork,<sup>160</sup> archaeological sites and artefacts of interest,<sup>161</sup> pharmaceutical material,<sup>162</sup> and environmental analysis.<sup>163</sup>

XRF experiments can be selectively tailored to improve sensitivity for a particular element of interest through use of a secondary target. The secondary target is situated between the X-Ray source and the sample and is usually made of a single metal; common examples are molybdenum, aluminium or copper. When irradiated by the source each metal will produce secondary X-Rays at a characteristic energy, as with any sample, and consequently the energy range (z-range) of the incident radiation is narrowed; by choosing a secondary target material with a z range equivalent to or slightly larger than the excitation energy of the analyte, sensitivity can be improved. Note as a consequence of this most of the original X-Ray intensity is lost and so a higher tube power is required.

However, despite its advantages XRF cannot currently achieve sufficiently low limits of detection (LOD) and limits of quantitation (LOQ); typically sensitivity is orders of magnitudes less than techniques such as ICP-MS. Work in the literature has aimed at improving XRF detection limits in a number of ways. Improvements to the technique itself have been investigated leading to the development of total-reflection XRF (TR-XRF) where the angle of incident radiation is below the critical angle such that it is almost entirely reflected.

Background contributions from scattered radiation are thus greatly reduced, and as a result measurement sensitivity is improved.<sup>164</sup> Preconcentration methods show promise in improving XRF, detection limits on the ppb level have been shown to be possible for some species using evaporative preconcentration such as the UltraCarry® (Rigaku, Japan).<sup>165</sup> Other preconcentration methods used include ion exchange,<sup>166</sup> precipitation, drying or freeze drying, and liquid-liquid extraction.<sup>167</sup>

Recent work by researchers at Warwick aiming to improve XRF detection limits for heavy metals has led to the development of electrochemical XRF (EC-XRF).<sup>168</sup> EC-XRF follows the same principles as XRF, except that an electrochemical pre-concentration step is used prior to measurement to electrodeposit the metal of interest onto a BDD electrode (as with stripping voltammetry). Increased mass transport to the electrode via convection from a rotating electrode is used to decrease metal pre-concentration times. Unlike stripping voltammetry where the metal is electrochemically stripped from the surface after deposition, XRF is used to both identify and quantify the metal species on the electrode. As mass transport is controlled in the system, the XRF signal can be quantitatively correlated with the original concentration of metals ions in solution. As discussed in **Section 1.4** BDD is an ideal electrode material for many reasons, in EC-XRF, boron and carbon atoms are ‘invisible’ to X-Rays, and therefore will not interfere with XRF analysis. Sub ppb detection levels have been obtained for heavy metals using EC-XRF.<sup>168</sup>

## 1.5 Confocal Laser Scanning Microscopy

One optical microscopy technique which can be used to image pH dependent processes is Confocal Laser Scanning Microscopy (CLSM),<sup>169</sup> with a pH sensitive fluorescent dye such as fluorescein.<sup>170</sup> During a CLSM experiment the subject is scanned in a series of points using a laser beam, the resulting image is reconstructed digitally to produce 2D or even 3D profiles.<sup>171</sup> A laser is directed through an aperture and the objective lens where it is focused on a point of the subject. When a fluorescent dye is used either in solution or tagged to a species of interest laser excitation at a particular wavelength causes a fluorescent signal to be generated. A pinhole is used to filter the emitted signal wavelength and remove any background fluorescence before detection.<sup>172</sup> A schematic diagram of a CLSM optical microscope arrangement is presented in *Figure 1.16*.

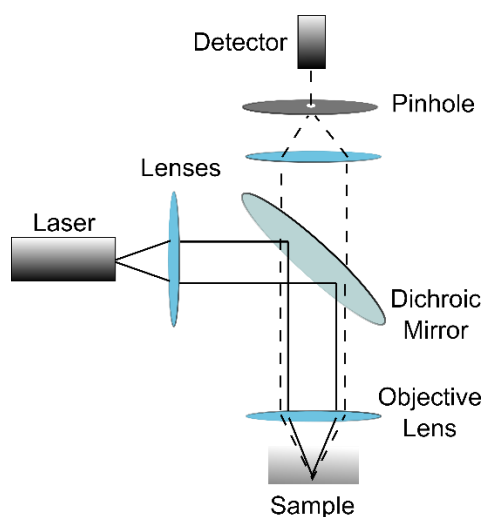


**Figure 1.16:** Schematic of a confocal laser scanning microscope.

## 1.6 Aims and Objectives

This thesis aims to utilise the benefits afforded by BDD electrodes towards *in situ* detection of heavy metals in aqueous environments. The effect of pH on the electroanalysis of heavy metals is considered; in Chapter 3 an individually addressable dual electrode (ring disc) system is developed towards answering some of the electroanalytical problems caused by non-ideal solution pH. Application of applied potentials or currents at the ring electrode sufficient to oxidize water results in the controlled production of protons, which flood the disc. This concept is investigated in the context of producing a local pH change, and is applied to the detection of the heavy metal Hg at BDD electrodes.

Chapter 4 proceeds to demonstrate how by systematically changing the pH of the measurement system it is possible to control the extent of pH dependent metal-ligand binding and in particular the concentration of the free metal ion. By employing a ring-disc electrode it is possible to perform all measurements in one measurement solution, without the need to remove the electrode from the solution. Moreover, the ability to control pH local to the electrode could aid in measurements of both total and free ion concentration in solution, something which is not currently possible *in situ* using one technique.

The desirable properties of BDD electrodes make them attractive for use *in situ*, even in the most extreme environments. However, the material used to seal (insulate) the BDD electrode is not often similarly robust. In Chapter 5 of this thesis a method for the production of BDD ring disc electrodes sealed in

an insulating diamond substrate is developed in answer to this problem. The method is optimised in order to produce high quality all diamond ring disc and dual-ring disc electrodes for use in *in situ* trace metal detection and pH control. One such device is then applied in Chapter 6 to the investigation of electrochemical pH generation in buffered systems, as opposed to the unbuffered model systems used in Chapters 3 and 4. This is an important investigation if this technique is to be used for *in situ* environmental analyses, as most natural and biological environments contain pH buffering species, such as carbonate<sup>173</sup> and phosphate<sup>174</sup> in order to maintain homeostasis.

Finally, an answer to the pitfall of electrochemical heavy metal detection in mixed metal solutions is explored in Chapter 7. The recently developed technique EC-XRF is applied to, and optimised for, the detection of two heavy metals of high importance, Cd and Hg. The chapter aims to establish optimum conditions for sensitive detection of these metals with low detection limits. It also explores the complications involved in Hg electrodeposition on a solid electrode.

Finally, Chapter 8 concludes the work presented in the aforementioned chapters and goes on to discuss the future directions of this work.

## 1.7 References

1. J. H. Duffus, *Pur. Appl. Chem.*, 2002, **74**, 793-807.
2. J. Daintith, *A dictionary of chemistry*, OUP Oxford, 2008.
3. F. Fu and Q. Wang, *J. Environ. Manage.*, 2011, **92**, 407-418.
4. A. Kudo. and S. Miyahara., *Water Sci. Technol.*, 1991, **23**, 283-290.
5. J. O. M. Bockris, *Environmental Chemistry*, Plenum Press, New York, 1977.
6. J. W. Hamilton, R. C. Kaltreider, O. V. Bajenova, M. A. Ihnat, J. McCaffrey, B. W. Turpie, E. E. Rowell, J. Oh, M. J. Nemeth and C. A. Pesce, *Environ. Health. Perspect.*, 1998, **106**, 1005.

7. P. Koedrith and Y. R. Seo, *Int. J. Mol. Sci.*, 2011, **12**, 9576-9595.
8. N. Pourang, *Environ. Monit. Assess.*, 1995, **35**, 207-219.
9. A. Salimi, V. Alizadeh and R. Hallaj, *Talanta*, 2006, **68**, 1610-1616.
10. M. Harada, *Crit. Rev. Toxicol.*, 1995, **25**, 1-24.
11. S. Hernberg, *Am. J. Ind. Med.*, 2000, **38**, 244-254.
12. World Health Organization Journal, 2013.
13. R. Carr, C. Zhang, N. Moles and M. Harder, *Environ. Geochem. Health*, 2008, **30**, 45-52.
14. F. M. G. Tack and M. G. Verloo, *Int. J. Environ. Anal. Chem.*, 1995, **59**, 225-238.
15. A. Tessier and D. R. Turner, *Metal speciation and bioavailability in aquatic systems*, Wiley Chichester, 1995.
16. D. J. Spry and J. G. Wiener, *Environ. Pollut.*, 1991, **71**, 243-304.
17. *Toxic Metal Chemistry in Marine Environments*, Taylor & Francis, 1992.
18. J. A. C. Broekaert, S. Gucer and F. Adams, *Metal Speciation in the Environment*, Springer Berlin Heidelberg, 2013.
19. Y. Chau and K. Lum-Shue-Chan, *Water Res.*, 1974, **8**, 383-388.
20. G. Cockerill and S. Reed, *Essential Fluid, Electrolyte and pH Homeostasis*, Wiley-Blackwell, 2011.
21. P. Gundersen and E. Steinnes, *Water Res.*, 2003, **37**, 307-318.
22. N. N. Greenwood and A. Earnshaw, *Chemistry of the elements*, Pergamon Press, 1984.
23. A. Zeng, E. Liu, S. N. Tan, S. Zhang and J. Gao, *Electroanalysis*, 2002, **14**, 1294-1298.
24. G. S. Reeder and W. R. Heineman, *Sens. Act. B Chem.*, 1998, **52**, 58-64.
25. L. M. L. Nollet and L. S. P. De Gelder, *Handbook of Water Analysis*, CRC Press, 2000.
26. S. Zhang, S. Wang and X.-q. Shan, *Chem. Spec. Bioavailab.*, 2001, **13**, 69-74.
27. S. Sauve, W. Hendershot and H. E. Allen, *Environ. Sci. Technol.*, 2000, **34**, 1125-1131.
28. I. Šinko and J. Doleal, *J. Electroanal. Chem. Interfac. Electrochem.*, 1970, **25**, 299-306.
29. A. Ringbom, *Complexation in analytical chemistry: a guide for the critical selection of analytical methods based on complexation reactions*, Interscience Publishers, 1963.
30. T. M. Florence, *Analyst*, 1986, **111**, 489-505.
31. M. Sillanpää, M. Orama, J. Rämö and A. Oikari, *Sci. Total Environ.*, 2001, **267**, 23-31.
32. K. Hirose, *Anal. Sci.*, 2006, **22**, 1055-1063.
33. L. K. Wang, J. P. Chen, Y. T. Hung and N. K. Shammass, *Heavy Metals in the Environment*, CRC Press, 2009.
34. A. T. Hubbard, *Encyclopedia of Surface and Colloid Science*, Taylor & Francis, 2002.
35. L. K. Wang, Y. T. Hung, H. H. Lo and C. Yapijakis, *Handbook of Industrial and Hazardous Wastes Treatment*, CRC Press, 2004.
36. E. Debrah, E. R. Denoyer and J. F. Tyson, *J. Anal. Atom. Spec.*, 1966, **11**, 127-132.
37. T. H. Nguyen, J. Boman, M. Leermakers and W. Baeyens, *Fresenius' J. Anal. Chem.*, 1998, **360**, 199-204.
38. K. C. Bowles and S. C. Apte, *Anal. Chem.*, 1998, **70**, 395-399.
39. W. H. Organization, *Guidelines for drinking-water quality: recommendations*, World Health Organization, 2004.
40. L. Yang, *Mass Spec. Rev.*, 2009, **28**, 990-1011.
41. R. Thomas, *Practical Guide to ICP-MS: A Tutorial for Beginners, Third Edition*, CRC Press, 2013.
42. S. Mitra and B. B. Kebbekus, *Environmental Chemical Analysis*, Taylor & Francis, 1997.



43. H. E. Taylor, *Inductively Coupled Plasma-mass Spectrometry: Practices and Techniques*, Academic Press, 2001.
44. S. Nelms, *Inductively Coupled Plasma Mass Spectrometry Handbook*, Blackwell, 2005.
45. J. W. Olesik, *Anal. Chem.*, 1991, **63**, 12A-21A.
46. S. I. Korfali and M. S. Jurdi, *Environ. Monit. Assess.*, 2010, **178**, 563-579.
47. J. Robinson, *Anal. Chem.*, 1960, **32**, 17A-29A.
48. S. M. Khopkar, *Basic Concepts Of Analytical Chemistry*, New Age International Publishers, 1998.
49. S. J. Haswell, *Atomic Absorption Spectrometry: Theory, Design, and Applications*, Elsevier, 1991.
50. S. Mitra, *Sample Preparation Techniques in Analytical Chemistry*, Wiley, 2004.
51. J. P. Hurley, M. M. Shafer, S. E. Cowell, J. T. Overdier, P. E. Hughes and D. E. Armstrong, *Environ. Sci. Technol.*, 1996, **30**, 2093-2098.
52. J. F. Alder, S. K. Perry and F. P. Brady, *Environ. Sci. Technol.*, 1975, **9**, 1039-1042.
53. A. Tessier, P. G. Campbell and M. Bisson, *Anal. Chem.*, 1979, **51**, 844-851.
54. M. Nicolai, C. Rosin, N. Tousset and Y. Nicolai, *Talanta*, 1999, **50**, 433-444.
55. K. Johnson, V. Elrod, J. Nowicki, K. Coale and H. Zamzow, *In situ monitoring of aquatic systems: chemical analysis and speciation.*, 2000, 223-252.
56. M. S. Varney, *Chemical sensors in oceanography*, CRC Press, 2000.
57. M. Pesavento, G. Alberti and R. Biesuz, *Anal. Chim. Acta.*, 2009, **631**, 129-141.
58. F. Melquiades and C. Appoloni, *Journal of Radioanal. Nucl. Chem.*, 2004, **262**, 533-541.
59. E. P. Achterberg and C. Braungardt, *Anal. Chim. Acta.*, 1999, **400**, 381-397.
60. M. B. Gumpu, S. Sethuraman, U. M. Krishnan and J. B. B. Rayappan, *Sens. Act. B Chem.*, 2015, **213**, 515-533.
61. E. Schonberger and W. Pickering, *Talanta*, 1980, **27**, 11-18.
62. O. El Tall, N. Jaffrezic-Renault, M. Sigaud and O. Vittori, *Electroanalysis*, 2007, **19**, 1152-1159.
63. J. H. Yoon, J. E. Yang, J. P. Kim, J. S. Bae, Y. B. Shim and M. S. Won, *Bull. Korean Chem. Soc.*, 2010, **31**, 141.
64. J. Wang, *Stripping analysis*, Wiley Online Library, 1985.
65. F. Long, A. Zhu, H. Shi, H. Wang and J. Liu, *Scientific reports*, 2013, **3**.
66. Z. Zou, A. Jang, E. MacKnight, P.-M. Wu, J. Do, P. L. Bishop and C. H. Ahn, *Sens. Act. B Chem.*, 2008, **134**, 18-24.
67. J.-M. Zen, A. Senthil Kumar and D.-M. Tsai, *Electroanalysis*, 2003, **15**, 1073-1087.
68. O. Farghaly, R. A. Hameed and A.-A. H. Abu-Nawwas, *Int. J. Electrochem. Sci.*, 2014, **9**, 3287-3318.
69. J. Buffle and M.-L. Tercier-Waeber, *TrAC Trends in Anal. Chem.*, 2005, **24**, 172-191.
70. A. J. Bard and L. R. Faulkner, *Electrochemical methods. Fundamentals and Applications*, John Wiley and Sons, 2nd edn., 2001.
71. J. J. Wang, *Analytical Electrochemistry*, CreateSpace Independent Publishing Platform, 2015.
72. T. L. Read and J. V. Macpherson, *J. Vis. Exp.*, 2016, **107**, e53484.
73. J. V. Macpherson, *Phys. Chem. Chem. Phys.*, 2015, **17**, 2935-2949.
74. R. S. Nicholson, *Anal. Chem.*, 1965, **37**, 1351-1355.
75. C. M. A. Brett and A. M. O. Brett, *Electrochemistry: Principles, Methods, and Applications*, Oxford University Press, 1993.
76. R. S. Sussmann, *CVD Diamond for Electronic Devices and Sensors*, Wiley, 2009.
77. F. G. Banica, *Chemical Sensors and Biosensors: Fundamentals and Applications*, Wiley, 2012.

78. R. N. Adams, *Electrochemistry at solid electrodes*, N. Dekker, 1969.
79. A. N. Patel, S.-y. Tan, T. S. Miller, J. V. Macpherson and P. R. Unwin, *Anal. Chem.*, 2013, **85**, 11755-11764.
80. F. G. Thomas and G. Henze, *Introduction to Voltammetric Analysis: Theory and Practice*, CSIRO Pub., 2001.
81. R. J. Reay, A. F. Flannery, C. W. Storment, S. P. Kounaves and G. T. A. Kovacs, *Sens. Act. B Chem.*, 1996, **34**, 450-455.
82. D. Jagner and S. Westerlund, *Anal. Chim. Acta.*, 1980, **117**, 159-164.
83. J. Barek, A. G. Fogg, A. Muck and J. Zima, *Crit. Rev. Anal. Chem.*, 2001, **31**, 291-309.
84. L. A. Hutton, M. E. Newton, P. R. Unwin and J. V. Macpherson, *Anal. Chem.*, 2011, **83**, 735-745.
85. J. G. Webster, *The Measurement, Instrumentation and Sensors Handbook*, Taylor & Francis, 1998.
86. M. de la Guardia and S. Garrigues, *Handbook of Green Analytical Chemistry*, Wiley, 2012.
87. K. Rajeshwar, J. Ibanez and G. Swain, *J. Appl. Electrochem.*, 1994, **24**, 1077-1091.
88. C. Wei, S. German, S. Basak and K. Rajeshwar, *J. Electrochem. Soc.*, 1993, **140**, L60-L62.
89. Y. Ikariyama and W. R. Heineman, *Anal. Chem.*, 1986, **58**, 1803-1806.
90. J. Pouilleau, D. Devilliers, H. Groult and P. Marcus, *J. Mater. Sci.*, 1997, **32**, 5645-5651.
91. M. M, Radhi. W, T, Tan. Z, B, Ab Rahman. A, B, Kassim, *Int. J. Electrochem. Sci.*, 2010, 615-629.
92. Y. Wei, C. Gao, F.-L. Meng, H.-H. Li, L. Wang, J.-H. Liu and X.-J. Huang, *J. Phys. Chem. C*, 2011, **116**, 1034-1041.
93. A. Afkhami, T. Madrakian, S. J. Sabounchei, M. Rezaei, S. Samiee and M. Pourshahbaz, *Sens. Act. B Chem.*, 2012, **161**, 542-548.
94. I. Cesarino, É. T. G. Cavalheiro and C. Brett, *Electroanalysis*, 2009, **22**, 61-68.
95. C. Babyak and R. B. Smart, *Electroanalysis*, 2004, **16**, 175-182.
96. D. Dragoe, N. Spătaru, R. Kawasaki, A. Manivannan, T. Spătaru, D. A. Tryk and A. Fujishima, *Electrochim. Acta*, 2006, **51**, 2437-2441.
97. E. A. McGaw and G. M. Swain, *Anal. Chim. Acta.*, 2006, **575**, 180-189.
98. A. Manivannan, D. A. Tryk and A. Fujishima, *Electrochem. Solid State Lett.*, 1999, **2**, 455-456.
99. J. Heinze, *Angew. Chem. Int. Edit.*, 1993, **32**, 1268-1288.
100. C. H. Bamford, C. F. H. Tipper† and R. G. Compton, *Electrode Kinetics: Principles and Methodology*, Elsevier Science, 1986.
101. J. V. Macpherson, N. Simjee and P. R. Unwin, *Electrochim. Acta*, 2001, **47**, 29-45.
102. F. Opekar and P. Beran, *J. Electroanal. Chem. Interfac. Electrochem.*, 1976, **69**, 1-105.
103. E. O. Barnes, G. E. M. Lewis, S. E. C. Dale, F. Marken and R. G. Compton, *Analyst*, 2012, **137**, 1068-1081.
104. J. A. Cooper and R. G. Compton, *Electroanalysis*, 1998, **10**, 141-155.
105. A. C. Fisher, *Electrode Dynamics*, Oxford University Press, 1996.
106. I. U. V. Pleskov and V. I. U. Filinovskii, *The rotating disc electrode*, Consultants Bureau, 1976.
107. P. Sonthalia, E. McGaw, Y. Show and G. M. Swain, *Anal. Chim. Acta.*, 2004, **522**, 35-44.
108. N. V. Alov and K. V. Oskolok, *Spectrochim. Acta. B Atom. Spec.*, 2003, **58**, 735-740.
109. G. Forsberg, J. W. O'Laughlin, R. G. Megargle and S. R. Koirtiyhann, *Anal. Chem.*, 1975, **47**, 1586-1592.

110. J. Wang, J. Lu, S. B. Hocevar, P. A. M. Farias and B. Ogorevc, *Anal. Chem.*, 2000, **72**, 3218-3222.
111. J. Wang, *Stripping analysis: principles, instrumentation, and applications*, VCH, 1985.
112. D. R. Gabe, *J. Appl. Electrochem.*, **27**, 908-915.
113. W. L. Tsai, P. C. Hsu, Y. Hwu, C. H. Chen, L. W. Chang, J. H. Je, H. M. Lin, A. Groso and G. Margaritondo, *Nature*, 2002, **417**, 139-139.
114. D. A. Skoog, D. M. West, F. J. Holler and S. R. Crouch, *Fundamentals of Analytical Chemistry*, Cengage Learning, 2013.
115. G. E. Batley, *Trace Element Speciation Analytical Methods and Problems*, Taylor & Francis, 1989.
116. P. W. May, *Philos. Trans. Royal Soc. London. A*, 2000, **358**, 473-495.
117. M. Kutz, *Handbook of Materials Selection*, Wiley, 2002.
118. G. E. Harlow and A. M. o. N. History, *The Nature of Diamonds*, Cambridge University Press, 1998.
119. Y. Sato and M. Kamo, in *The Properties of Natural and Synthetic Diamond*, Academic Press, London, 1992, pp. 423-469.
120. X. Blase, E. Bustarret, C. Chapelier, T. Klein and C. Marcenat, *Nat. Mater.*, 2009, **8**, 375-382.
121. G. Davies and INSPEC, *Properties and Growth of Diamond*, INSPEC, the Institution of Electrical Engineers, 1994.
122. F. P. Bundy, H. T. Hall, H. M. Strong and R. H. Wentorf, *Nature*, 1955, **176**, 51-55.
123. J. E. Field, *The Properties of Natural and Synthetic Diamond*, 1992.
124. K. E. Spear, J. P. Dismukes and E. Society, *Synthetic Diamond: Emerging CVD Science and Technology*, Wiley, 1994.
125. J. C. Angus, eds. E. Brillas and C. A. M. Huitle, John Wiley & Sons, Inc., 2011, ch. 4, pp. 79-81.
126. E. Ito, in *Mineral Physics: Treatise on Geophysics*, ed. G. D. Price, Elsevier Science, 2010, ch. 8, pp. 197-227.
127. M. Werner and R. Locher, *Reports on Progress in Physics*, 1998, **61**, 1665.
128. C. Lévy-Clémente, in *Diamond Electrochemistry*, 2005, ch. 5, pp. 80-114.
129. A. T. Collins, *Philos. Trans. Royal Soc. London. A*, 1993, **342**, 233-244.
130. J. H. T. Luong, K. B. Male and J. D. Glennon, *Analyst*, 2009, **134**, 1965-1979.
131. A. Fujishima, *Diamond Electrochemistry*, BKC, 2005.
132. G. Janssen, W. J. P. van Enckevort, W. Vollenberg and L. J. Giling, *Diamond Relat. Mater.*, 1992, **1**, 789-800.
133. Y. V. Pleskov, A. Y. Sakharova, M. D. Krotova, L. L. Bouilov and B. P. Spitsyn, *J. Electroanal. Chem.*, 1987, **228**, 19-27.
134. L. A. Hutton, J. G. Iacobini, E. Bitziou, R. B. Channon, M. E. Newton and J. V. Macpherson, *Anal. Chem.*, 2013, **85**, 7230-7240.
135. A. N. Correia and S. A. S. Machado, *Electrochim. Acta*, 1998, **43**, 367-373.
136. A. J. Bard, *J. Am. Chem. Soc.*, 2010, **132**, 7559-7567.
137. A. Kraft, *Int. J. Electrochem. Sci*, 2007, **2**, 355-385.
138. G. M. Swain, *J. Electrochem. Soc.*, 1994, **141**, 3382-3393.
139. R. S. Balmer, J. R. Brandon, S. L. Clewes, H. K. Dhillon, J. M. Dodson, I. Friel, P. N. Inglis, T. D. Madgwick, M. L. Markham, T. P. Mollart, N. Perkins, G. A. Scarsbrook, D. J. Twitchen, A. J. Whitehead, J. J. Wilman and S. M. Woollard, *J. Phys. Condens. Matter*, 2009, **21**, 364221.
140. S. Tanimoto and A. Ichimura, *J. Chem. Edu.*, 2013, **90**, 778-781.
141. J. A. Bennett, J. Wang, Y. Show and G. M. Swain, *J. Electrochem. Soc.*, 2004, **151**, E306-E313.

142. K. F. Blurton, *Electrochim. Acta*, 1973, **18**, 869-875.
143. M. C. Granger, M. Witek, J. Xu, J. Wang, M. Hupert, A. Hanks, M. D. Koppang, J. E. Butler, G. Lucazeau, M. Mermoux, J. W. Strojek and G. M. Swain, *Anal. Chem.*, 2000, **72**, 3793-3804.
144. I. Duo, C. Levy-Clement, A. Fujishima and C. Comninellis, *J. Appl. Electrochem.*, 2004, **34**, 935-943.
145. K. K. Cline, M. T. McDermott and R. L. McCreery, *J. Phys. Chem*, 1994, **98**, 5314-5319.
146. L. A. Hutton, M. E. Newton, P. R. Unwin and J. V. Macpherson, *Anal. Chem.*, 2009, **81**, 1023-1032.
147. R. Schaeffer, *Fundamentals of Laser Micromachining*, Taylor & Francis, 2012.
148. R. Windholz and P. A. Molian, *J. Mater. Sci.*, **33**, 523-528.
149. X. Wang, G. Y. Mak and H. W. Choi, *Laser micromachining and micro-patterning with a nanosecond UV laser*, INTECH Open Access Publisher, 2012.
150. A. Zweig, *J. Appl. Phys.*, 1991, **70**, 1684-1691.
151. A. K. Dubey and V. Yadava, *Int. J. Mach. Tools Manufact.*, 2008, **48**, 609-628.
152. H. Klank, J. P. Kutter and O. Geschke, *Lab. Chip.*, 2002, **2**, 242-246.
153. C. Hallgren, H. Reimers, D. Chakarov, J. Gold and A. Wennerberg, *Biomaterials*, 2003, **24**, 701-710.
154. Z. J. Ayres, A. J. Borrill, J. C. Newland, M. E. Newton and J. V. Macpherson, *Anal. Chem.*, 2016, **88**, 974-980.
155. W. Matthias, *Semicond. Sci. Technol.*, 2003, **18**, S41.
156. K. Das, V. Venkatesan, K. Miyata, D. L. Dreifus and J. T. Glass, *Thin Solid Films*, 1992, **212**, 19-24.
157. B. Beckhoff, B. Kanngießer, N. Langhoff, R. Wedell and H. Wolff, *Handbook of Practical X-Ray Fluorescence Analysis*, Springer Berlin Heidelberg, 2007.
158. P. Brouwer, *Almelo, Netherlands: PANalytical BV*, 2006.
159. J. Börjesson, M. Isaksson and S. Mattsson, *Acta Diabetol.*, 2003, **40**, s39-s44.
160. E. Aloupi, A. Karydas and T. Paradellis, *X-ray Spectrometry*, 2000, **29**, 18-24.
161. I. Liritzis and N. Zacharias, in *X-ray fluorescence spectrometry (XRF) in geoarchaeology*, Springer, 2011, pp. 109-142.
162. I. Campbell, Y. Xiao, B. Vrebos, L. Kempnaers, D. Coler and K. Macchiarola, *Journal*, 2010.
163. F. L. Melquiades and C. R. Appoloni, *Journal of Radioanalytical and Nuclear Chemistry*, 2004, **262**, 533-541.
164. R. A. Nadkarni, A. S. f. Testing and Materials, *Modern Instrumental Methods of Elemental Analysis of Petroleum Products and Lubricants*, ASTM, 1991.
165. Rigaku, Ultra-low (ppb) quantitative analysis using UltraCarry method for river water standard JAC0032, <http://www.rigaku.com/en/products/xrf/primus2/app009>, (accessed 24 March, 2016).
166. D. E. Leyden, T. A. Patterson and J. J. Alberts, *Anal. Chem.*, 1975, **47**, 733-735.
167. E. Marguá, R. Van Grieken, C. Fontàs, M. Hidalgo and I. Queralt, *Appl. Spectros. Rev.*, 2010, **45**, 179-205.
168. L. A. Hutton, G. D. O'Neil, T. L. Read, Z. J. Ayres, M. E. Newton and J. V. Macpherson, *Anal. Chem.*, 2014, **86**, 4566-4572.
169. C. Sheppard and D. Shotton, *Confocal Laser Scanning Microscopy*, BIOS Scientific, 1997.
170. S. Fiedler, R. Hagedorn, T. Schnelle, E. Richter, B. Wagner and G. Fuhr, *Anal. Chem.*, 1995, **67**, 820-828.
171. A. R. Cohen, B. Roysam and J. N. Turner, *J. Microscopy*, 1994, **173**, 103-114.

- 172. S. Jha, *Techniques in Confocal Microscopy*, Elsevier Science, 2010.
- 173. S. K. Lower, *Simon Fraser University*, 1999, **544**.
- 174. F. A. Bettelheim, W. H. Brown, M. K. Campbell and S. O. Farrell, *Introduction to Organic and Biochemistry*, Cengage Learning, 2009.

## 2 Experimental

### 2.1 Chemicals

All solutions were prepared using Milli-Q water, resistivity 18.2 M $\Omega$  cm at 25 °C (Millipore). Chemicals were used as provided unless stated otherwise and were measured using a four figure balance (Mettler Toledo). A list of the chemicals used can be found in **Table 2.1**. Bulk solution pH values were measured using a commercial pH probe (Mettler Toledo), adjustments were made using 0.1 M HNO<sub>3</sub> and 0.1 M KOH.

**Table 2.1:** List of chemicals used in this thesis and the suppliers.

Chemical	Supplier	Extra Information
Potassium Nitrate, KNO <sub>3</sub>	Sigma-Aldrich	99.999% Trace Metals Basis
Ruthenium (III) Hexaamine, Ru(NH <sub>3</sub> ) <sub>6</sub> <sup>3+</sup>	Strem Chemicals Ltd.	99%
Nitric acid, HNO <sub>3</sub>	Sigma-Aldrich	70%
Potassium Hydroxide, KOH	Sigma-Aldrich	≥ 85%
Hydrochloric Acid, HCl	Sigma-Aldrich	37%
Sulphuric Acid, H <sub>2</sub> SO <sub>4</sub>	Sigma-Aldrich	99.999%
Alumina Micropolish	Buehler	0.05 $\mu$ m
Cadmium nitrate tetrahydrate, Cd(NO <sub>3</sub> ) <sub>2</sub> ·4H <sub>2</sub> O	Sigma-Aldrich	99%
Mercury (II) nitrate monohydrate, Hg(NO <sub>3</sub> ) <sub>2</sub> ·H <sub>2</sub> O	Sigma-Aldrich	>98%

Sodium Nitrate, $\text{NaNO}_3$	Sigma-Aldrich	$\geq 99.9\%$
Copper (II) Nitrate hydrate, $\text{Cu}(\text{NO}_3)_2 \cdot x\text{H}_2\text{O}$	Sigma-Aldrich	99.999% trace metals basis
Triethylenetetramine dihydrochloride, $\text{NH}_2\text{CH}_2\text{CH}_2(\text{NHCH}_2\text{CH}_2)_2\text{NH}_2$	Sigma-Aldrich	98%
Fluorescein Sodium Salt, $\text{C}_{20}\text{H}_{10}\text{Na}_2\text{O}_5$	Sigma-Aldrich	98.5-100.5%
Sodium Tetraborate decahydrate, $\text{Na}_2\text{B}_4\text{O}_7 \cdot 10\text{H}_2\text{O}$	Sigma-Aldrich	$\geq 99\%$
Fixanal Buffer Concentrates	Sigma-Aldrich	pH 1-10
Iridium Tetrachloride hydrate	Sigma-Aldrich	99.9% trace metals basis
Oxalic Acid dihydrate	Sigma-Aldrich	$\geq 99\%$
Hydrogen Peroxide	Sigma-Aldrich	30%
Anhydrous Potassium Carbonate	Sigma-Aldrich	99.999%

## 2.2 Boron Doped Diamond

High quality Boron Doped Diamond electrode material was provided by the synthetic diamond growth company, Element Six, in the form of freestanding wafers grown via MWCVD. The wafers provided were  $\sim 600 \mu\text{m}$  thick and lapped to  $\sim \text{nm}$  roughness, as measured by AFM. The dopant density was  $\geq 10^{20}$  atom  $\text{cm}^{-3}$ , and therefore exhibited metal-like behaviour and was suitable for electrochemical studies.

### 2.2.1 Laser Micromachining Electrodes

Electrodes were prepared from the BDD wafer via laser micromachining (E-355-H-3-ATHI-O, Oxford Lasers, UK). Firstly, the desired shape was designed

in 2D geometries using Alphacam software (Vero Software, US). The resulting diagram was exported as G-Code, a computer numerical control (CNC) programming language which gives directions for the laser micromachining stage describing where to move, via what path, and how fast in order to create the shape.

The laser was initialised and warmed up for ~30 min prior to use, once stabilised the power at 10 kHz (100 % power) was measured and recorded. The BDD wafer was secured on an alumina plate using blu-tack™ at opposing edges; this was secured to the appropriate well in the stage. Once in place, the laser was optically focussed on the surface of the BDD using the camera, preferably in an unimportant area or on a test piece of equivalent thickness and roughness. A 1 s laser pulse at 20 % power, frequency = 100 Hz was performed. The stage was then stepped 100 µm in the *x* direction and 30 µm down in the *z* direction before repeating the pulse. If the lasered spot size (diameter, visible by eye) decreased this step was repeated until it started to increase again, however, if the laser spot created increased in size the *z* direction was adjusted in 30 µm increments in the opposite direction before repeating. The *z* value of the smallest spot size indicated the best focus for the surface of the substrate, **Figure 2.1**. When the laser is out of focus, this results in a larger spot size due to the divergence of the beam as you move away from the focal point; this causes a larger area of the substrate to be affected.



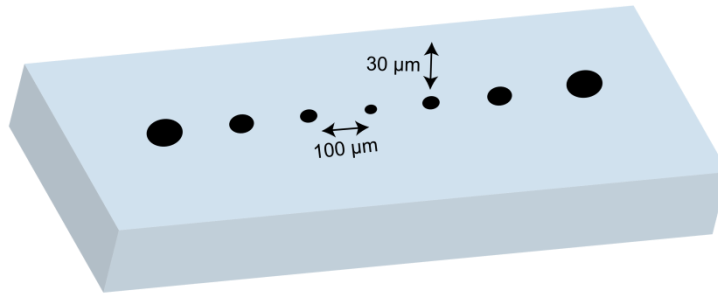


**Figure 2.1:** Schematic illustrating a line of laser pulses at different focus on the diamond surface. There is a  $100\ \mu\text{m}$  separation between the centre of each pulse in the  $x$  direction, and each adjacent pulse differs by  $30\ \mu\text{m}$  in the  $z$  direction. The smallest dot indicates the best focus.

Next, the stage was adjusted in the  $x$  and  $y$  directions such that the centre of the reverse side of the BDD was in the centre of the laser focus on the camera view. A trench of the desired geometry was lasered into the diamond at 50 % power, frequency = 100 Hz, speed  $0.3\ \text{mm s}^{-1}$ . The depth of this trench was measured via interferometry before the laser was refocused in the  $z$  direction (using the depth measured by interferometry) to the bottom centre of the trench; the laser step was repeated increasing the depth of the trench, which was measured once more. From this the approximate depth per pass was calculated, and used to set the  $z$ -step. This is essential for each new generation of electrodes as the laser power can vary over time, additionally poor laser focus can cause issues in achieving the desired dimensions of cut. Finally, the number of passes necessary to reach the depth of cut necessary was calculated. The cutting program designed using Alphacam was loaded, and at frequency = 10 kHz, 100% power, was used to laser individual devices out of the substrate.

### 2.2.2 Back contacting and Electrode Fabrication

The lasered electrodes were subjected to an acid-cleaning protocol. A beaker of concentrated  $\text{H}_2\text{SO}_4$  was positioned on a hot plate at room temperature into which the BDD was carefully placed. Loaded spatulas of  $\text{KNO}_3$  were added until it no longer dissolved ( $\sim 0.5$  g in 2 ml), then the beaker was covered with a watch glass and heated to  $\sim 300$  °C for at least 30 mins; the solution turned brown as heated and the  $\text{KNO}_3$  dissolved. After this time, and once there was no longer any brown colour to the solution the hot plate was turned off and the solution was cooled to room temperature. The cooled  $\text{H}_2\text{SO}_4$  was disposed of by dilution in room temperature water, and the BDD was rinsed thoroughly with Milli-Q water before drying in air; the electrodes were now ready to be back-contacted.

Ohmic contacts to the rear face of the BDD were prepared using standard sputtering (or evaporating) techniques. Layers of Ti/Au, 10 nm/300 nm thick respectively, were sputtered onto the rear of the BDD using a sputterer/evaporator at pressures below  $1 \times 10^{-5}$  mBar. After returning to standard pressure, the BDD was removed from the chamber and annealed at 400 °C for 5 hours enabling the Ti to form titanium carbide, which is crucial for the formation of an ohmic contact.<sup>1, 2</sup>

Electrodes were then assembled face down on adhesive Gel-Pak™ in a cylindrical Teflon mould, a thin layer of non-conductive epoxy (Epoxy Resin RX771C/NC, Aradur Hardener HY1300GB, Robnor Resins) was used to secure them in place. Insulated Cu wires were connected to the sputtered face of the

diamond using conductive silver epoxy (Circuitworks, ITW Chemtronics), and left to cure at room temperature. Finally, the Teflon mould was filled with non-conductive epoxy and cured overnight at room temperature before the device was removed. The front face of the electrode was polished with silicon carbide pads (Buehler) of decreasing roughness until the surface of the electrode was completely exposed, finishing with application of an alumina polish (0.05  $\mu\text{m}$  Micropolish, Buehler) and rinsing with Milli-Q water.

## **2.3 Characterisation of BDD Electrodes**

The material and electrochemical properties of the BDD electrodes were characterised as described in full in the article entitled *“Assessment of Boron Doped Diamond Electrode Quality and Application to In Situ Modification of Local pH by Water Electrolysis”*.<sup>2</sup> Of key importance in this work is the electrochemical characterisation, although Raman analysis is also used.

### **2.3.1 Raman Analysis of BDD**

The micro-Raman spectrometer (Renishaw) was turned on and left for ~30 min to allow time for the CCD Detector to cool down and the laser to initialise. The system was calibrated using a silicon wafer, which was placed in the instrument chamber before using the microscope to focus optically on the sample. It was then ensured that the laser spot was well defined and circular using laser view to observe, before calibration. Once calibrated, the silicon wafer was removed and replaced with the BDD electrode; again the microscope was focused both optically and via the laser spot. A Raman spectrum was measured between 200-1800  $\text{cm}^{-1}$  for an acquisition time <10 s at

100 % laser power, for five accumulations. An optical image of the area scanned was saved for reference. A peak at 1332 cm<sup>-1</sup> in the spectrum indicates the presence of sp<sup>3</sup> C (diamond) due to the presence of solely  $\sigma$  bonds, which result in a single diamond zone centre optical phonon peak, the sharper this peak the higher the purity of the diamond.<sup>3, 4</sup> The presence of NDC can also be detected, indicated by a broad peak centered at 1575 cm<sup>-1</sup> in the spectrum this originates from the stretching of paired sp<sup>2</sup> C sites; the larger the peak, the more NDC is present.<sup>5</sup> The  $\pi$  bonds formed by sp<sup>2</sup> carbon are more easily polarised than sp<sup>3</sup>  $\sigma$  bonds, and are resonantly enhanced by visible lasers; this leads to broader, more dominant peaks for sp<sup>2</sup> C.<sup>4</sup>

## 2.3.2 Electrochemical Characterisation of BDD

### 2.3.2.1 Capacitance

The BDD electrode was alumina polished, rinsed and placed in 20 ml KNO<sub>3</sub> solution; the Cu wire was connected to the working electrode connection of a potentiostat (CH Instruments Inc., US). An SCE reference electrode and Pt gauze counter electrode were connected and placed in the same solution. The potentiostat was used to sweep the potential at the working (BDD) electrode between -0.1 V and 0.1 V, starting at 0 V, for 10 repeats at 0.1 Vs<sup>-1</sup>. The second CV was analysed according to **Equation [2.1]**; the difference in anodic and cathodic current at 0 V was measured, halved, and divided by the scan rate and electrode area, calculating C in  $\mu\text{F cm}^2$ .

$$I(t) = C \frac{dV(t)}{dt} \quad [2.1]$$

Where,  $I$  is current (A),  $V$  is potential (V),  $t$  is time (s), and  $C$  is capacitance ( $\mu\text{F cm}^{-2}$ ).

### **2.3.2.2 Solvent Window**

As before, the electrode was cleaned, rinsed and placed in 0.1 M  $\text{KNO}_3$  in a three electrode cell. The potentiostat was now used to sweep the potential from 0 V to -2 V and then between -2 V and + 2 V repeatedly (4 sweeps). The second CV was converted to current density ( $\text{mA cm}^{-2}$ ) and analysed to measure the solvent window of the electrode; this is the potential window between the current limits  $\pm 0.4 \text{ mA cm}^{-2}$ . NDC presence in the electrode produces anodic peaks due to  $\text{sp}^2$  oxidation, and cathodic peaks due to catalysed oxygen reduction which shrink the solvent window.<sup>3</sup> For high quality,  $\text{sp}^2$  free, metal-like BDD electrodes the solvent window is expected to be  $>>3 \text{ V}$  with no evidence of oxygen reduction or NDC oxidation.<sup>2, 6</sup>

### **2.3.2.3 Redox Electrochemistry**

The electrode was cleaned as before and assembled in a three electrode cell in solution containing a well-defined redox mediator, in this case 1 mM ruthenium hexamine ( $\text{Ru}(\text{NH}_3)_6^{3+}$ ), and 0.1 M  $\text{KNO}_3$  supporting electrolyte. The potential was swept between +0.2 V and -0.8 V for scan rates between 0.05  $\text{V s}^{-1}$  and 0.2  $\text{V s}^{-2}$ . Using this particular mediator for BDD investigations is advantageous as it shows fast, outer sphere, electron transfer and is electroactive in a region which challenges p-type semiconducting BDD,<sup>3</sup> making it a good probe of the material quality. Additionally,  $\text{sp}^2$  content will catalyse oxygen reduction in this region. The voltage separation ( $\Delta E_p$ ) between

the anodic and cathodic peak of the CV was measured and compared to theory; for metal-like oxygen terminated BDD electrodes with good ohmic contacts, this value is expected to be <70 mV under standard conditions.<sup>7</sup> This increases when poor contact is made to the electrode, or when the material is not highly doped. Additionally, the peak current ( $i_p$ ) of the reduction process was measured and correlated with that expected from the Randles-Sevcik equation.

## 2.4 Field-Emission Scanning Electron Microscopy (FE-SEM)

In this thesis FE-SEM images of Hg deposits on the BDD electrode surface were obtained using a high resolution Zeiss Supra 55 VP, with a secondary electron detector at 2.5 kV at a working distance of 16-17 mm. Metal deposits were formed on the BDD surface electrochemically, this was rinsed very gently with Milli-Q water and air dried at room temperature. The electrode was secured onto a pin mount using conductive silver paint and a conductive carbon pad, ensuring the conductive paint was connected to the Ti/Au contacts on the reverse side of the BDD. The assembly was then mounted into the sample chamber, which is pumped down to high vacuum ( $1 \times 10^{-1}$  to  $1 \times 10^{-7}$  Pa) ready for FE-SEM imaging.

## 2.5 References

1. T. Tachibana, B. Williams and J. Glass, *Phys. Rev. B.*, 1992, **45**, 11975.
2. T. L. Read and J. V. Macpherson, *J. Vis. Exp.*, 2016, **107**, e53484.
3. J. V. Macpherson, *Phys. Chem. Chem. Phys.*, 2015, **17**, 2935-2949.
4. J. Filik, *Spectroscopy Europe*, 2005, **17**, 10.
5. F. Tuinstra and J. L. Koenig, *J. Chem. Phys.*, 1970, **53**, 1126-1130.
6. L. A. Hutton, J. G. Iacobini, E. Bitziou, R. B. Channon, M. E. Newton and J. V. Macpherson, *Anal. Chem.*, 2013, **85**, 7230-7240.
7. A. M. Bond, E. A. Mashkina and A. N. Simonov, *Developments in Electrochemistry: Science Inspired by Martin Fleischmann*, 2014, 21-47.

### **3 *In situ* Control of Local pH using a Boron Doped Diamond Ring Disc Electrode: Optimising Heavy Metal (Mercury) Detection**

#### **3.1. Overview**

A novel electrochemical approach to modifying aqueous solution pH in the vicinity of a detector electrode in order to locally investigate the effect of pH on the electrochemical measurement signal, is described in this chapter. A ring disc electrode was employed, where electrochemical decomposition of water on the ring was used to generate a flux of protons which adjusts the local pH controllably and quantifiably at the disc. Boron doped diamond (BDD) functioned as the electrode material given the stability of this electrode surface especially when applying high potentials (to electrolyse water) for significant periods of time. A pH sensitive iridium oxide electrode electrodeposited on the disc electrode demonstrated that applied positive currents on the BDD ring, up to + 50  $\mu\text{A}$ , resulted in a local pH decrease over four orders of magnitude in proton concentration. This induced pH change remained stable over the measurement time of 600 s. pH generation experiments were found to be in close agreement with finite element simulations. Localised generation of protons ( $\text{pH} = 2.0$ ) was found to significantly increase the stripping peak signature for the heavy metal, Hg, in close to neutral conditions. With the ability to create a localised pH change

electrochemically in the vicinity of the detector electrode this system could provide a simple method for optimised analysis at the source e.g. river and sea waters, as well as to provide information on both free (natural pH) metal and total (electrochemically adjusted pH) metal concentrations.

### **3.2. Introduction**

pH plays a crucial role in many important processes ranging from maintaining biological homeostasis,<sup>1</sup> influencing the mobility of heavy metals in the environment,<sup>2</sup> to controlling crystal dissolution/growth kinetics.<sup>3</sup> In electroanalysis, protons ( $H^+$ ) play a key role in different electrochemical reactions, often by acting as a catalyst<sup>4</sup> or by simply retarding competing side reactions.<sup>5</sup> In heavy metal detection, via electrodeposition and subsequent anodic stripping voltammetry (ASV),<sup>6</sup> pH is important as it controls metal ion availability (lability) which in turn affects the magnitude of the ASV response.<sup>6-7</sup> This is discussed in more detail in sections 1.2.2 and 1.3.5. In the laboratory, stripping analysis is often undertaken under conditions where an acetate buffer is deliberately added (as discussed in section 1.2.2)<sup>8</sup> or the solution is deliberately acidified.<sup>9</sup>

Mercury (Hg) is a highly toxic heavy metal contaminant from both industrial and natural sources, hence detection and quantification in aquatic environments is essential.<sup>10</sup> In stripping analysis, due to legislation Hg can no longer be employed as the electrode material of choice and is anyway unsuitable for Hg detection. As an alternative, boron-doped diamond (BDD) has attracted much attention<sup>11</sup> due to its wide solvent window, low



background currents and corrosion resistance.<sup>12</sup> Traditionally, Hg electroanalysis has been carried out using both model and real solutions, under acidic conditions ( $\leq \text{pH } 3$ ), to completely suppress metal hydroxide ( $\text{OH}^-$ ) formation.<sup>13,14</sup> There is significant interest in deployment of electrodes remotely e.g. river, sea or lake, where the pH is typically 6 - 9 in rivers<sup>15</sup> and 7.5 - 8.5 in sea water.<sup>16</sup> Hence it is of interest to consider how the electrochemical response varies for Hg ASV under conditions where it is possible to change the local pH of the measurement electrode.

It is well known that the electrochemical decomposition of water at sufficiently high oxidizing potentials leads to the formation of  $\text{H}^+$ , as shown in reaction scheme [3.1].<sup>17</sup>



In order to locally generate acidic conditions to promote efficient electroanalysis, a convenient electrochemical approach is to use a dual electrode (DE) system. DE come in various geometries, including bands,<sup>18</sup> ring discs<sup>19</sup> and microdisc<sup>20</sup> electrodes and have been used widely in electroanalysis; for example to investigate analyte detection in the presence of interfering species,<sup>21</sup> dissolution processes,<sup>22</sup> and the role of different species in electrochemical reactions.<sup>23</sup> DE systems also offer high sensitivity, enabling trace level detection.<sup>19b, 24</sup> To the best of our knowledge there are no reported studies of the use of a BDD DE arrangement where one electrode is used to optimise the pH environment of the other.<sup>25</sup>

In this chapter it is shown that by employing individually addressable BDD ring disc electrodes, it is possible to significantly increase the ASV signal for  $\text{Hg}^{2+}$  at a fixed concentration, in solutions where the bulk pH is close to neutral. This is achieved by generating acidic fluxes at the ring electrode during electrochemical deposition and stripping of electrodeposited Hg at the disc. The successful application of this approach to Hg bodes extremely well for the *in situ* electroanalysis of other heavy metals directly at the source.

### 3.3. Experimental

#### 3.3.1. Solutions

All solutions were prepared using Milli-Q water (resistivity 18.2 M $\Omega$  cm at 25 °C) and all reagents were used as received. The supporting electrolyte employed was 0.1 M  $\text{KNO}_3$  unless otherwise stated. Electrochemical characterization was carried out using 1 mM  $\text{Ru}(\text{NH}_3)_6^{3+/2+}$  (98% hexamine-ruthenium(III) chloride, Aldrich), 0.1 M  $\text{H}_2\text{SO}_4$  (>95%, Fisher Chemical) and  $\text{KNO}_3$  (99%, Aldrich). Known pH calibration solutions were made up from FIXANAL buffer concentrates (Sigma-Aldrich). Hg solutions were prepared from  $\text{Hg}(\text{NO}_3)_2 \cdot \text{H}_2\text{O}$  (Merck), and the pH adjusted where necessary with 1 M  $\text{HNO}_3$  (70%, Fisher Chemical) and 1 M  $\text{KOH}$  (Fisher Chemical). The iridium oxide solution used was prepared as described in the literature;<sup>26</sup> 4.45 mM iridium tetrachloride, 1 mL  $\text{H}_2\text{O}_2$  (30% w/w) and 39 mM oxalic acid dihydrate were added sequentially to 100 mL water and stirred for 30 min, 10 min, and 10 min intervals respectively. Anhydrous potassium carbonate was added until a pH of 10.5 was achieved resulting in a pale yellow-green solution. This was

stirred for 48 h until the solution had stabilized and appeared blue in colour. The iridium oxide solution was refrigerated between uses.

### 3.3.2. BDD probe fabrication

High quality ( $sp^2$  free) conducting polycrystalline BDD (pBDD) thickness  $\sim 650\text{ }\mu\text{m}$  (DIAFILM EA grade,<sup>27</sup> Element Six, Harwell, UK) was supplied in wafer form and laser micromachined (E-355H-3-ATHI-O system, Oxford Lasers) into both columns ( $1\text{ mm} \pm 0.08\text{ mm}$  diameter) and rings (outer diameter =  $1745\text{ }\mu\text{m} \pm 2.5\text{ }\mu\text{m}$ , inner diameter =  $1445\text{ }\mu\text{m} \pm 2.5\text{ }\mu\text{m}$ ). The pBDD was acid cleaned in concentrated  $\text{H}_2\text{SO}_4$  ( $> 95\%$ , Fisher Chemical), saturated with  $\text{KNO}_3$ , on a hot plate for 30 min. The dimensions of the ring disc electrode were measured using an optical microscope (Axio Imager, Zeiss). Ti/Au electrical contacts 10 nm and 200 nm thick, respectively, were sputtered onto the back of the disc and annealed at  $500\text{ }^\circ\text{C}$  for 4 hr, whilst the backside of the ring was graphitized using the laser, which provides a convenient and sufficiently ohmic contact.<sup>28</sup> The pBDD ring was placed as centrally as possible around the pBDD column in a Teflon mould, and sealed in place with epoxy resin (Epoxy Resin RX771C/NC, Aradur Hardener HY1300GB, Robnor Resins). Copper wires were connected via conductive silver epoxy (Circuitworks, ITW Chemtronics) to the Ti/Au contact on the disc and the graphitized region of the ring. Once the epoxy had set the electrodes were removed from the mould and polished with silicon carbide pads (Buehler) of decreasing roughness until the surface of the ring disc was exposed. Finally an alumina polish ( $0.05\text{ }\mu\text{m}$  Micropolish, Buehler) was applied. This process is illustrated in **Figure 3.1**.

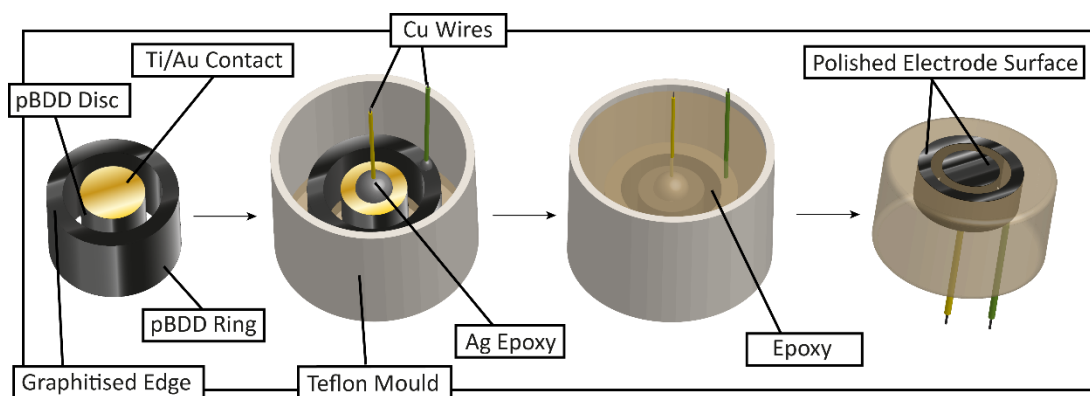


**Figure 3.1:** Schematic showing the process for assembling an epoxy sealed BDD ring disc electrode.

In order to characterize  $H^+$  generation at the ring electrode, a pH sensitive iridium oxide film was employed as the disc electrode. The film was electrodeposited using a three electrode system with a non-leak Ag|AgCl reference electrode and a platinum counter. Deposition was carried out using a potentiostat (CHI730A, CH Instruments Inc.) connected to a desktop computer; a potential of +0.7 V was applied for a total of 900 s. Cyclic voltammograms (CV) were run in iridium oxide solution and  $H_2SO_4$  before and after deposition to confirm film formation and elucidate deposition potential. The pH response of the film is reliant on hydration,<sup>29</sup> so electrodes were stored in pH 7 phosphate buffer solution and left to hydrate for two days before use. The film's response to pH was characterized via calibration in known pH buffer solutions using a two electrode system. The open circuit potential (OCP) was measured for 30 s in each buffer in order of decreasing acidity; this was reversed then repeated to obtain at least three measurements at each pH over the period of several days to assess the pH sensor accuracy and precision.

### 3.3.3. pH generation

H<sup>+</sup> generation experiments on the ring electrode were conducted using an IVIUM COMPACTSTAT with a Peripheral Differential Amplifier (PDA) module which allowed the simultaneous recording of the OCP at the disc electrode vs. a non-leak Ag|AgCl reference electrode. A constant current in the range 0 to +50  $\mu$ A (sufficient to give the desired pH shift) was applied to the ring for 600 s in an unbuffered pH 6.4 KNO<sub>3</sub> solution to generate different local H<sup>+</sup> concentrations which were measured at the iridium oxide disc electrode. For simultaneous amperometric Hg detection and galvanostatic H<sup>+</sup> generation experiments, the generating currents were applied using a Keithley Source Meter.

### 3.3.4. Mercury Detection

Initial experiments were conducted using 1 mM Hg<sup>2+</sup> solutions in 0.1 M KNO<sub>3</sub> with the solution adjusted to a defined pH, in the range 2.0 – 6.4 (measured using a pH probe (SevenEasy S20, Mettler Toledo)). For ring disc experiments, in order to allow time for H<sup>+</sup> diffusion from the ring to the disc, there was a wait time of 60 s between the start of H<sup>+</sup> generation at the ring and the commencement of CV at the disc. CVs were recorded from +1.5 V to -1.2 V and then back to +1.5 V at a scan rate of 0.1 V s<sup>-1</sup> with H<sup>+</sup> generated by the ring throughout this period. The negative potential limit was deliberately chosen in order to minimize H<sup>+</sup> reduction at the disc electrode. An *in situ* cleaning step to remove any un-stripped Hg from the surface of the disc electrode involved applying a potential of +2 V versus Ag|AgCl for 400 s between experiments;

this was found to be sufficient to return the electrode response to its pre-deposition state verified by running a CV in supporting electrolyte ( $\text{KNO}_3$ ).

### 3.3.5. COMSOL Simulation

To quantify pH changes across the detector electrode in response to the diffusional flux of  $\text{H}^+$  generated at the ring electrode, a finite element method model (FEM) was employed using COMSOL Multiphysics 4.3a (COMSOL LAB, Sweden) software. A schematic of the simulated domain is shown in **Figure 3.2**. The model consisted of a square box of width ( $w_T$ ) = 50 mm and height ( $h$ ) = 50 mm, with coordinates  $r$  and  $z$  respectively, producing a 2D axisymmetric section defined by four boundaries, 1, 2, 3 and 4, and representing a water cylinder. The ring disc system is defined by subdividing boundary 1; the disc (boundary 1a) is defined by  $w_1$  ( $r = 0.461$  mm) and the ring (boundary 1c) is defined by the distance between  $w_2$  and  $w_3$  ( $r = 0.723$  mm and  $r = 0.873$  mm, respectively), the remainder of boundary 1 represents the insulating epoxy surface (boundary 1b). These dimensions are representative of the experimental system.

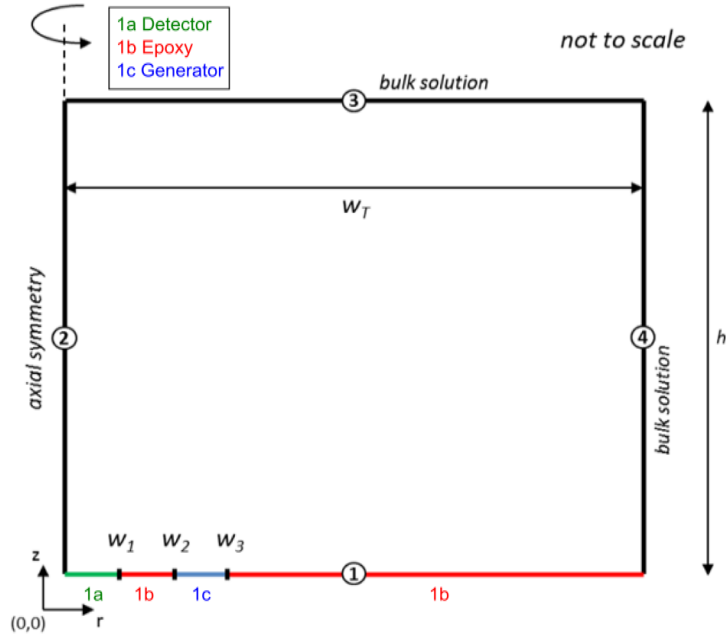


**Figure 3.2:** Schematic diagram of the simulation domain; an axisymmetric section of a water cylinder on top of a ring disc electrode arrangement defined by points  $w_{1-3}$  and lengths  $h$  and  $w_T$ .

The size of the box is chosen such that the diffusion of generated  $H^+$  does not reach the edge on the timescale of the simulation. 1a, the detector disc electrode, is assumed to be electrochemically inert (*i.e.* no electrolysis of  $H^+$ ; no flux, *vide infra*), as is 1b, which is made from insulating material. 1c, the generator ring electrode, has an inward flux defined across the surface corresponding to the generation of  $H^+$  by electrolysis of water.

The flux is assumed to be proportional to the current passed through the electrode;

$$\mathbf{n} \cdot \mathbf{N}_p = \frac{i_{gen}}{AF} \quad [3.2]$$

where  $\mathbf{n}$  is the unit normal vector,  $N_p$  is the total inward flux across boundary 1c,  $i_{gen}$  is the total current at the electrode,  $A$  is the area of the electrode and  $F$

is Faraday's constant ( $=96485 \text{ C mol}^{-1}$ ). Boundaries 3 and 4 were defined as having a fixed  $[\text{H}^+]$  of  $10^{-6.4} \text{ M}$  (bulk pH 6.4), while boundary 2 was defined by an axisymmetric constraint. The diffusion coefficient of  $\text{H}^+$  ( $D_p$ ) was set to  $9.31 \times 10^{-5} \text{ cm}^2 \text{ s}^{-1}$  in accordance with the literature<sup>30</sup> and the initial concentration of  $\text{H}^+$   $c_p$  was set to  $10^{-6.4} \text{ M}$ , corresponding to the bulk pH of the experimental medium.

Diffusion of  $\text{H}^+$  from the generator electrode was modelled according to Fick's second law;

$$\frac{\partial c_p}{\partial t} = D_p \nabla^2 c_p \quad [3.3]$$

A mesh was generated with an element length of  $2 \text{ } \mu\text{m}$  at sub-boundaries 1a, 1b and 1c; the remaining domain was meshed continuously at a growth rate of 1.01x per element away from these boundaries to a maximum element size of 0.5 mm. The total mesh consisted of 461,389 elements. The simulation was solved in a time-dependant manner for a total of 600 s using the PARDISO solver as implemented in COMSOL.

**Table 3.1:** Summary of boundary conditions used for the simulation of the pH during the ring generation experiment.

Boundary	Boundary type	Coordinates	Equation
1a	Detector disc	$0 \leq r \leq w_1$ $z = 0$	$0 = \nabla c \cdot \mathbf{n}$
1b	Epoxy mount material	$w_1 \leq r \leq w_2$ and $w_3 \leq r \leq w_T$ $z = 0$	$0 = \nabla c \cdot \mathbf{n}$
1c	Generator ring	$w_2 \leq r \leq w_3$ $z = 0$	$\mathbf{n} \cdot \mathbf{N}_{1c} = \frac{i_{gen}}{A \cdot F}$



2	Axis of symmetry	$r = 0$ $0 \leq z \leq h$	$0 = \nabla c \cdot \mathbf{n}$
3	Bulk solution	$0 \leq r \leq w_T$ $z = h$	$c = c^*$
4	Bulk solution	$r = w_T$ $0 \leq z \leq h$	$c = c^*$

In **Table 3.1**,  $N_{1c}$  represents the total inward flux across the boundary 1c, and  $c^*$  represents the concentration of the electroactive species in the bulk solution.

### 3.4. Results and Discussion

#### 3.4.1. Effect of pH on Hg stripping

**Figure 3.3** shows the Hg stripping peaks recorded at a 0.922 mm diameter pBDD disc electrode at a scan speed of  $0.1 \text{ V s}^{-1}$  with the solution adjusted to pH values of 2.0, 5.0 and 6.4. The solution contained 1 mM  $\text{Hg}(\text{NO}_3)_2 \cdot \text{H}_2\text{O}$  and the data shows only the oxidative (stripping) part of the CV. A typical complete CV is shown in **Figure 3.3** inset, for a pH 2.0 solution where Hg can be seen to electrodeposit on the electrode at +0.23 V vs Ag|AgCl on the cathodic scan. Going more negative, the wave at -1.0 V is likely to be due to the reduction of oxygen at the electrodeposited Hg, as  $\text{sp}^2$  free BDD does not electrocatalyse oxygen under these pH conditions.<sup>27</sup> On the anodic scan there is a clear stripping peak at +0.52 V. As the pH is increased from 2.0 to 5.0 and then to 6.4 the stripping peak shifts significantly more negative to +0.17 V and becomes much broader, with the peak currents decreasing significantly in magnitude.

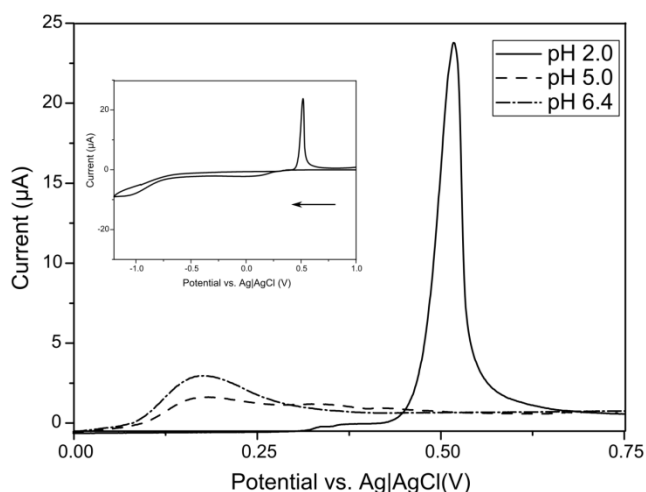


**Figure 3.3:** Stripping peaks recorded at a 0.922 mm diameter pBDD disc electrode at  $0.1 \text{ V s}^{-1}$  in  $1 \text{ mM Hg}^{2+}$  solutions ( $0.1 \text{ M KNO}_3$ ) at pH 2.0, pH 5.0, and pH 6.4. Starting potential was  $+1.5 \text{ V}$  scanning negative to  $-1.2 \text{ V}$  and then back to  $+1.5 \text{ V}$ . Inset shows the full Hg deposition and stripping CV for a pH 2.0 solution.

The shift in peak position may be indicative of different morphology deposits (e.g. isolated droplets versus thin film) due to differing amounts of Hg deposited on the surface as has been seen previously for metals deposited on pBDD.<sup>31</sup>

**Figure 3.4** shows a speciation plot, simulated using Mineql+, as a function of pH for the formation of free  $\text{Hg}^{2+}$ ,  $\text{HgOH}^+$  and  $\text{Hg}(\text{OH})_2$  under experimental conditions i.e.  $\text{Hg}^{2+} = 1 \text{ mM}$ .<sup>32</sup> The concentration of free  $\text{Hg}^{2+}$  changes most rapidly between 2 – 4 pH units. At pH 2, Hg is predominantly in the  $\text{Hg}^{2+}$  form and thus is freely available for metal deposition and stripping, resulting in the pronounced stripping peak shown in **Figure 3.3**. For pH 5.0 and 6.4, **Figure 3.4** suggests that Hg exists in the form  $\text{Hg}(\text{OH})_2$ ; it is evident that for pH values above 2.0  $\text{Hg}^{2+}$  becomes bound by  $\text{OH}^-$  and the concentration of free, electrochemically active, Hg decreases.

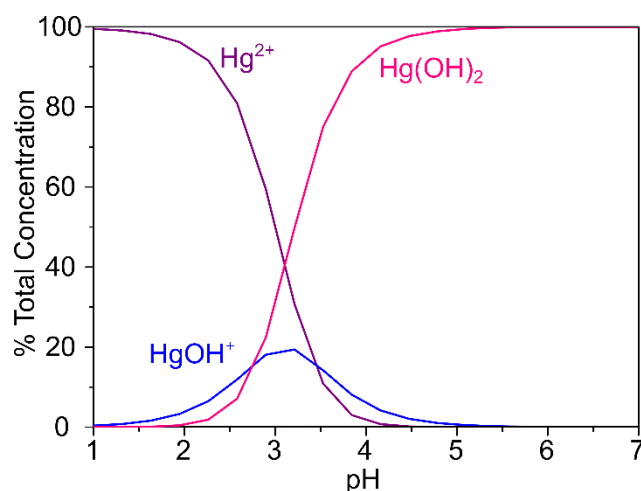


**Figure 3.4:** Simulated speciation of 1 mM Hg in solution from Mineql+ speciation software, showing the % total Hg concentration in each form across the pH range 1-7.

### 3.4.2. Electrochemical Characterisation of Electrodes

The individually addressable BDD ring disc electrode was electrochemically characterized prior to use using the fast one electron transfer outer sphere redox couple (1 mM)  $\text{Ru}(\text{NH}_3)_6^{3+}$  in 0.1 M  $\text{KNO}_3$ . **Figure 3.5** shows typical CVs for the disc and ring electrode (left and right respectively) over the potential scan rate range,  $\nu$ , 10  $\text{mV s}^{-1}$  to 500  $\text{mV s}^{-1}$ . For the electrode sizes employed, near reversible peak-to-peak voltage separations ( $\Delta E_p$ ) were obtained indicating close to reversible behavior, as expected.<sup>33</sup> For example, at 50  $\text{mV s}^{-1}$  and 100  $\text{mV s}^{-1}$  the ring and the disc electrodes showed values of 75 mV (50  $\text{mV s}^{-1}$ ) and 69 mV (100  $\text{mV s}^{-1}$ ), and 69 mV (50  $\text{mV s}^{-1}$ ) and 70 mV (100  $\text{mV s}^{-1}$ ) respectively. Plots of peak current,  $i_p$  versus  $\nu^{1/2}$  gave straight lines with gradients  $8 \times 10^{-6}$  and  $9 \times 10^{-6} \text{ C (sV)}^{-1/2}$  and  $R^2$  values 0.9997 and 0.9993 for ring and disc electrodes respectively.

For the electrode geometries and sizes employed planar diffusion was expected to dominate on the experimental timescales explored,<sup>34</sup> in

accordance with the linear relationship between  $i_p$  and  $v^{1/2}$ . Randles Sevcik analysis gave an effective electrode radius for the disc = 0.56 mm (assuming  $D = 8.8 \times 10^{-6} \text{ cm}^2 \text{ s}^{-1}$ )<sup>35</sup>, slightly larger than that expected. This suggests that the BDD disc is protruding slightly from the insulating epoxy surround,<sup>34</sup> which is not surprising as during fabrication the epoxy polishes at a much faster rate than the BDD.

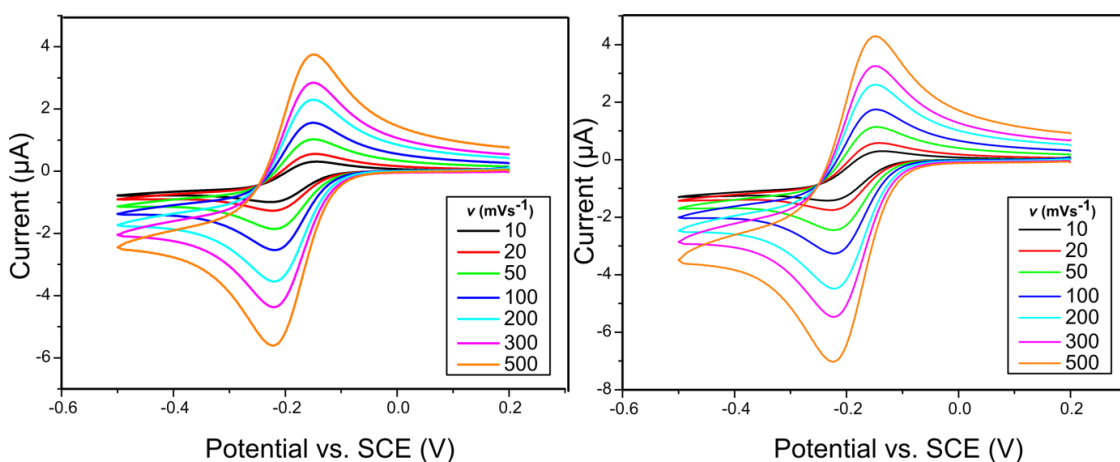


**Figure 3.5:** CVs in 1 mM  $\text{Ru}(\text{NH}_3)_6^{3+}$  for the BDD disc (left) and ring (right) electrodes at scan rates in the range 10 – 500  $\text{mV s}^{-1}$ .

### 3.4.3. *In situ* $\Delta\text{pH}$ generation

The generation of  $\text{H}^+$  using the ring electrode in order to modify the local pH environment of the disc was characterized using a pH sensitive disc, in the ring-disc set-up. A schematic of the dual electrode is shown in **Figure 3.6(a)**. This electrode arrangement was used for all studies and contained a pBDD disc of diameter 0.922 mm, surrounded by a ring of outer and inner diameter 1.745 mm and 1.445 mm respectively, sealed in non-conductive epoxy.

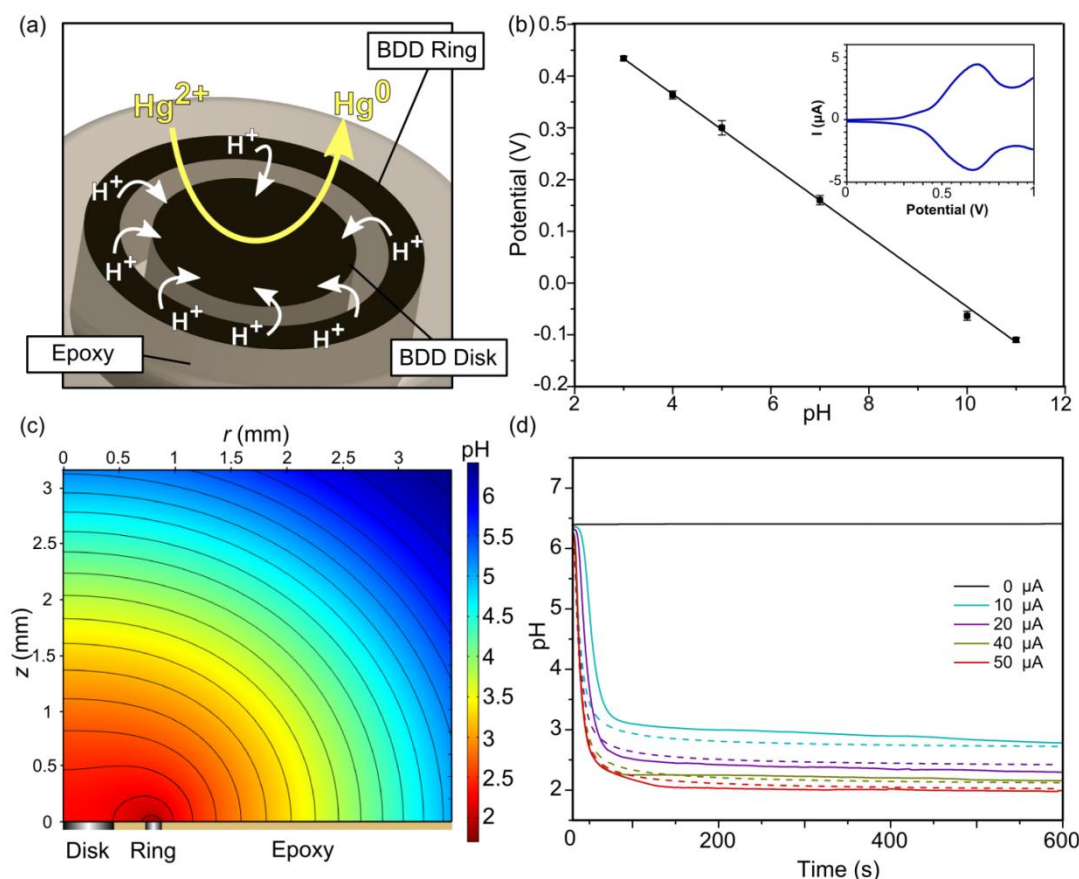


**Figure 3.6:** (a) Schematic of the co-planar ring disc electrode geometry (not to scale) under constant current conditions where  $H^+$  is generated at the ring and  $Hg$  is detected at the disc. (b) A typical OCP vs. pH calibration curve for the iridium oxide coated pBDD disc electrode. Inset shows the behaviour of the iridium oxide film in 1 M  $H_2SO_4$ , as the electrode is cycled between 0 V and +1 V. (c) axisymmetrical  $r$ - $z$   $H^+$  concentration profile for  $H^+$  generation at the pBDD ring electrode at  $t = 60$  s, for  $i_{ring} = +50 \mu A$ . (d) pH response vs  $t$  of the iridium oxide pBDD electrode (in the ring disc geometry) over a timescale of 600 s for  $i_{ring}$  (at the ring electrode) = 0, +10, +20, +30, +40 and +50  $\mu A$  (solid = experimental data, dashed = simulated data).

In order to confirm successful iridium oxide film deposition on the disc, a CV in  $H_2SO_4$  was recorded; **Figure 3.6(b)** inset. The shape of this CV arises from the reversible Ir(III/IV) redox process<sup>7</sup>, and is characteristic of an electrodeposited iridium oxide film.<sup>29</sup> The pH response of the iridium oxide electrode was characterized in different pH buffered solutions in the range pH 2.0 to pH 11.0. **Figure 3.6(b)** shows the calibration curve of pH versus OCP.

The calibration plot shows a linear pH response with a super Nernstian slope ( $-68 \pm 0.82$  mV/pH,  $E^0 = 0.64$  V,  $R^2 = 0.9993$ ), which is in agreement with previous observations and is due to the complex equilibrium reaction characteristics of iridium oxide films.<sup>29, 36</sup>  $E^0$  describes the OCP at pH 0, which is dependent on film thickness.<sup>37</sup> The film calibration remained stable throughout experimentation over a period of approximately two months, comparing well with the film stabilities reported in literature.<sup>29, 38</sup>

**Figure 3.6(c)** shows the simulated radial, vertical ( $r,z$ ) pH profile at time,  $t = 60$  s (when the CV commences scanning) for an applied galvanostatic ring current ( $i_{\text{ring}}$ ) of  $+50 \mu\text{A}$ ;  $r,z$  pH profiles for  $t = 1, 5, 10, 30$  and  $600$  s ( $i_{\text{ring}} = +50 \mu\text{A}$ ) and  $i_{\text{ring}} = +10, +20, +30$  and  $+40 \mu\text{A}$  ( $t = 60$  s) are provided in *section 3.4.4*. The simulated time-dependant pH, over  $600$  s, gives the average pH at the surface of the disc electrode and is shown in **Figure 3.6(d)** (dashed lines), alongside the experimentally measured pH (solid lines) for different applied  $i_{\text{ring}}$  of  $+10 \mu\text{A}$ ,  $+20 \mu\text{A}$ ,  $+30 \mu\text{A}$ ,  $+40 \mu\text{A}$  and  $+50 \mu\text{A}$  over  $600$  s. Both simulations and experiment show a rapid drop in pH during the first  $30$  s which then stabilizes with time, remaining relatively constant for the duration of the measurement. This reflects the time taken for  $\text{H}^+$  to transit from the ring and flood the disc. As  $i_{\text{ring}}$  is increased the pH recorded at the disc electrode decreases, due to the increase in concentration of generated  $\text{H}^+$ .

Importantly, the data clearly shows that for a ring disc arrangement of the dimensions reported herein, it is possible to locally modify the  $\text{H}^+$  concentration in the vicinity of the disc by over four orders of magnitude,

from pH 6.4 to pH 2.0 by applying ring currents up to + 50  $\mu\text{A}$ . **Figure 3.6(d)** also shows that there is relatively good agreement between the simulated disc pH-time profiles and the experimentally recorded data. Discrepancies may be due to; (i) the model assumes a perfectly symmetrical ring disc electrode geometry which, due to the manual assembly method employed during fabrication, was difficult to achieve; (ii) the response time of the iridium oxide sensor is not instantaneous due to the intrinsic capacitance of the material;<sup>37b</sup> (iii) the model does not account for natural convection, which may have an effect at long times.<sup>39</sup>

Note, under these conditions where the  $\text{H}^+$  generating electrode is driven at high potentials for long periods of time most other electrodes are likely to suffer from instability problems. For example, under similar constant current conditions, lithographically fabricated Pt microband electrodes were found to passivate due to oxide layer build-up negatively affecting the electrochemical behaviour.<sup>40</sup>

#### **3.4.4. Simulation of pH profile at varied time and applied currents**

The diffusion of  $\text{H}^+$  from the ring across the surface of the disc and into the bulk solution was simulated as described in section 3.3.5.  $r,z$  plots of the pH profile for the ring disc for  $i_{\text{ring}} = +50 \mu\text{A}$  and  $t = 1, 5, 10, 30, 60$  and  $600 \text{ s}$  are shown in **Figure 3.7(a-f)** respectively. The pH profile over the disc electrode changes rapidly during the first 30 s (as shown in **Figure 3.7(a – d)**) as  $\text{H}^+$  transit from the ring to the disc. For  $t > 30 \text{ s}$  the change in pH profile in the

vicinity of the disc is far less dramatic and reaches a steady-state pH value of 2.0, as shown here and in the pH-time profiles displayed in **Figure 3.6(d)**.

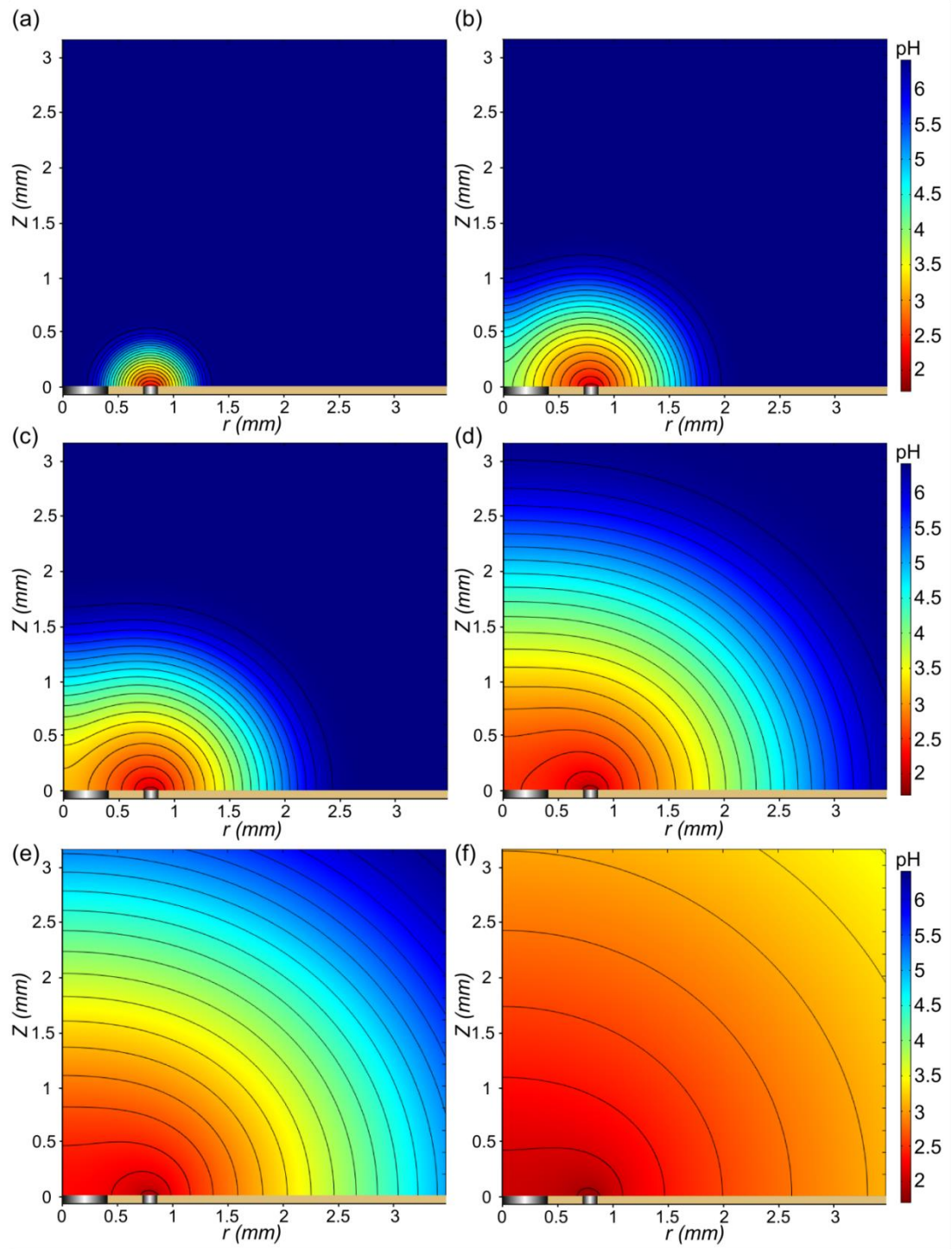


**Figure 3.7:** Simulated pH profiles for  $i_{ring} = +50 \mu A$  at  $t =$  (a) 1 s, (b) 5 s, (c) 10 s, (d) 30 s, (e) 60 s, and (f) 600 s, showing the evolution of the pH profile with time. The pH colour scale is identical for all six profiles and the ring and disc placements are illustrated above the  $r$  axis.



**Figure 3.8** shows the change in  $r,z$  pH profile for  $t = 60$  s changes as  $i_{ring}$  is increased from (a)  $+10 \mu\text{A}$ ; (b)  $+20 \mu\text{A}$ ; (c)  $+30 \mu\text{A}$  to (d)  $+40 \mu\text{A}$ , as the galvanostatic current is increased, the flux of  $\text{H}^+$  from the ring increases, resulting in a lower pH recorded at the disc electrode (**Figure 3.6(c)**).

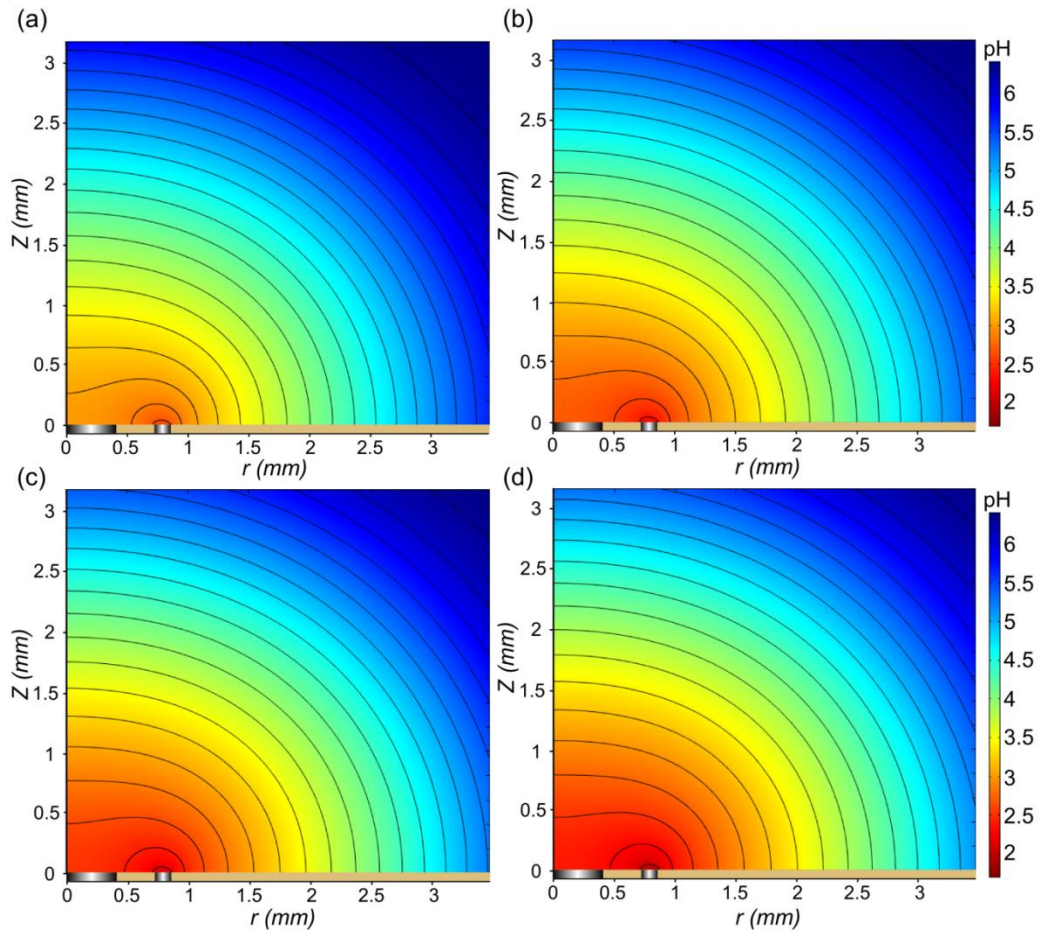


**Figure 3.8:** Simulated pH profiles after 60 s generation for  $i_{ring} =$  (a)  $+ 10 \mu\text{A}$ , (b)  $+ 20 \mu\text{A}$ , (c)  $+ 30 \mu\text{A}$ , and (d)  $+ 40 \mu\text{A}$ . The pH colour scale is identical for all four profiles and the ring and disc placements are illustrated above the  $r$  axis.

### 3.4.5. Simultaneous $\Delta\text{pH}$ generation and Hg detection

**Figure 3.9** (red line) shows the resulting CV response for stripping of Hg at the disc electrode (in the ring-disc arrangement) at a potential scan rate of  $0.1 \text{ V s}^{-1}$  in a solution containing  $1 \text{ mM Hg(NO}_3)_2 \cdot \text{H}_2\text{O}$  and  $0.1 \text{ M KNO}_3$ ,  $\text{pH} = 6.4$ . The stripping peak position occurs at  $+0.17 \text{ V}$  and the charge passed,  $Q = 4.1 \text{ } \mu\text{C}$ . Also shown (purple) is the stripping response for  $i_{\text{ring}} = +50 \text{ } \mu\text{A}$ , in the same solution conditions. The ring electrode was held under constant current conditions for  $60 \text{ s}$  prior to commencement of the CV in order to allow the pH at the disc electrode to stabilize. In accordance with **Figure 3.6(d)**,  $i_{\text{ring}} = +50 \text{ } \mu\text{A}$  generates a steady-state  $\text{pH} = 2.0$  locally at the disc electrode (see **Figure 3.6(d)**). Under these conditions a well-defined stripping peak (peak position  $+0.52 \text{ V}$ ) is observed, where  $Q = 10.5 \text{ } \mu\text{C}$ . Also shown is the stripping response (blue) recorded in a  $\text{pH} 2.0$  solution, peak position  $= +0.52 \text{ V}$ ,  $Q = 10.4 \text{ } \mu\text{C}$ , which is in very good agreement with that recorded under constant current conditions, in a  $\text{pH} 6.4$  solution. **Figure 3.9** clearly shows that by controlling the local pH environment of the disc electrode it is possible to obtain Hg stripping responses in near neutral solutions which very closely resemble that of a bulk acidified solution.

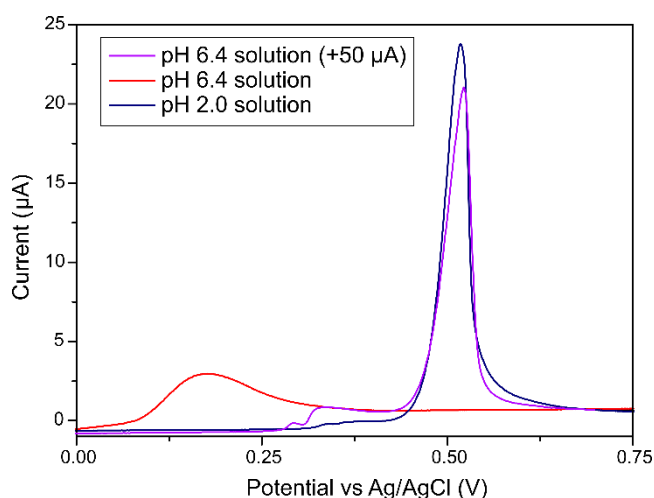


**Figure 3.9:** Hg stripping peaks recorded on the disc of the ring disc electrode at  $0.1 \text{ V s}^{-1}$  in  $1 \text{ mM Hg}^{2+}$  solutions at pH 6.4 (red), pH 2.0 solution (blue), and pH 6.4 solution (purple) but with  $i_{\text{ring}} = +50 \text{ µA}$  to generate a local pH of 2.0 over the disc electrode.

### 3.5. Conclusion

The effect of pH on the stripping characteristics of Hg is demonstrated both in bulk solution and then *in situ* using a dual pBDD electrode approach, where an outer ring electrode is employed to control the pH of the inner disc electrode.  $\text{H}^+$  generation through the decomposition of water under constant current conditions on the ring electrode allowed the pH to be controlled locally at the surface of the disc electrode. The use of pBDD, which is electrocatalytically inert, meant the electrode surface was stable under high applied currents for long periods of time. With the electrode geometries employed, an  $i_{\text{ring}} = +50 \text{ µA}$  resulted in the pH at the disc decreasing from the starting pH of 6.4 to pH = 2.0. The generated pH was found to remain stable over time (measurement times up to 600 s were employed) after an initial equilibration period and showed good agreement with simulated data.

The resulting Hg stripping response for the disc electrode under neutral conditions but with an *in situ* generated pH = 2.0, was very similar to that when the bulk solution was deliberately acidified to pH 2.0. Under pH 2 conditions, the mercury is in the free electroactive  $\text{Hg}^{2+}$  form, whereas under alkaline conditions the Hg becomes complexed by  $\text{OH}^-$  making it electrochemically inaccessible. This causes the decrease in current and shifting of the stripping peak observed. When a current is applied to the ring electrode in bulk pH 6.4 solution the complexed Hg local to the electrode is released, allowing deposition and stripping of the Hg to occur as if in pH 2.0 solution.

A move to all-diamond ring disc devices would improve the lifetime and durability of the electrode. It would also allow more precise control over the geometries of the electrodes employed, and therefore optimisation for trace level analyte detection. As a result, greater electrode reproducibility and deployment in even the harshest environments without suffering corrosion or degradation would be possible. Moving from quiescent solutions to flow would also allow for detection of much lower analyte concentrations and shorten the time required for electrodeposition and thus overall analysis (work is currently on-going in both these areas). Finally by employing negative applied currents this approach can also be used to locally increase pH in a controllable fashion.<sup>41</sup>

### 3.6. References

1. Cockerill, G.; Reed, S., *Essential Fluid, Electrolyte and pH Homeostasis*. Wiley-Blackwell: 2011.

2. (a) Winfrey, M. R.; Rudd, J. W. M., Environmental factors affecting the formation of methylmercury in low pH lakes. *Environ. Toxicol. Chem.* **1990**, 9 (7), 853-869; (b) Sauvé, S.; Hendershot, W.; Allen, H. E., Solid-Solution Partitioning of Metals in Contaminated Soils: Dependence on pH, Total Metal Burden, and Organic Matter. *Environ. Sci. Technol.* **2000**, 34 (7), 1125-1131.
3. (a) Jones, C. E.; Unwin, P. R.; Macpherson, J. V., In Situ Observation of the Surface Processes Involved in Dissolution from the Cleavage Surface of Calcite in Aqueous Solution Using Combined Scanning Electrochemical–Atomic Force Microscopy (SECM-AFM). *ChemPhysChem* **2003**, 4 (2), 139-146; (b) McGeouch, C.-A.; Edwards, M. A.; Mbogoro, M. M.; Parkinson, C.; Unwin, P. R., Scanning Electrochemical Microscopy as a Quantitative Probe of Acid-Induced Dissolution: Theory and Application to Dental Enamel. *Anal. Chem.* **2010**, 82 (22), 9322-9328; (c) Okitsu, K.; Sharyo, K.; Nishimura, R., One-Pot Synthesis of Gold Nanorods by Ultrasonic Irradiation: The Effect of pH on the Shape of the Gold Nanorods and Nanoparticles. *Langmuir* **2009**, 25 (14), 7786-7790.
4. Chung, T. D.; Anson, F. C., Electrochemical Monitoring of Proton Transfer across Liquid/Liquid Interfaces on the Surface of Graphite Electrodes. *Anal. Chem.* **2000**, 73 (2), 337-342.
5. Krishnamoorthy, K.; Zoski, C. G., Fabrication of 3D Gold Nanoelectrode Ensembles by Chemical Etching. *Anal. Chem.* **2005**, 77 (15), 5068-5071.
6. Zeng, A.; Liu, E.; Tan, S. N.; Zhang, S.; Gao, J., Stripping Voltammetric Analysis of Heavy Metals at Nitrogen Doped Diamond-Like Carbon Film Electrodes. *Electroanalysis* **2002**, 14 (18), 1294-1298.
7. Reeder, G. S.; Heineman, W. R., Electrochemical characterization of a microfabricated thick-film carbon sensor for trace determination of lead. *Sens. Act. B Chem.* **1998**, 52 (1–2), 58-64.
8. (a) Šinko, I.; Doleal, J., Simultaneous determination of copper, cadmium, lead and zinc in water by anodic stripping polarography. *J. Electroanal. Chem. Interfac. Electrochem.* **1970**, 25 (2), 299-306; (b) Ringbom, A., *Complexation in analytical chemistry: a guide for the critical selection of analytical methods based on complexation reactions*. Interscience Publishers: 1963; (c) Chau, Y.; Lum-Shue-Chan, K., Determination of labile and strongly bound metals in lake water. *Water Res.* **1974**, 8 (6), 383-388; (d) Wang, J.; Tian, B., Mercury-free disposable lead sensors based on potentiometric stripping analysis of gold-coated screen-printed electrodes. *Anal. Chem.* **1993**, 65 (11), 1529-1532; (e) Hočevár, S. B.; Švancara, I.; Vytřas, K.; Ogorevc, B., Novel electrode for electrochemical stripping analysis based on carbon paste modified with bismuth powder. *Electrochim. Acta* **2005**, 51 (4), 706-710; (f) Segura, R. A.; Pizarro, J. A.; Oyarzun, M. P.; Castillo, A. D.; Díaz, K. J.; Placencio, A. B., Determination of Lead and Cadmium in Water Samples by Adsorptive Stripping Voltammetry Using a Bismuth film/1-Nitroso-2-Naphthol/Nafion Modified Glassy Carbon Electrode. *Int. J. Electrochem. Sci.* **2016**, 11 (2), 1707-1719.
9. (a) Giacomino, A.; Abollino, O.; Malandrino, M.; Mentasti, E., Parameters affecting the determination of mercury by anodic stripping voltammetry using a gold electrode. *Talanta* **2008**, 75 (1), 266-273; (b) Sosa, V.; Barceló, C.; Serrano, N.; Ariño, C.; Díaz-Cruz, J. M.; Esteban, M., Antimony film screen-printed carbon electrode for stripping analysis of Cd(II), Pb(II), and Cu(II) in natural samples. *Anal. Chim. Acta.* **2015**, 855, 34-40; (c) Bobrowski, A.; Królicka, A.; Maczuga, M.; Kolaniak, A., Anodic Stripping Voltammetric Determination of Copper Traces in Carbonate Minerals and Fly Ash Extracts Using a Screen-Printed Electrode Modified In Situ with Antimony Film. *Insight. Anal. Electrochem.* **2015**; (d) Cinti, S.; Santella, F.;

- Moscone, D.; Arduini, F., Hg<sup>2+</sup> detection using a disposable and miniaturized screen-printed electrode modified with nanocomposite carbon black and gold nanoparticles. *Environ. Sci. Pollut. Res.* **2016**, 1-8.
10. Kudo., A.; Miyahara., S., A Case History; Minamata mercury pollution in Japan - from loss of human lives to decontamination. *Water Sci. Technol.* **1991**, 23, 283-290.
  11. (a) Compton, R. G.; Foord, J. S.; Marken, F., Electroanalysis at Diamond-Like and Doped-Diamond Electrodes. *Electroanalysis* **2003**, 15 (17), 1349-1363; (b) McGaw, E. A.; Swain, G. M., A comparison of boron-doped diamond thin-film and Hg-coated glassy carbon electrodes for anodic stripping voltammetric determination of heavy metal ions in aqueous media. *Anal. Chim. Acta.* **2006**, 575 (2), 180-189; (c) Dragoe, D.; Spătaru, N.; Kawasaki, R.; Manivannan, A.; Spătaru, T.; Tryk, D. A.; Fujishima, A., Detection of trace levels of Pb<sup>2+</sup> in tap water at boron-doped diamond electrodes with anodic stripping voltammetry. *Electrochim. Acta* **2006**, 51 (12), 2437-2441; (d) Manivannan, A.; Tryk, D. A.; Fujishima, A., Detection of Trace Lead at Boron-Doped Diamond Electrodes by Anodic Stripping Analysis. *Electrochem. Solid State Lett.* **1999**, 2 (9), 455-456.
  12. (a) Luong, J. H. T.; Male, K. B.; Glennon, J. D., Boron-doped diamond electrode: synthesis, characterization, functionalization and analytical applications. *Analyst* **2009**, 134, 1965-1979; (b) Swain, G. M.; Ramesham, R., The electrochemical activity of boron-doped polycrystalline diamond thin film electrodes. *Anal. Chem.* **1993**, 65 (4), 345-351; (c) Kraft, A., Doped diamond: a compact review on a new, versatile electrode material. *Int. J. Electrochem. Sci* **2007**, 2 (5), 355-385.
  13. (a) Kumar Jena, B.; Retna Raj, C., Gold Nanoelectrode Ensembles for the Simultaneous Electrochemical Detection of Ultratrace Arsenic, Mercury, and Copper. *Anal. Chem.* **2008**, 80 (13), 4836-4844; (b) Manivannan, A.; Seehra, M. S.; Tryk, D. A.; Fujishima, A., ELECTROCHEMICAL DETECTION OF IONIC MERCURY AT BORON-DOPED DIAMOND ELECTRODES. *Anal. Lett.* **2002**, 35 (2), 355-368.
  14. (a) Bernalte, E.; Sánchez, C. M.; Gil, E. P., Determination of mercury in ambient water samples by anodic stripping voltammetry on screen-printed gold electrodes. *Anal. Chim. Acta.* **2011**, 689 (1), 60-64; (b) Kanchana, P.; Sudhan, N.; Anandhakumar, S.; Mathiyarasu, J.; Manisankar, P.; Sekar, C., Electrochemical detection of mercury using biosynthesized hydroxyapatite nanoparticles modified glassy carbon electrodes without preconcentration. *RSC Adv.* **2015**, 5 (84), 68587-68594.
  15. Carr, R.; Zhang, C.; Moles, N.; Harder, M., Identification and mapping of heavy metal pollution in soils of a sports ground in Galway City, Ireland, using a portable XRF analyser and GIS. *Environ. Geochem. Health* **2008**, 30 (1), 45-52.
  16. . Ocean acidification due to increasing atmospheric carbon dioxide 2005. [http://dgc.stanford.edu/labs/caldeiralab/Caldeira%20downloads/RoyalSociety\\_OceanAcidification.pdf](http://dgc.stanford.edu/labs/caldeiralab/Caldeira%20downloads/RoyalSociety_OceanAcidification.pdf) (accessed 26/02/13).
  17. (a) Michaud, P. A.; Panizza, M.; Ouattara, L.; Diaco, T.; Foti, G.; Comninellis, C., Electrochemical oxidation of water on synthetic boron-doped diamond thin film anodes. *J. Appl. Electrochem.* **2003**, 33 (2), 151-154; (b) Palmas, S.; Polcaro, A. M.; Vacca, A.; Mascia, M.; Ferrara, F., Influence of the operating conditions on the electrochemical disinfection process of natural waters at BDD electrodes. *J. Appl. Electrochem.* **2007**, 37 (11), 1357-1365.
  18. (a) Fosset, B.; Amatore, C.; Bartelt, J.; Wightman, R. M., Theory and experiment for the collector-generator triple-band electrode. *Anal. Chem.* **1991**, 63 (14), 1403-1408; (b) Fosset, B.; Amatore, C. A.; Bartelt, J. E.; Michael, A. C.; Wightman, R. M.,

- Use of conformal maps to model the voltammetric response of collector-generator double-band electrodes. *Anal. Chem.* **1991**, *63* (4), 306-314.
19. (a) Liljeroth, P.; Johans, C.; Slevin, C. J.; Quinn, B. M.; Kontturi, K., Micro ring–disk electrode probes for scanning electrochemical microscopy. *Electrochem. Commun.* **2002**, *4* (1), 67-71; (b) Barnes, E. O.; Lewis, G. E. M.; Dale, S. E. C.; Marken, F.; Compton, R. G., Generator-collector double electrode systems: A review. *Analyst* **2012**, *137* (5), 1068-1081.
  20. Cutress, I. J.; Wang, Y.; Limon-Petersen, J. G.; Dale, S. E. C.; Rassaei, L.; Marken, F.; Compton, R. G., Dual-microdisk electrodes in transient generator–collector mode: Experiment and theory. *J. Electroanal. Chem.* **2011**, *655* (2), 147-153.
  21. Dale, S. E. C.; Vuorema, A.; Ashmore, E. M. Y.; Kasprzyk-Horden, B.; Sillanpää, M.; Denuault, G.; Marken, F., Gold-gold junction electrodes: the disconnection method. *The Chemical Record* **2012**, *12* (1), 143-148.
  22. Sasaki, H.; Miyake, M.; Maeda, M., Enhanced Dissolution Rate of Pt from a Pt–Zn Compound Measured by Channel Flow Double Electrode. *J. Electrochem. Soc.* **2010**, *157* (5), E82-E87.
  23. Damjanovic, A.; Genshaw, M.; Bockris, J. O. M., The role of hydrogen peroxide in oxygen reduction at platinum in H<sub>2</sub>SO<sub>4</sub> solution. *J. Electrochem. Soc.* **1967**, *114* (5), 466-472.
  24. Aoki, K.; Morita, M.; Niwa, O.; Tabei, H., *J. Electroanal. Chem.* **1988**, *256*, 269-282.
  25. Livshits, D., Method and apparatus for adjusting the pH of a liquid. Google Patents: 2000.
  26. (a) Yamanaka, K., *Jpn. J. App. Phys.* **1989**, (28), 623; (b) Yamanaka, K., *Jpn. J. App. Phys.* **1991**, (30), 1285.
  27. Hutton, L. A.; Iacobini, J. G.; Bitziou, E.; Channon, R. B.; Newton, M. E.; Macpherson, J. V., Examination of the Factors Affecting the Electrochemical Performance of Oxygen-Terminated Polycrystalline Boron-Doped Diamond Electrodes. *Anal. Chem.* **2013**, *85* (15), 7230-7240.
  28. Geis, M. W.; Rothschild, M.; Kunz, R. R.; Aggarwal, R. L.; Wall, K. F.; Parker, C. D.; McIntosh, K. A.; Efremow, N. N.; Zayhowski, J. J.; Ehrlich, D. J., Electrical, crystallographic, and optical properties of ArF laser modified diamond surfaces. *Appl. Phys. Lett.* **1989**, *55* (22), 2295-2297.
  29. Bitziou, E.; O'Hare, D.; Patel, B. A., Simultaneous Detection of pH Changes and Histamine Release from Oxyntic Glands in Isolated Stomach. *Anal. Chem.* **2008**, *80* (22), 8733-8740.
  30. Robinson, R. A.; Stokes, R. H., *Electrolyte Solutions*. 2nd ed.; Butterworth: London, 1959.
  31. Hutton, L. A.; Newton, M. E.; Unwin, P. R.; Macpherson, J. V., Factors Controlling Stripping Voltammetry of Lead at Polycrystalline Boron Doped Diamond Electrodes: New Insights from High-Resolution Microscopy. *Anal. Chem.* **2011**, *83* (3), 735-745.
  32. Kelter, P. B.; Mosher, M. D.; Scott, A., *Chemistry: The Practical Science*. Houghton Mifflin: 2008.
  33. Patten, H. V.; Meadows, K. E.; Hutton, L. A.; Iacobini, J. G.; Battistel, D.; McKelvey, K.; Colburn, A. W.; Newton, M. E.; Macpherson, J. V.; Unwin, P. R., Electrochemical Mapping Reveals Direct Correlation between Heterogeneous Electron-Transfer Kinetics and Local Density of States in Diamond Electrodes. *Angew. Chem.* **2012**, *124* (28), 7108-7112.
  34. Ferrigno, R.; Brevet, P.; Girault, H., Finite element simulation of the chronoamperometric response of recessed and protruding microdisc electrodes. *Electrochim. Acta* **1997**, *42* (12), 1895-1903.

35. Macpherson, J. V.; O'Hare, D.; Unwin, P. R.; Winlove, C. P., Quantitative spatially resolved measurements of mass transfer through laryngeal cartilage. *Biophys. J.* **1997**, *73* (5), 2771-2781.
36. Wipf, D. O.; Ge, F.; Spaine, T. W.; Baur, J. E., Microscopic Measurement of pH with Iridium Oxide Microelectrodes. *Anal. Chem.* **2000**, *72* (20), 4921-4927.
37. (a) Terashima, C.; Rao, T. N.; Sarada, B. V.; Spataru, N.; Fujishima, A., Electrodeposition of hydrous iridium oxide on conductive diamond electrodes for catalytic sensor applications. *J. Electroanal. Chem.* **2003**, *544* (0), 65-74; (b) Elsen, H. A.; Monson, C. F.; Majda, M., Effects of Electrodeposition Conditions and Protocol on the Properties of Iridium Oxide pH Sensor Electrodes. *J. Electrochem. Soc.* **2009**, *156* (1), F1-F6.
38. Salimi, A.; Alizadeh, V.; Hallaj, R., Amperometric detection of ultra trace amounts of Hg(I) at the surface boron doped diamond electrode modified with iridium oxide. *Talanta* **2006**, *68* (5), 1610-1616.
39. Amatore, C.; Szunerits, S.; Thouin, L.; Warkocz, J.-S., The real meaning of Nernst's steady diffusion layer concept under non-forced hydrodynamic conditions. A simple model based on Levich's seminal view of convection. *J. Electroanal. Chem.* **2001**, *500* (1-2), 62-70.
40. Angerstein-Kozłowska, H.; Conway, B. E.; Sharp, W. B. A., The real condition of electrochemically oxidized platinum surfaces: Part I. Resolution of component processes. *J. Electroanal. Chem. Interfac. Electrochem.* **1973**, *43* (1), 9-36.
41. Bitziou, E.; Joseph, M. B.; Read, T. L.; Palmer, N.; Mollart, T.; Newton, M. E.; Macpherson, J. V., In Situ Optimization of pH for Parts-Per-Billion Electrochemical Detection of Dissolved Hydrogen Sulfide Using Boron Doped Diamond Flow Electrodes. *Anal. Chem.* **2014**, *86* (21), 10834-10840.



## 4 Manipulation and measurement of pH sensitive metal–ligand binding using electrochemical proton generation and metal detection

### 4.1 Overview

In this chapter, electrochemical pH generation at a ring disc electrode was used to manipulate the metal-ligand binding of a pH sensitive system. It is demonstrated that a generator-detector (ring-disc) electrode system can be used to both perturb and monitor the pH dependent equilibrium of copper ( $\text{Cu}^{2+}$ ) in the presence of the ligand triethylenetetraamine (TETA) *in situ*. The effect of pH on speciation was investigated electrochemically in a range of bulk pH solutions, and confirmed using a combination of simulation and UV-Vis titration. An individually addressable BDD ring-disc electrode was used to control and measure  $\text{Cu}^{2+}$  speciation via electrochemical generation of protons at the ring electrode, whilst simultaneously measuring free  $\text{Cu}^{2+}$  at the disc. It is shown that it is possible to switch between  $\text{Cu}^{2+}$  in the 100% bound form ( $\text{pH} \geq 5.01$ ) to 100% free ( $\text{pH} \leq 2.50$ ) *in situ* simply by generating sufficient protons in the vicinity of the detector.

### 4.2 Introduction

Many important chemical processes such as: acid-base; hydrolysis; complexation; extraction, redox; solubility and precipitation, are governed by a pH dependent chemical equilibrium.<sup>1-6</sup> Experimentally, analysis of the

change in species concentration (or activity) with pH is often carried out using different solutions of varying (and known) pH. However, for certain reactions it is advantageous not only to be able to investigate the process *in situ* but also to locally manipulate solution pH; pushing the pH dependent equilibrium in a preferred direction.

pH dependent metal-ligand complexation is of importance in a wide range of fields, including medicine<sup>7</sup> e.g. chelation treatments for cancer therapy,<sup>8</sup> waste water treatment,<sup>9</sup> environmental research e.g. toxic metal availability in aqueous solutions and human function,<sup>10</sup> for example the binding of oxygen to haemoglobin in blood.<sup>11</sup> To illustrate the concept of pH manipulation and show how by careful control of local solution pH we can control the extent of metal-ligand binding, *in situ*, we focus on aqueous heavy metals, a key concern due to their toxicity.<sup>12</sup> For many cases, the free (labile) species is bioavailable and therefore more toxic than the complexed species and is often of primary interest.<sup>13, 14</sup> However, as the bound species acts as a reservoir of free species that can be released when the equilibrium shifts, due to e.g. a pH change,<sup>15</sup> understanding the pH dependent relationship and manipulating it during measurement can be important.

Concentrations of free and complexed metal species are often measured using techniques such as UV-Vis spectroscopy<sup>16</sup>, inductively coupled plasma mass spectrometry (ICP-MS) or optical emission spectrometry,<sup>17</sup> voltammetry<sup>18</sup> and potentiometry,<sup>19, 20</sup> thermometry<sup>21</sup> and conductometry.<sup>22</sup> The majority of these techniques do not provide information on the individual concentrations of

both the free species and the ligand bound metal species. For example, ICP-MS will measure total metal concentration, whilst voltammetry and related techniques, measure only the free metal ion concentration (at the given measurement pH).<sup>23</sup>

Electrochemistry is a popular method for detection of aqueous species,<sup>12</sup> due to its relative ease of use and low cost, and its potential for application *in situ*; removing the necessity to take samples away from the real environment for analysis, which can affect the equilibrium of the sample and give false measurements of free vs. bound species.<sup>24, 25</sup> Interest in pH control via electrochemical methods is evident,<sup>26, 27,28, 29</sup> with applications such as pH titration,<sup>30</sup> chemical species quantification<sup>31</sup> etc. already highlighted in Chapters 1 and 3.

For this study we focus on copper,<sup>32</sup> a heavy metal identified as being of key concern worldwide due to both its prevalence as a trace metal and its toxicity.<sup>33</sup> Although necessary in small quantities in the body, copper is also extremely toxic when absorbed in excess, causing oxidative stress damage to organs; copper has also been linked to Alzheimer's disease.<sup>34</sup> For pH dependent ligand binding studies, triethylenetetramine (TETA) serves as a model system for Cu<sup>2+</sup> complexation. TETA is a therapeutic molecule used in the treatment of Wilson's disease, the latter characterized by copper accumulation in vital organs of the body.<sup>35</sup>



## 4.3 Experimental

### 4.3.1 Solutions

All chemicals used in this chapter were used as received and prepared using Milli-Q water (resistivity 18.2 MΩ cm at 25°C) unless stated otherwise. The supporting electrolyte used in all electrochemical experiments was 0.1 M KNO<sub>3</sub> (99%, Aldrich), and electrodes were characterized electrochemically prior to use in 0.1 M KNO<sub>3</sub> (99%, Aldrich), and 1 mM Ru(NH<sub>3</sub>)<sub>6</sub><sup>3+/2+</sup> (98% hexamine-ruthenium(III) chloride, Aldrich). Bulk pH adjustments were made using 0.1 M HCl or 0.1 M KOH (Fisher Scientific). Cu<sup>2+</sup> and TETA solutions were prepared from stock solutions of 10 mM Cu(NO<sub>3</sub>)<sub>2</sub> (Aldrich), and 10 mM triethylenetetramine dihydrochloride (Aldrich) respectively. Note no supporting electrolyte was used for UV-Vis solutions due to the appearance of a nitrate peak in the region of interest.<sup>36</sup>

### 4.3.2 Electrode Fabrication

A 600 μm thick wafer of high quality (minimal sp<sup>2</sup> content) boron doped diamond (BDD) was laser micromachined (E-355H-3-ATHI-O system, Oxford Lasers) into a column of 500 μm radius and a hollow cylinder of inner radius 760 μm and outer radius 810 μm. The BDD was then acid cleaned in KNO<sub>3</sub> (Sigma Aldrich) saturated, concentrated H<sub>2</sub>SO<sub>4</sub> (>95 %, Fisher Chemical) for 30 minutes at ~300 °C until brown fumes were no longer observed and then sonicated in Milli-Q water (resistivity 18.2 MΩ cm at 25 °C) for 10 mins. The front surface of the BDD column and hollow cylinder were adhered to a glass slide using a thin layer of super glue (Loctite) and the rear surface sputtered

(Moorfield) with Ti/Au (10/300 nm), before removing the glue with acetone and then annealing at 400 °C for 5 hours. The front face of the cylinder and surrounding hollow cylinder were placed on adhesive Gel-Pak (Gel-Pak, Hayward CA), onto which a vacuum grease coated teflon mould (cylindrical, 1.5 cm inner diameter and 3 cm outer diameter, depth = 1 cm), was also placed, and sealed in place with a thin layer of non-conductive epoxy resin (Epoxy Resin RX771C/NC, Aradur Hardener HY1300GB, Robnor Resins), see **Figure 4.1**. Insulated copper wires were individually connected, using a dissection microscope (Motic) to aid alignment to the sputtered Au contact pads on each electrode using conductive silver epoxy (Circuitworks, ITW Chemtronics). Finally, the mould was filled with the same non-conductive epoxy. Once dry (after ~24 hrs) the electrode was removed and the excess epoxy on the front surface polished back with silicon carbide paper (Carbimet, Buehler) of decreasing roughness to reveal the co-planar ring disc electrodes. Before use the electrodes were polished with alumina polish (0.05 µm Micropolish, Buehler) and rinsed with Milli-Q water.

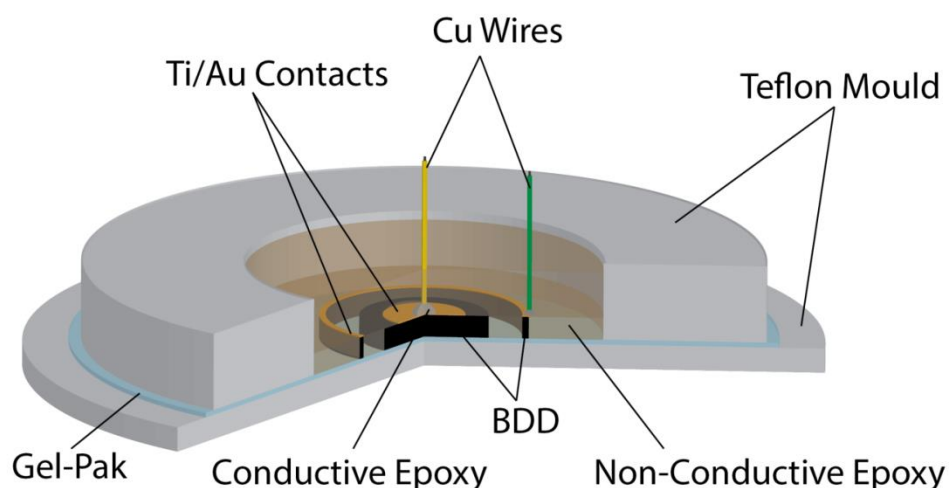


**Figure 4.1:** Schematic of BDD ring disc assembly in the teflon mould. Conductive silver epoxy is used to attach copper wires to the Ti/Au contacts on the rear of the electrodes, before sealing the arrangement with non-conductive epoxy.

### 4.3.3 UV-Vis Spectroscopy

UV-Vis (Varian, Cary 50 Bio UV-Visible Spectrometer) titration data were obtained by dropwise addition of 0.1 M HCl to a mixture of 100  $\mu\text{M}$   $\text{Cu}^{2+}$  and 100  $\mu\text{M}$  TETA in a stirred solution. Between additions the pH value was measured using a pH probe (Mettler Toledo) and a  $\sim 3 \text{ cm}^3$  sample taken for UV-Vis absorbance measurements in a quartz cuvette (1  $\text{cm}^2$  cross-section, optical path length 1 cm), before replacement into the experimental solution.

### 4.3.4 Mineql+ speciation simulation

TETA has four protonation constants,  $\log K_p$ , ( $\log K_1 = 9.79$ ,  $\log K_2 = 9.11$ ,  $\log K_3 = 6.68$ , and  $\log K_4 = 3.28$ ).<sup>37</sup> The un-protonated (TETA) and singly protonated (HTETA) can bind to  $\text{Cu}^{2+}$ , whilst the two, three and four protonated ( $\text{H}_2$ ,  $\text{H}_3$ ,  $\text{H}_4$ ) TETA ligands cannot. The pH dependent speciation curves for the  $\text{Cu}^{2+}$  TETA system can be determined using

MINEQL+ chemical equilibrium modelling software in conjunction with known values for  $\beta^{37}$ , the complex formation constant and  $K_f$ , where:

$$\log \beta = \sum \log K_f \quad [4.2]$$

The speciation models were prepared using the  $\log \beta$  values for TETA above for 100  $\mu\text{M}$  1:1 Cu TETA mixtures. Ionic strength was set to 300  $\mu\text{M}$  and 0.1003 M for comparison with UV-Vis and electrochemical experiments respectively. Titrations were run for  $\log K$  of pH between 1 and 10 for 40 points.

### 4.3.5 Electrochemistry

#### 4.3.5.1 Bulk pH Electrochemistry

For electrochemical detection of  $\text{Cu}^{2+}$  in 1:1 solutions of either 1 mM, or 100  $\mu\text{M}$   $\text{Cu}(\text{NO}_3)_2$  and TETA with 0.1 M  $\text{KNO}_3$  supporting electrolyte at bulk pH 2.0 – 6.35 (pH adjusted using 0.1 M  $\text{HNO}_3$  and 0.1 M  $\text{KOH}$ ), a simple three electrode arrangement was used; the BDD disc was connected as the working electrode vs. an SCE reference electrode and a Pt wire counter electrode. The BDD ring remains unconnected for these experiments. For ASV experiments Cu was deposited on the electrode surface at -0.5 V for 60 s using an amperometric i-t method (CHI730A Potentiostat, CH Instruments Inc), ASV experiments were performed immediately following electrodeposition by scanning in a positive potential direction using linear sweep voltammetry from -0.25 V to +0.5 V at a potential scan rate of 0.1 V  $\text{s}^{-1}$ . CV experiments were conducted in a similar arrangement, however the cathodic potential range used was varied between -0.3 V to -1 V.

#### **4.3.5.2 *pH generation***

For  $\text{Cu}^{2+}$  detection with proton generation the electrode set up for the detector (disc electrode) was as described in section 4.3.5.1, the ring (generator) electrode was connected as a working electrode, vs. a second Pt counter electrode, to a galvanostat (Keithley Source Meter). The electrodes were placed in a solution of 100  $\mu\text{M}$   $\text{Cu}(\text{NO}_3)_2$  and 100  $\mu\text{M}$  TETA with 0.1 M  $\text{KNO}_3$  supporting electrolyte, adjusted to bulk pH 6.4 using KOH. To generate a local pH change, a constant current in the range 0.1 – 2  $\text{mA cm}^{-2}$  was applied to the ring electrode using the galvanostat for a period of 300 s. After 300 s the current applied to the ring was maintained and the potential at the detector electrode was switched on using the potentiostat (-0.5 V for 60 s vs. SCE as before) for electrodeposition of  $\text{Cu}^{2+}$ . The potential was then immediately swept from -0.25 V to +0.5 V at 0.1  $\text{Vs}^{-1}$ . For CV experiments the parameters used were as described in 4.3.5.1, with the addition of a range of currents applied to the generator (ring) electrode for 3 minutes prior to, and during, experiments on the disc; the electrode arrangement for generation was as described above.

### **4.4 Results and Discussion**

#### **4.4.1 Preliminary Studies**

##### **4.4.1.1 *TETA interference***

Of primary importance to this investigation was the selectivity of measurement towards  $\text{Cu}^{2+}$  in mixed  $\text{Cu}^{2+}$  and TETA solution. It was thus essential to establish the electroactivity of TETA, and any potential for



interference across the pH range investigated. As such, both electrochemical and UV-Vis experiments were conducted in copper free solutions, containing solely TETA and, where necessary, supporting electrolyte; results are shown in **Figure 4.2** and **Figure 4.3** respectively.

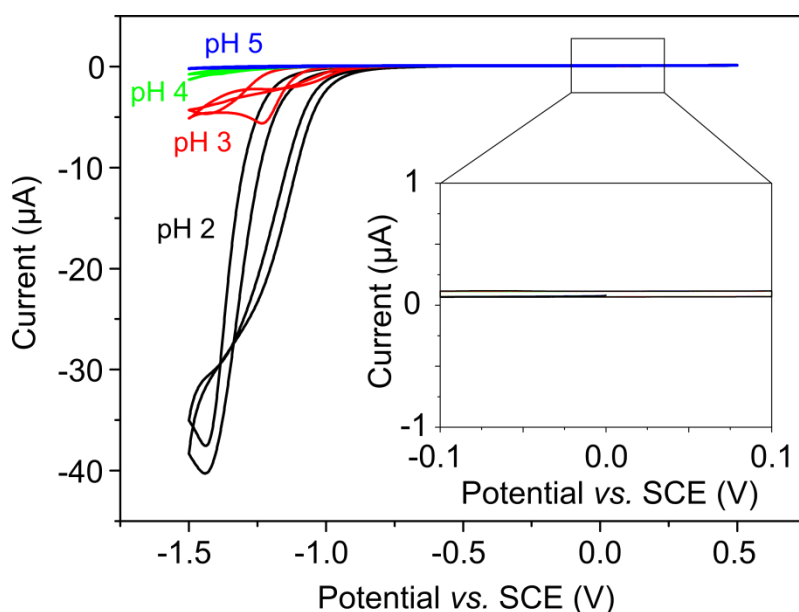


**Figure 4.2:** CVs in 100  $\mu\text{M}$  TETA solution with 0.1 M  $\text{KNO}_3$  supporting electrolyte at different bulk pH values, pH adjusted using 0.1 M HCl and 0.1 M KOH. Inset shows zoomed region where  $\text{Cu}^{2+}$  stripping signal would appear in Cu containing solutions.

CVs were measured between + 0.5 V and -1.5 V in 1 mM TETA solution with 0.1 M  $\text{KNO}_3$  supporting electrolyte, scanning first in the negative direction at 0.1 V  $\text{s}^{-1}$ . In  $\text{Cu}^{2+}$  containing solutions one would expect to observe a signal between 0 V and +0.5 V corresponding to stripping of deposited copper from the electrode, and a cathodic deposition peak at approximately -0.15 V.<sup>38</sup> As such, these regions were of particular interest for TETA only experiments. Any observed signal for TETA in this region could interfere with a Cu stripping peak and complicate analysis, or alternatively possible TETA reduction could

compete with  $\text{Cu}^{2+}$  reduction. However, it can be seen from the lack of signal in **Figure 4.2** that TETA is electrochemically inactive in the regions of interest for all pH values. The proposed Cu TETA system is therefore electrochemically viable for investigation of manipulation of metal-ligand binding via *in situ* pH control. Note the appearance of a cathodic peak of increasing current magnitude with decreasing pH, which is due to the reduction of protons.

The absorption maximum for the  $\text{Cu}[\text{TETA}]$  complex is expected at approximately 250 nm.<sup>37</sup> In order for UV-Vis titration to be of use in supporting simulated speciation diagrams it is of key importance that neither uncomplexed copper, nor TETA absorb in this region. As such, UV-Vis experiments were conducted at a range of bulk pH values for individual 100  $\mu\text{M}$  Cu, and 100  $\mu\text{M}$  TETA solutions. As can be seen in **Figure 4.3(a)** no absorbance from  $\text{Cu}^{2+}$  is evident in this region over the pH range investigated. Note, at higher concentrations (~10 mM) an absorbance maximum for  $\text{Cu}^{2+}$  can be observed in the region 500-900 nm, however due to its low molar absorptivity the concentrations here are too low to produce a visible signal as discussed in section 4.4.4. The absorbance of TETA can be seen in **Figure 4.3(b)**, and although it appears to be affected somewhat by pH changes it remains sufficiently far from 250 nm such that it poses no real interference issues.

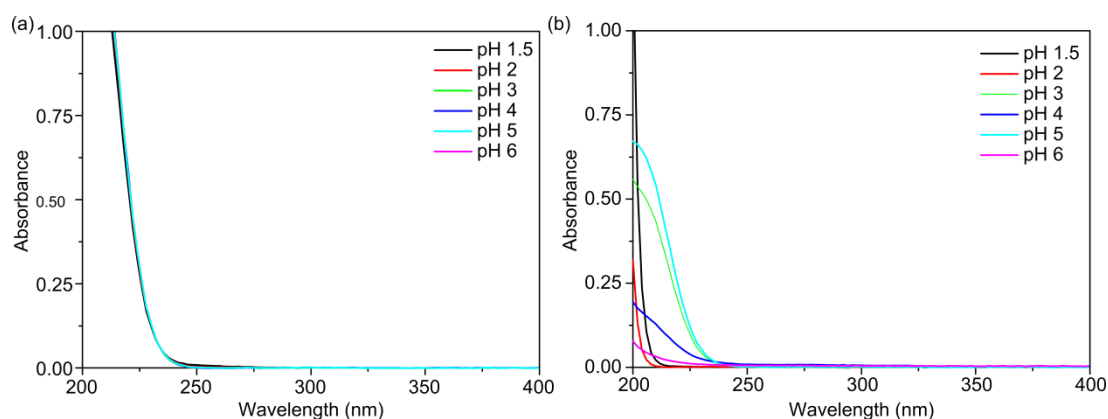


**Figure 4.3:** UV-Vis absorbance between 200 – 400 nm for (a) 100  $\mu\text{M}$   $\text{Cu}^{2+}$  and (b) 100  $\mu\text{M}$  TETA solutions at a range of pH values between pH 1.5 – 6.0 (adjusted using HCl).

#### 4.4.1.2 Investigating Deposition Potential

Preliminary experiments to establish suitable experimental parameters for electrochemical copper detection were conducted using CVs in 1 mM  $\text{Cu}^{2+}$  and 1 mM TETA solutions at pH 2. Initial experiments investigated the effect of cathodic potential on the stripping peak height. The cathodic potential limit was set to a range of parameters between -0.3 V and -1 V ( $E_{1/2}$  for  $\text{Cu}^{2+}$  reduction = -0.06 V, **Figure 4.4**), whilst the maximum anodic potential was maintained at +0.5 V throughout. Typical results are shown in **Figure 4.5**.

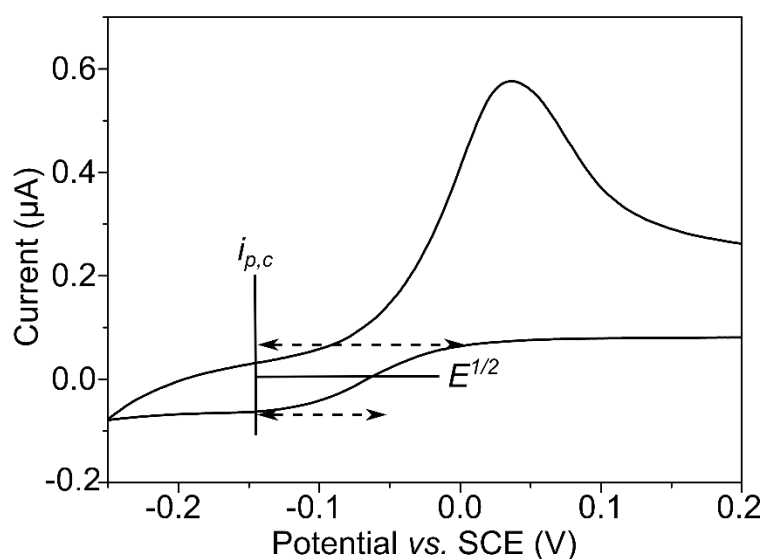


**Figure 4.4:** CV for 100  $\mu\text{M}$  Cu in 0.1 M  $\text{KNO}_3$  supporting electrolyte at pH 2, showing calculation of  $E_{1/2}$ .

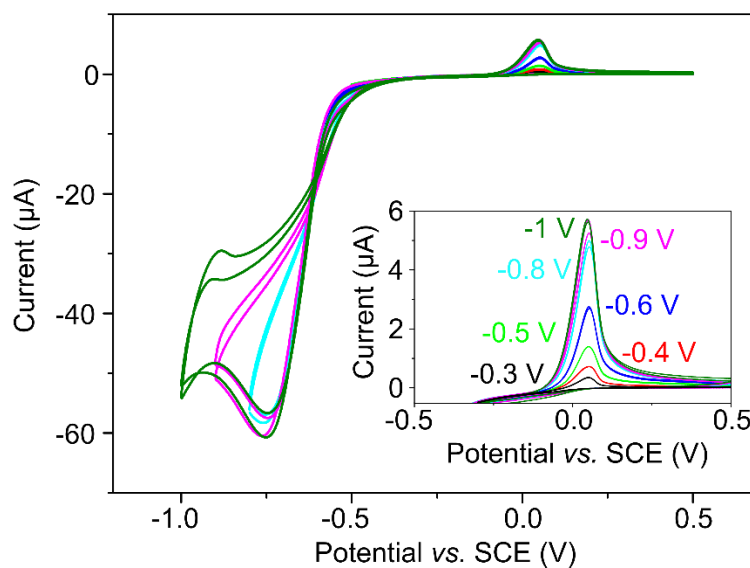


**Figure 4.5:** CVs in 1 mM Cu and 1 mM TETA mixture in 0.1 M  $\text{KNO}_3$  supporting electrolyte at pH 2 (adjusted using 0.1 M  $\text{HNO}_3$ ), scanned out to varying cathodic potentials (-0.3 V, -0.4 V, -0.5 V, -0.6 V, -0.8 V, -0.9 V, -1 V). Inset shows a zoomed area of the  $\text{Cu}^{2+}$  stripping peak.

**Figure 4.5** shows that as the cathodic window is extended more negative the Cu stripping peak increases in size, due to a combination of increased overpotential and increased deposition time. Between -0.6 V and -0.8 V the

stripping peak increases significantly, whereas as higher overpotentials are reached the difference in signal height becomes less pronounced, possibly due to incomplete stripping of copper when higher quantities are deposited.

For windows extended beyond -0.5 V a large ( $\sim 61 \mu\text{A}$ ) cathodic peak is present at -0.75 V in **Figure 4.5**. It is likely that this peak is due to the presence of copper in large enough quantities on the electrode surface catalysing the reduction of protons, causing the appearance of a large proton wave. Note, on bare BDD the proton wave appears at -1.71 V. An estimation of the expected peak current,  $i_p$ , for a given proton concentration can be made using the Randles Sevcik equation (assuming the CV is diffusion limited), see **Chapter 1**. At pH 2 ( $10 \text{ mM H}^+$ )  $i_p$  is calculated as  $64.5 \mu\text{A}$  (assuming a  $D$  of  $9.31 \times 10^{-5} \text{ cm}^2 \text{ s}^{-1}$ )<sup>39</sup> very close to the experimental  $i_p$  of  $61 \mu\text{A}$ .

For the *in situ* pH experiments the deposition parameters employed must be considered carefully. Although it is observed that more negative deposition potentials provide higher copper stripping currents, the onset of a proton reduction wave in the presence of appreciable copper (From **Figure 4.4**,  $E_{1/2} = -0.055 \text{ V}$ ) at low pH may cause interference. As such a deposition potential of -0.5 V was chosen for further experiments.

#### **4.4.1.3 Investigation of Proton Wave as a method to measure pH**

The appearance of a quantifiable proton wave on copper-plated BDD is a possible approach for measuring the local pH generated during experiments. As such it was of interest to investigate further, as shown in **Figure 4.6**, for bulk defined pH solutions initially. For different pH solutions ( $1 \text{ mM Cu}$  at pH

6.03, pH 2.30, and pH 2.00),  $i_p$  is comparable to that expected using the Randles Sevcik equation (dotted lines on **Figure 4.6**). As the pH increases, the magnitude of the proton wave decreases, due to lower proton concentration and begins to shift to more negative potentials.

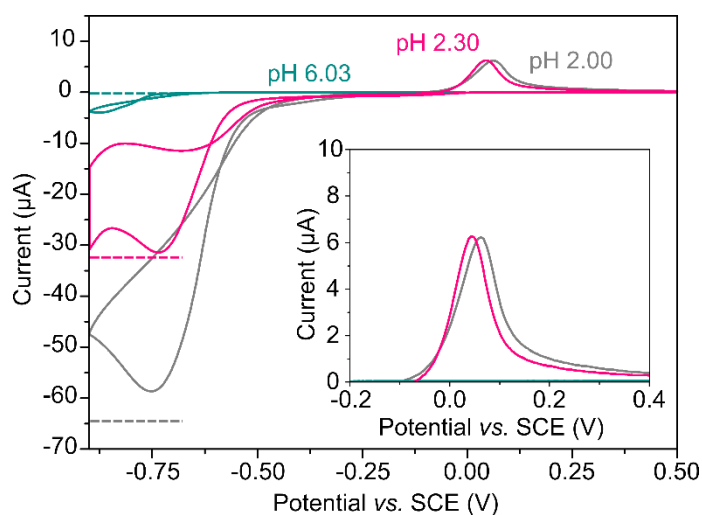


**Figure 4.6:** CVs in 1 mM Cu and 1 mM TETA mixtures with 0.1 M KNO<sub>3</sub> supporting electrolyte at pH 2.00 (Grey) 2.30 (Pink) and 6.03 (Turquoise), adjusted using 0.1 M HNO<sub>3</sub> and 0.1 M KOH at 0.1 mVs<sup>-1</sup>. Inset shows copper stripping peaks.

In order to investigate the usefulness of this phenomenon under *in situ* pH generation conditions, the experiment was repeated for a pH 6.03 bulk solution, in which a range of currents (10, 15, 50 and 70 μA) were applied to the generator (ring) electrode prior to and during Cu<sup>2+</sup> detection at the disc, **Figure 4.7**. Average generated pH values across the disc electrode were calculated from the cathodic peak current for each experiment. The resulting pH values are shown in **Figure 4.7**, and correlate well with other experimental data measured using an IrOx coated disc electrode (see Chapter 3).

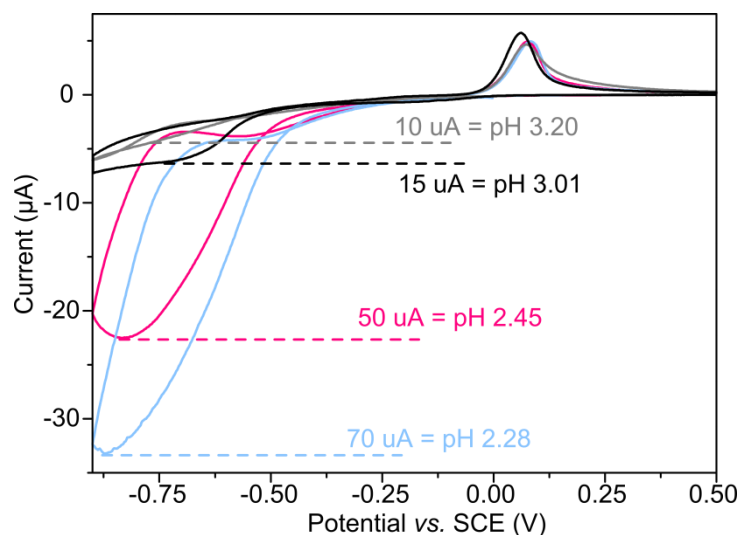


**Figure 4.7:** CV at  $0.1 \text{ Vs}^{-1}$  in  $1 \text{ mM Cu}^{2+}$  and  $1 \text{ mM TETA}$  solution with  $0.1 \text{ M KNO}_3$  supporting electrolyte adjusted to bulk pH 6.03 using KOH. A range of generator currents (10, 15, 50 and  $70 \mu\text{A}$ ) were applied to the ring electrode for 3 mins prior to, and during, CV recordings. Dashed lines denote the pH value calculated using peak current.

Experiments were repeated with solution concentrations of  $100 \mu\text{M Cu}$  and  $100 \mu\text{M TETA}$ , as these conditions would be used in further work, for a generator current of  $15 \mu\text{A}$ . The results are shown in **Figure 4.8**.

As copper concentration is decreased, smaller quantities of copper in solution, result in a decrease in the amount of copper deposited on the electrode (and also possible changes in deposition morphology).<sup>40</sup> These appear to reduce the catalytic effect on proton reduction (**Figure 4.8**) as the proton wave is pushed out further into the cathodic window.

At pH 6.35 in a solution containing  $100 \mu\text{M Cu}^{2+}$ ,  $i_p$  is significantly larger (almost  $\times 400$ ) than predicted by theory ( $-1.95 \mu\text{A}$  as opposed to the expected  $2.88 \text{ nA}$ ); a similar effect is observed for  $1 \text{ mM}$  solution at pH 6.03 in **Figure 4.6**. However, it is thought that the signal seen could be due to oxygen reduction (calculated to be  $i_p = 6.22 \mu\text{A}$ ), assuming for oxygen  $C = 0.25 \text{ mM}$ ,  $n$

= 4, and  $D = 2.1 \times 10^{-5}$ ,<sup>41</sup> which would clearly mask the expected very low proton reduction currents, at such low proton concentrations. For a pH 6.35 solution when 15  $\mu\text{A}$  was applied to the generator for 3 mins prior to, and during, the CV (black data) the proton wave gives an estimated pH of 3.00 across the disc, which correlates with that seen in more concentrated copper solutions (**Figure 4.7**). However, it is important to consider possible proton consumption effects (i.e. local depletion of the proton concentration) when measuring the pH in this way, in the presence of a finite concentration of generated protons.

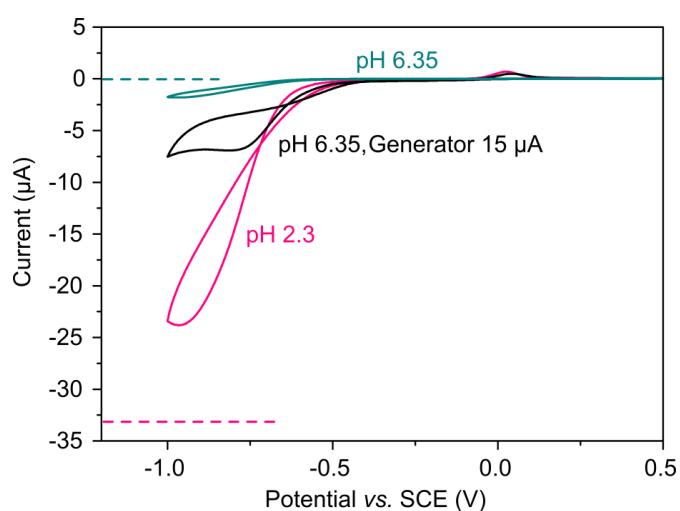


**Figure 4.8:** CVs at  $0.1 \text{ Vs}^{-1}$  in  $100 \mu\text{M Cu}^{2+}$  and  $100 \mu\text{M TETA}$  solution with  $0.1 \text{ M KNO}_3$  for bulk pH 6.35 (turquoise) and 2.3 (pink) solutions (adjusted using  $0.1 \text{ M HNO}_3$  and  $\text{KOH}$ ), dashed lines show theoretical proton wave currents. A CV in pH 6.35 solution with  $15 \mu\text{A}$  applied to the generator electrode for 3 mins prior to, and during, the CV is shown in black, the average pH across the disc is calculated to be pH 3.00.

This effect can be simulated to find the average pH predicted across the disc (detector) electrode vs. time, as shown in **Figure 4.9**, for a  $15 \mu\text{A}$  current applied to the ring (generator) electrode, under conditions where the disc electrode consumes protons. Upon application of the galvanostatic current, the pH at the disc electrode initially drops rapidly before plateauing at



approximately pH 2.60 until 300 s when a CV is performed on the disc. As the potential at the disc is swept in the negative direction a sharp spike in the pH profile can be observed, corresponding to reduction of available protons near the electrode surface. However, as the potential is reversed and then becomes positive the pH can be seen to recover rapidly. Hence for a truly non-invasive measurement of pH locally, under *in situ* generation conditions, adoption of potentiometric techniques are probably preferred.

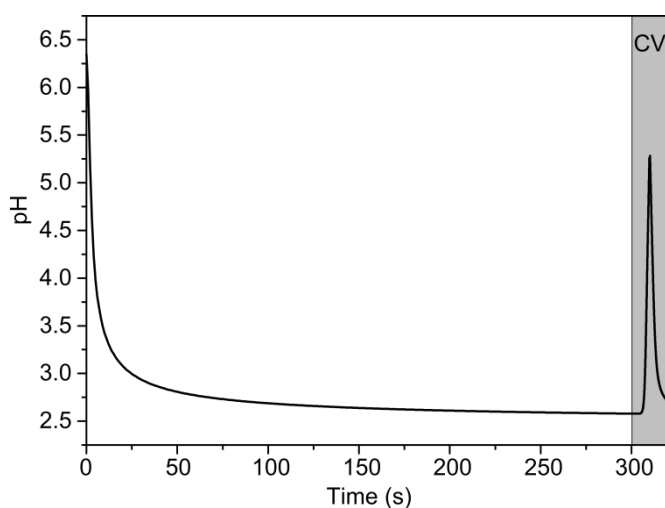


**Figure 4.9:** Simulation of the average pH vs. time across the disc (detector) electrode for an applied generator current of  $15\ \mu\text{A}$ . At 300s a CV is run on the disc electrode at  $0.1\ \text{V s}^{-1}$ , the resulting pH change is highlighted in grey.

#### 4.4.2 UV-Vis Titration of Cu TETA vs. simulated speciation curves

In order to establish the effect of pH on Cu binding with TETA, speciation curves were simulated using the MINEQL+ speciation software, and are compared with experimental UV-Vis data. **Figure 4.10(a)** shows the speciation curves, expressed as % of total copper concentration, for free  $\text{Cu}^{2+}$  (black line),  $\text{Cu}[\text{HTETA}]^{3+}$  (blue line),  $\text{Cu}[\text{TETA}]^{2+}$  (red line) and combined  $\text{Cu}[\text{TETA}]^{2+} + \text{Cu}[\text{HTETA}]^{3+}$  (purple line) as a function of pH over the range 1 – 10, for  $100\ \mu\text{M}\ \text{Cu}^{2+}$  and 100

$\mu\text{M}$  TETA. At pH values  $< 2.5$ , all  $\text{Cu}^{2+}$  exists in the free form, whilst for pH values  $\geq 4.46$ , all the  $\text{Cu}^{2+}$  is bound to TETA ligands and therefore not freely available.

In order to verify this speciation, UV-Vis data were obtained for the dropwise pH titration of a  $100\ \mu\text{M}$   $\text{Cu}^{2+}$ ,  $100\ \mu\text{M}$  TETA mixture. The resulting absorbance data, over  $200\ \text{nm} - 400\ \text{nm}$ , for pHs in the range  $1.69 - 5.23$ , are shown in **Figure 4.10(b)**. An absorption maximum is observed at  $\sim 250\ \text{nm}$  which is in good agreement with that seen previously for the  $\text{Cu}[\text{TETA}]^{2+}$  ligand-metal complex (absorptivity  $\sim 3900\ \text{M}^{-1}\ \text{cm}^{-1}$ ).<sup>37</sup> The absorption characteristics for  $\text{Cu}[\text{HTETA}]^{3+}$  are expected to be very similar to those for  $\text{Cu}[\text{TETA}]^{2+}$  and therefore the peak maximum is likely to represent the absorption characteristics of both species (*vide infra*). The absorption data are presented as (peak maximum for a given pH value) / (peak maximum for 100 % bound  $\text{Cu}^{2+}$  *i.e.* for pH values  $\geq 4.46$ )  $\times 100\%$  (■) and displayed in **Figure 4.10(a)**. As shown there is a good fit between the experimental UV-Vis data achieved and the simulated speciation curve for combined  $\text{Cu}[\text{TETA}]^{2+}$  and  $\text{Cu}[\text{HTETA}]^{3+}$ , confirming that the experimental UV-Vis peak maximum most likely represents the absorption of both  $\text{Cu}[\text{TETA}]^{2+}$  and  $\text{Cu}[\text{HTETA}]^{3+}$ .

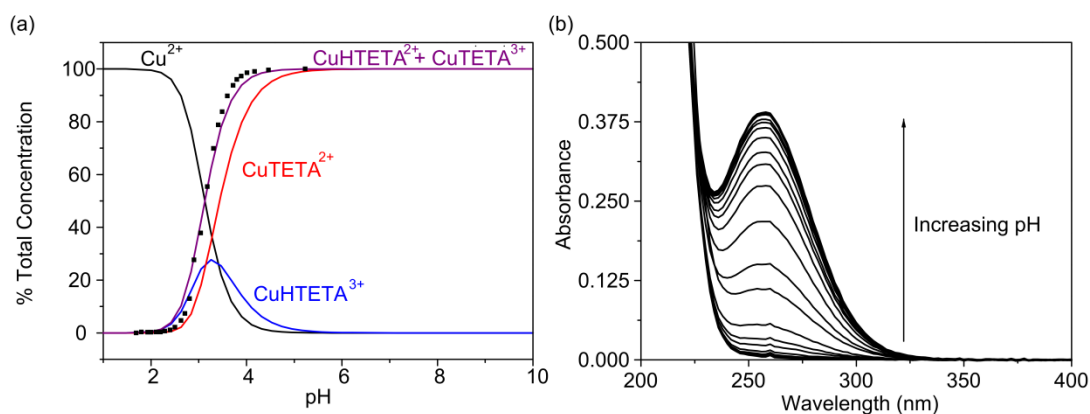


**Figure 4.10:** (a) Simulated speciation curves for 100  $\mu\text{M}$   $\text{Cu}^{2+}$  ( $\text{Cu}(\text{NO}_3)_2$ ) and 100  $\mu\text{M}$  TETA (ionic strength = 300  $\mu\text{M}$ ) across the pH range 1 - 10, expressed as % of total copper for free  $\text{Cu}^{2+}$  (black),  $\text{Cu}[\text{HTETA}]^{3+}$  (blue),  $\text{Cu}[\text{TETA}]^{2+}$  (red) and total  $\text{Cu}[\text{HTETA}]^{3+} + \text{Cu}[\text{TETA}]^{2+}$  (purple). (b) UV-Vis data, corresponding to  $\text{Cu}[\text{HTETA}]^{3+} + \text{Cu}[\text{TETA}]^{2+}$  for a pH titration of 100  $\mu\text{M}$   $\text{Cu}^{2+}$  and 100  $\mu\text{M}$  TETA mixture via 25 dropwise additions of HCl (starting pH = 5.23, end pH = 1.69). Peak maxima / peak maximum (for maximum absorbance)  $\times 100$  % (■) is plotted on (a).

#### 4.4.3 UV-Vis titration of different ratios of Cu:TETA

The effect of Cu to TETA ratio was also investigated using UV-Vis. pH titrations of  $\text{Cu}^{2+}$  and TETA mixtures at three different concentration ratios (Cu:TETA), 1:1, 2:1, and 1:2, where 1 part is equivalent to 100  $\mu\text{M}$ , were conducted. Absorbance peak maximum is plotted vs. concentration in **Figure 4.11**, for a range of calibration solutions between 10  $\mu\text{M}$  and 200  $\mu\text{M}$ . Calibrations were prepared in a 1:1 ratio of Cu:TETA at pH 5.0 such that the  $\text{Cu}^{2+}$  ions were in the 100 % bound form, providing maximum absorbance. Peak maximum showed good linearity ( $R^2 = 0.9997$ ) with respect to concentration across the range investigated, and was found to be reproducible across two sets of calibrations with three UV-Vis measurements for each.

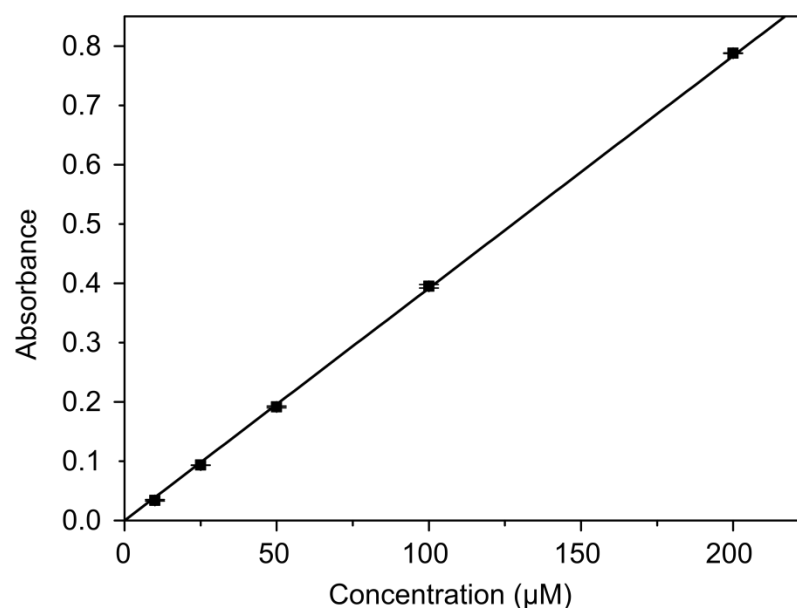


**Figure 4.11:** Calibration data for absorbance peak maxima when  $\text{Cu}^{2+}$  is 100% bound by TETA (pH 5.0) at concentrations between 10 and 200  $\mu\text{M}$  (1:1 ratio) Slope =  $0.00392 \pm 0.0000314$ ,  $R^2 = 0.9997$ .

Subsequently, the calibration from **Figure 4.11** was applied to UV-Vis titration data for the three different concentration ratios, the results of which can be found in **Figure 4.12**. For all three ratios the sigmoidal shape one would expect is evident; however there are some obvious differences. For the 1:1 and 1:2 ratios, where a maximum of 100  $\mu\text{M}$   $\text{Cu}^{2+}$  is present in the system, the sigmoidal shape can be seen to plateau at pH 4.46 and 3.90 respectively. The plateau absorbance in both cases is equivalent to a total  $\text{Cu}[\text{TETA}]^{2+}$  and  $\text{Cu}[\text{HTETA}]^{3+}$  concentration of  $\sim 100 \mu\text{M}$ , correlating with the 1:1 binding mechanism suggested in literature. Interestingly, for the 2:1 Cu:TETA mixture the plateau occurs at a similar pH to the 1:1 solution, but at a  $\text{Cu}[\text{TETA}]^{2+} + \text{Cu}[\text{HTETA}]^{3+}$  concentration of 114  $\mu\text{M}$ , exceeding the available concentration of TETA. This is thought to be an indication that in a solution of excess  $\text{Cu}^{2+}$  it is possible to form binuclear complexes with TETA,<sup>42</sup> which absorb more

strongly at this wavelength than their mononuclear counterpart. It is observed that the point at which all  $\text{Cu}^{2+}$  is released from complex is approximately the same for all three solutions, suggesting that the protonation of TETA (and therefore release of  $\text{Cu}^{2+}$ ) at acidic pHs is largely independent of Cu:TETA ratio.

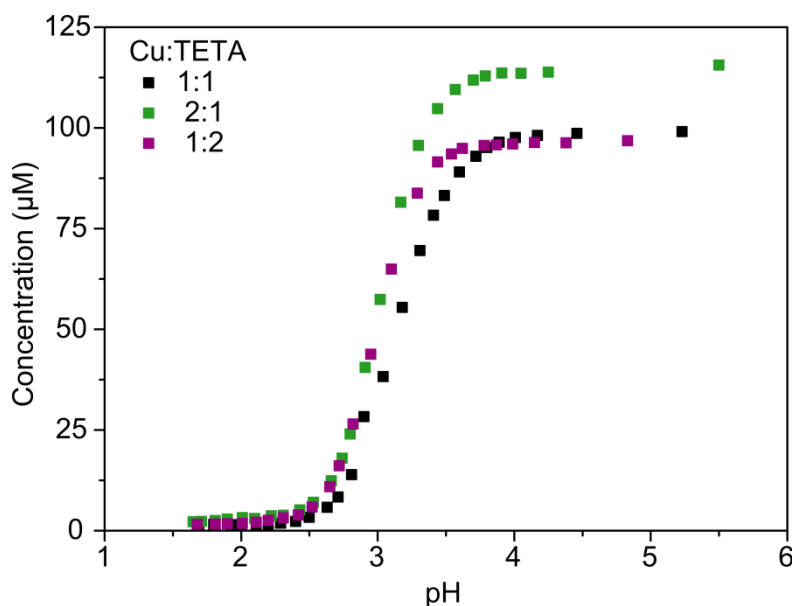


**Figure 4.12:** Absorbance peak maximum data for mixtures of  $\text{Cu}^{2+}$  and TETA at different ratios 1:1 (■), 1:2 (■), and 2:1 (■), Cu:TETA, where 1 part is equivalent to 100  $\mu\text{M}$ .

#### 4.4.4 UV-Vis of Cu TETA in the visible range

Free (hydrated)  $\text{Cu}^{2+}$  should be visible in the range 500 - 900 nm,<sup>43</sup> however given its low absorption coefficient,<sup>43</sup> in combination with the concentrations employed in section 4.4.2, a measurable signal was not discernible. As such, UV-Vis experiments in this range were conducted with a 100 fold increase in analyte concentration (10 mM  $\text{Cu}^{2+}$ , 10 mM TETA), absorbance data is shown in **Figure 4.13**.

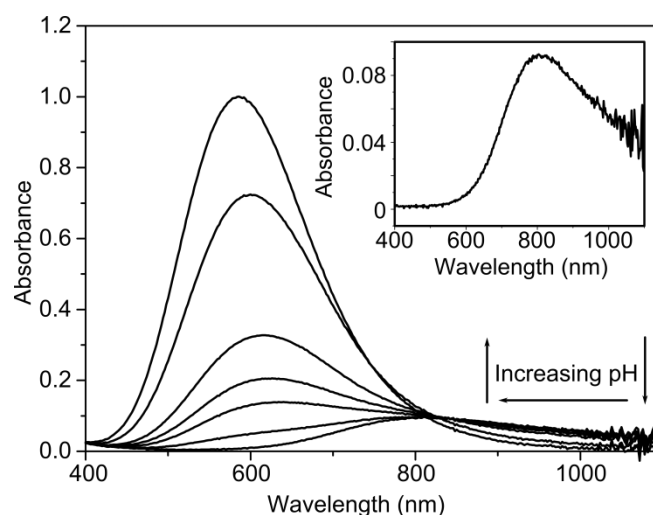


**Figure 4.13:** UV-Vis data, corresponding to  $\text{Cu}^{2+}$ , and  $\text{Cu}[\text{HTETA}]^{3+} + \text{Cu}[\text{TETA}]^{2+}$  for a pH titration of 10 mM  $\text{Cu}^{2+}$  and 10 mM TETA mixture via dropwise additions of HCl (starting pH = 1.69, end pH = 5.23). Inset shows an enlarged version of the free  $\text{Cu}^{2+}$  peak at acidic pH for clarity.

For acidic pH values, when  $\text{Cu}^{2+}$  is 100% free, a peak maximum can be observed at ~805 nm. As the pH is increased, the peak maximum can be seen to shift to lower wavelengths and increase in absorbance, corresponding to deprotonation of the TETA ligand which results in binding of the  $\text{Cu}^{2+}$  to form  $\text{Cu}[\text{HTETA}]^{3+}$  and  $\text{Cu}[\text{TETA}]^{2+}$  as discussed previously. This can be observed visibly as the colour of the solution transitions from a pale green-blue to a vivid dark blue. Due to the overlap of the peak tail from the high pH data with the free  $\text{Cu}^{2+}$  peak maxima this data provides only qualitative evidence of the existence of free  $\text{Cu}^{2+}$  under acidic conditions, becoming bound as the pH increases. However, coupled with the data from section 4.4.2 it is confirmed that pH controls the binding of  $\text{Cu}^{2+}$  ions with the ligand TETA.

#### 4.4.5 Bulk pH electrochemistry vs. simulated speciation curves

**Figure 4.14(a)** shows the ASV current-voltage signals for stripping voltammetry experiments in 100  $\mu\text{M}$   $\text{Cu}^{2+}$  and 100  $\mu\text{M}$  TETA solutions

adjusted to bulk pH values of 2.5, 2.99, 3.52, 4.05, and 5.01. At pH 5.01, no electrochemical signal is seen, as expected based on the fact that  $\text{Cu}^{2+}$  is fully complexed with TETA and electrochemically inaccessible. As the pH is decreased and TETA becomes protonated, forming first HTETA then increasing in protonation, until fully protonated ( $\text{H}_4\text{TETA}$ ),  $\text{Cu}^{2+}$  ions are released from the metal-ligand complex and are freely available for electroreduction. The lower the pH the more  $\text{Cu}^{2+}$  available for electroreduction (until it has all been released), this manifests itself in an increasing peak height (and area under the curve) as the pH of the solution is lowered.

The simulated  $\text{Cu}^{2+}$  TETA speciation curve is shown in **Figure 4.14(b)**, adjusted to account for the change in ionic strength of the solution due to the presence of supporting electrolyte ( $\text{KNO}_3$ ) in the electrochemical experiment. Note  $\text{NO}_3^-$  shows a characteristic absorption at  $\sim 210 - 220 \text{ nm}^{44}$  in the UV-Vis spectrum and therefore cannot be added to the solutions in **Figure 4.10**. The peak current,  $i_p$ , ( $\blacklozenge$ ) normalized with respect to the maximum,  $i_{p,\text{max}}$  recorded under acidic conditions, where the  $\text{Cu}^{2+}$  is completely unbound,  $\times 100 \%$ , is shown also on **Figure 4.14(b)**. It is clear that for the ASV experiments recorded in the different pH solutions there is good agreement between the electrochemical signal which relates to free  $\text{Cu}^{2+}$  and the speciation curve for free  $\text{Cu}^{2+}$ , under these solution conditions.

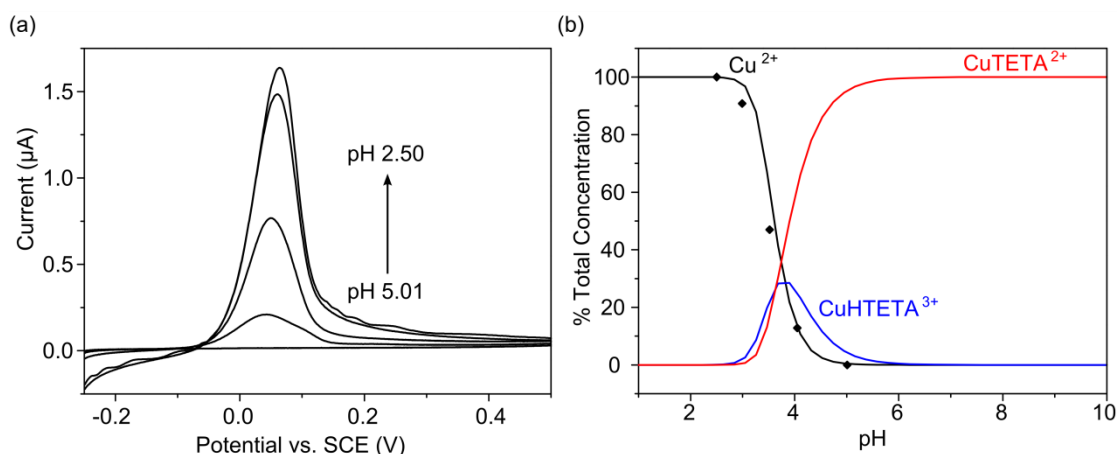


**Figure 4.14:** (a) ASV curves for  $\text{Cu}^{2+}$  stripping for solution pH values in the range 2.50, 2.99, 3.52, 4.05, 5.01, in a  $100 \mu\text{M}$   $\text{Cu}^{2+}$  and  $100 \mu\text{M}$  TETA solution with  $0.1 \text{ M}$   $\text{KNO}_3$  added as supporting electrolyte, scan rate =  $0.1 \text{ V s}^{-1}$ . (b) ASV ( $i_p / i_{p,\max} \times 100 \%$ ) data ( $\blacklozenge$ ) plotted as a function of pH. Also shown are the simulated speciation curves for the equivalent solution experimental conditions for free  $\text{Cu}^{2+}$  (black),  $\text{CuHTETA}^{3+}$  (blue),  $\text{CuTETA}^{2+}$  (red), ionic strength =  $0.1003 \text{ M}$ .

#### 4.4.6 pH generation results

Experiments were then carried out under bulk pH = 6.4 conditions. A constant current (in the range  $0.10 - 2 \text{ mA cm}^{-2}$ ) was applied to the generator electrode (versus a Pt counter electrode) for a period of 300 s to generate a steady-state flux of protons (via oxidation of water); the higher the current density the greater the flux. Note higher than  $6 \text{ mA cm}^{-2}$  causes significant bubbles (oxygen) to form which can be problematic for copper electrodeposition and stripping. With the current still applied, the potential at the detector electrode was then switched on ( $-0.5 \text{ V}$  for 60s, versus SCE) to electrodeposit any free  $\text{Cu}^{2+}$  onto the electrode surface and then swept anodically between  $-0.25 \text{ V}$  and  $+0.5 \text{ V}$  at  $0.1 \text{ V s}^{-1}$  to remove electrodeposited Cu from the surface. The resulting ( $i_p / i_{p,\max} \times 100 \%$ ) data, derived from the recorded ASVs



(normalised and shown in **Figure 4.15**) during *in situ* pH generation is displayed in **Table 4.1**.

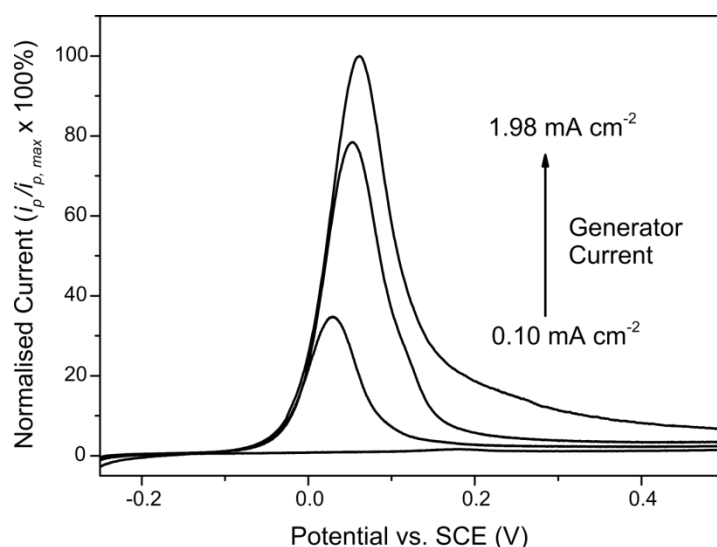


**Figure 4.15:** LSV data corresponding to **Table 1** in the main text, showing normalised stripping peaks ( $i_p/i_{p,max} \times 100\%$ ) of  $100 \mu\text{M Cu}^{2+}$  in the presence of  $100 \mu\text{M TETA}$  at the detector electrode, for a range of constant currents applied to the generator ( $0.1 - 1.98 \text{ mA cm}^{-2}$ ).

**Table 4.1:** Comparison of experimentally recorded ASV ( $i_p/i_{p,max} \times 100\%$ ) data as a function of the applied generator current in  $100 \mu\text{M Cu}^{2+}$  and  $100 \mu\text{M TETA}$  solution with  $0.1 \text{ M KNO}_3$ .

Current Density ( $\text{mA cm}^{-2}$ )	% ( $i_p/i_{p,max}$ )	Generated pH from Speciation Curve
0.10	0	$5.0 \leq$
0.20	35	3.8
0.395	79	3.4
1.98	100	$\leq 2.5$

Importantly, the same trend can be observed in **Table 4.1** as for **Figure 4.14(a)**, where increasing the applied current density, which causes a decrease in the local solution pH, causes the ASV stripping peak currents to increase in size. The maximum peak current was recorded for a galvanostatic current of  $1.98 \text{ mA cm}^{-1}$ . Applied current densities greater than this gave similar peak currents. Currents of  $\geq 1.98 \text{ mA cm}^{-2}$  were

therefore assumed to have made the local solution sufficiently acidic to free the  $\text{Cu}^{2+}$  and fully protonate the TETA. Using the speciation curve in **Figure 4.14(b)** and by plotting the observed ( $i_p / i_{p, \text{max}} \times 100\%$ ) it was possible to estimate the local pH at the electrode surface for the different applied galvanostatic currents, also shown in **Table 4.1**.

#### 4.5 Conclusion

In summary, this chapter has shown that using an electrochemical proton generator coupled to an electrochemical measurement (detector) system it is possible to both change and monitor the speciation of a pH sensitive metal-ligand complex, *in situ*. Importantly, for the complex  $\text{Cu}[\text{TETA}]^{2+}$  it was possible to switch between  $\text{Cu}^{2+}$  in the 100% bound form ( $\text{pH} \geq 5.01$ ) to 100% free  $\text{Cu}^{2+}$  ( $\text{pH} \leq 2.50$ ), *in situ*, simply by generating sufficient protons in the vicinity of the  $\text{Cu}^{2+}$  detector electrode. This is of interest as it offers the possibility of investigating a wide range of pH dependant equilibrium processes *in situ*; provided one of the species in the equilibrium is electrochemically active. Moreover, for pH-dependant metal-ligand binding it provides the opportunity to quantify both total and free metal ion concentrations in one measurement, provided the metal can be electrodeposited and subsequently stripped from the surface. This can be performed by simply making a voltammetric measurement of metal concentration at the native solution pH and then by sufficiently lowering the pH to release all the bound metal, making a measurement of total metal concentration. It was also observed that for highly concentrated ( $> 1 \text{ mM}$ ) copper

solutions it is possible to use the proton wave as an indicator of generated pH. However, there are issues associated at lower concentrations of copper and higher pH values which mean the proton wave should only be used as a guide and requires further investigation to become useful. Finally, to achieve very low levels of detection (~ ppb) it would be necessary to optimise the generator-detection electrode geometry to provide sufficiently high detection sensitivity, e.g. dual microband electrodes in flow.<sup>29</sup>

## 4.6 References

1. Q. Zhang, Z. Hou, B. Louage, D. Zhou, N. Vanparijs, B. G. De Geest and R. Hoogenboom, *Angew. Chem. Int. Ed.*, 2015, **54**, 10879-10883.
2. R. A. Alberty, *J. Biol. Chem.*, 1968, **243**, 1337-1343.
3. S. T. Yang, S. A. White and S. T. Hsu, *Ind. Eng. Chem. Res.*, 1991, **30**, 1335-1342.
4. B. A. Kairdolf and S. Nie, *J. Am. Chem. Soc.*, 2011, **133**, 7268-7271.
5. J. K. Blaho and K. A. Goldsby, *J. Am. Chem. Soc.*, 1990, **112**, 6132-6133.
6. A. Zaban, S. Ferrere, J. Sprague and B. A. Gregg, *J. Phys. Chem. B*, 1997, **101**, 55-57.
7. C. J. Jones and J. Thornback, *Medicinal Applications of Coordination Chemistry*, Royal Society of Chemistry, 2007.
8. D. R. Williams, *Chem. Rev.*, 1972, **72**, 203-213.
9. F. Fu and Q. Wang, *J. Environ. Manage.*, 2011, **92**, 407-418.
10. K. L. Haas and K. J. Franz, *Chem. Rev.*, 2009, **109**, 4921-4960.
11. *Textbook of Medical Biochemistry*, Elsevier Health Sciences APAC, 2014.
12. T. M. Florence, *Analyst*, 1986, **111**, 489-505.
13. A. Tessier and D. R. Turner, *Metal speciation and bioavailability in aquatic systems*, J. Wiley, 1995.
14. B. Salbu and E. Steinnes, *Trace Elements in Natural Waters*, CRC-Press, 1994.
15. L. M. Mosley, R. Daly, D. Palmer, P. Yeates, C. Dallimore, T. Biswas and S. L. Simpson, *Appl. Geochem.*, 2015, **59**, 1-10.
16. M. Pesavento, *Anal. Chim. Acta.*, 1983, **153**, 249-255.
17. G. Hanrahan, *Modelling of Pollutants in Complex Environmental Systems*, ILM Publications, 2010.
18. D. C. Harris, *Quantitative Chemical Analysis*, W. H. Freeman, 2010.
19. E. Hamidi-Asl, D. Daems, K. De Wael, G. Van Camp and L. J. Nagels, *Anal. Chem.*, 2014, **86**, 12243-12249.
20. Y. Y. He, M. Luo, X. Y. Zhang and J. Meng, *Electrochim. Acta*, 2015, **165**, 416-421.
21. J. Sestak, in *Science of heat and thermophysical studies: a generalized approach to thermal analysis*, Elsevier, 2005, ch. 12, pp. 344-377.
22. N. A. Ghalwa, M. Hamada, H. M. Abu-shawish, A. A. Swareh, M. A. Askalany and T. Siam, *J. Electroanal. Chem.*, 2012, **664**, 7-13.
23. G. Aragay, J. Pons and A. Merkoçi, *Chem. Rev.*, 2011, **111**, 3433-3458.

24. W. F. Pickering, in *Chemical Speciation in the Environment*, Blackwell Science Ltd, 2007, DOI: 10.1002/9780470988312.ch2, pp. 7-29.
25. T. Midorikawa, E. Tanoue and Y. Sugimura, *Anal. Chem.*, 1990, **62**, 1737-1746.
26. N. M. Contento and P. W. Bohn, *Biomicrofluidics*, 2014, **8**, 044120.
27. N. M. Contento, S. P. Branagan and P. W. Bohn, *Lab. Chip.*, 2011, **11**, 3634-3641.
28. T. L. Read, E. Bitziou, M. B. Joseph and J. V. Macpherson, *Anal. Chem.*, 2014, **86**, 367-371.
29. E. Bitziou, M. B. Joseph, T. L. Read, N. Palmer, T. Mollart, M. E. Newton and J. V. Macpherson, *Anal. Chem.*, 2014, **86**, 10834-10840.
30. M. G. Afshar, G. A. Crespo and E. Bakker, *Angew. Chem. Int. Ed.*, 2015, **54**, 8110-8113.
31. L. Rassaei and F. Marken, *Anal. Chem.*, 2010, **82**, 7063-7067.
32. W. Kaim and J. Rall, *Angew. Chem. Int. Ed. Eng.*, 1996, **35**, 43-60.
33. R. A. Wuana and F. E. Okieimen, *ISRN Ecology*, 2011, **2011**, 20.
34. G. J. Brewer, *Clin. Neurophysiol.*, 2010, **121**, 459-460.
35. J. M. Walshe, *The Lancet*, 1982, **319**, 643-647.
36. K. S. Johnson and L. J. Coletti, *Deep Sea Res. PT1. Oceanogr. Res.*, 2002, **49**, 1291-1305.
37. V. M. Nurchi, G. Crisponi, M. Crespo-Alonso, J. I. Lachowicz, Z. Szewczuk and G. J. S. Cooper, *Dalton Trans.*, 2013, **42**, 6161-6170.
38. L. A. Hutton, G. D. O'Neil, T. L. Read, Z. J. Ayres, M. E. Newton and J. V. Macpherson, *Anal. Chem.*, 2014, **86**, 4566-4572.
39. R. G. Mortimer, *Physical Chemistry*, Elsevier Science, 2008.
40. L. A. Hutton, M. E. Newton, P. R. Unwin and J. V. Macpherson, *Anal. Chem.*, 2011, **83**, 735-745.
41. E. L. Cussler, *Diffusion: mass transfer in fluid systems*, Cambridge university press, 2009.
42. D. Kharitonov, E. Golubeva, V. Pergushov, A. Kokorin and V. Smirnov, *Kinetics and catalysis*, 2001, **42**, 673-678.
43. J. R. Lalanne, F. Carmona, L. Servant and L. Servant, *Optical Spectroscopies of Electronic Absorption*, World Scientific, 1999.
44. F. A. J. Armstrong, *Anal. Chem.*, 1963, **35**, 1292-1294.

## **5 Development of Coplanar, Diamond Insulated, Boron Doped Diamond Ring Disc Electrodes.**

### **5.1. Overview**

As discussed in chapters 1 and 3, highly doped BDD shows great potential as an electrode material.<sup>1</sup> However, fabrication of suitable electrodes in a variety of geometries in an insulating material that does not compromise the material properties of the BDD presents significant challenges. For applications such as pH generation/control,<sup>2, 3</sup> where extreme currents are applied to the electrode for extended periods of time, the epoxy sealing material used previously was found to erode and eventually fail, rendering the electrode eventually useless. An ideal solution to this would be to use a sealing material which matches the mechanical and chemical properties of the BDD electrodes, the obvious choice in this case being to seal the electrode in an electrically insulating form of the same material.

In this chapter a novel solution to this problem is described, and a fabrication method for single and multiple individually addressable, coplanar BDD electrodes encapsulated in insulating diamond is presented. Finite element simulations are employed to investigate the effects of ring disc geometry on electrochemical pH generation, enabling electrode design to be tailored to the application. Using a laser micromachining approach, the desired electrode geometries are machined into insulating diamond substrates, followed by

overgrowth of high quality polycrystalline BDD, and subsequently polished to reveal coplanar all-diamond structures with approximately nanometer roughness. It is shown that electrical contacts can be formed via top contacting of Ti/Au pads, or via laser machined back contacts, where the laser can be used to produce non-diamond carbon at the back of the electrode. This chapter presents the fabrication of individually addressable ring, band and disc electrodes, with a focus on ring disc electrodes. The BDD overgrown into the insulating diamond is shown to be NDC free and to possess excellent electrochemical properties, in terms of extended solvent windows, electrochemical reversibility and capacitance.

## **5.2. Introduction**

The interest of BDD as an electrode material has been discussed as a theme in this work, attracting attention for its ultrawide solvent window in aqueous media, low capacitive currents, and high resistance to fouling and corrosion.<sup>4-6</sup> Typically BDD used in electrochemical applications is polycrystalline micro- or nano- thin film diamond grown on a substrate. When grown thick enough, the BDD can be removed from the growth substrate to produce freestanding material, typically with larger crystallite grains due to the increased thickness of the material. In nanocrystalline and microcrystalline BDD without carefully controlled growth conditions NDC content can be high, which is detrimental to electrochemical behavior.<sup>7</sup>

Freestanding diamond, compared to thin film BDD on a non-diamond growth substrate, allows more freedom in the geometries and electrode assemblies

available for use as it is robust enough to withstand mechanical and chemical processing methods. However for the majority of researchers, typically electrochemical studies are conducted with a cell of defined geometry placed, or clamped, over a piece of BDD to create a defined geometric area.<sup>8, 9</sup> For thin film BDD, electrical contacts are made either to the base of the conductive growth substrate (e.g. Si) or to the top if the substrate on which the diamond has been grown is insulating. For freestanding BDD, contacts can be made directly to the BDD. Freestanding BDD also offers the advantage of being machinable e.g. using laser micromachining, into defined structures (e.g. cylinder, cuboid, *etc.*) then electrically back contacted and sealed in an insulating sheath such as glass,<sup>10</sup> or polymer e.g. PTFE,<sup>11, 12</sup> epoxy<sup>5, 13</sup> or PEEK,<sup>14</sup> producing electrode formats more akin to conventional commercially available electrode materials like Pt, Au and glassy carbon. Disc electrodes with diameters in the range of tens of microns<sup>15</sup> to several millimeters<sup>7, 10</sup> have been fabricated this way.

BDD microelectrodes have been produced by growing thin films of BDD onto sharpened W wires and sealing with epoxy and glass.<sup>16</sup> However, the mechanical and chemical stability of the insulating material used is always inferior to that of the BDD, limiting potential applications; for example in the previous chapters of this thesis where the epoxy surrounding the generator electrode was found to erode and eventually fail as a result of the extreme currents necessary for generation.

The ideal solution to this problem is to use a material with the same extreme chemical and mechanical properties as those of the BDD electrodes; the obvious choice in this case is to insulate the BDD in an electrically insulating (undoped) form of the same material, creating all-diamond devices. A move to all-diamond devices offers several advantages over other methods: formation of a robust seal between the electrode and insulator; resistance to chemical and thermal stress and abrasive wear; and longevity in extreme environments. There have been limited previous attempts in the literature to produce all-diamond electrodes. A freestanding BDD substrate was used with laser ablation to create pillared BDD structures. These were subsequently overgrown with insulating diamond and polished to reveal an array of coplanar BDD microdisc electrodes encapsulated in insulating diamond as illustrated in *Figure 5.1*.<sup>17</sup>

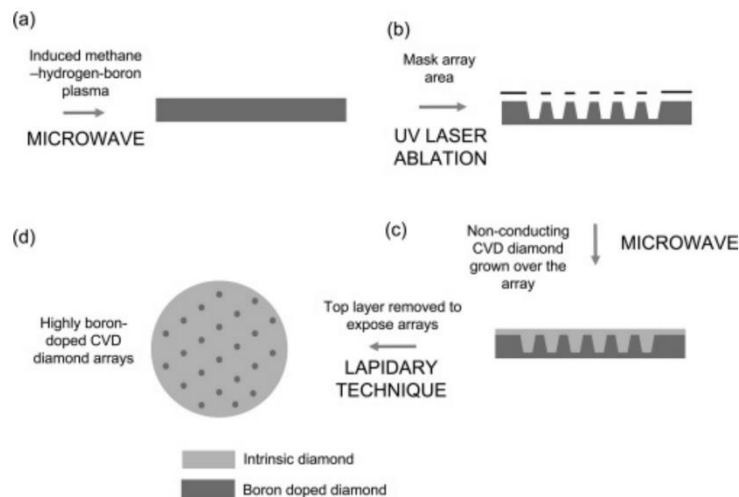


**Figure 5.1:** Schematic showing the process used to create BDD UME arrays encased in insulating diamond. Figure taken from Macpherson et al.<sup>17</sup>



However, using this approach the electrodes are not individually addressable and insulating diamond growth must be carefully controlled to avoid defects, pinholes and cracks.<sup>17, 18</sup> A three layer growth process has also been described, with a microlayer of BDD sandwiched between two layers of insulating diamond. A macrohole cut through the structure created an all diamond ring electrode suitable for use in flow studies.<sup>19</sup> Nanocrystalline BDD, patterned to isolate insulating diamond overgrowth from defined regions resulted in a nonaddressable recessed BDD UME array as shown in **Figure 5.2**.<sup>20</sup>

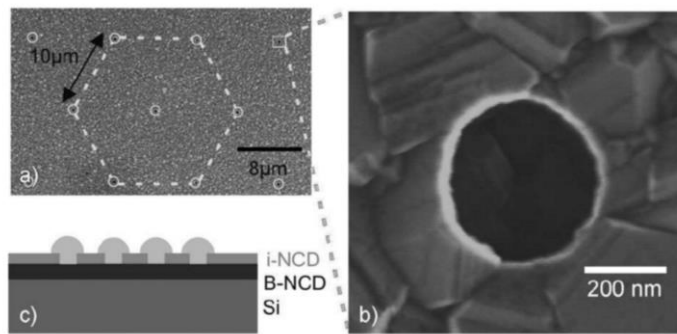


**Figure 5.2:** Nanocrystalline BDD UME array developed by Nebel et al.<sup>20</sup> (a) and (b) show SEM images of the array and a single UME respectively. (c) Illustrates the layered structure. Figure taken from Nebel et al.<sup>20</sup>

More recently, a method was developed in the group to create individually addressable, coplanar all-diamond devices in any 2D geometry.<sup>21</sup> In brief, trenches of the desired geometry are laser micromachined into an insulating diamond substrate, before overgrowth with a layer of BDD. The front surface is then polished back, removing the excess BDD and revealing the electrode shapes sealed in insulating diamond as shown in **Figure 5.3**. Contacts can be formed either to the top of the electrodes (normally conductive BDD tracks

are added to the electrode design) or through holes machined in the back of the substrate. In this chapter this method is highlighted through the design, fabrication and characterization of all-diamond ring disc devices. Other geometries have also been investigated for a range of applications, including dual band electrodes for hydrogen sulphide detection under flow conditions.<sup>22</sup>

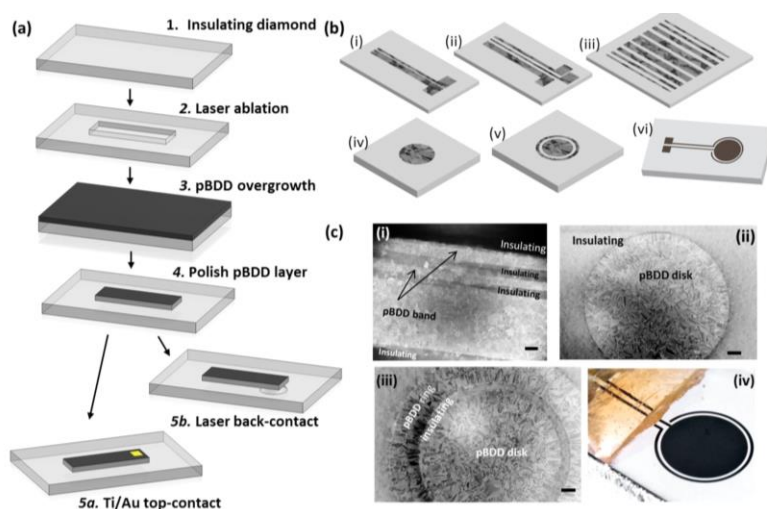


**Figure 5.3:** Figure demonstrating (a) the process developed to produce co-planar all diamond electrodes, (b) some example electrode geometries possible using this method, and (c) SEM and optical images of actual all diamond devices created using this method. Figure taken from Joseph et al.<sup>23</sup>

## 5.3. Experimental

### 5.3.1. Solutions

All solutions were used as supplied and prepared using Milli-Q water (Millipore) with a resistivity of 18.2 MΩ cm at 25 °C unless stated otherwise. Electrochemical characterization was conducted using 0.1 M KNO<sub>3</sub> (Sigma Aldrich) supporting electrolyte and 1 mM Ru(NH<sub>3</sub>)<sub>6</sub><sup>3+/2+</sup> redox mediator solutions.

### 5.3.2. COMSOL Simulation

Finite element simulations were carried out, the boundary conditions for which are described in **Chapter 3**. A current density of  $6.63 \text{ mA cm}^{-2}$ , as described in **Chapter 3** was found to be the highest generator current density which produced no observable bubbles. This current density was applied to the generator electrode in each simulation. The ring disc can be thought of as a generator – detector type system where the ring generates protons which locally change the pH environment of the disc. The disc acts as a detector of other redox species. In this study, the geometric parameters disc radius, ring width, and electrode separation were varied in order to investigate the effect on the change in pH in the vicinity of the disc electrode.

### 5.3.3. Dual Ring Discs

Also tested were dual ring disc electrodes with a view to producing electrodes capable of making several different measurements simultaneously with pH generation, such as a pH generation/detection feedback mechanism with simultaneous trace metal analysis.

## 5.4. Results and Discussion

### 5.4.1. Electrode Fabrication

All stages of material growth were performed by Element Six (Harwell, Oxford, UK). Typically insulating substrates were 1 mm thick and mechanically polished on the growth face to a surface roughness of  $<2 \text{ nm}$ . Structures of the desired geometry were machined using a high power laser micromachiner (E-355-H-3-ATHI-O, Oxford Lasers, UK), before acid cleaning as described in

**Chapter 2.** The substrates were then overgrown with BDD using MW-CVD, excess BDD removed by polishing, and acid cleaned for a second time. This process is illustrated in **Figure 5.4**. Electrical contact was made to the rear of the electrode using laser micromachined holes as described in **section 5.4.1.1**.

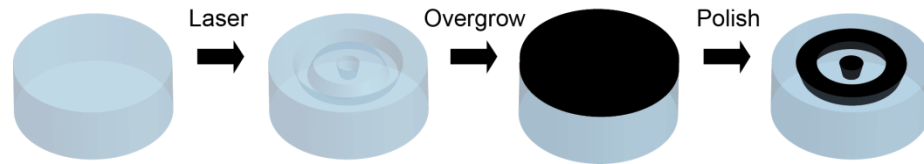


**Figure 5.4:** Schematic illustrating the process for creating BDD ring disc electrodes sealed in an insulating diamond substrate. Insulating diamond is laser micromachined into trenches of the desired geometry, overgrown with BDD, then polished back to reveal the electrode faces.

#### **5.4.1.1. Laser micromachining and back contacting**

Contacts to the back of the BDD electrode were formed via laser micromachining. When machining holes to back contact all-diamond devices there are several important points to consider. Firstly, the hole must be deep enough to reach the back of the BDD but not so deep as to go all the way through the front surface. Secondly, to maintain individual addressability, the holes for individual electrodes must not overlap with other electrodes or holes. In order to do this the laser must initially be focused and the parameters calibrated to produce holes of the desired depth.

Firstly, the laser is focused on the back surface of the insulating diamond in a blank area, and the depth per pass is subsequently measured and calculated as described in **Chapter 2**. From this the approximate depth per pass is used to set the z-step, this is especially important for back contacting as over-lasering could result in holes through the thin BDD layer whilst under-lasering will not

contact the electrode, poor laser focus can also cause these issues. Finally, the number of passes (N) necessary to reach the back of the BDD is calculated for each electrode on the substrate, and N-2 passes are applied with the above parameters. The depth of the hole is once again measured via interferometry and the final layers are lasered and tested sequentially with a multimeter until contact is achieved, illustrated in **Figure 5.5**. The final hole depth is confirmed using interferometry. A circular cutting program at frequency = 10 kHz, 100% power, is used to laser individual devices out of the substrate in 3 mm diameter cylinders, with the electrodes in the centre.

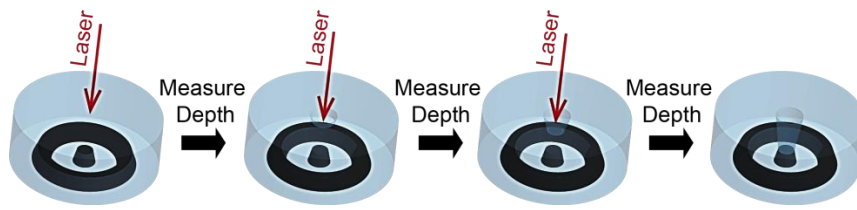


**Figure 5.5:** Illustration of the process of laser back contacting the disc of an all diamond ring disc electrode. A circular laser program is applied for 1 pass, before the depth is measured using interferometry, this is repeated and the depths used to calculate the number of laser passes needed to reach the rear of the BDD electrode (shown in the final step).

The electrodes were acid cleaned once more. In order to form an ohmic contact to the BDD a Ti/Au layer was sputtered into the lasered contact holes. Upon annealing TiC is formed at the interface between the Ti and the BDD, the Au protects the outer Ti surface from oxidation; this has been found to produce well defined ohmic behaviour. It is important to maintain the individual addressability of the electrodes when sputtering, as such circular holes are lasered in an adhesive kapton mask in the same arrangement as those in the all-diamond device. The mask is aligned over the back of the electrode with the help of a dissection microscope (Motic, US) and secured in

place, leaving the contact holes clear but ensuring the rest of the diamond is covered, this process is illustrated in **Figure 5.6**. The all-diamond devices are then sputtered with a 10/300 nm layer of Ti/Au and subsequently annealed at 400 °C for 5 hours.

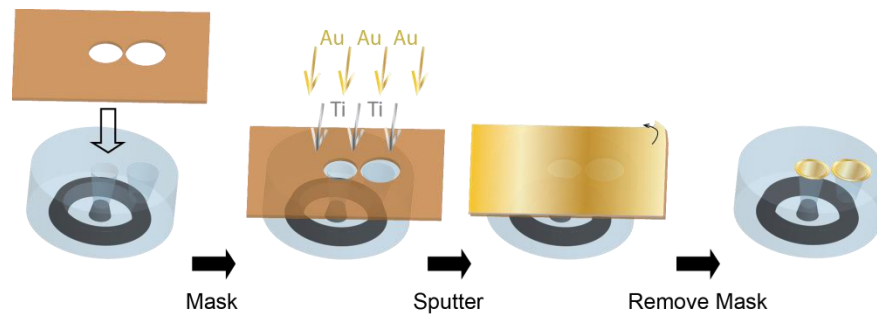


**Figure 5.6:** Schematic illustrating the Ti/Au sputter contacting of a back contacted all-diamond ring disc device. Firstly, a Lasered kapton mask is placed over the rear of the electrode, leaving only the lasered back contact holes clear. A 10 nm layer of Ti is sputtered over the entire surface, followed by a 300 nm layer of Au. The mask is peeled back revealing the Ti/Au sputtered contacts; the electrode is now ready to be annealed.

Once annealed and cooled to room temperature, the all-diamond electrodes were tested using a multimeter to ensure electrical contact is achieved and the individual electrodes remain isolated. The electrodes are placed face down on gel pak inside a cylindrical Teflon mould. Individual cores of a multi core Cu wire (small enough to fit in the contact holes) are placed in the laser micromachined back contacting holes with the aid of a dissection microscope and micropositioners, and secured in place using conductive silver epoxy (Circuitworks, ITW Chemtronics). This is left to dry for 24 hours. The teflon mould is half-filled with a 2 part mixture of non-conductive epoxy (RX771C/NC, Robnor, UK), ensuring the silver epoxy is coated but the free ends of the wires are left uncovered, and left to dry for a further 24 hours. A ~0.5 cm section of insulation is stripped from both ends of insulated Cu wires,

these are soldered to the bare ends of those attached to the electrode ensuring no contact between electrodes. Finally, the mould is filled completely with non-conductive epoxy such that the soldered wire connections are completely covered, and left to dry for 24 hours. Once dry, the electrode is removed from the mould and the front surface is polished with alumina before testing.

## **5.4.2. Initial All-Diamond Ring Discs**

### **5.4.2.1. *Initial Results***

A series of ring disc electrodes of varying geometries were produced in a 10 mm × 10 mm insulating diamond substrate. In order to reduce production costs it is essential to fit as many electrodes on one substrate as possible; As a consequence the disc radius for each electrode was limited to ~500 µm and the total electrode radius (including ring and separation) to ~1200 µm, allowing the electrodes to be produced in 2 mm diameter columns, resulting in 25 electrodes per substrate. A scaled up diagram of the first substrate of electrode geometries is shown in **Figure 5.7**.

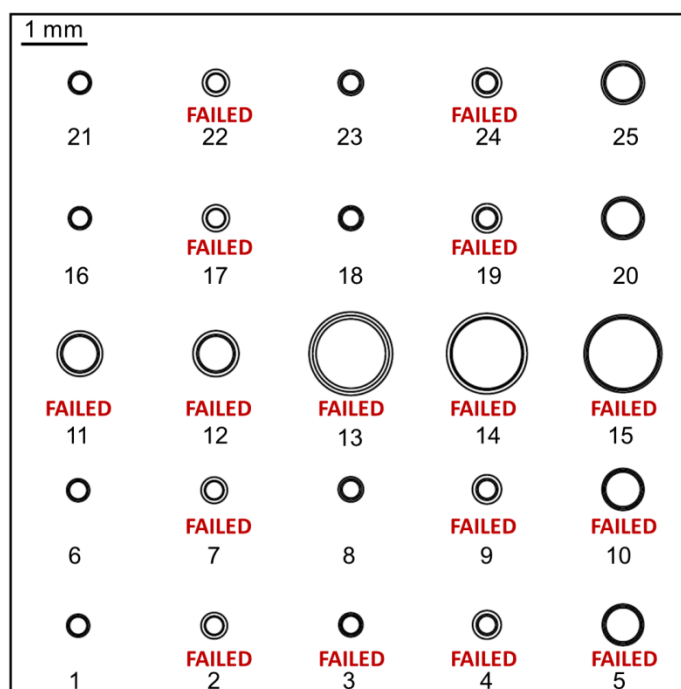


**Figure 5.7:** Scaled up diagram of the first substrate of all-diamond ring disc electrodes. Disc radii range from 125  $\mu\text{m}$  to 500  $\mu\text{m}$ , ring widths used were either 50  $\mu\text{m}$  or 100  $\mu\text{m}$ , and electrode separation was either 25  $\mu\text{m}$  or 50  $\mu\text{m}$  (sizes as programmed for lasering). Electrodes are numbered 1 to 25, “Failed” denotes electrodes with large defects present after growth. The black circles represent the locations of the outer circumference of the ring and disc electrodes for each device.

The label “Failed” is used to denote electrodes which were found to have large defects after overgrowth and polishing, as observed under optical microscope and FE-SEM. A series of typical secondary electron FE-SEM images to illustrate a “good”, “bad”, and “ok” device are presented in **Figure 5.8**, and details for the entire substrate can be found in **Table 5.1**. Very few of the ring electrodes on this substrate were good enough for electrochemical use, many exhibited large cracks, and some with pinholes between grain boundaries. In contrast the majority of disc electrodes were successful, with only 12% showing defects.



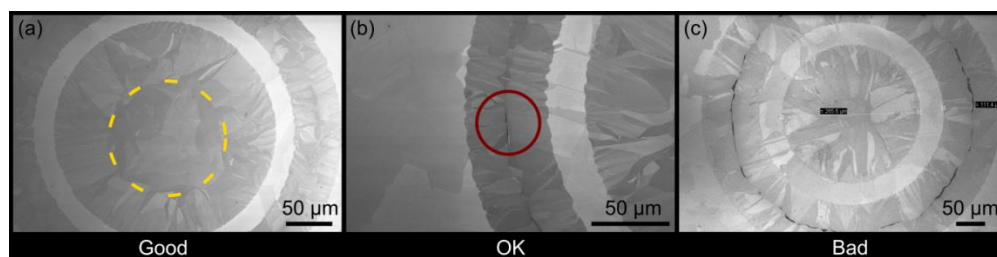


**Figure 5.8:** SEM images showing representative examples of (a) a “Good”, successful all-diamond ring disc electrode, yellow dashes highlight the “halo” where sidewall and bottom growth meet, (b) an “OK” all-diamond ring disc electrode, which is successful but has some small defects (highlighted in red), and (c) a “Bad” all-diamond ring disc electrode, with dark cracks visible around the centre of the ring. Note, the darker areas in each image with clear grain structure are BDD and the paler areas are insulating diamond.

Discs 1, 3 and 4 were found to have several small pinholes (observed as small black spots) present at the grain boundaries around what is described as the “halo”; this is the interface between grains where lateral sidewall growth meets vertical growth from the base of the machined trench,<sup>23</sup> highlighted in yellow in **Figure 5.8(a)**. These pinholes may be the result of insufficient knitting of grains at the interface, causing weak points which are prone to breakage during polishing.

It is likely that growth proceeds according to the diagram in **Figure 5.9(a)** where in a wide, shallow trench the lateral and vertical growth occur at a similar rate, the halo observed may be formed where areas of more significantly different growth rates meet. The orientation of the grains in **Figure 5.8(a)** lend weight to this argument as those outside the halo appear to be aligned perpendicular to the interface, extending from the edge towards the centre as if propagating from the side, whereas those in the centre are more rounded indicating vertical growth. Where the interface has had sufficient time to develop during growth it is thought that the grains knit together more

strongly and are less likely to be damaged, causing pinholes, during polishing. Indeed further investigations of cross sectioned substrates have shown a lack of subsurface voids in similarly processed all-diamond disc electrodes, indicating good intergrowth of grains.<sup>23</sup>

**Table 5.1:** Table of all-diamond ring disc devices in generation 1, measurements taken from FE-SEM images and analysis of successful electrode growth. Halo defines the region where diamond growing from the side wall meets diamond growing from the trench base.

Device #	Disc	Halo Size	Ring	Disc Radius (μm)	Separation (μm)	Ring Width (μm)
1	Ok	50/50	OK	130	16	54
2	Good	None	Bad	127.5	14.5	108
3	Ok	Thin	Bad	127.5	42.5	55
4	Ok	Thick	Bad	131	37	107
5	Good	Thin	Bad	252.5	42.5	55
6	Good	Thick	Good	129	21	53
7	Good	Thick	Bad	130.5	12.5	107
8	Good	Thin	OK	130.5	40.5	54
9	Good	Thin	Bad	255.5	44.5	111
10	Good	Thin	Bad	255.5	37.5	57
11	Good	Thick	Bad	256.5	38.5	105
12	Good	Thick	Bad	258	31	111
13	Good	Thin	Bad	511.5	32.5	106
14	Good	Thin	Bad	508.5	36.5	105
15	Good	Thin	Bad	514.5	25.5	60
16	Good	50/50	Good	128.5	16.5	55
17	Good	Thick	Bad	129.5	12.5	108
18	Good	Thin	OK	128.5	43.5	53
19	Good	Thick	Bad	132.5	32.5	110
20	Good	Thin	Ok	256.5	34.5	59
21	Good	50/50	Ok	129	16	55
22	Good	Thick	Bad	128.5	11.5	110
23	Good	Thin	OK	129.5	37.5	58
24	Good	Thick	Bad	132.5	30.5	112
25	Good	Thin	OK	258	30	62

It is notable in **Figure 5.8(b)** and **(c)** that the narrower ring electrodes are dominated entirely by lateral sidewall growth. Many of the ring electrodes

exhibit cracks which propagate around the centre (highlighted in red in **Figure 5.8(b)** and clearly evident in **Figure 5.8(c)**), where the lateral growth from each side of the trench wall meets.

In contrast to the disc electrodes, which were all grown in 50  $\mu\text{m}$  depth trenches, the rings were machined such that the trench width to depth was 1:1. The defects observed in the ring electrodes are likely to have occurred during overgrowth, due to poor intergrowth in these regions. From the evidence of dominant sidewall growth, and observations that only  $\sim 50\text{ }\mu\text{m}$  width (and therefore depth) rings were defect free, it is postulated that for deeper trenches a different growth mechanism occurs. It is likely that where the trench is deeper, diffusion of carbon to the base of the trench takes significantly longer, such that the sidewalls near the top grow at an increasingly higher rate, leading to decreased vertical growth, and in worse cases voids caused by shadowing as illustrated in **Figure 5.9(b)** and (c). It is clear that for future generations the machined trenches should be shallow ( $<50\text{ }\mu\text{m}$ ) regardless of ring width in order for successful growth.

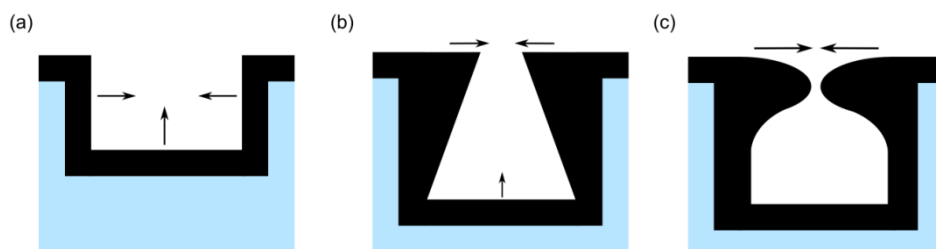


**Figure 5.9:** Schematics illustrating BDD overgrowth in (a) a shallow trench where lateral and vertical growth are similar, (b) a deep trench where lateral growth dominates and vertical growth is limited, and (c) a deep trench where lateral growth completely shadows the bottom of the trench, preventing vertical growth and leaving a void.

Interestingly, for all devices the interface between the insulating diamond and the BDD is defect free. In **Figure 5.8(b)** there is clear continuation of the different growth faces from the insulating diamond into the BDD, indicating homoepitaxial growth between the two. The difference in contrast is much more evident in the BDD regions due to non-uniform uptake of boron into different polycrystalline crystal facets.<sup>24</sup> This homoepitaxial growth leads to a strong interface between the electrode and insulator, and this lack of weak points makes the device less prone to corrosion and degradation over time. This is promising for pH generation studies where previously the insulating material adjacent to the electrode was found to erode, and eventually fail, under the influence of the extreme currents applied to the generator.

#### **5.4.2.2. Characterisation**

The electrodes were characterised using the protocol described in **Chapter 2**.<sup>25</sup> Micro-Raman spectroscopy (514.5 nm) data is presented in **Figure 5.10** and **Figure 5.11**, although measured for ring disc device number 1 (RD1) from **Figure 5.7** this data is representative of all electrodes in this generation and is used as a qualitative assessment of NDC content and boron concentration.<sup>26</sup> **Figure 5.10** presents data for an area of insulating diamond; the sharp peak at  $1332\text{ cm}^{-1}$  is characteristic of  $\text{sp}^3$  diamond carbon, indicating undoped polycrystalline diamond as expected. There is no evidence of the asymmetry (Fano resonance) usually present in a boron doped sample.<sup>7, 27, 28</sup> This suggests that this method of growth has successfully avoided the issue observed in a previous method, where overgrowth of insulating diamond into machined

BDD results in diffusion of boron into the insulating layer due to etching and redeposition of the boron<sup>29</sup> (unpublished work).

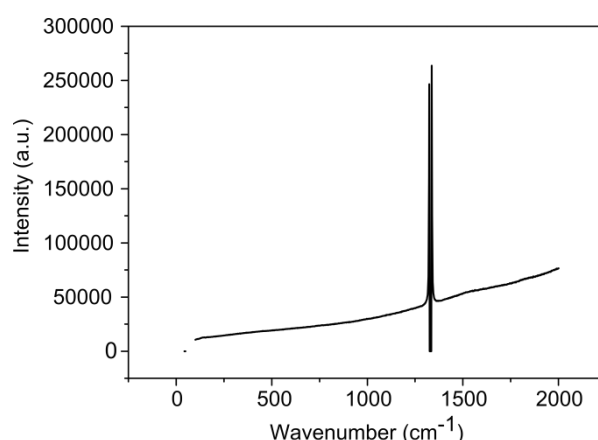


**Figure 5.10:** Representative example of raman data on an insulating diamond area of a generation 1 all-diamond ring disc electrode using a 514.5 nm laser and 50× magnification.

On the contrary, in **Figure 5.11**, where Raman data for the BDD ring, (a) and (b), and disc, (c) and (d), are shown the  $sp^3$  peak, although still clearly visible, is shifted slightly and decreased in intensity due to the high boron concentration.<sup>7</sup> The presence of a highly asymmetric Fano resonance, typically observed for boron dopant levels  $>10^{20}$  atoms  $cm^{-3}$  with higher asymmetry for increased boron content, reflects the high levels of boron present in the lattice and indicates the electrodes are highly doped. This is corroborated by the presence of peaks at  $\sim 500$  and  $1230$   $cm^{-1}$ , which although present to some extent in all four spectra are much larger in those of darker grains (b) and (d) suggesting higher boron uptake in these grains.<sup>7</sup> NDC is indicated in raman spectra by the presence of broad peaks between  $1400$  and  $1600$   $cm^{-1}$ ,<sup>30</sup> no evidence of these peaks is observed in the all-diamond ring disc spectra.

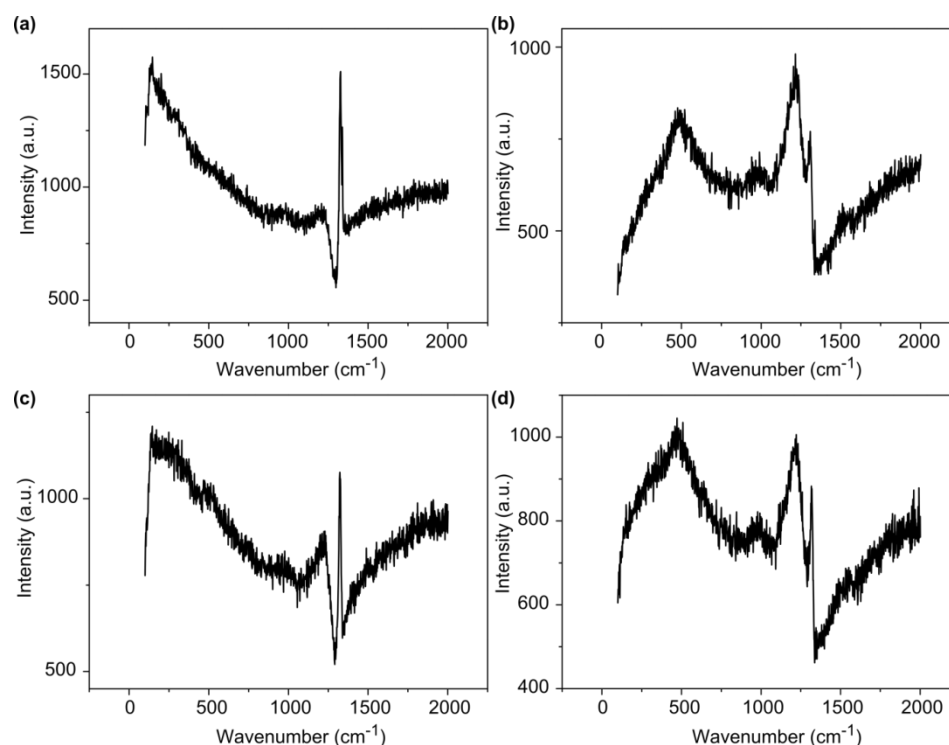


**Figure 5.11:** Representative examples of Raman data for a BDD ring and disc in a generation 1 all-diamond ring disc for (a) Ring, light grain. (b) Ring, dark grain. (c) Disc, light grain. (d) Disc, dark grain. This data was collected from RD1 using a 514.5 nm laser and 50× magnification.

Overall this data points towards successful production of high quality, highly doped BDD ring and disc electrodes insulated in a high quality B free diamond substrate. Several of the electrodes (RD1 and RD2o) were subsequently electrically contacted and assembled according to the method described in Section 5.4.1.

The most effective way to ascertain NDC surface presence in the BDD regions is to record solvent windows in electrolyte solutions.<sup>31, 32</sup> This provides sensitive analysis of the entire surface area, whereas in Raman spectroscopy typically only individual spots are interrogated. Raman mapping, where the surface is analysed on a point by point basis is an extremely lengthy procedure. Both the capacitive contribution, and surface oxidation/reduction

processes affected by NDC presence can be observed in the background CV response. NDC is oxidized to an appreciable extent just prior to the onset of water oxidation, allowing NDC containing electrodes to be easily identified by the corresponding current peaks.<sup>1, 25</sup> It has been commented previously that BDD does not catalyse oxygen reduction, however in the presence of NDC oxygen is sluggishly reduced, evidenced by a clear cathodic current at negative potentials.

**Figure 5.12** presents a solvent window collected for the RD20 disc, the CV is largely free of background processes with very little evidence of NDC oxidation in the anodic window for both this electrode and for RD1, suggesting there is no, or very small amounts of NDC present in these devices. Double layer capacitance measurements were also used to assess the quality of the electrodes; high capacitance values are indicative of low quality BDD,<sup>25, 33</sup> and also poor sealing between insulating and doped diamond.<sup>23</sup>

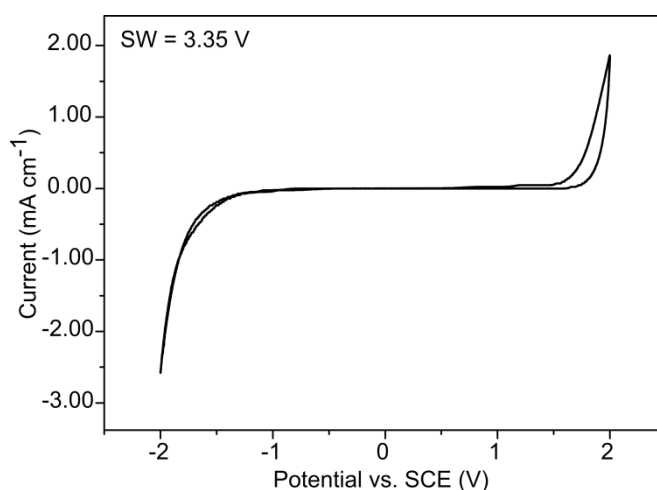


**Figure 5.12:** Example solvent window, recorded in 0.1 M  $\text{KNO}_3$  at  $100 \text{ mVs}^{-1}$  for the disc of RD20, diameter  $500 \mu\text{m}$ .

Note, high capacitance can also be caused by poorly contacted electrodes. Capacitance data for both electrodes are presented in **Table 5.2**. A well contacted high quality BDD electrode is expected to have capacitance values  $<7 \mu\text{F cm}^{-2}$ , values between this and  $10 \mu\text{F cm}^{-2}$  are generally acceptable for use, whereas for poor quality electrodes the capacitance increases well beyond this in some cases. In both cases the recorded capacitance values are high ( $>10 \mu\text{F cm}^{-2}$ ), with significantly larger values for the ring electrodes; this indicates either unsuccessful contacts or poor quality material. However, the Raman and solvent window data suggest the latter is unlikely and the electrical contact was thus investigated further (see below).



**Table 5.2:** Summary of electrochemical characterisation data for all-diamond devices RD1 and RD20.

Electrode #	Ring					Disc				
	Capacitance ( $\mu\text{F cm}^{-2}$ )	Solvent Window (V)	$\Delta E_p$ (mV)	Theoretical $I_p$ ( $\mu\text{A}$ )	Experimental $I_p$ ( $\mu\text{A}$ )	Capacitance ( $\mu\text{F cm}^{-2}$ )	Solvent Window (V)	$\Delta E_p$ (mV)	Theoretical $I_p$ ( $\mu\text{A}$ )	Experimental $I_p$ ( $\mu\text{A}$ )
<b>1</b>	13.73	1.56	71	0.16	0.2	26	2.6	85	0.14	0.15
<b>20</b>	10.34	3.35	63	0.3	0.4	19.35	3.25	76	0.52	0.52

To further assess the electrochemical characteristics of these devices CVs were performed at a range of scan rates (10 – 500 mV s<sup>-1</sup>) in solutions containing the redox mediator Ru(NH<sub>3</sub>)<sub>6</sub><sup>3+</sup>, and supporting electrolyte. The theoretical separation between anodic and cathodic current peaks ( $\Delta E_p$ ), in accordance with the Nernst equation, is 59 mV for a 1 electron process. For the all-diamond devices investigated here  $\Delta E_p$  was found to be somewhat larger generally ranging between 70 – 85 mV, although a value of 63 mV was recorded for the disc of RD20. The theoretical  $I_p$  values (at 100 mV s<sup>-1</sup>) for the reduction of Ru(NH<sub>3</sub>)<sub>6</sub><sup>3+</sup> are also presented in **Table 5.2**, alongside the experimentally measured values, assuming a diffusion-controlled process. Generally, the experimental values although slightly higher, fit to theory within 0.1  $\mu$ A. It is thought that these results add further evidence for electrical connection issues; wires were connected to these electrodes using silver paint. Replacing with conductive silver epoxy has since been found to improve the electrochemical response by lowering capacitance and decreasing  $\Delta E_p$ , as shown in section 5.4.4.

#### **5.4.3. Effect of Geometries on pH Generation (simulation)**

Having developed a method for all-diamond ring disc fabrication on early generations of test electrodes, and learned lessons on producing successful high quality devices, the applications of the electrodes were considered. The ability to tailor all-diamond devices to an application is one of the attractions of this new fabrication method, however in order to do this one must consider the desirable properties required for the said application. In this case the ring

disc electrodes were designed for use in sensitive electrochemical detection of aqueous trace metal species with simultaneous *in situ* pH control. There are several desirable characteristics for this device. Firstly, the ring must produce a sufficiently large and uniform pH change (to  $\Delta\text{pH} \geq 2$ ) over a relatively short time period (preferably  $< 60$  s). The generated pH must remain stable over a long enough period of time to conduct electrochemical measurements at the disc ( $> 300$  s). In order to design the optimum ring disc electrode according to these parameters it is essential to understand how the geometry of the electrode might affect its behaviour. Finite element simulations were employed to design an electrode of ideal geometry; the disc radius, ring width and electrode separation were investigated in order to establish how these parameters might affect the pH generation profile across the disc electrode.

#### **5.4.3.1. Disc Radius**

The effect of disc radius on the average pH reached across its surface for fixed pH generation parameters was investigated via finite element modelling. The current density applied to the ring electrode was kept constant at  $6.63 \text{ mA cm}^{-2}$  for all simulations, and the ring width and electrode separation maintained at  $100 \text{ }\mu\text{m}$  and  $50 \text{ }\mu\text{m}$  respectively. The simulation was run for a range of disc radii between  $125 \text{ }\mu\text{m}$  and  $1500 \text{ }\mu\text{m}$ , average pH vs. time plots are presented in

#### **Figure 5.13.**

There is a clear relationship between disc radius and the pH generation profile achieved in the model. As the disc radius decreases the plateau pH reached

decreases in a linear fashion. Also of note, an increase in the speed at which pH plateau is achieved is observed. For larger disc radii, protons generated at the surrounding ring must diffuse further before the entire disc is affected, this has the effect of both slowing the initial pH decrease and increasing the average pH reached across the disc; the pH effect of a given concentration of generated protons is spread over a larger area. This suggests that in order for maximal pH change a small disc is desirable; however the size dimension may be limited by factors such as fabrication, and application of the disc electrode.

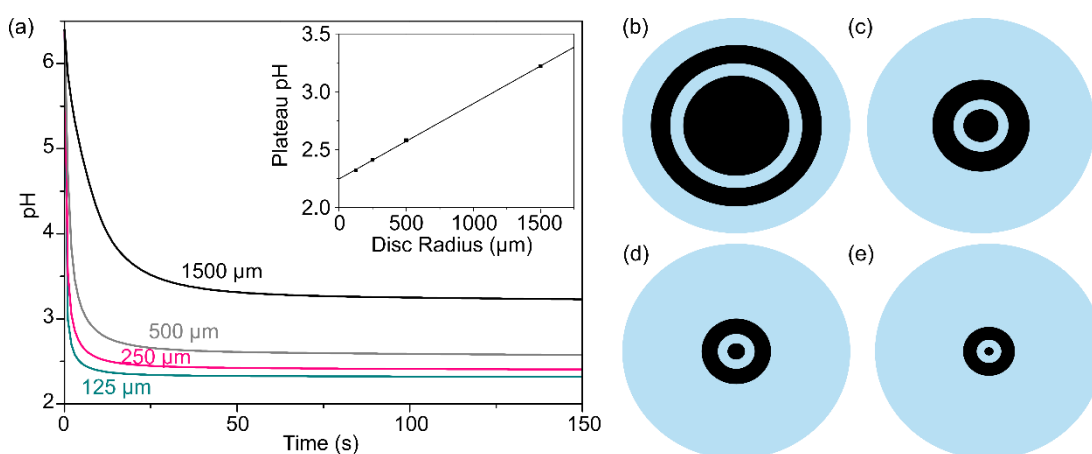


*Figure 5.13: (a) Simulated average pH vs. time profiles at the disc electrode for a range of ring discs with different disc radii, 1500  $\mu\text{m}$ , 500  $\mu\text{m}$ , 250  $\mu\text{m}$ , 125  $\mu\text{m}$ . Ring width was maintained at 100  $\mu\text{m}$ , and electrode separation at 50  $\mu\text{m}$  for all simulations. The current density applied to the ring (generator) was 6.63  $\text{mA cm}^{-2}$ . Inset shows plot of disc radius vs. plateau pH,  $R^2 = 0.9996$ . Schematics illustrating electrodes with disc radius (b) 1500  $\mu\text{m}$ , (c) 500  $\mu\text{m}$ , (d) 250  $\mu\text{m}$ , and (e) 125  $\mu\text{m}$ , not to scale.*

#### **5.4.3.2. Ring Width**

Further to this, the effect of generator (ring) width on generated pH was investigated. Once more, for comparability the current density applied to the ring electrode was kept at 6.63  $\text{mA cm}^{-2}$  for all simulations. The disc radius and electrode separation were maintained at 500  $\mu\text{m}$  and 50  $\mu\text{m}$  respectively.

Simulations were run for a range of ring widths between 50  $\mu\text{m}$  and 260  $\mu\text{m}$ , average pH vs. time plots are presented in

**Figure 5.14.** Once more, an effect is observed in relation to the changing electrode size. As the ring width is increased the average pH across the disc electrode decreases; however, the time taken to reach a plateau also increases.

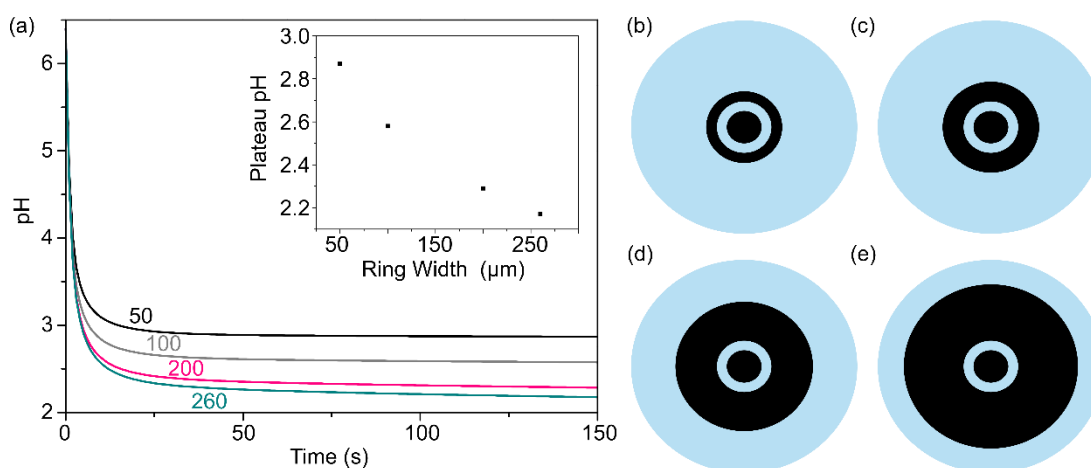


**Figure 5.14:** (a) Simulated average pH vs. time profiles across the disc electrode for a range of ring disc electrodes with different ring width, 50  $\mu\text{m}$ , 100  $\mu\text{m}$ , 200  $\mu\text{m}$ , 260  $\mu\text{m}$ . Disc radius was maintained at 500  $\mu\text{m}$ , and electrode separation at 50  $\mu\text{m}$  for all simulations. The current density applied to the ring (generator) was 6.63  $\text{mA cm}^{-2}$ . Schematics illustrating electrodes with ring width (b) 1500  $\mu\text{m}$ , (c) 500  $\mu\text{m}$ , (d) 250  $\mu\text{m}$ , and (e) 125  $\mu\text{m}$ , not to scale.

For a larger ring electrode the protons generated at the inner edge are equivalent to those on a smaller ring, since the inner diameter, disc, and separation are identical. However, those protons generated at the centre of the ring electrode have further to diffuse before reaching the detector, leading to a slower equilibration of the concentration gradient and therefore a longer time to reach plateau. The increased size of the generator results in a larger quantity of generated protons which, given the disc geometry remains

unchanged, results in a higher detected proton concentration and therefore lower plateau pH.

#### 5.4.3.3. *Electrode Separation*

Finally, the effect of generator/detector separation on pH change at the disc was investigated. The current density applied to the ring electrode was maintained at  $6.63 \text{ mA cm}^{-2}$ , the disc radius and ring width were maintained at  $500 \text{ }\mu\text{m}$  and  $100 \text{ }\mu\text{m}$  respectively. Simulations were run for a range of electrode separations between  $25 \text{ }\mu\text{m}$  and  $200 \text{ }\mu\text{m}$ , average pH vs. time plots are presented in **Figure 5.15**. The difference observed for electrodes with different separations is noticeably smaller than that for the other two parameters tested; however there is still some effect evident. A decreased distance between generator and detector results in a lower average pH reached across the disc, and in a faster time. Again, this is due to the decreased diffusion distance resulting in higher flux and therefore allowing more rapid pH change.

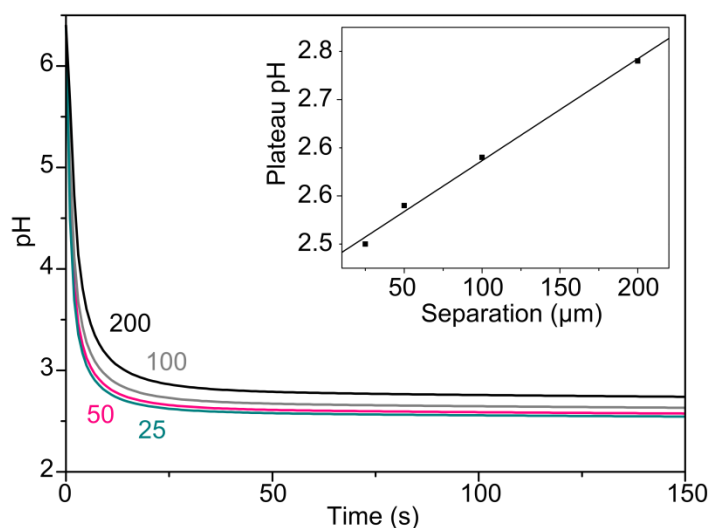


**Figure 5.15:** Simulated average pH vs. time profiles across the disc electrode for a range of ring disc electrodes with different electrode separations,  $25 \text{ }\mu\text{m}$ ,  $50 \text{ }\mu\text{m}$ ,  $100 \text{ }\mu\text{m}$ ,  $200 \text{ }\mu\text{m}$ . Disc radius was maintained at  $500 \text{ }\mu\text{m}$ , and ring width at  $100 \text{ }\mu\text{m}$  for all simulations. The

*current density applied to the ring (generator) was  $6.63 \text{ mA cm}^{-2}$ . Inset shows a plot of electrode separation vs. plateau pH.*

Initially, it is of interest to achieve the lowest possible plateau pH in the fastest time; these results indicate that this could be achieved by decreasing the radius of the detector and the separation between electrodes. The ring width should be large enough to take advantage of the decreased pH achieved, whilst not so large that the time taken to reach this pH is excessive. However, although this is the ideal case there are limits to what is possible with current fabrication methods. One such limit is the ability to create a back contacted ring disc with disc radii less than  $125 \text{ }\mu\text{m}$  using laser micromachining strategies. The minimum size achievable is controlled by the resolution of the laser vs. depth of the trench. To some extent, the smaller the hole the shallower the growth will be and eventually successful overgrowth will be affected by this as the polishing step is only accurate to  $\sim 5 \text{ }\mu\text{m}$ .

Laser resolution/spot size will also have an effect on the minimum achievable separation; some amount of material will inevitably be weakened around the edge of the lasered area, and will eventually lose structural integrity when too narrow. Another consideration is the ability to produce reliably isolated back contact holes; if the electrodes are smaller than the minimum size possible for contacting holes then isolation will be impossible. Similarly the smaller and closer together the contact holes are, the harder it is to manually attach isolated wires. Other fabrication methods, such as a combination of micro-sized BDD pillars with insulating diamond and BDD overgrowth, may solve

some of these issues, allowing smaller electrode sizes and separations to be achieved, and will be discussed in **Chapter 8**.

Another consideration is the future uses of these devices; it may for example be of interest to have a third electrode available, perhaps in order to simultaneously measure the generated pH whilst performing analyses (e.g. trace metals). At this stage it was unnecessary to account for this in the model, as a second ring electrode placed outside the original generator will have no effect on the geometry, and therefore generated pH, across the other two electrodes.

As a result dual-ring disc electrodes were developed, wherein the outer electrode separation is equivalent to the inner electrode separation (100  $\mu\text{m}$ ), and the inner and outer ring widths are identical (100  $\mu\text{m}$ ), and the disc radius is 250  $\mu\text{m}$ . These parameters are chosen to ensure swift diffusion of protons across the surface, and a large resulting pH change, whilst maintaining ease of individual back-contacting.

#### **5.4.4. Electrochemical Characterisation of dual-ring discs**

The dual-ring disc electrodes described above were fabricated as before, and characterised electrochemically. Due to the larger area of the outer ring electrode two electrical contacts (using sputtered Ti/Au and conductive silver epoxy with Cu wires) were made to opposing sides of the ring; this served the dual purpose of allowing the contacts to be easily compared to better judge whether any issues were due to material quality or poor contacts. Also, when



connected together this provides the ability to avoid any resistive effects through the electrode which may occur when only contacted at one extreme.

The electrochemical characteristics of the dual-ring disc electrode are summarised in **Table 5.3**. In general all three electrodes exhibit excellent electrochemistry; with solvent windows  $>3$  V, Capacitance  $<7 \mu\text{F cm}^{-1}$ , and  $\Delta E_p \leq 70$  mV. This indicates high quality BDD electrodes with minimal NDC content and good ohmic contacts. It is interesting to note that the capacitance for the inner ring electrode is very low small ( $2.5 \mu\text{F cm}^{-1}$ ), which may indicate lower doped material. However, this has been observed in other devices in the same generation, which have been analysed using Secondary Ion Mass Spectrometry (SIMS) and found this to be consistently not the case. Other growth processes such as power, growth rate, reactor ageing and thermal management may contribute to lower capacitance in the material, as might processing methods such as laser micromachining. As the material appears to be highly doped and the other electrochemistry is good the low capacitance is not an issue; generally low capacitance is a desirable property in any case. It is possible that were the material dominated by lower doped grains, this could affect the capacitance, note that the boron doping levels will all still be above the metallic threshold.

**Table 5.3:** Summary of electrochemical characteristics of dual-ring disc electrode 1.

Disc	Capacitance ( $\mu\text{F cm}^{-1}$ )	5.58
	Solvent Window (V)	3.1
	$\Delta E_p$	64
Inner Ring	Capacitance ( $\mu\text{F cm}^{-1}$ )	2.5
	Solvent Window (V)	3.46
	$\Delta E_p$	70
Outer Ring	Capacitance ( $\mu\text{F cm}^{-1}$ )	5.38
	Solvent Window (V)	3.24
	$\Delta E_p$	70

As mentioned previously, the outer ring electrode was connected to two separate wires at opposite sides of the ring. Electrochemical characterisation was performed at each wire separately and was found to be very consistent, as observed in the capacitance CV in **Figure 5.16**, where the response for both wires is indicated, one in black and one in grey. Measurements at both connections produced almost identical responses, which is a good indication that not only is the material quality very good but also that ohmic contact to the wires was consistent and successfully achieved.

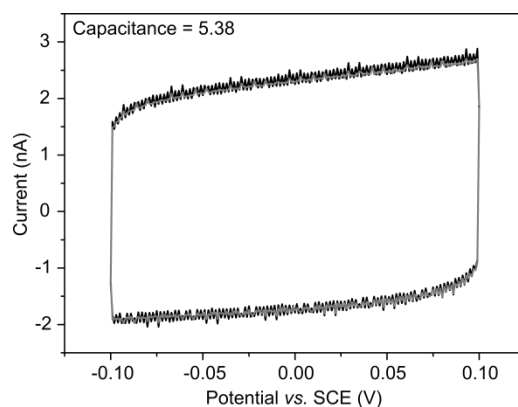


**Figure 5.16:** Example data for an all-diamond dual-ring disc electrode, showing capacitance (double layer) for the outer ring; this electrode had two connections, capacitance data for each is shown (grey & black) to be almost identical.

## 5.5. Conclusions

In this chapter a novel method for the preparation of co-planar, individually addressable all-diamond ring disc devices is described. Initial problems such as poor electrical contacts, presence of NDC, and inhibited ring growth due to laser trench depth were overcome in later generations of devices; in general shallower laser trenches produced successful ring electrodes, and silver epoxy was found to improve contacts in comparison to silver paint. FEM simulations led to an understanding of the effects of ring disc geometry on pH generation profile. It was found that small disc radii, narrow electrode separation and wide rings provide larger pH changes on shorter timescales; a desirably quality for simultaneous pH control and analyte detection. In order to maintain ease of fabrication of electrode geometries a compromise in electrode sizes was necessary and the final design incorporated a 250  $\mu\text{m}$  disc radius, 100  $\mu\text{m}$  separation and 100  $\mu\text{m}$  ring. A further ring with identical width and separation was added to the outside for potential future experiments. Electrochemical characterization of an all-diamond dual-ring disc electrode indicated

successful production of high quality, NDC free BDD electrodes, with ohmic contacts suitable for use in future *in situ* pH control experiments.

## 5.6. References

1. J. V. Macpherson, *Phys. Chem. Chem. Phys.*, 2015, **17**, 2935-2949.
2. T. L. Read, E. Bitziou, M. B. Joseph and J. V. Macpherson, *Anal. Chem.*, 2014, **86**, 367-371.
3. T. L. Read, M. B. Joseph and J. V. Macpherson, *Chem. Commun.*, 2016, DOI: 10.1039/C5CC09326K.
4. G. M. Swain and R. Ramesham, *Anal. Chem.*, 1993, **65**, 345-351.
5. M. Panizza and G. Cerisola, *Electrochim. Acta*, 2005, **51**, 191-199.
6. H. B. Martin, A. Argoitia, U. Landau, A. B. Anderson and J. C. Angus, *J. Electrochem. Soc.*, 1996, **143**, L133-L136.
7. L. A. Hutton, J. G. Iacobini, E. Bitziou, R. B. Channon, M. E. Newton and J. V. Macpherson, *Anal. Chem.*, 2013, **85**, 7230-7240.
8. M. C. Granger, M. Witek, J. Xu, J. Wang, M. Hupert, A. Hanks, M. D. Koppang, J. E. Butler, G. Lucazeau, M. Mermoux, J. W. Strojek and G. M. Swain, *Anal. Chem.*, 2000, **72**, 3793-3804.
9. T. Yano, D. A. Tryk, K. Hashimoto and A. Fujishima, *J. Electrochem. Soc.*, 1998, **145**, 1870-1876.
10. L. A. Hutton, M. E. Newton, P. R. Unwin and J. V. Macpherson, *Anal. Chem.*, 2009, **81**, 1023-1032.
11. T. N. Rao, I. Yagi, T. Miwa, D. A. Tryk and A. Fujishima, *Anal. Chem.*, 1999, **71**, 2506.
12. A. Salimi, M. E. Hyde, C. E. Banks and R. G. Compton, *Analyst*, 2004, **129**, 9-14.
13. C. Prado, G.-U. Flechsig, P. Grundler, J. S. Foord, F. Marken and R. G. Compton, *Analyst*, 2002, **127**, 329-332.
14. Ľ. Švorc, J. Sochr, M. Rievaj, P. Tomčík and D. Bustin, *Bioelectrochemistry*, 2012, **88**, 36-41.
15. D. Wakerley, A. G. Guell, L. A. Hutton, T. S. Miller, A. J. Bard and J. V. Macpherson, *Chem. Commun.*, 2013, **49**, 5657-5659.
16. B. V. Sarada, T. N. Rao, D. A. Tryk and A. Fujishima, *J. Electrochem. Soc.*, 1999, **146**, 1469-1471.
17. A. L. Colley, C. G. Williams, U. D'Haenens Johansson, M. E. Newton, P. R. Unwin, N. R. Wilson and J. V. Macpherson, *Anal. Chem.*, 2006, **78**, 2539-2548.
18. M. Pagels, C. E. Hall, N. S. Lawrence, A. Meredith, T. G. J. Jones, H. P. Godfried, C. S. J. Pickles, J. Wilman, C. E. Banks, R. G. Compton and L. Jiang, *Anal. Chem.*, 2005, **77**, 3705.
19. L. A. Hutton, M. Vidotti, J. G. Iacobini, C. Kelly, M. E. Newton, P. R. Unwin and J. V. Macpherson, *Anal. Chem.*, 2011, **83**, 5804-5808.
20. J. Hees, R. Hoffmann, N. Yang and C. E. Nebel, *Chemistry – A European Journal*, 2013, **19**, 11287-11292.
21. C. S. Johnson and J. T. Hupp, *J. Electroanal. Chem.*, 1993, **345**, 351-362.
22. E. Bitziou, M. B. Joseph, T. L. Read, N. Palmer, T. Mollart, M. E. Newton and J. V. Macpherson, *Anal. Chem.*, 2014, **86**, 10834-10840.
23. M. B. Joseph, E. Bitziou, T. L. Read, L. Meng, N. L. Palmer, T. P. Mollart, M. E. Newton and J. V. Macpherson, *Anal. Chem.*, 2014, **86**, 5238-5244.

24. H. V. Patten, K. E. Meadows, L. A. Hutton, J. G. Iacobini, D. Battistel, K. McKelvey, A. W. Colburn, M. E. Newton, J. V. Macpherson and P. R. Unwin, *Angew. Chem. Int. Edit.*, 2012, **51**, 7002-7006.
25. T. L. Read and J. V. Macpherson, *J. Vis. Exp.*, 2016, **107**, e53484.
26. A. Fujishima, *Diamond Electrochemistry*, BKC, 2005.
27. K. Ushizawa, K. Watanabe, T. Ando, I. Sakaguchi, M. Nishitani-Gamo, Y. Sato and H. Kanda, *Diamond Relat. Mater.*, 1998, **7**, 1719-1722.
28. F. Pruvost and A. Deneuve, *Diamond Relat. Mater.*, 2001, **10**, 531-535.
29. L. Hutton and H. V. Patten, unpublished work.
30. S. Praver and R. J. Nemanich, *Philos. Trans. Royal Soc. London. A*, 2004, **362**, 2537-2565.
31. L. A. Hutton, J. G. Iacobini, E. Bitziou, R. B. Channon, M. E. Newton and J. V. Macpherson, *Anal. Chem.*, 2013, **85**, 7230.
32. J. A. Bennett, J. Wang, Y. Show and G. M. Swain, *J. Electrochem. Soc.*, 2004, **151**, E306-E313.
33. R. N. Adams, *Electrochemistry at solid electrodes*, N. Dekker, 1969.

## 6 Investigating pH generation in buffered systems

### 6.1. Outline

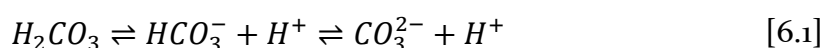
One of the key themes throughout this work is the application of *in situ* pH control to metal detection; however, in order for this technique to offer true *in situ* capabilities it is essential that the effect of buffer presence on pH generation is understood. This is because in some systems *e.g.* seawater, river water, blood, and intracellular fluid naturally occurring buffers are present. In this chapter confocal microscopy is used to visualize the profile of pH generation across the electrode in solutions of varying buffer concentrations. This work aims to establish to what extent local pH generation is hindered in buffered solutions and whether it is possible to overcome this effect in buffers at real-world concentrations.

### 6.2. Introduction

Natural waters generally range between pH 6-9 (Freshwater pH = 6-9, Seawater pH = 7.5 - 8.5)<sup>1</sup>; where the majority of natural aquatic life has adapted to survive in these limited conditions. Under these conditions metal ions are likely to be ligand complexed and not present in the labile state. In the environment, there are many factors that have the potential to affect solution pH, from the type of bedrock<sup>2</sup> to pollution.<sup>3</sup> In an unbuffered system this could cause large scale pH changes and affect the environmental homeostasis, creating long lasting damage to ecosystems. However, the

presence of natural buffering systems in the environment maintains the balance in the majority of cases.

According to Le Chatelier's Principle,<sup>4</sup> pH dependent equilibria between species in solution are able to resist pH change via adjustment of the equilibrium position, effectively providing a reservoir of H<sup>+</sup> ions.<sup>5</sup> Generally buffering in natural water systems (*e.g.* river and ocean) is dominated by the carbonate equilibria<sup>2</sup> described in Equation [6.1], although other systems such as borate,<sup>6</sup> sulphate<sup>7</sup> and phosphate<sup>2b</sup> also contribute to the overall buffering capacity. When small changes in pH occur the buffer system is able to counter this change via an adjustment of the equilibrium in the opposing direction.



Buffers are not present solely in environmental waters, but are also important for many other biological systems, including intracellular fluid, and the cardiovascular system.<sup>8</sup> The aforementioned carbonate system is also of vital importance in blood, maintaining a pH of 7.4 and avoiding acidosis or alkalosis (conditions caused by the decrease or increase of blood pH).<sup>9</sup>

Concentrations of hydrogen carbonate (HCO<sub>3</sub><sup>-</sup>) and carbonic acid (H<sub>2</sub>CO<sub>3</sub>) in the human body are controlled by two separate mechanisms.<sup>10</sup> As a result of metabolic processes which in general release H<sup>+</sup>, a much larger concentration of hydrogen carbonate than carbonic acid is present (20:1).<sup>11</sup> Carbonic acid concentration is controlled via respiration; an increase or decrease in breathing rate can swiftly alter carbonic acid concentration in response to

metabolic changes (*e.g.* brought about by exercise). Excess hydrogen carbonate is released as waste via the kidneys, a comparatively slow process.

Another important biological buffer is the phosphate system, widely used in laboratory experiments, it is also vital in regulating the pH of intracellular fluid and preventing cell death.<sup>12</sup> Phosphate buffer consists of hydrogen phosphate ( $\text{HPO}_4^{2-}$ ) and dihydrogen phosphate ( $\text{H}_2\text{PO}_4^-$ ) ions in the equilibrium described in equation [6.2].



The efficiency of a buffer in resisting pH change, the “buffering capacity”, can be expressed as the amount of strong acid or base required to change 1 L of solution by one pH unit (Equation 6.3).<sup>13</sup> The higher the buffering capacity,  $\beta$ , of a buffer, the more effective it will be at resisting pH change.

$$\beta = \frac{\Delta B}{\Delta pH} \quad [6.3]$$

Where  $\Delta B$  is the gram equivalent of strong acid or base to change the pH of 1 L buffer solution, and  $\Delta pH$  is the pH change. Buffering capacity in environmental and biological media is dependent on both the ratio of salt to acid or base, and on the total concentration of buffer present.<sup>14</sup> This varies significantly depending on the nature of the environment. Seawater, for example, has a higher buffer concentration than freshwater (approximately 1.5 mM compared to 0.9 mM);<sup>2a</sup> even this varies depending on whether it is surface water (open system) or deep ocean water (closed system). The



relationship between buffer concentration and buffering capacity is described by the Van Slyke equation, equation 6.4.

$$\beta = 2.3C \frac{K_a[H_3O^+]}{(K_a + [H_3O^+])^2} \quad [6.4]$$

Where  $C$  is the total buffer concentration, equivalent to the molar concentration sum of acid and salt, and  $K_a$  is the acid dissociation constant.<sup>13</sup>

For *in situ* pH adjustment, as discussed in Chapter 1, buffering equilibria present in the system make it harder to adjust the solution pH (if required) for analysis. *Ex situ* adjustment is possible by removing samples from the environment and adjusting the pH through additions of concentrated acid or alkali.<sup>15</sup> However, adding chemicals directly to the water system for *in situ* analysis is not realistic for several reasons, including notably dilution effects and possible harmful effects to the environment.

One common approach to making the measurement under pH conditions which differ from that of the bulk buffer solution is the use of membrane based sensors such as the Clark cell type electrode system.<sup>16</sup> Here the solution behind the membrane, where the sensor sits, is typically at a different pH to that in the external solution. However, membrane systems can have drawbacks which include slow response times, and being prone to clogging, a frequent problem with Clark cell electrodes.<sup>16b</sup>

For direct contact solution sensors in hydroponic nutrient tanks, **Figure 6.1(a)**, it has been shown that in solution volumes of finite size (up to 100 m<sup>3</sup>) it is possible to overcome the buffering capacity of a carbonate system

electrochemically via the electrolytic decomposition of water.<sup>17</sup> The use of thin layer sample chambers allows a similar control over buffering species, as demonstrated in the use of a selective electrochemical ion pump, illustrated in **Figure 6.1(b)**. Here  $H^+$  are released into the sample through a polarized ion selective membrane containing a high concentration of ionophore, any base present in the thin layer of sample is neutralized and the subsequent pH change is measured at an opposing pH responsive detection membrane; measured at zero current vs. a reference.<sup>18</sup> Pt UMEs (5  $\mu m$  to 35 nm radii) have also been used in conjunction with fluorescence spectroscopy to both adjust the local pH and visualize the resulting pH change. Here the UME is used to electrochemically generate  $H^+$  and  $OH^-$  in buffered solutions, with the pH change monitored using pH sensitive fluorophores, as illustrated in **Figure 6.1(c)**.<sup>19</sup> This allowed three-dimensional mapping of the generated pH profiles in solution achieving a maximum change of four pH units for all buffer concentrations tested (1.25 - 10 mM), at a distance of 50  $\mu m$  in the z direction from the UME tip.

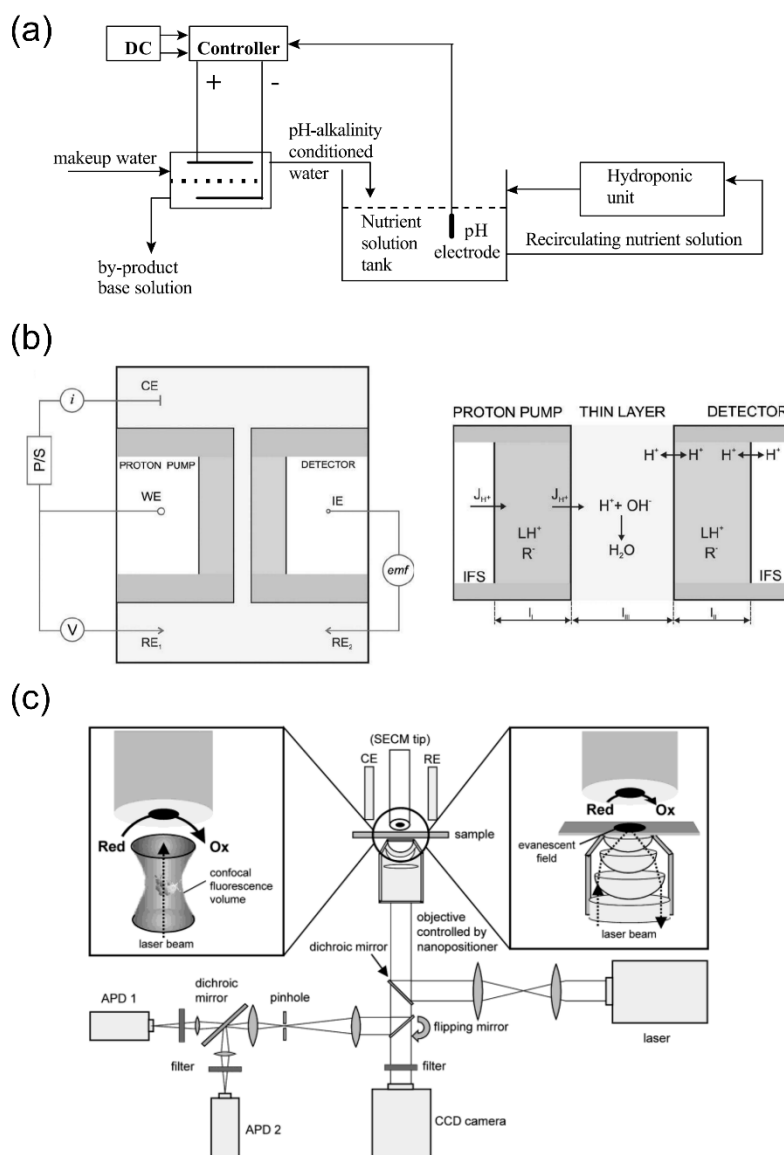


**Figure 6.1:** Schematics illustrating literature examples of pH control. (a) Via electrochemical decomposition of water in hydroponic nutrient tanks,<sup>17</sup> (b) thin layer cell with proton pump and proton selective detector membrane,<sup>18</sup> and (c) experimental setup of the combined SECM-SMFS system, where the SECM tip is used to induce a pH change.<sup>19</sup>

BDD electrodes for localised pH generation and control have been demonstrated in chapters 3 and 4 of this thesis, but if *in situ* electrochemical pH control is to be of use in biological media, and environmental waters, it is of interest to investigate its viability in buffered conditions. As discussed above, one technique which enables the visualization of pH changes is

confocal laser scanning microscopy (CLSM), in combination with pH sensitive fluorophores.<sup>19-20</sup> Confocal Microscopy has been used to investigate pH sensitive species for applications from targeted drug delivery where fluorescent molecules are released and detected via CLSM under given pH conditions,<sup>21</sup> to investigations of electrode and surface reactions where pH is influenced by electrochemical processes at the electrode.<sup>20b</sup>

This chapter aims to investigate the effect of buffered solutions on electrochemical control of local pH at BDD electrodes, using CLSM and the pH sensitive fluorophore, fluorescein, in order to assess the viability of this technique for *in situ* use in environmental and biological systems.

## **6.3. Experimental**

### **6.3.1. Solutions**

Borate buffer solutions were prepared from a pH 8.5 stock solution of 0.05 M sodium tetraborate decahydrate, and 0.1 M HCl. Supporting electrolyte (0.1 M KNO<sub>3</sub>) was added to all experimental solutions. A 100  $\mu$ M fluorescein stock solution was prepared using fluorescein sodium salt. Milli-Q water (resistance 18.2 M $\Omega$  at 25°C) was used in the preparation of all solutions. Fluorescein solutions were stored in foil-wrapped vials and only used under yellow light in order to avoid photobleaching.

### **6.3.2. Confocal Laser Scanning Microscopy**

CLSM (Leica TCS SP5X Supercontinuum laser scanning confocal microscope, mounted on a Leica DMI6000 CS inverted microscope) was used to image the pH generation profile at the electrode surface in solutions at a series of buffer

concentrations (0, 0.1, 1, 10 mM) in order to cover the common range found in natural waters, river and sea (0.9 mM to 1.5 mM).<sup>2a</sup> Borate buffer was chosen as although it does not play a large part in environmental systems, contributing only 5% to total alkalinity in seawater,<sup>22</sup> it buffers across an appropriate pH range (pH 8.2-10.1)<sup>23</sup> for maximum fluorescence intensity from fluorescein ( $pK_a = 6.43$ ).<sup>24</sup> An Ar laser with an excitation wavelength of 488 nm was used with a 480-570 nm detector window, and a 10 × / 0.3 HC PL Fluotar dry lens. For these experiments, an all diamond dual ring-disc electrode, illustrated in **Figure 6.2**, was used (disc radius 250  $\mu\text{m}$ , separations = 100  $\mu\text{m}$  and ring widths = 100  $\mu\text{m}$ ) as characterised in Chapter 5, section 5.4.4. However, in this case only the inner ring was utilized.

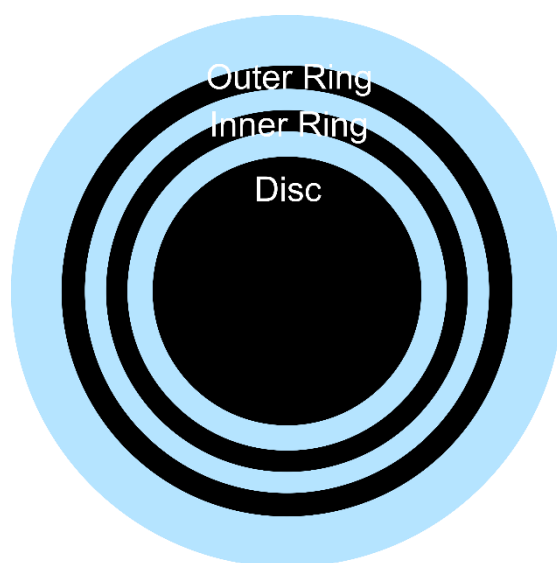


**Figure 6.2:** Illustration of an all diamond dual-ring disc electrode (disc radius 250  $\mu\text{m}$ , separations = 100  $\mu\text{m}$  and ring widths = 100  $\mu\text{m}$ ), where black represents BDD and blue represents insulating diamond. Only the Inner ring was used for the experiments described in this chapter.

Before use, a glass capillary (2 mm outer diameter) was secured perpendicular to the rear of the device using non-conductive epoxy, this was used to secure the electrode to the micropositioner (PI instrument, XYZ translation) on the

microscope stage. The initial pH of each experimental solution was measured using a commercial glass pH probe (Mettler Toledo) to ensure  $\text{pH} \geq 7$  for maximum fluorescence intensity, calculated from calibration experiments where fluorescence intensity was found to plateau below pH 5 and above pH 7;<sup>25</sup> it was necessary to adjust the pH of the unbuffered solution using 0.1 M KOH prior to experiments.

The electrode was secured to the stage, and adjusted in the  $x$ ,  $y$ , and  $z$  directions until optical focus was achieved, ensuring that due to the size of the device in epoxy it was sufficiently far from the base of the solution to avoid hindering mass transport. The inner ring (WE) of the electrode was connected to an external galvanostat (Keithley Source Meter) vs. a Pt gauze counter electrode, which was placed in the solution as far from the working electrode as possible, **Figure 6.3** illustrates this experimental arrangement. The current applied to the generator (ring) electrode was maintained at  $16.7 \mu\text{A}$  ( $6.6 \text{ mA cm}^{-2}$ ) for all experiments. Two types of CLSM image were recorded,  $xt$  and  $xyt$ ; scans of  $xyt$  were recorded for 10s with 68 ms frames (frame rate = 14.7 frames per second).  $xt$  scans were recorded for a line scan,  $\sim 20 \mu\text{m}$  from the electrode surface for 8192 lines, line averaged over 8 lines to improve the signal to noise ratio and normalised at the maximum intensity, pH generation commenced after  $\sim 25 \text{ s}$ .

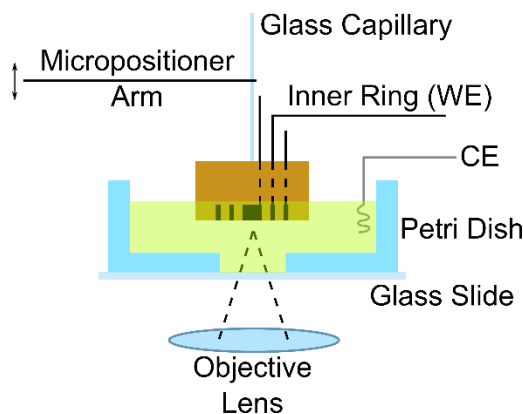
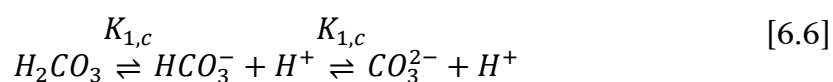
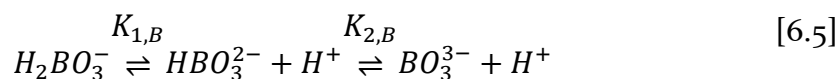


**Figure 6.3:** Illustration of the experimental electrode arrangement used for the imaging of proton generation via CLSM.

### 6.3.3. FEM Simulation of Borate Buffer

The model used to simulate pH generation at a ring disc electrode in **Chapter 3** was adapted to include borate buffer in aqueous solution, using the borate equilibrium described in Equation 6.5. Briefly, a radially symmetrical domain was defined; The radial boundary of the defined water cylinder at  $x=0$  is subdivided to describe a ring disc electrode of disc radius  $250\ \mu\text{m}$ , electrode separation  $100\ \mu\text{m}$ , and ring width  $100\ \mu\text{m}$ , where the remaining boundary is insulating material. A diffusional flux of protons is applied to the ring electrode according to Fick's Laws, as previously described.

Also taken into account were the borate, and carbonate equilibria described in Equations 6.5 and 6.6, due to dissolved  $\text{CO}_2$ , and the water equilibrium described in Equation 6.7. To begin, parameters were defined according to the experimental input conditions of the system; these are described in **Table 6.1**.



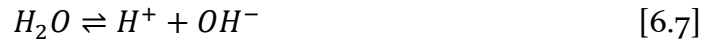


**Table 6.1:** Initial conditions of the system defined as parameters according to experimental inputs.

Parameter	Value
Initial pH	8.88 or 8.67
Total Borate (mM)	0.1, 1, or 10
Total Carbonate (mM)	1

From these, a set of equilibria were defined providing a description of the initial conditions of the system, assuming the system starts at equilibrium. The resulting parameters added to the model are presented in **Table 6.2**.

**Table 6.2:** Parameters added to the pH generation simulation to describe borate buffer and dissolved carbon dioxide equilibria. \*<sup>26</sup>

Parameter	Equations
Concentration $H_2BO_3$	$c_{H_2BO_3} = \frac{c_{tot}}{\left(1 + \frac{(10^{-pK_{1,B}})}{(10^{-pH})}\right) \left(1 + \frac{(10^{-pK_{2,B}})}{(10^{-pH})}\right)}$
Concentration $HBO_3$	$c_{HBO_3} = \frac{c_{tot}}{\left(1 + \frac{(10^{-pK_{2,B}})}{(10^{-pH})}\right) + \left(\frac{(10^{-pH})}{(10^{-pK_{1,B}})}\right)}$
Concentration $BO_3$	$c_{BO_3} = \frac{c_{tot}}{\left(1 + \frac{(10^{-pH})}{(10^{-pK_{2,B}})}\right) \left(1 + \frac{(10^{-pH})}{(10^{-pK_{1,B}})}\right)}$
Concentration $H^+$	$10^{-pH}$
$pK_{1,B} (H_2BO_3)$	$-\log_{10}(K_{1,B}) = 4$
$pK_{2,B} (HBO_3)^*$	$-\log_{10}(K_{2,B}) = 9.24$
Concentration $H_2CO_3$	$c_{H_2CO_3} = \frac{c_{tot,C}}{\left(1 + \frac{(10^{-pK_{1,c}})}{(10^{-pH})}\right) \left(1 + \frac{(10^{-pK_{2,c}})}{(10^{-pH})}\right)}$
Concentration $HCO_3$	$c_{HCO_3} = \frac{c_{tot,C}}{\left(1 + \frac{(10^{-pK_{2,c}})}{(10^{-pH})}\right) + \left(\frac{(10^{-pH})}{(10^{-pK_{1,c}})}\right)}$
Concentration $CO_3$	$c_{CO_3} = \frac{c_{tot,C}}{\left(1 + \frac{(10^{-pH})}{(10^{-pK_{2,c}})}\right) \left(1 + \frac{(10^{-pH})}{(10^{-pK_{1,c}})}\right)}$
$pK_{1,c} H_2CO_3$	$-\log_{10}(K_{1,c}) = 6.35$
$pK_{2,c} HCO_3$	$-\log_{10}(k_{2,c}) = 10.33$
Concentration $OH^-$	$\frac{1 \times 10^{-14}}{[H^+]}$



Using these parameters the buffering reactions which occur in solution were derived from the Henderson-Hasselbalch equation, which allows the calculation of the pH of a buffer solution from its  $pK_a$  and concentrations of the acid and its conjugate base.<sup>27</sup> After definition of the initial conditions, the parameters in **Table 6.2** were allowed to change according to the relationships described in **Table 6.3**. The concentration of  $H^+$  was changed according to an applied flux at one point in the system ( $6.63 \text{ mA cm}^{-2}$  applied to the ring electrode) and all other species were allowed to change accordingly. Note that the activity coefficient,  $\gamma$ , was applied to all terms containing  $H^+$ , where  $\gamma$  is defined by the Davies equation,<sup>28</sup> a modification of Debye-Huckel theory<sup>29</sup> and calculated using Equations 6.8 and 6.9, and  $I$  is the ionic strength, Equation 6.10.<sup>30</sup>

$$\gamma = 10^{-\log f} \quad [6.8]$$

$$\log f = -0.5 \left( \left( \frac{\sqrt{I}}{1 + \sqrt{I}} \right) - 0.2 \times I \right) \quad [6.9]$$

$$I = \frac{1}{2} \sum_{i=1}^n C_i z_i^2 \quad [6.10]$$

Where  $C$  is the molar concentration of the ions (M), and  $z$  is the charge on the ion.

**Table 6.3:** Reaction equations for chemical species present in solution. *FR* denotes the rate constant, here assumed to be  $1 \times 10^6$ , and  $K_w$  is equal to  $10^{-13.995}$  at  $25^\circ\text{C}$ .<sup>31</sup>

Reactions	Time Dependent Equations
(mol m <sup>-2</sup> s <sup>-1</sup> )	
H <sup>+</sup>	$FR \left( (K_{2,B} \times HBO_3 - H \times BO_3) + (K_{1,B} \times H_2BO_3 - H \times HBO_3) \right. \\ + (K_{1,c} \times H_2CO_3 - H \times HCO_3) + (K_{2,c} \times HCO_3 - H \times CO_3) \\ \left. + (K_w - H \times OH) \right)$
HBO <sub>3</sub> <sup>2-</sup>	$FR \left( (K_{1,B} \times H_2BO_3 - H \times HBO_3) - (K_{2,B} \times HBO_3 - H \times BO_3) \right)$
H <sub>2</sub> BO <sub>3</sub>	$-FR(K_{1,B} \times H_2BO_3 - H \times HBO_3)$
BO <sub>3</sub> <sup>3-</sup>	$FR(K_{2,B} \times HBO_3 - H \times BO_3)$
H <sub>2</sub> CO <sub>3</sub>	$-FR(K_{1,c} \times H_2CO_3 - H \times HCO_3)$
HCO <sub>3</sub> <sup>-</sup>	$FR \left( (K_{1,c} \times H_2CO_3 - H \times HCO_3) - (K_{2,c} \times HCO_3 - H \times CO_3) \right)$
CO <sub>3</sub> <sup>2-</sup>	$FR(K_{2,c} \times HCO_3 - H \times CO_3)$
OH <sup>-</sup>	$FR(K_w - H \times OH)$

## 6.4. Results and Discussion

### 6.4.1. Confocal fluorescence microscopy for investigation of pH generation in borate buffer.

Confocal fluorescence microscopy was used in conjunction with pH generation at the all diamond dual ring-disc electrode to investigate the effect of buffer on electrogenerated local pH. The pH sensitive fluorophore fluorescein was added (8 μM) to each experimental solution. Fluorescein (pK<sub>a</sub> = 6.43)<sup>24</sup> reaches maximum fluorescence intensity at pH 7 and 50% at pH 6.1,<sup>25</sup>

providing a convenient method for visualisation of proton generation at the electrode.

Initial experiments were conducted in 0.1 M  $\text{KNO}_3$  solutions, with no buffer present. The solution pH was adjusted prior to experiments using 0.1 M KOH, to ensure maximum fluorescence intensity. An initial pH = 8.34 was recorded. A current density of  $+6.63 \text{ mA cm}^{-2}$  ( $16.66 \text{ } \mu\text{A}$ ) was applied, equivalent to the maximum current found to produce no bubbles in **Chapter 3**, to the inner ring of the electrode and the fluorescence response was recorded. Successful pH generation under these conditions has been demonstrated in **Chapters 2 and 3**, achieving a pH change of up to four pH units, so should be an adequate test of the confocal experiment. Both *xt* and *xyt* scans were recorded, the resulting data is presented in **Figure 6.4**.

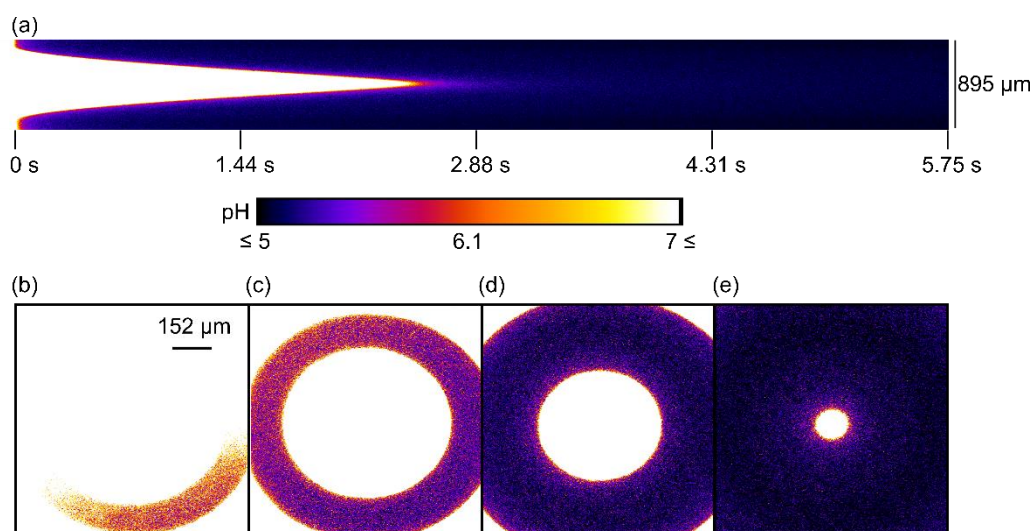


**Figure 6.4:** Confocal data for pH generation with  $16.66 \text{ } \mu\text{A}$  ( $+6.63 \text{ mA cm}^{-2}$ ) applied to the ring of an all diamond dual-ring disc electrode. Measured  $\sim 20 \text{ } \mu\text{m}$  below the electrode surface in solutions containing 0.1 M  $\text{KNO}_3$  and  $8 \text{ } \mu\text{M}$  Fluorescein, initial pH 8.34. (a) *xt* data, and *xyt* data for (b) 0.2 s, (c) 0.4 s, (d) 1.6 s, and (e) 6 s after beginning generation. False coloured for clarity.

The evolution of a proton generation profile in unbuffered background electrolyte solution in the presence of fluorescein is clearly visible via confocal fluorescence microscopy, as evidenced by the scans presented in **Figure 6.4**. A scan of  $x$  ( $\mu\text{m}$ ) vs.  $t$  (s) is presented in **Figure 6.4(a)**, where  $x$  is a slice across the centre of the ring disc centred approximately in the middle of the disc, illustrated in **Figure 6.5**, and the scan starts at the left ( $t=0$ ). Before applying a potential, the pH of the solution is such that fluorescein fluoresces with maximum intensity (shown white in **Figure 6.4**). After the ring electrode is switched on to generate  $\text{H}^+$  a drop in fluorescence intensity is observed initially at the edges of the scan (on the ring), indicating the pH dropping below pH 7; this decrease in pH can be observed, with time, expanding across the electrode before meeting in the centre, where it remains relatively constant due to the fact minimum intensity has been reached, i.e. the pH must be  $\leq 5$ .

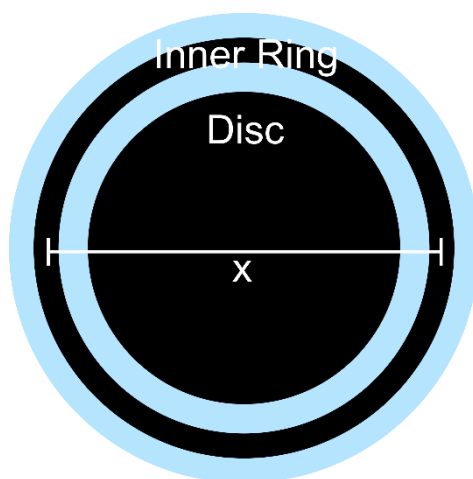


**Figure 6.5:** Schematic showing the location of the line scan ' $x$ ' in  $xt$  experiments.

Interestingly, a (very) slight asymmetry in the  $xt$  scan can be observed. This is more evident in **Figure 6.4(b)-(d)** where snapshots of the same process

imaged via *xyt* scans are presented at times of (b) 0.2 s, (c) 0.4 s, (d) 1.6 s, and (e) 6 s. This is most likely due to the electrode not sitting perfectly planar with respect to the microscope optics such that one side of the ring is slightly further away, and as a result the pH change, evidenced by the change in fluorescence intensity, is not symmetrical.

The same methodology was applied to the ring electrode but now in the presence of different concentration borate buffer solutions. The electrode was kept as close to the same position as for **Figure 6.4** as possible. The resulting *xt* data for Buffer solutions with concentrations of 0.1 mM, and 1 mM, and 10 mM, are presented in **Figure 6.6(a)** and **(b)** and **(c)** respectively.

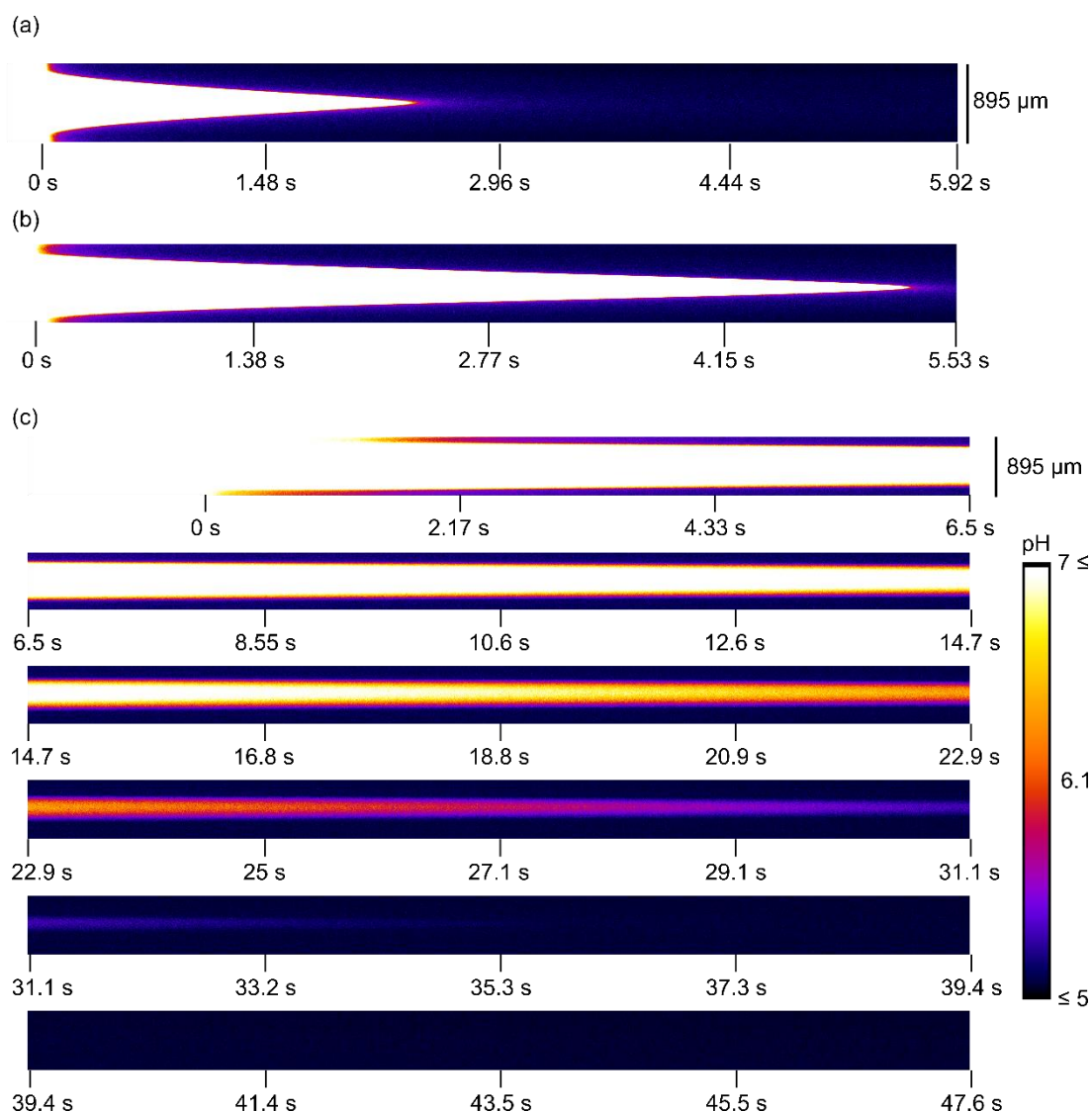


**Figure 6.6:** Confocal xt data for pH generation with  $16.66 \mu\text{A}$  ( $+6.63 \text{ mA cm}^{-2}$ ) applied to the ring of an all diamond dual-ring disc electrode. Measured  $\sim 20 \mu\text{m}$  below the electrode surface in solutions containing  $0.1 \text{ M KNO}_3$ ,  $8 \mu\text{M}$  Fluorescein, and (a)  $0.1 \text{ mM}$  borate buffer (pH 8.67), (b)  $1 \text{ mM}$  borate buffer (pH 8.88), and (c)  $10 \text{ mM}$  borate buffer (pH 8.88), time (s) increases from top to bottom through individual images, and left to right through the 6 images.

In all cases a decrease in fluorescence intensity with time is observed across the entire electrode. This demonstrates that electrochemical pH generation at a ring electrode is indeed possible in solutions containing up to  $10 \text{ mM}$  buffer; sufficient for many natural water systems. At very low concentrations of buffer ( $0.1 \text{ mM}$ ) the pH generation profile appears to behave very similarly to that in unbuffered solution. However, as buffer concentration increases both the

initial decrease of pH at the ring, and the diffusion of protons across the electrode can be seen to become inhibited, with a slowed solution response to pH change; indicating that buffer solutions  $\geq 1$  mM are capable of resisting the generated pH change to some extent. As buffer concentration increases, the progression of the pH generation profile across the electrode slows further.

In order for a significant pH change to be observed the buffering capacity must first be overcome. As discussed previously the buffering capacity is directly related to buffer concentration, as this increases, the buffering capacity also increases. The buffer equilibrium adjusts to consume any extra protons added to the system until the buffering capacity is overcome, inhibiting the diffusion of protons across the electrode.

#### **6.4.2. Simulation of pH generation in borate buffer**

From the data presented in **Figure 6.6** for 0.1, 1 and 10 mM buffer (pH 8.88) it is possible to look at the effectiveness of locally changing pH under different buffer conditions, in more detail. **Figure 6.7** illustrates schematically the measurement made. At a distance of  $\sim 20$   $\mu\text{m}$  from the electrode surface (in the z direction) at each point (one pixel) from the centre of the ring (0 mm) to the edge of the confocal image (in the x direction), the time taken for the pH to reach 6.1, which corresponds to a decrease in the fluorescent signal intensity by 50%,<sup>24-25</sup> is shown (Figure 6.8).

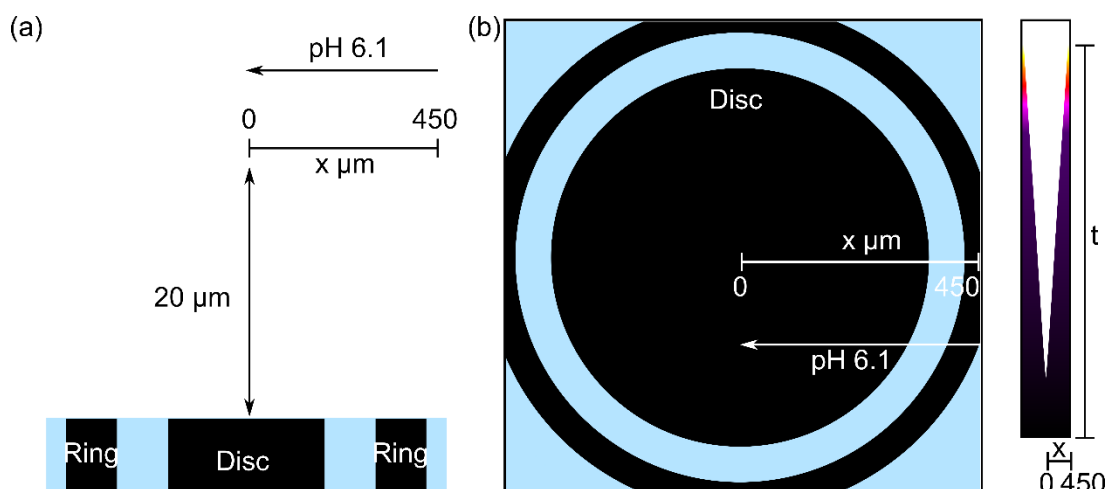


**Figure 6.7:** Schematic demonstrating the analysis of confocal  $xt$  data in relation to the electrode surface (a) Vertical cross section, and (b) Horizontal view of the electrode surface with example  $xt$  data for comparison.

**Figure 6.8(a)** thus illustrates the increased time taken for the proton front to advance across the electrode in more concentrated buffer solutions. For buffered solutions it takes  $\leq 5$  s (0.1 mM = 2.23 s, and 1 mM = 4.93 s) for the signal intensity to reach pH 6.1 at the centre of the disk (0 mm). For the 10 mM solution it takes 11.64 s. Note for unbuffered it takes 2.25 s, which is very similar to the 0.1 mM buffered solution, suggesting that in 0.1 mM buffer the proton generation profile is uninhibited. Note, the 10 mM confocal data in **Figure 6.8** were smoothed via an adjacent averaging method (where each data point is replaced with the mean value of it and its two adjacent values) in order to remove excess noise.



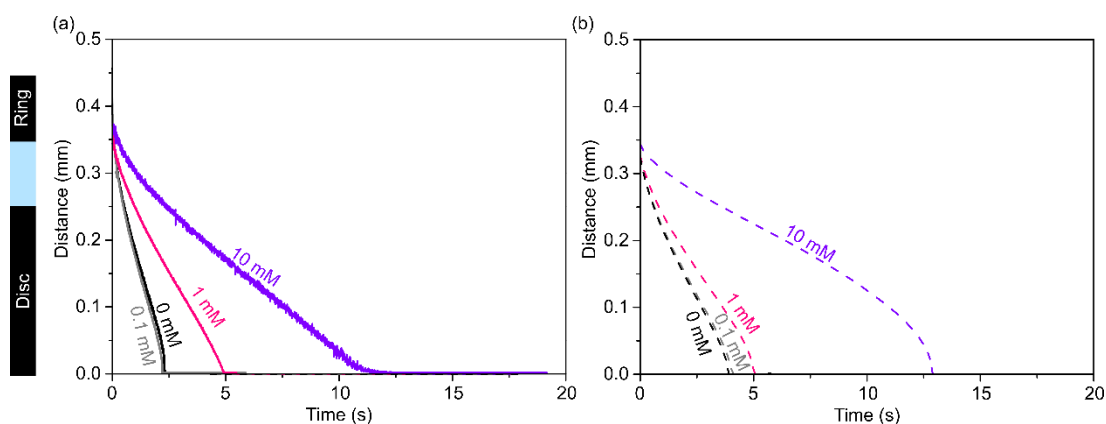


**Figure 6.8:** (a) Experimental and (b) simulated progression of the proton front at pH 6.1 (50% fluorescence intensity) across the disc electrode with time from confocal xt data for: 0 mM (black), 0.1 mM (grey), and 1 mM (pink), and 10 mM (purple) borate buffer solutions, in 0.1 M  $\text{KNO}_3$  and 8  $\mu\text{M}$  fluorescein. 10 mM data smoothed via adjacent averaging to remove noise.

To see if this behavior could be simulated, finite element methods, as described in **Chapter 3**, were employed. A line the length of the disc radius plus separation (350  $\mu\text{m}$ ) was taken 20  $\mu\text{m}$  above the simulated disc surface (approximately equivalent to the experimental data). The time progression of the proton front across this line, for pH = 6.1, was simulated (dashed lines), as shown in **Figure 6.8(b)**.

The trend in the advance of pH change (the proton front) with time is consistent between both experimental and simulation data; however, there are some clear differences. The model fits quite closely to the 1 mM experimental data, but overestimates the time taken to reach pH 6.1 at the centre of the electrode in both 0 mM and 0.1 mM solutions. Interestingly for 10 mM buffer the end point of the model is close to the experimental data, yet the curve of the experimental data is much flatter than that for either the model or the experimental data for all other concentrations. The consistency in the trend between experimental and simulated data is promising; however, the fact that

the data do not overlay indicates there are some issues with either the experiment or the model (or both). Evidently the system is much more complicated than initially thought; further work is necessary before the simulation can be applied to predicting the effect of other buffer systems on electrochemical pH generation.

Although the data shown provide clear evidence of the possibility of overcoming natural buffering effects via electrogenerated pH control at an all diamond ring disc electrode, more experiments are necessary to fully understand and optimise the system. In this initial set of experiments it should be noted that the initial solution pH values, although all  $>7$ , vary by approximately half a pH unit. Other than the unbuffered solution, experiments were conducted at the solution pH of the prepared buffer without adjustment; it is suggested that future experiments be conducted from a standard initial pH, adjusted using KOH and  $\text{HNO}_3$  during buffer preparation, in order to avoid causing any potential disparity.

## **6.5. Conclusion**

The work presented in this chapter clearly demonstrates the effect of buffered solutions on local electrochemical pH control. With the aid of a confocal fluorescence microscope, it is shown that overcoming the buffering capacity of borate buffer is possible up to a concentration of at least 10 mM (likely higher, although this has not yet been tested). As buffer concentration is increased, some inhibition of pH generation can be observed in the increased time taken for pH 6.1 (50% fluorescence intensity) to be reached across the entire

electrode. It is estimated that a pH change of at least three pH units is achieved in each buffer solution, from a start pH of 8.8 to below the 50% fluorescence intensity of fluorescein at pH 6.1; a promising indication for the use of BDD electrodes for *in situ* pH generation in real world systems. It is thought that pH control via this method should be possible in a large range of naturally buffered solutions, tailored to concentration by simply adjusting the driving current on the generator electrode, or the electrode geometry. Work towards developing a model for pH generation in borate buffer has been presented, which once complete could be used to predict the effect of other buffer systems.

## 6.6. References

1. (a) UK Environmental Standards and Conditions (Phase 1) 2008. [http://www.wfduk.org/sites/default/files/Media/Environmental%20standards/Environmental%20standards%20phase%201\\_Finalv2\\_010408.pdf](http://www.wfduk.org/sites/default/files/Media/Environmental%20standards/Environmental%20standards%20phase%201_Finalv2_010408.pdf); (b) Ocean acidification due to increasing atmospheric carbon dioxide 2005. [http://dgc.stanford.edu/labs/caldeiralab/Caldeira%20downloads/RoyalSociety\\_OceanAcidification.pdf](http://dgc.stanford.edu/labs/caldeiralab/Caldeira%20downloads/RoyalSociety_OceanAcidification.pdf) (accessed 26/02/13).
2. (a) Lower, S. K., Carbonate equilibria in natural waters. *Simon Fraser University* **1999**, 544; (b) Philip, N., Kinetic control of dissolved phosphate in natural rivers and estuaries: A primer on the phosphate buifer mechanism1. *Oceanography* **1988**, 33 (4 -Part 2).
3. (a) Tiwary, R. K., Environmental Impact of Coal Mining on Water Regime and Its Management. *Water Air Soil Poll.* **132** (1), 185-199; (b) Malmqvist, B.; Rundle, S., Threats to the running water ecosystems of the world. *Environ. Conserv.* **2002**, 29 (02), 134-153.
4. Bettelheim, F. A.; Brown, W. H.; Campbell, M. K.; Farrell, S. O.; Torres, O., *Introduction to General, Organic and Biochemistry*. Cengage Learning: 2015.
5. Hunt, A., *Dictionary of Chemistry*. Taylor & Francis: 2014.
6. Duarte, P.; Santana-Casiano, J. M., *Oceans and the Atmospheric Carbon Content*. Springer Netherlands: 2010.
7. Wolkersdorfer, C., *Water Management at Abandoned Flooded Underground Mines: Fundamentals, Tracer Tests, Modelling, Water Treatment*. Springer Berlin Heidelberg: 2008.
8. Hee, S. Q., *Biological Monitoring: An Introduction*. Wiley: 1993.

9. Bettelheim, F. A.; Brown, W. H.; Campbell, M. K.; Farrell, S. O.; Torres, O., *Introduction to Organic and Biochemistry*. Cengage Learning: 2012.
10. Atkins, P.; de Paula, J., *Elements of Physical Chemistry*. OUP Oxford: 2013.
11. Hinwood, B. G., *A Textbook of Science for the Health Professions*. Nelson Thornes: 1997.
12. Garrett, R. H.; Grisham, C. M., *Biochemistry*. Cengage Learning: 2012.
13. Raj, G., *Advanced Physical Chemistry*. Goel Publishing House: 1978.
14. Ghosh, T. K.; Jasti, B. R., *Theory and Practice of Contemporary Pharmaceutics*. Taylor & Francis: 2004.
15. (a) Alder, J. F.; Perry, S. K.; Brady, F. P., Application of energy-dispersive x-ray fluorescence to trace metal analysis of natural waters. *Environ. Sci. Technol.* **1975**, *9* (12), 1039-1042; (b) Batley, G. E.; Gardner, D., Sampling and storage of natural waters for trace metal analysis. *Water Res.* **1977**, *11* (9), 745-756.
16. (a) Lawrence, N. S.; Jiang, L.; Jones, T. G.; Compton, R. G., A thin-layer amperometric sensor for hydrogen sulfide: the use of microelectrodes to achieve a membrane-independent response for Clark-type sensors. *Anal. Chem.* **2003**, *75* (10), 2499-2503; (b) Clarke, D.; Fraher, P., Model-based validation of a DOx sensor. *Cont. Eng. Pract.* **1996**, *4* (9), 1313-1320; (c) *Hydrogen Sulfide Sensor User Manual*; Unisense: 2012.
17. Spinu, V.; Langhans, R.; Albright, L., Electrochemical pH control in hydroponic systems. *II Modelling Plant Growth, Environmental Control and Farm Management in Protected Cultivation 456* **1997**, 275-282.
18. Afshar, M. G.; Crespo, G. A.; Bakker, E., Thin-Layer Chemical Modulations by a Combined Selective Proton Pump and pH Probe for Direct Alkalinity Detection. *Angew. Chem. Int. Ed.* **2015**, *54* (28), 8110-8113.
19. Boldt, F.-M.; Heinze, J.; Diez, M.; Petersen, J.; Börsch, M., Real-Time pH Microscopy down to the Molecular Level by Combined Scanning Electrochemical Microscopy/Single-Molecule Fluorescence Spectroscopy. *Anal. Chem.* **2004**, *76* (13), 3473-3481.
20. (a) Leenheer, A. J.; Atwater, H. A., Imaging Water-Splitting Electrocatalysts with pH-Sensing Confocal Fluorescence Microscopy. *J. Electrochem. Soc.* **2012**, *159* (9), H752-H757; (b) Rudd, N. C.; Cannan, S.; Bitziou, E.; Ciani, I.; Whitworth, A. L.; Unwin, P. R., Fluorescence Confocal Laser Scanning Microscopy as a Probe of pH Gradients in Electrode Reactions and Surface Activity. *Anal. Chem.* **2005**, *77* (19), 6205-6217; (c) Cannan, S.; Douglas Macklam, I.; Unwin, P. R., Three-dimensional imaging of proton gradients at microelectrode surfaces using confocal laser scanning microscopy. *Electrochem. Commun.* **2002**, *4* (11), 886-892.
21. (a) Bae, Y.; Fukushima, S.; Harada, A.; Kataoka, K., Design of environment-sensitive supramolecular assemblies for intracellular drug delivery: Polymeric micelles that are responsive to intracellular pH change. *Angew. Chem. Int. Ed.* **2003**, *42* (38), 4640-4643; (b) Wang, Z.; Ma, G.; Zhang, J.; Yuan, Z.; Wang, L.; Bernards, M.; Chen, S., Surface protonation/deprotonation controlled instant affinity switch of nano drug vehicle (NDV) for pH triggered tumor cell targeting. *Biomaterials* **2015**, *62*, 116-127.
22. Zeebe, R. E.; Sanyal, A.; Ortiz, J. D.; Wolf-Gladrow, D. A., A theoretical study of the kinetics of the boric acid–borate equilibrium in seawater. *Marin. Chem.* **2001**, *73* (2), 113-124.
23. Stoll, V. S.; Blanchard, J. S., Chapter 6 Buffers: Principles and Practice<sup>1</sup>. In *Methods in Enzymology*, Richard, R. B.; Murray, P. D., Eds. Academic Press: 2009; Vol. Volume 463, pp 43-56.

24. Sjöback, R.; Nygren, J.; Kubista, M., Absorption and fluorescence properties of fluorescein. *Spectrochim. Acta. A. Mol. Biomol. Spec.* **1995**, 51 (6), L7-L21.
25. Al Botros, R. Analytical Approaches for Probing Surface Properties and Reactivity. University of Warwick, Coventry, 2015.
26. Berl, W., *Physical Methods in Chemical Analysis*. Elsevier Science: 2012.
27. Clugston, M.; Flemming, R., *Advanced Chemistry*. OUP Oxford: 2000.
28. Davies, C. W., *Ion association*. Butterworths: 1962.
29. Atkins, P.; de Paula, J., *Atkins' Physical Chemistry*. OUP Oxford: 2010.
30. Burgot, J. L., *Ionic Equilibria in Analytical Chemistry*. Springer New York: 2012.
31. Elliott, J. R.; Lira, C. T., *Introductory Chemical Engineering Thermodynamics*. Pearson Education: 2012.

## 7 Towards EC-XRF Analysis of Hg and Cd

### 7.1. Outline

Although electrochemical analysis offers many advantages for detection of trace metals in the environment, it also has some drawbacks. One of the major issues with electroanalysis by techniques such as ASV is the potential ambiguity of the analytical signal. In multi metal systems, or more concentrated solutions (*e.g.* 10  $\mu\text{M}$  Pb)<sup>1</sup>, for example, multiple stripping peaks are often observed.<sup>1, 2</sup> This is due to interactions between metal ions during deposition on a solid electrode surface, such as codeposition,<sup>2, 3</sup> suppression,<sup>4</sup> and enhancement,<sup>5</sup> metal depositing onto previously deposited metal, and the resulting variation in deposition morphologies.<sup>6</sup> Moreover, the thermodynamic  $E^\circ$  value for each metal represents the standard electrode potential for metal electrode - metal ion interactions, where metal ions are deposited on bare metal solid under equilibrium conditions,<sup>7, 8</sup> and thus can only ever be used as a guide for predicting which metals are present in solution. Commercial techniques such as the OVA (Modern Water, UK), and the Nano-Band™ Explorer (US) normally have to implement a pre-treatment procedure such as digestion, and acid or UV treatment, along with standards and other reagents.

It is thus not straightforward to identify the metal species responsible for a particular peak in a real environmental solution, where many metals are likely

to be present. A recent technique developed in the group aims to combat this issue, by combining the pre-concentration capabilities afforded by electrodeposition with the well characterised elemental identification of XRF.<sup>9</sup> In this chapter EC-XRF is applied to the analysis of two heavy metals of great interest, Hg and Cd, with the aim of developing an optimised analysis method and improving on current detection capabilities. Hg is particularly of interest as it is the only metal to form as a liquid at room temperature on the electrode surface.

## 7.2.Introduction

A running theme throughout this project has been the application of electroanalytical devices to heavy metal detection. In general, electrochemical sensors are well suited to this, exhibiting low (ng/L) detection limits<sup>10</sup> and relatively low costs in comparison with other commonly used techniques. Electrochemical sensors have received much attention for use in *in situ* analyses, offering easy portability due to their low operating power and small size. However, there are issues associated with electrochemical methods which can cause difficulty in achieving the high specificity desirable in an *in situ* sensor. In concentrated solutions, or mixed metal solutions, deposition morphology and inter-metallic interactions of electrodeposited species can result in multiple analytical signals.<sup>11-13</sup> Identifying the species responsible for each signal is not necessarily a straightforward task, although the  $E^0$  gives a guide as to the expected peak location for a metal it is only representative of metal ions on a bare electrode at standard conditions,<sup>7, 8</sup> and signal

identification is further complicated as the number of metal ions present in the system grows. In contrast, many spectroscopic and spectrometric techniques offer the ability to distinguish between elements with ease, due to the signals originating from well-defined transitions between energy levels e.g. electronic, vibrational, rotational.<sup>14</sup>

XRF is a popular method of chemical analysis across a wide range of scientific disciplines, from archaeology<sup>15</sup> to medicine.<sup>16</sup> XRF instruments range in size and portability, from handheld<sup>17</sup> to benchtop,<sup>18</sup> and beamline based synchrotron XRF;<sup>19</sup> making it an extremely versatile technique. As discussed in detail in **Chapter 1** XRF uses the emitted fluorescence of an irradiated sample to probe the elemental composition, allowing reliable identification and quantification even in complex mixed metal samples. However, despite its many advantages, with typical detection limits of ppm XRF does not provide sufficient sensitivity (down to ppb) for applications such as environmental trace metal analysis.<sup>20</sup>

Much work in the XRF field has been directed towards the improvement of XRF detection sensitivity, via methods such as total reflection (TR-) XRF<sup>21, 22</sup> and various pre-concentration techniques. Common pre-concentration methods investigated include solid phase extraction,<sup>23</sup> precipitation,<sup>24</sup> and controlled evaporation.<sup>25</sup> Electrodeposition has proved useful in tandem with other techniques including AAS,<sup>26</sup> and surface plasmon resonance spectroscopy.<sup>12</sup> However, as an XRF sample pre-concentration method, electrodeposition remains relatively unexplored. To date, niobium electrodes



as a sample carrier for Hg deposition and detection ( $\text{LOD} = 4 \text{ ng l}^{-1}$ ) in TR-XRF measurements have been demonstrated by Ritschel *et al*,<sup>27</sup> and a copper cathode was employed for mixed metal analysis by Wavelength Dispersive XRF by Zawisza *et al* ( $\text{LOD } 0.2 \mu\text{g} - 9 \mu\text{g}$ ).<sup>28</sup>

Recently we have reported the development of EC-XRF, where BDD electrodes in a RDE setup are used as a pre-concentration method for XRF analysis of trace metals.<sup>9</sup> In brief, metal ions are electrodeposited onto the BDD surface in the pre-concentration step. The BDD electrode is then removed and analysed using under vacuum conditions using a benchtop XRF system (Rigaku). EC-XRF has been demonstrated to provide ppb detection limits for both single and mixed metal solutions of Cu and Pb, with the XRF sensitivity enhanced by over 4 orders of magnitude (compared to traditional energy dispersive XRF combined with evaporative pre-concentration). Further development of the technique has since resulted in development of an *in situ* EC-XRF methodology enabling direct, potentially on-site, analysis of heavy metals.<sup>29</sup>

In this chapter, the application of EC-XRF to detection of key trace metals Cd, and Hg is described. The importance of electrochemical cell design is discussed, along with the effects of RDE rotation rate and electrodeposition potential. The choice of supporting electrolyte for each metal of interest is found to be of importance when used in conjunction with XRF analysis, and the analysis method for both metals is optimized towards the improvement of LODs over current XRF capabilities. Some of the challenges towards Hg analysis via EC-XRF are also explored.

## 7.3. Experimental

### 7.3.1. Solutions

Solutions were prepared in Milli-Q water ( $18.2 \text{ M}\Omega \text{ cm}$  at  $25^\circ\text{C}$ ).

### 7.3.2. Electrochemistry

Electrochemical deposition is conducted in a specially designed in-house built rotating disc arrangement, **Figure 7.1**, where the working electrode is a 25 mm diameter BDD disc with a sputtered Ti/Au contact ring on the reverse side (**Figure 7.2(a)**).

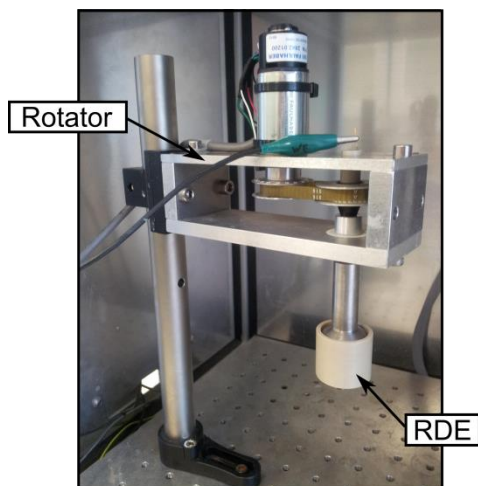


**Figure 7.1:** In house built rotating disc assembly.

The BDD electrode is placed face down in the rotator assembly, **Figure 7.2(b)**, which consists of a PEEK cap with a 14 mm diameter hole in the centre and a metal rotator rod; these components are screwed together sandwiching the BDD between them. Rubber o-rings are placed in front of the BDD, in purpose designed grooves in the cap, to ensure a water-tight seal. The BDD RDE is placed, inverted, into the deposition solution in a typical 3 electrode cell with

an SCE or Ag|AgCl reference electrode and a Pt counter as illustrated in **Figure 7.2(c)**.

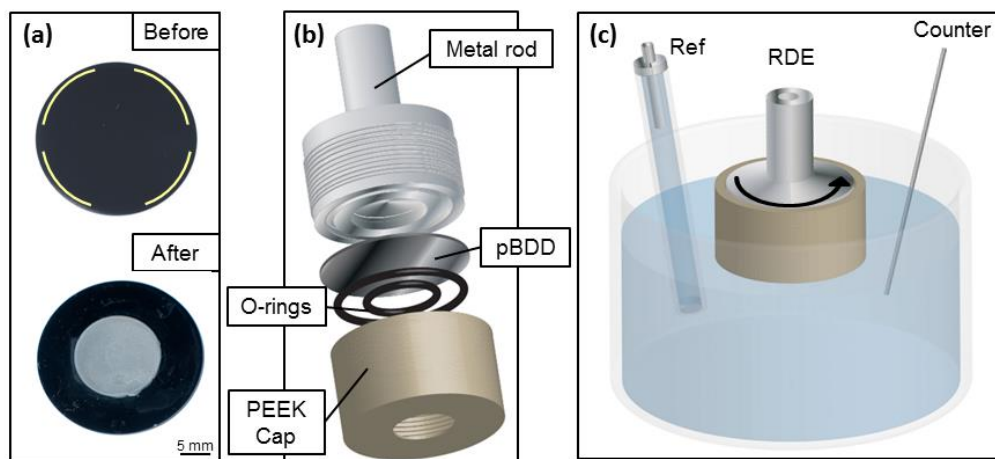


**Figure 7.2:** (a) Optical images of BDD electrode before and after electrochemical deposition of 10 ppm Pb. Gold on the ‘before’ image indicates the location of the Ti/Au contacts on the backside of the BDD disc. (b) Schematic showing the deconstructed rotating disc arrangement. (c) Schematic of the experimental set-up for electrochemical deposition using the BDD rotating disc electrode.

Electrochemistry was conducted in this arrangement using a potentiostat (CHI730A, CH Instruments Inc., TX). Before use, the BDD was cleaned using alumina polish (0.05  $\mu\text{m}$  Micropolish, Buehler, Germany) and a water saturated polishing pad (Microcloth, Buehler, Germany) then rinsed to remove any residual alumina. The RDE was connected to an in-house built rotator and rotated at speeds of up to 25 Hz in 50 ml of solution. In order to pre-concentrate metal ions on the BDD surface, the electrode was held at a constant potential for a defined time period. After deposition the BDD is carefully removed from the RDE assembly and rinsed gently with Milli-Q water to remove excess salt crystals, then air dried prior to XRF analysis.

### 7.3.3. XRF

XRF analyses were carried out using an energy dispersive XRF (ED-XRF) (NEX-CG, Rigaku, Japan). The X-ray tube had a Pd anode, and was run at 50 kV with a 1 mA current, secondary targets were used to ensure optimal excitation of each analytical species (Mo for Hg analysis and Cu for Cd analysis). After preparation by electrodeposition, the BDD electrode was placed face down (towards the X-ray source) in the XRF, and measured under moderate vacuum (12 Pa) for 300 s. The X-ray source provides an elliptical (largest ~1.2 cm diameter) area of investigation.

XRF only detection limits (i.e. without pre-concentration by electrodeposition) were measured using the Rigaku evaporative “UltraCarry” methodology, comprising a plastic sample ring covered with an X-ray transmissive hydrophobic film with an absorbent sample pad in the centre. On each plate 200 µL sample was pipetted onto the central pad and heated on a hot plate at <50 °C until the solution had completely evaporated (typically ~60 min). Subsequently, XRF analysis was carried out through the reverse side of the UltraCarry, as the sample film is thin enough that scattering of the X-rays is not an issue.

## 7.4. Results and Discussion

Prior to EC-XRF experiments the BDD rotating disc assembly was characterised electrochemically, to ensure that despite the large size of the electrode (1.4 cm diameter) it was sufficiently doped to perform efficient deposition. This procedure is described in detail in the paper by Hutton *et al.*<sup>9</sup>

however the rotator assembly used herein had been modified since reference 17, to avoid solution leaking round to the contacts due to flex in the Teflon cap providing a poor seal. Thus it was necessary to re-characterise the electrochemical behaviour.

Near reversible behaviour in 0.1 M Ru(NH<sub>3</sub>)<sub>6</sub><sup>3+</sup> was observed with this new adapted rotator design, producing  $\Delta E_p$  values of 66 mV at 0.1 Vs<sup>-1</sup> as shown in **Figure 7.3(a)**; the BDD electrodes used were of the same generation as in reference 17, and therefore equivalently doped. The steady state limiting value for reduction of Ru(NH<sub>3</sub>)<sub>6</sub><sup>3+</sup> at a scan rate of 0.1 Vs<sup>-1</sup> and rotation rate of 20 Hz, presented in **Figure 7.3(b)**, was close (0.92 mA) to that expected from the Levich equation, **Equation [7.1]**, (0.95 mA)<sup>30</sup>.

$$i_L = 0.62nFAD^{\frac{2}{3}}\omega^{\frac{1}{2}}\nu^{-\frac{1}{6}}C \quad [7.1]$$

Where  $i_L$  is the limiting current (A),  $n$  is the number of electrons transferred,  $F$  is Faraday's Constant (96485 C mol<sup>-1</sup>),  $A$  is electrode area (cm<sup>2</sup>),  $D$  is the diffusion coefficient (cm<sup>2</sup> s<sup>-1</sup>),  $\omega$  is rotation speed (rad s<sup>-1</sup>),  $\nu$  is the kinematic viscosity (cm<sup>2</sup> sec<sup>-1</sup>), and Concentration  $C$  is in (mol cm<sup>-3</sup>). The slight deviation could be due to the diamond sitting recessed (by ~2 mm) in the RDE set-up possibly leading to perturbations in the diffusional flux away from Levich. Deviations further from theory were observed as the rotation rate increased, so for consistency a rotation rate of 20 Hz was used throughout.

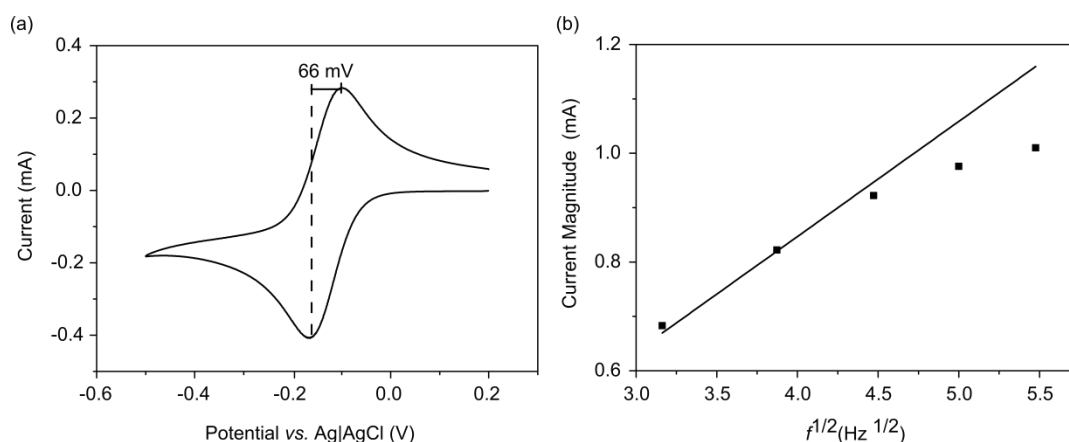


**Figure 7.3:** CVs in 1 mM  $\text{Ru}(\text{NH}_3)_6^{3+/2+}$  solution containing 0.1 M  $\text{KNO}_3$  supporting electrolyte, using new rotator electrode for (a) Stationary conditions (b) Comparison of limiting currents for rotation rates of 10, 15, 20, 25 and 30 Hz (▪) with theoretical values predicted using the Levich equation (black line). Adapted from Hutton et al (2014).<sup>9</sup>

In order to highlight the advantage of EC-XRF over the Rigaku patented evaporation (pre-concentration) method<sup>31</sup> (UltraCarry®) XRF peak intensity for 0.25 ppm solutions of Hg (in 0.1 M  $\text{KNO}_3$ ) were compared for XRF and EC-XRF. For XRF, solution was deposited on an UltraCarry substrate in droplet form and left to dry for 4000 s on a hot plate at  $<50^\circ\text{C}$ , and for EC-XRF electrodeposition was carried out at  $-1.75\text{ V}$  also for 4000 s. The substrates were subsequently analysed via XRF first, using the Mo secondary target to interrogate the highest intensity  $\text{Hg}_{\text{I}\alpha}$  line. The resulting XRF data is presented in **Figure 7.4**, where it is evident that although a clear signal is visible for the  $\text{Hg}_{\text{I}\alpha}$  line using EC-XRF (pink line), there is no discernible peak for the equivalent UltraCarry (purple line) experiment. In order to ensure Hg detection via XRF UltraCarry was possible, the experiment was repeated at concentrations of 0.5 ppm (purple dots) and 1 ppm (purple dashes). For increased concentrations the corresponding  $\text{Hg}_{\text{I}\alpha}$  peak became evident, although still small in comparison to that for EC-XRF, and increased

proportionally. The limit of quantitation (LOQ,  $10\sigma + \mu$ , where  $\sigma$  is standard deviation of the background noise, and  $\mu$  is the mean) and limit of detection (LOD,  $3\sigma + \mu$ ) were calculated from the mean measured noise intensity ( $0.0254 \text{ cps mA}^{-1}$ ), to be approximately 440 ppb and 76 ppb respectively. Note, in addition to the UltraCarry XRF peaks shown, a 100 ppm Hg sample was also used in these calculations.

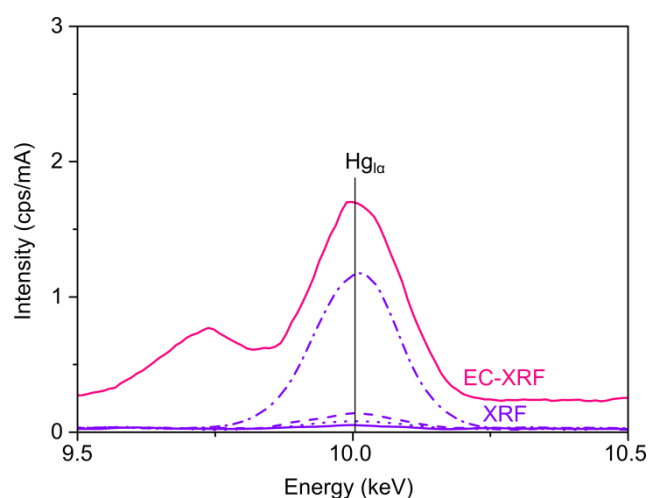


**Figure 7.4:** XRF data showing EC-XRF data for 0.25 ppm Hg (pink) vs. UltraCarry (purple) data for 0.25 ppm (solid), 0.5 ppm (dot), 1 ppm (dash), and 10 ppm (dot-dash). Experiments were conducted from solutions containing 0.1 M  $\text{KNO}_3$  supporting electrolyte, deposition time for EC-XRF and drying time for UltraCarry were kept constant at 4000 s. Electrodeposition for EC-XRF was conducted at -1.75 V.

A similar experiment was conducted for 1 ppm Cd solutions in 0.1 M  $\text{NaNO}_3$  supporting electrolyte. Note, a higher concentration of Cd was used for these experiments than for Hg as no signal was observed for the UltraCarry method at lower concentrations. However, in this case the  $\text{Cd}_{\text{I}\alpha}$  line was investigated using the Cu secondary target, as the Mo fluorescence energy is not sufficiently close to the  $\text{Cd}_{\text{k}\alpha}$  or  $\text{Cd}_{\text{l}\alpha}$  binding energies (23.17 keV and 3.13 keV respectively) for optimum fluorescence. The data presented in **Figure 7.5** clearly demonstrate that once again, the EC-XRF technique (pink) exhibits

superior sensitivity when compared with the UltraCarry method (purple) under equivalent conditions, where very little signal is apparent at concentrations below 1 ppm Cd (solid lines). Even at 100 ppm Cd (purple dot-dash), the UltraCarry XRF signal is ~30% of the EC-XRF signal for 1 ppm Cd. LOQ and LOD values for UltraCarry measurements of Cd were calculated to be 1.784 ppm (48.17  $\mu\text{M}$ ) and 0.587 ppm (15.85  $\mu\text{M}$ ) respectively from the mean measured noise intensity (0.062 cps/mA).

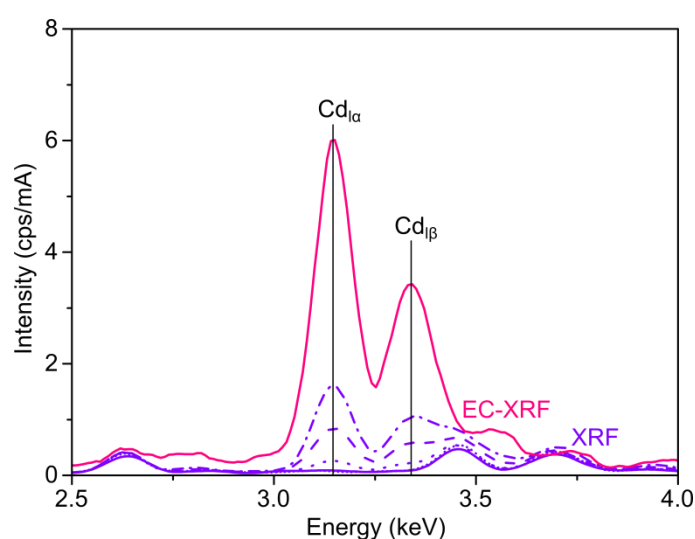


**Figure 7.5:** XRF data for Cd solutions in 0.1 M  $\text{NaNO}_3$ , showing EC-XRF data (Pink) vs. UltraCarry XRF (Purple) data at 1 ppm (solid), and additionally for UltraCarry XRF 100 ppm (dash-dot), 50 ppm (dashed), 10 ppm (dot), and 0.5 ppm (half-dot) concentrations of Cd.

## 7.4.1. Cd Detection

### 7.4.1.1. Choice of Supporting Electrolyte

One important consideration when analyzing Cd via XRF is the supporting electrolyte; for most experiments in this thesis  $\text{KNO}_3$  has been the supporting electrolyte of choice, however in the case of Cd analysis via XRF alone, K containing salts are not ideal. The  $\text{K}_{\text{K}\alpha}$  line appears at 3.31 keV, very close to the  $\text{Cd}_{\text{I}\beta}$  line at 3.13 keV; generally K-lines are more intense than L-lines. As the



supporting electrolyte is present in excess this leads to the  $\text{Cd}_{\text{L}\alpha}$  signal being obscured by  $\text{K}_{\text{K}\alpha}$ , as observed previously by Hutton *et al.*<sup>9</sup> However, as K is electrochemically inactive this interference does not present an issue for EC-XRF, a promising indication for environmental analyses where  $\text{K}^+$  is often present in relatively large quantities.<sup>32</sup> For Cd analysis via XRF and EC-XRF in order to keep the supporting electrolyte consistent between experiments, 0.1 M  $\text{NaNO}_3$  was employed, as the  $\text{Na}_{\text{K}\alpha}$  line at 1.04 keV is sufficiently far from that for Cd.

#### **7.4.1.2. Optimising Deposition Parameters**

Initial EC-XRF experiments, as shown in Figures **Figure 7.5** and **Figure 7.4**, for Cd and Hg detection produced promising results in comparison to conventional XRF capabilities. In order to develop the method further the effect of a variety of experimental parameters on EC-XRF signal intensity were investigated, with a view to optimising detection limits for both metals. For the purposes of maintaining comparability with the current UltraCarry XRF method, the EC deposition time was set at 4000 s for most experiments in this chapter. Deposition time was also investigated as ideally the overall experimental time should be as short as possible.

#### **7.4.1.3. Deposition Time**

**Figure 7.6** shows the effect of halving the deposition time (2000 s) for 1 ppm Cd solutions deposited at -1.75 V for both 4000 s (pink) and 2000 s (purple), at 20 Hz. As can be observed, when the deposition time is cut by half the peak intensity also falls by ~50%, from 5.58 cps  $\text{mA}^{-1}$  to 2.96 cps  $\text{mA}^{-1}$ , indicating

that under these time conditions deposition occurs linearly; however to establish whether this relationship holds over a wide time regime more experiments are required. These deposition times were used to illustrate the effect as the UltraCarry pre-concentration method also takes ~4000 s prior to analysis. However, in order for quantitative analysis to be possible a larger sample of deposition times should be investigated.

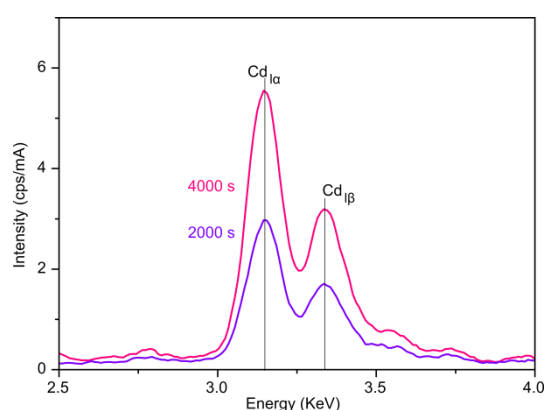


**Figure 7.6:** EC-XRF data demonstrating the effect of deposition time for 1 ppm Cd solutions deposited at -1.75 V for 4000 s (pink) and 2000 s (purple).

The effect of deposition potential on EC-XRF peak intensity was also investigated ( $E_{1/2} = -1.23\text{V}$  vs. SCE). It is observed in **Figure 7.8** that as the magnitude of deposition potential is increased, the signal intensity also increases indicating a voltage limited system (*i.e.* the deposition potential applied limits the deposition rate). However, the magnitude with which intensity increases is reduced, suggesting that the system may be affected by the formation of bubbles at the electrode surface under more extreme potentials. It is likely that the deposition potential could be further increased to produce larger XRF signals, although as the potential approaches -2 V the cathodic edge of the solvent window, **Figure 7.7**, is reached resulting in water

reduction at the electrode. Reduction of the solvent during electrodeposition can limit deposition efficiency, interfering with metal deposition and also producing bubbles; in this format, with a downwards facing recessed electrode, bubbles become stuck to the electrode surface and as a result reduce the active electrode area. Once more, in order to fully quantify the effect of deposition potential it is of interest to conduct further experiments at more potentials.

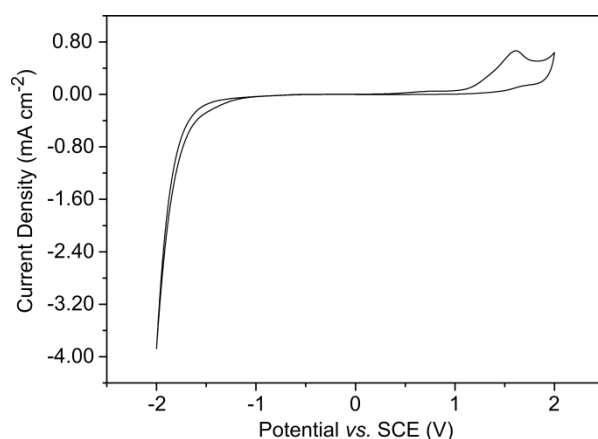


**Figure 7.7:** Solvent window for BDD EC-XRF electrode in 0.1 M KNO<sub>3</sub>.

As such experiments were conducted at potentials no more negative than -1.75 V to avoid excess bubble formation. A move to an impinging jet type<sup>33</sup>, or channel flow<sup>34, 35</sup> system may allow the application of more extreme deposition potentials to further increase detection sensitivities, as any bubbles produced would be carried away from the electrode surface. Alternatively, working under pressurized conditions would suppress bubble formation, also allowing the application of more extreme deposition potentials.<sup>36, 37</sup>

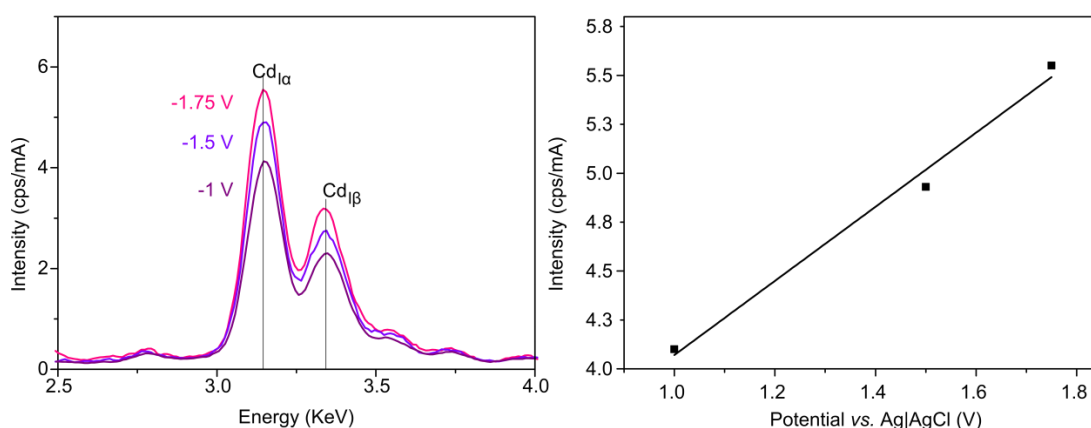


**Figure 7.8:** (a) EC-XRF data demonstrating the effect of deposition potential for 1 ppm Cd solutions deposited for 4000 s at -1 V, -1.5 V, and -1.75V. (b) deposition potential vs. EC-XRF signal intensity.

#### 7.4.1.4. Calibration

To quantify the detection capabilities afforded by EC-XRF analysis for Cd, a series of solutions at different Cd concentrations (0.05, 0.1, 0.25, 0.5, 0.75 and 1 ppm) were analysed after electrodeposition at -1.75 V (where the signal intensity is highest) for 4000 s, at 20 Hz. Typical results are presented in **Figure 7.9(a)**. A concentration vs. peak intensity calibration line, produced from 3 experimental repeats, is presented in **Figure 7.9(b)**; the EC-XRF response was found to be linear (slope =  $6.21 \pm 0.15$  cps mA<sup>-1</sup> ppm<sup>-1</sup>,  $R^2 = 0.997$ ) over the measured range, with minimal deviation evident from the small error bars. The LOQ and LOD were calculated from the measured noise intensity (0.099 cps mA<sup>-1</sup>), to be 25 ppb (0.68 μM), and 18 ppb (0.49 μM) respectively. Lower detection limits could be obtained via longer deposition; however this demonstrates a marked improvement over the UltraCarry method, where the LOD is over 30x larger.

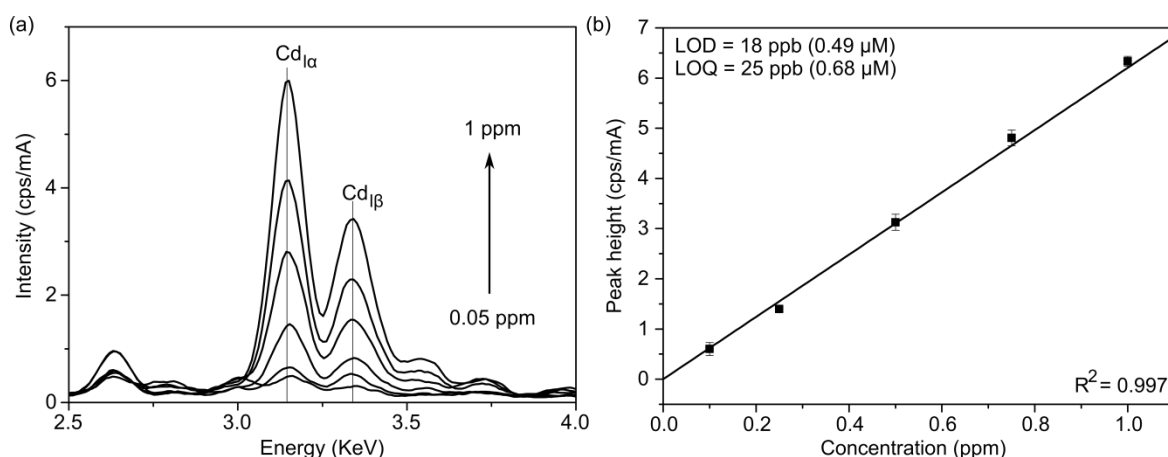


**Figure 7.9:** (a) EC-XRF data and (b) Calibration data showing mean EC-XRF Cd<sub>Iα</sub> peak intensity vs. Cd deposition solution concentration for 3 experimental repeats; slope =  $6.21 \pm 0.15 \text{ cps mA}^{-1} \text{ ppm}^{-1}$ ,  $R^2 = 0.997$ . Electrodeposition was conducted prior to experiments for 4000 s at -1.75 V for solutions of Cd concentrations between 0.05 ppm and 1 ppm.

## 7.4.2. Hg Detection

### 7.4.2.1. Calibration

Similarly, an attempt to quantify Hg detection limits was made using deposition conditions of -1.75 V for 4000 s over a range of Hg concentrations (0.05, 0.1, 0.25, 0.5, 0.75, and 1 ppm), at 20 Hz. Typical data is presented in **Figure 7.10(a)**. However, a plot of peak intensity vs. concentration (**Figure 7.10(b)**), shows that the relationship is not linear for this liquid metal system; markedly higher intensities are seen at the higher concentrations. This is unexpected based on previous results in the literature for Pb, Cu<sup>9</sup> and Pd<sup>38</sup> systems which all show linear behavior between peak intensity and concentration over a wide concentration range. With a liquid metal deposited on the surface, other factors must be contributing the non-linearity. Two of these, the effect of washing and effect of rotation on electrodeposition of Hg were investigated in more detail.

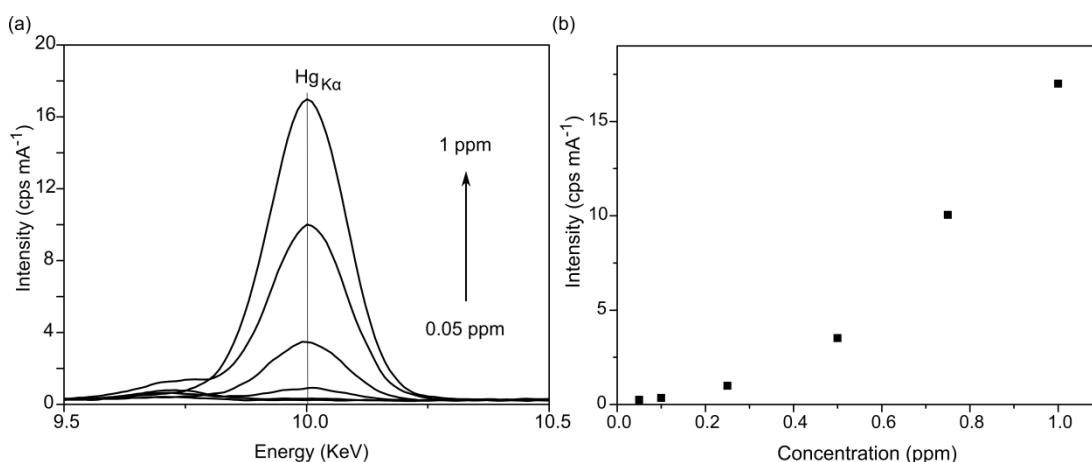


**Figure 7.10:** (a) EC-XRF data and (b) XRF signal intensity vs. deposition solution concentration, for different concentrations of Hg (0.05 ppm to 1 ppm) deposited for 4000 s at -1.75 V.

#### 7.4.2.2. Effect of Electrode Washing and Rotation

In order to establish whether washing the electrodes after Hg electrodeposition was responsible for loss of signal due to Hg removal, EC-XRF experiments were conducted with and without washing for a 1 ppm Hg solution deposited at -1.75 V for 4000 s. The washing step involved rinsing the electrode gently but thoroughly with Milli-Q water after electrodeposition had taken place. The unwashed electrode instead had a droplet of Milli-Q water pipetted on top and then tipped off, in an attempt to dissolve and remove any excess salt. Both electrodes were dried in air before analysis. As can be seen in **Figure 7.11**, the signal intensity for the washed sample (purple) is significantly lower than that for the unwashed sample (pink), indicating that deposited Hg is prone to removal by even the gentle washing procedure normally used for EC-XRF. Note that in XRF experiments alone the signal for 1 ppm Hg is barely discernible, **Figure 7.4**, so it is unlikely that Hg ions present in solution are contributing significantly after evaporation.

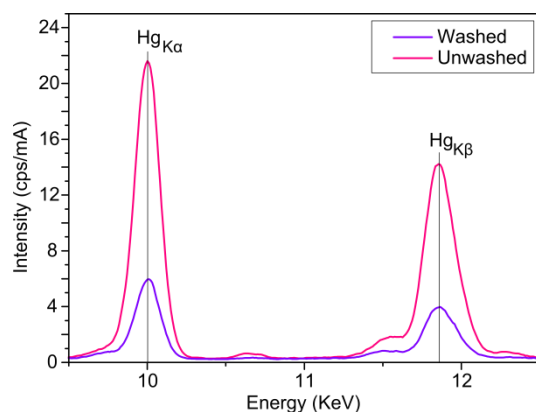


**Figure 7.11:** EC-XRF data for 1 ppm Hg solutions deposited at -1.75 V for 4000 s with (purple) and without (pink) washing after deposition, demonstrating that some XRF signal intensity is lost after the washing process.

The other important question raised by EC-XRF detection of Hg is whether rotation of the electrode during deposition has any effect on deposition morphology or stability, and if so to what extent. It has been observed in literature that under certain conditions a Hg film electrode will maintain stability under rotation,<sup>39, 40</sup> microjet<sup>41</sup> and channel<sup>42, 43</sup> flow conditions.<sup>44, 45</sup> However, they are unstable under high flow rates<sup>46</sup> and it is likely that if the deposited Hg does not form a complete surface, and instead forms isolated droplets, these will be more prone to motion. Some effort towards understanding this was made, in the form of FE-SEM investigations of a Hg deposited surface. A 1 ppm solution was deposited on the electrode at -1.75 V for 4000 s with a 20 Hz rotation speed, the electrode was then rinsed using a pipette as described above (to avoid loss of Hg during washing). FE-SEM images of different areas of the electrode are presented in **Figure 7.12**.

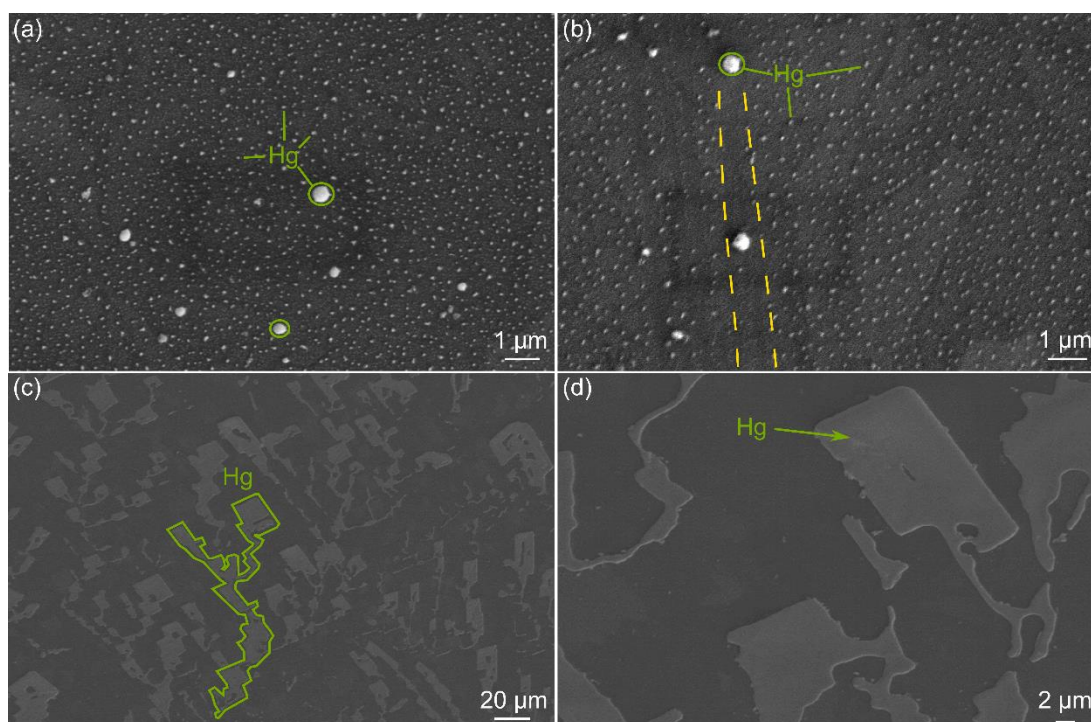


**Figure 7.12:** SEM images for 1 ppm Hg deposited under rotating conditions for 4000s at -1.75 V. All images are from different areas of the same electrode and the same instance of deposition. (a) Droplets (indicated by green lines); some appear to be coalescing into larger droplets (highlighted in green circles). (b) Droplets (e.g. highlighted in green) with clear channels (example bordered in yellow dashes). (c) Branched channels with square pools at the terminus (e.g. Green highlighted area). (d) Square/rectangular terminus of branched structures (e.g. highlighted by green arrow).

The image in **Figure 7.12(a)** was taken from a central area of the electrode and exhibits small ( $<1\ \mu\text{m}$ ) roughly spherical particles or droplets, with some larger objects thought to be droplets formed from the coalescence of multiple smaller ones, examples highlighted in green. This was corroborated in e.g. **Figure 7.12(b)**, where empty tracks, highlighted by yellow border, could be observed between the small droplets often with a larger droplet at the end, suggesting the larger droplets may be rolling across the BDD surface during rotation, collecting smaller droplets in the process. **Figure 7.12(c)** was taken towards the edge of the BDD deposition area, here instead of small droplets



larger branching tracks are visible with very regular square-edged terminus (highlighted in green and viewed at higher resolution in *Figure 7.12(d)*); possibly resulting from streams of Hg droplets converging and then diverging in the direction of solution flow, and forming pools after cessation of the deposition procedure. Though the BDD is polished flat on a nm scale, it is known that grains with different dopant levels polish at different rates<sup>47, 48</sup> leaving protruding grains, as higher B content makes the diamond very slightly softer. It is therefore possible that the observed Hg features follow the grain morphology of the BDD.

It appears that under rotating conditions, electrodeposited Hg is indeed prone to not only being washed off the electrode but also to forming mobile droplets and rivers on the surface. In order to further examine this phenomenon, future studies should be conducted under stationary deposition conditions and at a variety of Hg concentrations for comparison. Clearly though, there is an issue with Hg loss which will complicate EC-XRF analysis. One suggestion for improvement is to form trenches in the electrode surface which could be used to capture Hg and prevent its loss; concentric circle channels, pits, and spider-web type channels (concentric circles connected via asymmetrical radial channels) are all possible examples to be explored.

#### **7.4.3. Selective Deposition From a Mixed Metal Solution**

Another advantage of electrodeposition over other common XRF pre-concentration techniques is the potential for selective metal deposition from a complex sample. Where there are two or more metals in solution with

sufficiently different electrodeposition potentials it is possible to selectively deposit the metal with the least negative potential, by applying a potential larger than this but less negative than that of the other metal(s). In order to test this, a mixed solution of Hg and Cd was investigated. Firstly, the  $E_{1/2}$  for each metal was established using LSV under stationary conditions in 0.5 ppm single metal solutions of Cd and Hg, **Figure 7.13(a)** and **(b)** respectively, to ensure they were sufficiently isolated. As can be observed, the nucleation potential for Cd on BDD vs. SCE was approximately -0.9 V ( $E_{1/2} = -1.23$  V), whereas for Hg it was much less electronegative at approximately +0.4 V ( $E_{1/2} = +0.2$  V). This suggests it should be possible to selectively deposit Hg by holding the electrode at a potential  $-0.9 < V \leq +0.1$ , allowing deposition only of Hg. Due to the complicated nature of codeposition of different metals for quantitative analysis, especially at higher concentrations, it may be preferable to either selectively electrodeposit the metal of interest or exhaustively remove the interfering metal from solution. Note, this relies on small enough volumes of sample for exhaustive depletion.

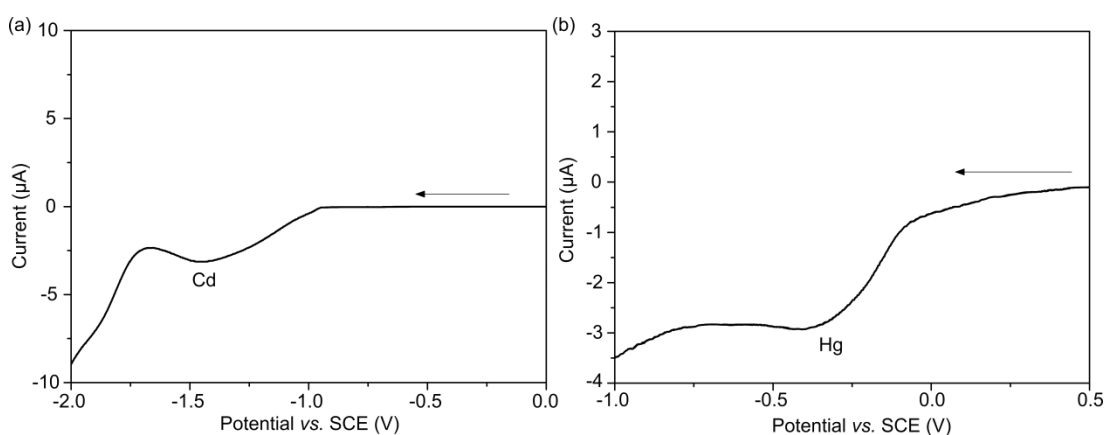


**Figure 7.13:** LSVs showing the onset of electrodeposition for (a) Cadmium and (b) Mercury at 0.5 ppm.

To test this, EC-XRF experiments were used to analyse the deposition of Hg and Cd on a BDD electrode first at a potential within the “Hg only” range, and subsequently a potential at which both metals would deposit. Initially a potential of -0.5 V was applied for 4000 s, rotating at 20 Hz, in a mixed solution of 1 ppm Hg and 1 ppm Cd; the electrode was removed from the solution and analysed as described previously via XRF for both Cd and Hg. After analysis the electrode was cleaned and replaced in a fresh solution, where deposition was conducted at -1.75 V for 4000 s, rotating at 20 Hz, before repeating the XRF analysis. The resulting data is presented in **Figure 7.14**; as expected no signal is observed for Cd under deposition at -0.5 V, but at -1.75 V a clear  $\text{Cd}_{\text{L}\alpha}$  peak is visible (**Figure 7.14(a)**). For Hg however, the  $\text{Hg}_{\text{K}\alpha}$  signal is clearly present at both deposition potentials, and scales with potential as observed for Cd in **section 7.4.1.2**. Note that due to the revised washing procedure to avoid Hg loss, the peak currents are much higher than those observed in the attempted Hg calibration. The Cd peak currents are also increased, this is thought to be due to enhancement from codeposition interactions as discussed previously for mixed metal solutions.

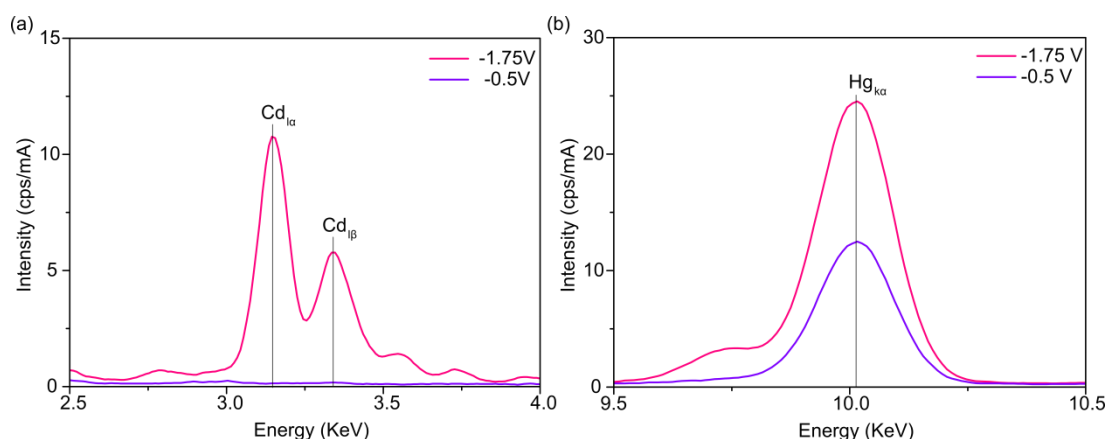


**Figure 7.14:** EX-XRF data for (a) Cd and (b) Hg, in mixed metal solutions of 1 ppm Hg and 1 ppm Cd deposited at -0.5 V and 1.75 V for 4000 s.

Exhaustive depletion also would be possible using this technique, provided electrolysis is run long enough for a given volume of solution. It is calculated that for a 1 ppm  $\text{Hg}^{2+}$  solution, of solution volume  $50 \text{ cm}^3$ , exhaustive removal results in a mass of 0.05 mg Hg deposited on the EC-XRF electrode surface. From the Hg reduction current ( $\sim -3 \mu\text{A}$  at -0.5 V) in **Figure 7.13(b)** for 0.5 ppm Hg, it is calculated that at 4000 s a mass of 0.012 mg Hg is deposited, 50 % of the total Hg mass for exhaustive depletion.

## 7.5. Conclusion

In this chapter a method is developed towards the quantitative detection of Cd and Hg in both individual and mixed metal solutions. Deposition parameters were established for optimum Cd detection under conditions equivalent to those used for the current UltraCarry pre-concentration method. Using these parameters EC-XRF LOQ and LODs for Cd were found to be 25 ppb ( $0.68 \mu\text{M}$ ) and 18 ppb ( $0.49 \mu\text{M}$ ) respectively, a significant ( $>30$  fold) improvement over the UltraCarry method. For Hg however, a consistent calibration was not achieved and it was found that the liquid nature of the electrodeposited metal

caused difficulties in analysis, likely complicated by a combination of droplet coalescence and movement during rotation and loss during washing. As such, further work in this area is suggested to enable the capture of liquid Hg on the electrode for analysis. In addition a repeat Hg calibration should be made using the revised washing procedure, to investigate whether this improves linearity across the entire concentration range. Furthermore it has been demonstrated that in a mixed metal solution of Hg and Cd, selective deposition of Hg is possible; leading to potential applications for EC-XRF in analysis of specific metals in mixed metal systems, where selective electrodeposition or exhaustive depletion may be preferable due to complicated codeposition effects, especially since the development of an *in situ* EC-XRF procedure.<sup>29</sup>

## 7.6. References

1. L. A. Hutton, M. E. Newton, P. R. Unwin and J. V. Macpherson, *Anal. Chem.*, 2011, **83**, 735-745.
2. N. V. Alov and K. V. Oskolok, *Spectrochim. Acta. B Atom. Spec.*, 2003, **58**, 735-740.
3. D. R. Gabe, *J. Appl. Electrochem.*, **27**, 908-915.
4. G. Forsberg, J. W. O'Laughlin, R. G. Megargle and S. R. Koirtiyhann, *Anal. Chem.*, 1975, **47**, 1586-1592.
5. J. Wang, J. Lu, S. B. Hocevar, P. A. M. Farias and B. Ogorevc, *Anal. Chem.*, 2000, **72**, 3218-3222.
6. J. Wang, *Stripping analysis: principles, instrumentation, and applications*, VCH, 1985.
7. C. D. Taylor and P. Marcus, *Molecular Modeling of Corrosion Processes: Scientific Development and Engineering Applications*, Wiley, 2015.
8. D. R. Gabe and D. W. Hopkins, *Principles of Metal Surface Treatment and Protection: Pergamon International Library of Science, Technology, Engineering and Social Studies: International Series on Materials Science and Technology*, Elsevier Science, 2014.
9. L. A. Hutton, G. D. O'Neil, T. L. Read, Z. J. Ayres, M. E. Newton and J. V. Macpherson, *Anal. Chem.*, 2014, **86**, 4566-4572.
10. J. Wang, *Stripping analysis*, Wiley Online Library, 1985.
11. L. A. Hutton, J. G. Iacobini, E. Bitziou, R. B. Channon, M. E. Newton and J. V. Macpherson, *Anal. Chem.*, 2013, **85**, 7230-7240.
12. S. Wang, E. S. Forzani and N. Tao, *Anal. Chem.*, 2007, **79**, 4427-4432.

13. C. Babyak and R. B. Smart, *Electroanalysis*, 2004, **16**, 175-182.
14. S. M. Khopkar, *Basic Concepts Of Analytical Chemistry*, New Age International Publishers, 1998.
15. M. Gay, M. Alfeld, M. Menu, E. Laval, P. Arias, R. Ontañón and I. Reiche, *J. Anal. Atom. Spec.*, 2015, **30**, 767-776.
16. K. Geraki, M. J. Farquharson and D. A. Bradley, *Physics in Medicine and Biology*, 2002, **47**, 2327.
17. E. Frahm and R. C. P. Doonan, *J. Archaeol. Sci.*, 2013, **40**, 1425-1434.
18. E. Marguí, B. Zawisza and R. Sitko, *TrAC Trends in Anal. Chem.*, 2014, **53**, 73-83.
19. M. West, A. T. Ellis, P. J. Potts, C. Strelí, C. Vanhoof and P. Wobrauschek, *J. Anal. Atom. Spec.*, 2015, **30**, 1839-1889.
20. F. L. Melquiades and C. R. Appoloni, *Journal of Radioanalytical and Nuclear Chemistry*, 2004, **262**, 533-541.
21. R. P. Stoessel and A. Prange, *Anal. Chem.*, 1985, **57**, 2880-2885.
22. F. Meirer, A. Singh, P. Pianetta, G. Pepponi, F. Meirer, C. Strelí and T. Homma, *TrAC Trends in Anal. Chem.*, 2010, **29**, 479-496.
23. K. Hagiwara, T. Inui, Y. Koike, M. Aizawa and T. Nakamura, *Talanta*, 2015, **134**, 739-744.
24. S. Taguchi, M. Asaoka, E. Hirokami, N. Hata, H. Kuramitz, T. Kawakami and R. Miyatake, *Anal. Methods*, 2015, **7**, 6545-6551.
25. M. Moradi, Y. Yamini, J. Kakehmam and K. Ahmadi, *J. Iran. Chem. Soc.*, 2014, **12**, 831-838.
26. E. Bulska, *Pur. Appl. Chem.*, 2001, **73**, 1-7.
27. A. Ritschel, P. Wobrauschek, E. Chinea, F. Grass and C. Fabjan, *Spectrochim. Acta. B Atom. Spec.*, 1999, **54**, 1449-1454.
28. B. Zawisza and R. Sitko, *Spectrochim. Acta. B Atom. Spec.*, 2007, **62**, 1147-1152.
29. G. D. O'Neil, M. E. Newton and J. V. Macpherson, *Anal. Chem.*, 2015, **87**, 4933-4940.
30. A. J. Bard and L. R. Faulkner, *Electrochemical methods. Fundamentals and Applications*, John Wiley and Sons, 2nd edn., 2001.
31. A. Okhrimovskyy, T. Moriyama and K. Tsuji, *MEMOIRS-FACULTY OF ENGINEERING OSAKA CITY UNIVERSITY*, 2006, **47**, 21.
32. H. Stosnach, *Spectrochim. Acta. B Atom. Spec.*, 2006, **61**, 1141-1145.
33. J. L. Melville, B. A. Coles, R. G. Compton, N. Simjee, J. V. Macpherson and P. R. Unwin, *J. Phys. Chem. B*, 2003, **107**, 379-386.
34. E. Bitziou, M. B. Joseph, T. L. Read, N. Palmer, T. Mollart, M. E. Newton and J. V. Macpherson, *Anal. Chem.*, 2014, **86**, 10834-10840.
35. R. B. Channon, M. B. Joseph, E. Bitziou, A. W. T. Bristow, A. D. Ray and J. V. Macpherson, *Anal. Chem.*, 2015, **87**, 10064-10071.
36. E. C. Potter, *Electrochemistry: principles & applications*, Cleaver-Hume Press, 1961.
37. G. G. Wildgoose, D. Giovannelli, N. S. Lawrence and R. G. Compton, *Electroanalysis*, 2004, **16**, 421-433.
38. Z. J. Ayres, M. E. Newton and J. V. Macpherson, *Analyst*, **In Submission**.
39. A. Economou and P. R. Fielden, *Analyst*, 1993, **118**, 47-51.
40. P. J. Daly, D. J. Page and R. G. Compton, *Anal. Chem.*, 1983, **55**, 1191-1192.
41. J. V. Macpherson and P. R. Unwin, *Anal. Chem.*, 1997, **69**, 5045-5051.
42. F. Zhou, J. T. Aronson and M. W. Ruegnitz, *Anal. Chem.*, 1997, **69**, 728-733.
43. E. B.-T. Tay, S.-B. Khoo and S.-W. Loh, *Analyst*, 1989, **114**, 1039-1042.
44. F.-M. Matysik and G. Werner, *Analyst*, 1993, **118**, 1523-1526.
45. A. Economou, A. K. Clark and P. R. Fielden, *Analyst*, 2001, **126**, 109-113.
46. A. Economou and P. R. Fielden, *Analyst*, 2003, **128**, 205-213.

47. B. S. El-Dasher, J. J. Gray, J. W. Tringe, J. Biener, A. V. Hamza, C. Wild, E. Wörner and P. Koidl, *Appl. Phys. Lett.*, 2006, **88**, 241915.
48. J. V. Macpherson, *Phys. Chem. Chem. Phys.*, 2015, **17**, 2935-2949.

## 8 Conclusions and Future Directions

### 8.1. Conclusions

BDD has attracted much interest in recent years for a huge range of electroanalytical applications. As discussed in detail in Chapter 1 its extreme physical and chemical properties such as: resistance to corrosion and fouling, chemical inertness, biocompatibility, and hardness, make it a desirable material for many purposes. In addition to this the wide solvent window, and low background currents characteristic of good quality, highly doped BDD make it extremely promising as a replacement for the now prohibited Hg electrode.

One such application of BDD is the electrochemical detection of trace heavy metal species in the environment; the toxicity and widespread environmental impact of heavy metals makes them a key interest for analysts worldwide. Despite this interest electroanalysis of trace metals still presents a variety of issues, especially where *in situ* measurement is concerned. One key issue is the often significant effect of pH on heavy metal speciation, availability, and therefore electroanalysis. In this thesis novel approaches to *in situ* electroanalysis of heavy metals were developed and applied to detection of Hg, Cd, and Cu, the latter in the presence of a pH sensitive Cu-binding ligand.

Chapter 3 describes the development and characterisation of an epoxy sealed, individually addressable BDD ring disc electrode as a means to control the



local pH of the detector electrode. This concept is illustrated by detecting  $\text{Hg}^{2+}$ , using anodic stripping voltammetry.

In particular, the electrochemical oxidation of  $\text{H}_2\text{O}$  at the ring (generator) electrode was used to produce a flux of  $\text{H}^+$  across the disc (detector) electrode, decreasing the local pH. An electrodeposited  $\text{IrO}_x$  film on the disc electrode enabled characterisation of the generated pH for a given generator current. It was found that a local change of over four pH units was possible (from pH 6.4 to pH 2.0), for current densities of  $6.63 \text{ mA cm}^{-2}$ , which remained stable for at least 600 s (sufficient time for electroanalysis of Hg to be conducted).

Using pH generation conditions which can produce a local environment where all the  $\text{Hg}^{2+}$  is in labile form (i.e.  $\text{pH} \leq 2$ ), it was shown that a  $\text{Hg}^{2+}$  stripping response in a bulk pH 6.4 solution equivalent to that in an (ideal) bulk pH 2 solution, could be produced. This is sufficient to prevent any complexation of  $\text{Hg}^{2+}$  with  $\text{OH}^-$  ions. It is believed that this technique holds great potential for use *in situ* in the aqueous environment. In particular by changing pH locally it is possible to determine free metal content at the measurement pH and then by decreasing pH, total free metal content, which is equivalent to traditional ICP-MS or ICP-OES measurements.

Often in the environment the metal can be complexed to a whole host of ligands which reduce the availability of metal species of interest for electrochemical detection. In Chapter 4 a similar ring disc device was applied to investigate, manipulate and measure  $\text{Cu}^{2+}$  speciation in the presence of the pH dependent  $\text{Cu}^{2+}$  binding ligand TETA. It was demonstrated via a

combination of UV-Vis titration and speciation simulations that  $\text{Cu}^{2+}$  exists uncomplexed at low pH values, when the TETA ligand is fully protonated. Electroanalysis in a series of solutions at different bulk pH confirmed this correlation of  $\text{Cu}^{2+}$  speciation with pH.

It was further demonstrated that by simply generating sufficient protons in the vicinity of the detector electrode it was possible to switch from 100% bound copper (at pH values  $\geq 5.01$ ), to 100% free  $\text{Cu}^{2+}$  (at pH values  $\leq 2.50$ ) allowing monitoring of Cu speciation (using stripping voltammetry). This approach could be used to investigate a wide range of pH dependent equilibria. Additionally, it also offers the opportunity for quantification of both total and free metal ion concentration in one measurement, a highly useful tool for *in situ* analyses.

One issue highlighted by the work in Chapters 3 and 4 was the poor durability of the epoxy-BDD seal. In each case the epoxy around the generator was found to eventually erode and fail under the influence of such extreme generator currents, possibly due to bubble formation at the electrode edges. Chapter 5 addresses this issue, describing the development and characterisation of high quality co-planar diamond insulated BDD ring disc electrodes. The use of non-conductive diamond as an insulating material for the electrodes provides the same extreme material and chemical properties as the electrode material itself. Coupled with homoepitaxial growth at the electrode boundaries, this allows the production of devices with long-term stability and the ability to endure such extreme electrode currents. It was

found that, after some development, the method described could be used to produce high quality BDD ring disc electrodes (or any other 2D geometry) which exhibit excellent electrochemical properties and can be tailored to the desired application.

Until this point, the pH generation work had been conducted in simple, unbuffered salt solutions. However, in the natural environment there are many other factors present which may affect the effectiveness of pH generation. One such factor is natural buffer systems which, in order to maintain homeostasis, will act to oppose any changes in pH. As such, for the BDD pH generation devices to have any use *in situ* it is important that the effect of buffered systems on the generated pH profile is understood, and that any buffering can be overcome.

In chapter 6 the pH generation profile, using a ring-disc set-up, for a given applied current was monitored in a series of different buffer solutions at different concentrations (0 mM, 0.1 mM, 1 mM and 10 mM) via confocal microscopy. It was observed that, for all concentrations tested, generation of a localised pH change was indeed possible. Additionally, as may be expected, increasing the buffer concentration caused the advance of the  $H^+$  front across the disc electrode to slow. FEM simulations were used in an attempt to model the system; however a successful fit was only achieved for the 1 mM buffer solution, indicating a much more complex system than initially thought. Ideally, simulation could be used to predict the behaviour of the pH generation electrode in a range of environmentally relevant buffers, such as

phosphate and carbonate. The results in this chapter indicate that pH control should indeed be possible under environmental buffer concentrations, a promising sign for the future development of this technique.

Finally, another issue for electroanalysis of heavy metals using stripping voltammetry is the ambiguity in stripping peak assignment in unknown mixed metal solutions. Combining electrochemical pre-concentration of metals on an electrode surface with XRF analysis provides a method with the sensitivity due to the pre-concentration capabilities of electroanalysis and the ease of chemical identification and quantification characteristic to XRF. The newly developed EC-XRF technique was applied in Chapter 7 to the detection of two key heavy metals, Hg and Cd. Important considerations to heavy metal analysis with this technique included electrode placement, supporting electrolyte, and rotator design. A linear calibration for Cd solutions was achieved, with a LOD of 18 ppb (0.49  $\mu\text{M}$ ), an improvement of  $\sim 30\times$  over standalone XRF methods, with potential scope to reach even lower detection limits. However, Hg analysis proved more challenging and it is thought that the liquid nature of deposited Hg metal at room temperature under the influence of rotation caused the loss of deposited analyte at high concentrations. This led to the non-linearity of the XRF signal intensity with relation to concentration. Further investigation into a solution for this issue is necessary; a possible consideration is patterning of the electrode surface in order to trap the Hg and prevent it running out of the analytical area.

## 8.2. Future Directions

Several proof of concept methods for improving electrochemical heavy metal detection have been described and demonstrated in this thesis. These methods could have a great impact on *in situ* monitoring of heavy metals, and indeed for other species and applications.<sup>1</sup> In addition to the work presented herein I believe there is much scope for further development, some ideas for future directions are presented in the remainder of this chapter.

### 8.2.1. Towards Ideal All Diamond Ring Disc Devices for pH Generation and control.

In this work the development of co-planar all diamond ring disc devices for *in situ* electrochemical pH control was described. It was established through FEM simulations that decreasing the size of the disc electrode increased the rate of pH change and also the magnitude of the pH change, both of which are desirable properties. Decreasing the disc size also has the advantage of, at micro-scales, approaching hemispherical diffusion, thus improving detection sensitivity due to the increased flux of analyte to the surface. However, as explained previously current device sizes are limited by the fabrication method. Ideally the method would be improved such that micro-dimension disc electrodes could be produced in a diamond insulated ring disc system. One proposal is a combination of two previously used methods of all-diamond device production; a BDD substrate ( $\leq 100\ \mu\text{m}$ ) could be laser micromachined such that a micro-sized pillar is formed,<sup>2</sup> this would be overgrown with insulating diamond and the front surface polished back to reveal a BDD UME encased in insulating diamond, **Figure 8.1**.<sup>3, 4</sup>

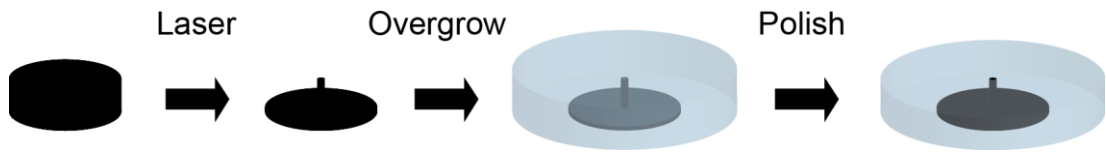


**Figure 8.1:** Schematic of the proposed method for all diamond ring-UME growth, step 1 forming the BDD UME disc in insulating diamond.

Laser trenches of the desired dimensions (i.e. 100  $\mu\text{m}$  width) would be machined into the top surface of the insulating diamond, surrounding the BDD UME. Once again the substrate will be overgrown and polished back but this time with a layer of BDD, resulting in a BDD UME surrounded by a separate BDD ring and all insulated in diamond, **Figure 8.2**. The rear of the UME will be coplanar with the rear surface of the insulating diamond, allowing direct application of Ti/Au contacts, however as before the ring electrode will require laser machined back contacting holes prior to sputter deposition of the contacts. Another option would be to change to fabrication procedures which use etching, however it would likely be necessary to go to single crystal diamond to avoid grain size limitations as the electrode size decreases.



**Figure 8.2:** Schematic of the proposed method for all diamond ring-UME growth. Step 2, producing the ring.

### 8.2.2. Towards Ideal All Diamond Ring Disc Devices for *in situ* pH Generation and measurement with simultaneous analyte detection.

It has recently been demonstrated that BDD electrodes can be used to measure pH when selectively functionalised with laser ablated  $sp^2$  regions.<sup>5</sup> An obvious future avenue would be to combine this method with the *in situ* pH generation technique described in this thesis, producing a device capable of both generating a pH change and measuring it whilst simultaneously detecting any pH sensitive analyte of interest. This offers the advantage over the IrOx film used in this thesis due to the increased stability of BDD over an electrodeposited film, especially for potential use in long term *in situ* measurements. In order to do this one electrode of a dual-ring disc device will be laser micromachined after growth to introduce pH sensitive  $sp^2$  regions. The device will be acid cleaned before back contacts are made as described previously; it is important at this stage to ensure any back contacts to the pH detector electrode do not overlap with the micromachined pits, as this could create holes through the front face of the diamond. As such it is suggested that the outer ring electrode be functionalized for pH detection, allowing maximal coverage with minimal overlap with the back contact. In this arrangement the middle ring would be used to control pH change, as if the electrode separation is kept constant on both sides this should flood both the pH detector and the analytical electrode equally.

In order to test the device, an iridium oxide film on the disc (detector) could be used to detect generated pH change (as in **Chapter 3**), and compared to

the response at the functionalized BDD pH sensor ring. Thus allowing calibration for any offset between the pH change observed at the disc, and that at the BDD pH sensor due to their different locations. For studies where a particular generated pH change is desirable, a feedback system could be setup wherein if the detected pH drops or increases beyond a certain value a signal is sent to the generator to correct for this. A device such as this would offer dynamic *in situ* pH control with simultaneous analyte detection, where the all diamond nature will allow it to withstand much more extreme environments than may otherwise be possible. In addition, the ability to improve deposition efficiency in stationary solution by adjusting local pH could potentially solve the issues with Hg loss observed during EC-XRF experiments.

### 8.3. References

1. N. Lowry, A. McLister, K. McCreadie and J. Davis, *Medical Hypotheses*, 2015, **85**, 192-196.
2. D. Wakerley, A. G. Guell, L. A. Hutton, T. S. Miller, A. J. Bard and J. V. Macpherson, *Chem. Commun.*, 2013, **49**, 5657-5659.
3. A. L. Colley, C. G. Williams, U. D'Haenens Johansson, M. E. Newton, P. R. Unwin, N. R. Wilson and J. V. Macpherson, *Anal. Chem.*, 2006, **78**, 2539-2548.
4. M. Pagels, C. E. Hall, N. S. Lawrence, A. Meredith, T. G. J. Jones, H. P. Godfried, C. S. J. Pickles, J. Wilman, C. E. Banks, R. G. Compton and L. Jiang, *Anal. Chem.*, 2005, **77**, 3705.
5. Z. J. Ayres, A. J. Borrill, J. C. Newland, M. E. Newton and J. V. Macpherson, *Anal. Chem.*, 2016, **88**, 974-980.